PSL UNIVERSITÉ PARIS

THÈSE DE DOCTORAT
DE L'UNIVERSITÉ PSL

Préparée à l'École Normale Supérieure

Realisation of Laughlin's topological charge pump in an atomic Hall cylinder

Soutenue par
Aurélien FABRE
Le 02 décembre 2022

Ecole doctorale n° 564
Physique en Île-de-France

Spécialité
Physique quantique

Composition du jury :

Isabelle BOUCHOULE Université Paris-Saclay	*Présidente du jury*
Martin WEITZ University of Bonn	*Rapporteur*
Laurent SANCHEZ-PALENCIA École polytechnique	*Rapporteur*
Leonardo MAZZA Université Paris-Saclay	*Examinateur*
Sylvain NASCIMBENE École Normale Supérieure	*Directeur de thèse*

ENS | PSL

Laboratoire Kastler Brossel
Physique quantique et applications

COLLÈGE DE FRANCE 1530

Abstract

This thesis presents experimental studies performed with ultracold samples of atomic dysprosium. The electronic properties of dysprosium lead to a large magnetic moment, a large total angular momentum $J = 8$ in the electronic ground state and a rich spectrum of narrow optical transitions with non-negligible tensor light shifts. Our work relies on using lasers tuned close to such transitions to manipulate atomic spin states and we begin by briefly describing a set of experiments that study the entanglement of non-classical states prepared in the ground level manifold, by explicitly partitioning the system via optical coupling.

The main focus of this manuscript is the realisation of artificial gauge fields for the motion of neutral atoms. The simulation of a quantum Hall system benefits from the large spin in the electronic ground level, which we interpret as a synthetic lattice with $2J + 1 = 17$ sites. These lattice sites are coupled by two-photon Raman transitions using counter-propagating laser beams, where the net momentum acquired in a hopping process is equivalent to a spatially varying Aharonov-Bohm phase. Combining spin couplings with different hopping ranges, we effectively engineer an atomic cylinder with a cyclic axis composed of three sites and a uniform radial field, yielding a quantum Hall effect on its surface. We control an additional longitudinal magnetic flux that pierces the cylinder and realise Laughlin's topological charge pump, a quantised particle transport process related to the integer quantum Hall effect. We measure the first Chern number, a topological invariant, and confirm the non-trivial topology of our system of non-interacting particles.

We also present preliminary experimental results on quantum Hall physics in four dimensions by optically coupling two independent synthetic dimensions encoded in the atomic spin to two spatial ones. We then describe theoretically the role of interatomic interactions on the atomic Hall cylinder and highlight their properties along the synthetic dimension. Finally, we discuss a proposal for the realisation of an artificial gauge field for the motion of dysprosium atoms in real space, mediated by the coupling between the internal and external degrees of freedom.

Résumé

Cette thèse présente des études expérimentales réalisées avec des échantillons ultrafroids de dysprosium atomique. Les propriétés électroniques du dysprosium conduisent à un grand moment magnétique, un grand moment angulaire total $J = 8$ dans l'état fondamental électronique et un riche spectre de transitions optiques fines avec des décalages lumineux tensoriels non négligeables. Notre travail repose sur l'utilisation de lasers accordés à proximité de telles transitions pour manipuler les états de spin atomiques. Nous commençons par décrire brièvement un ensemble d'expériences qui étudient l'intrication d'états non classiques préparés dans le niveau fondamental, en partitionnant explicitement le système via un couplage optique.

L'objet principal de ce manuscrit est la réalisation de champs de jauge artificiels pour le mouvement d'atomes neutres. La simulation d'un système de Hall quantique est facilitée par le grand spin dans le niveau électronique fondamental, que nous interprétons comme un réseau synthétique avec $2J + 1 = 17$ sites. Ces sites du réseau sont couplés par des transitions Raman à deux photons à l'aide de faisceaux laser contrapropageants, où l'impulsion acquise dans un processus de saut est équivalente à une phase d'Aharonov-Bohm variant dans l'espace. En utilisant une combinaison de couplages de spin de différentes portées, nous préparons de manière effective un cylindre atomique avec un axe cyclique composé de trois sites et un champ radial uniforme, produisant un effet Hall quantique sur sa surface. Nous contrôlons un flux magnétique longitudinal supplémentaire qui perce le cylindre et réalisons l'expérience de pompe topologique de Laughlin, un processus de transport quantifié de particules lié à l'effet Hall quantique entier. Nous mesurons le premier nombre de Chern, un invariant topologique, et confirmons la topologie non triviale de notre système de particules en l'absence d'interaction.

Nous présentons également des résultats expérimentaux préliminaires sur la physique de Hall quantique à quatre dimensions en couplant optiquement deux dimensions synthétiques indépendantes encodées dans le spin atomique à deux dimensions spatiales. Nous décrivons ensuite théoriquement le rôle des interactions interatomiques sur le cylindre de Hall atomique et mettons en évidence leurs propriétés dans la dimension synthétique. Enfin, nous discutons une proposition pour la réalisation d'un champ de jauge artificiel pour le mouvement des atomes de dysprosium dans l'espace réel, induit par le couplage entre les degrés de liberté internes et externes.

Remerciements

Ces quelques mots viennent poser une conclusion personnelle aux trois années qui se concrétisent dans ce manuscrit et je souhaite ici remercier toutes les personnes qui y ont participé, chacun à leur niveau.

Mes premiers remerciements vont à mes collègues de l'Institut de Physique du Collège de France et du Laboratoire Kastler-Brossel, avec qui j'ai partagé ces années en passant par toutes les émotions possibles (souvent corrélées à l'état de fonctionnement de la manip, et c'est le lot des expérimentateurs). Être bien entouré par des collègues, aujourd'hui amis, est essentiel pour garder une motivation et un dynamisme intacts, sur le temps long de la thèse et des projets menés au laboratoire. Je ne peux qu'espérer trouver pareils collègues pour mon futur travail.

Mon directeur de thèse, Sylvain Nascimbene, m'a accueilli en stage de master au printemps 2019 sur l'expérience Dysprosium, puis en thèse en septembre. J'ai eu la chance de rencontrer un chercheur à la fois brillant scientifiquement et très disponible pour ses doctorants. Sa créativité et sa capacité à appréhender des thématiques de recherche variées ont ouvert de nombreuses voies et sont la source des projets que je présente dans ce manuscrit. Les nombreuses discussions que nous avons eues, sur les projets que nous menions ou de nouvelles idées, ont grandement participé à ma compréhension des concepts présentés ici et des challenges de notre champ de recherche. Même s'il reconnaît qu'il ne pourrait pas faire fonctionner la manip seul, ses connaissances expérimentales lui ont permis d'être pertinent à chaque fois que nous avons eu des problèmes techniques, c'est-à-dire très souvent. Au-delà de l'aspect professionnel, je me suis reconnu dans son caractère posé et j'ai apprécié de pouvoir discuter librement avec lui. Mes remerciements vont également à Raphael Lopes, qui m'a encadré au quotidien pendant ma première année et m'a formé à l'expérience Dysprosium et à un grand nombre de compétences expérimentales, en optique notamment. Après son retrait partiel pour se consacrer à la construction de sa propre expérience, les discussions que nous avons eues ont questionné ma compréhension des phénomènes que nous étudions et m'ont permis de progresser.

Je souhaite remercier Jean Dalibard qui dirige l'équipe Condensats de Bose-Einstein et à qui est associé la chaire Atomes et Rayonnement du Collège de France. J'ai pu bénéficier de ses connaissances et de son recul au cours de réunions sur les papiers que nous écrivions, ainsi que de ses cours magistraux chaque année, qui sont des mines d'informations présentées avec clarté. Je remercie aussi les autres chercheurs permanents de l'équipe, Jérôme Beugnon et Fabrice Gerbier, ainsi qu'Alexei Ourjoumtsev, pour les discussions impromptues dans les couloirs du laboratoire qui m'ont souvent redirigé vers de nouvelles idées et aidé à approfondir mon sujet de recherche. Ma gratitude va également à Carmen Toderasc, qui assure

le bon fonctionnement de l'équipe avec efficacité et gentillesse.

Le travail que j'ai accompli a toujours été un travail d'équipe, mené avec les autres doctorants et postdocs de l'expérience Dysprosium. Je veux les remercier tous pour ces moments passés ensemble, d'abord les anciens, Thomas, Vasiliy, Alex et Tanish, puis les nouveaux, Jean-Baptiste, Quentin, Qi et Nehal. Les premiers m'ont tout appris sur la manip et j'ai participé à transmettre le flambeau aux seconds, qui maîtrisent parfaitement l'expérience et poursuivent le travail dans de nouvelles directions. Tanish occupe une place particulière dans cette équipe pour moi parce que nous avons partagé plus de trois ans au laboratoire, avec des périodes difficiles où il a fallu retravailler des étapes entières de la manip pour la rendre fonctionnelle à nouveau. Cela a contribué à forger notre amitié et je garde finalement de ces moments de très bons souvenirs, avec de la bonne musique pour se motiver (du jazz ou une playlist low-fi dénichée sur youtube) et presque toujours un tournevis dans la poche (que je ramenais évidemment trop souvent au bureau, voire chez moi...). Jean-Baptiste, qui nous a rejoint ensuite et s'est rapidement intégré dans l'équipe, a aussi partagé avec moi presque trois ans de thèse et nous avons mené tous ensemble les projets scientifiques que je décris ici. Ce binôme puis trinôme a joué un rôle crucial dans ma thèse et je leur suis infiniment reconnaissant pour ces années passées ensemble au labo.

Mon arrivée dans le groupe a été presque simultanée à celles de Chloé et Rémy, l'une sur Rubidium, l'autre sur Ytterbium, mes deux partners in crime. Nous nous sommes mutuellement accompagnés et soutenus pendant trois ans, avec pas mal de fous rires, de restaurants et de sorties en dehors du travail pour se changer les idées (un grand merci à Chloé pour m'avoir donné la motivation pour aller à la piscine le dimanche matin à 8h). Je leur souhaite le meilleur pour leurs soutenances à venir (parce que oui, vous êtes les prochains !). Plus généralement, je remercie tous les membres du groupe Condensats de Bose-Einstein et des jeunes équipes du Collège de France, avec qui j'ai partagé de nombreux bons moments dans la salle de pause, sur la terrasse au $5^{\text{ème}}$ étage, mais aussi à l'extérieur, que ce soit au Strada, à Tran Tran Zai, à Mimi Ramen ou au Piano Vache le vendredi soir.

Je remercie les membres du jury de ma soutenance, Isabelle Bouchoule, Martin Weitz, Laurent Sanchez-Palencia et Leonardo Mazza d'avoir accepté de consacrer du temps à la lecture du manuscrit et de participer à la soutenance. Je suis reconnaissant pour leur implication et la discussion qui a suivi la soutenance. La soutenance sanctionne la fin du doctorat et j'ai été heureux qu'elle ait eu lieu en leur présence, dans le lieu où j'ai travaillé pendant ces trois dernières années.

J'adresse un grand merci à mes amis, qui m'entourent depuis plus ou moins longtemps, jusqu'à aujourd'hui et pour encore très très longtemps j'espère. Je suis particulièrement reconnaissant d'avoir pu partager la journée de la soutenance avec ceux qui ont pu venir (et n'ont pas compris grand chose vu les premiers retours !). Je remercie aussi Dimitri, soutien sans faille au cours de la thèse et de la rédaction parfois épuisante du manuscrit.

Mes plus grands remerciements vont à ma famille, et tout particulièrement à mes parents et à mon frère, à mes côtés depuis toujours, pour avoir été des piliers solides à chaque étape importante de ma vie. Ils m'ont soutenu dans tous les chemins que j'ai choisi d'emprunter et je leur dédie ce manuscrit.

Contents

Introduction

Quantum physics has proven to be an effective theory for predicting the behaviour of the elementary constituents of our universe. Its application to macroscopic systems has been fruitful for the study of intriguing collective effects, as outlined in the publication entitled "More is different" [1]. The symmetries of physical laws play a central role in the description of these systems, as does the concept of spontaneous symmetry breaking which allows for states that do not respect the underlying symmetry. Ferromagnetism in materials such as iron and the crystallisation of atoms to form solids belong to this class of states.

The discovery of robust plateaus of conductivity in a two-dimensional electron gas subjected to a magnetic field [2], now called the integer quantum Hall effect, initiated new theoretical investigations of the electronic quantum states and highlighted a new classification of the phases of matter. It led to an interdisciplinary exchange between physics and a field of mathematics called topology, first highlighted by the seminal contribution of Thouless, Kohmoto, Nightingale and Nijs (TKNN) [3] on the quantisation of conductivity in two-dimensional metals. The topology defines classes of systems that are geometrically similar, meaning that they can be continuously deformed into each other. The classification is based on topological invariants defined for the system as a whole and having integer values, such as the genus of a connected three-dimensional surface.

This concept now permeates many areas of physics and is at the heart of what are called topological insulators [4–6]. These systems are normal insulators with a gapped bulk but host gapless edge modes that are topologically protected and insensitive to disorder, due to the absence of states for backscattering [7]. They have been proposed for robust topologically-protected applications, most notably in photonics [8] and quantum computing [9]. The two-dimensional topological insulators all belong to a single class represented by the well-known quantum spin Hall insulator [10–13], the counterpart of the two-dimensional quantum Hall system with time-reversal symmetry. Ongoing research is now focusing on systems with three or more dimensions, *e.g.* those hosting Weyl points [14], which are classified according to their dimensionality [15] and integer invariants, such as a $\mathbb{Z}_2$ topological invariant for systems with time-reversal symmetry [4, 16]. This classification is also valid for topological superconductors, where the boundaries possess Majorana bound states [17].

Laughlin's seminal contribution to the integer quantum Hall effect [18] emphasized that signatures of topological states are accessible using pumping, a process of particle transport in periodically-driven potentials. His work considers a cylindrical geometry with a radial magnetic field and a tunable magnetic flux that pierces the cylinder, as

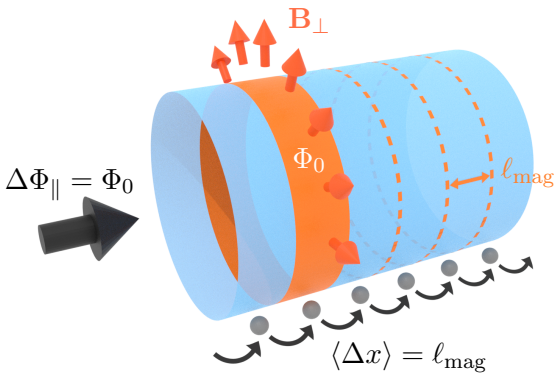

Figure 1 – Laughlin's argument for the quantisation of the conductivity. Scheme of a two-dimensional electronic system in a cylindrical geometry, with a radial magnetic field $\mathbf{B}_\perp$, yielding a quantum Hall effect, and a longitudinal magnetic field producing a magnetic flux $\Phi_\parallel$ threading the cylinder. The orange area, pierced by one flux quantum Φ_0, defines the length ℓ_{mag} separating localised electronic states. The threading of a single flux quantum $\Delta\Phi_\parallel = \Phi_0$ shifts electron occupations, causing electrons to be pumped from one edge to the other, corresponding to a quantised center-of-mass displacement $\langle \Delta x \rangle = \ell_{\mathrm{mag}}$.

represented in Fig. 1. There, a cyclic variation of the Hamiltonian via the control of the magnetic flux induces a quantised motion of particles, provided that the dynamic is adiabatic. The motion is protected by the non-trivial topological invariant that characterises the filled bands. His approach has been extended to a broader class of pumps [19, 20] and studied on various platforms, using photonic waveguides [21], quantum dots [22, 23] or cold atoms [24, 25].

Cold atoms are at the heart of this research because of our ability to control them at the level of the single atom or photon [26]. This field of research has expanded after technological breakthroughs with the development of laser sources used for trapping and cooling [27] of atomic samples towards quantum degeneracy [28]. Ultracold atoms are relevant candidates to put into practice the idea first proposed by Feynman [29], to simulate a quantum system by mapping its Hamiltonian on another system with finer control. Condensed-matter models have been investigated using cold atoms, benefiting from the ability to easily tune experimental knobs, such as the interatomic interactions, and the measurement of microscopic observables. For example, optical lattices [30], periodic potentials made of light, and neutral fermionic atoms play the role of an ionic crystal potential and electrons respectively. In the limit of deep potentials, these systems simulate the Fermi-Hubbard model [31], which can host strongly-correlated states similar to those involved in high-temperature superconductivity in cuprates [32].

The study of quantum Hall physics with cold atoms cannot be implemented directly with a magnetic field due to their neutral charge. This limitation has been overcome by engineering systems in which the particle motion is governed by an analogue of the magnetic field for a charged particle, a so-called artificial

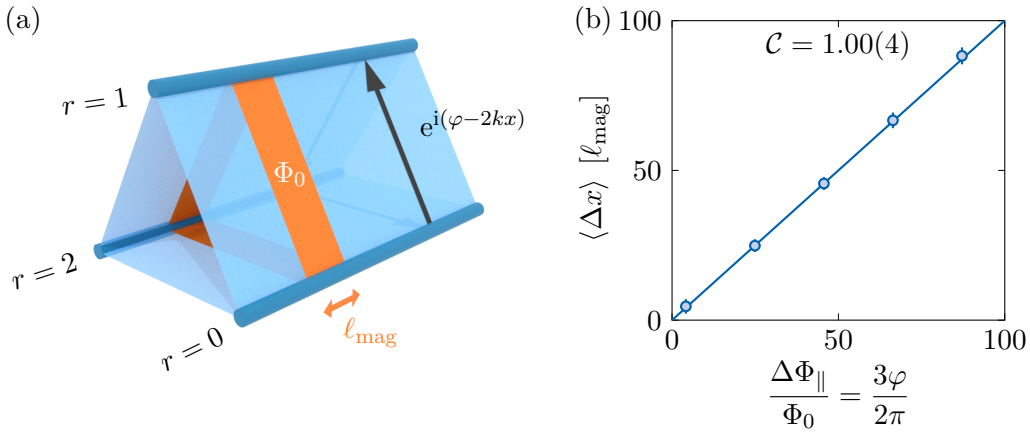

Figure 2 – Realisation of Laughlin's topological charge pump in an atomic system. Panel (a): Scheme of our realisation of an atomic Hall cylinder with a longitudinal axis x and three sites $r = 0$, 1 and 2, cyclically-coupled with a controllable phase φ that plays the role of the longitudinal magnetic flux. A radial magnetic field induces a Hall effect on the surface of the cylinder and the orange area is threaded by a flux quantum Φ_0. Panel (b): Displacement of the center-of-mass along x as a function of the threaded longitudinal magnetic flux $\Delta\Phi_\parallel$. The measurements are averaged over the Brillouin zone to probe the first Chern number $\mathcal{C}$, the topological invariant characterising the ground band of the system.

gauge field. For example, quantum Hall systems have been implemented using rotating Bose-Einstein condensates [33, 34] and atoms in shaken lattices [35, 36]. An alternative road uses the mediation of the spin by light coupling to the external degrees of freedom to engineer an artificial gauge field [37]. These platforms have reached the regime where interatomic interactions modify the quantum states with the appearance of vortices arranged in an Abrikosov lattice [38], similar to vortices in type-II superconductors subjected to a magnetic field. An extension of these approaches toward non-abelian gauge fields requires spin-orbit coupling between the quasi-degenerate internal states and the atomic motion, which has been realised in two-dimensional systems [39] and recently in three-dimensional ones [40].

Another approach for the simulation of topological systems relies on the engineering of a hybrid system composed of spatial and synthetic dimensions, where the latter can refer to dimensions encoded in the internal degrees of freedom of the atoms for example [41, 42]. An external coupling can connect electronic states of an atom, which are reinterpreted as sites of a one-dimensional lattice with a hopping term between neighbours. Artificial gauge fields in such systems have been produced using two-photon optical transitions, which couple the internal states with a complex spatially-dependent hopping phase similar to an Aharonov-Bohm phase [43, 44]. Synthetic dimensions also facilitate the exploration of systems with dimensions greater than three or with more complex geometry [45], by using a combination of couplings of different ranges for instance.

Atoms with a large total angular momentum in the ground state are well-suited to such applications, as the corresponding large synthetic dimension allows the exploration of both the bulk and edge modes in the presence of an artificial gauge field [46]. Lanthanide atoms, such as dysprosium with a total angular momentum $J = 8$ in its ground state, have a complex electronic structure characterised by the presence of narrow optical transitions away from broad ones. Compared to alkali atoms where such isolated transitions cannot be found, the regime of strong spin coupling with limited heating is accessible. Dysprosium atoms also benefit from the non-negligible tensor polarisability in the vicinity of narrow transitions that expands our spin-coupling toolbox and from the presence of long-range anisotropic magnetic dipole-dipole interactions which enriches the accessible phases of matter [47]. In this thesis, we focus on our experimental engineering of an atomic Hall cylinder, with a cyclic dimension of three sites encoded in the internal degrees of freedom of dysprosium atoms, and on our realisation of Laughlin's topological charge pump, summarised in Fig. 2.

Chapter 1 describes the key properties of dysprosium atoms and their interest for the implementation of artificial gauge fields. We provide the basic elements of the light-matter interaction, which is at the heart of all the experiments carried out during this thesis. We briefly present the laser systems that we use for the manipulation of dysprosium atoms, and in particular their frequency locking using atomic references that was developed early in the thesis.

Chapter 2 focuses on the experimental apparatus that produces a cold atomic sample. We owe a great debt to all the former members of our research group who built the experiment and contributed to its successive upgrades. Some recent changes, such as the transverse cooling of the atomic jet, the active compensation of magnetic field fluctuations and the processing of recorded absorption images, are detailed. We give an overview of our experimental techniques to characterise off-resonant laser beams, which have been regularly used for the installation of new beams.

Chapter 3 briefly presents our work on entanglement in quantum states. We interpret the large spin of dysprosium atoms as a set of virtual qubits of spin 1/2, symmetric upon particle exchange, and encode non-classical states. The notion of entanglement in these states is clarified by optically partitioning the spin into two subsystems. We also study the robustness of the entanglement in paradigmatic states upon decoherence via the loss of a qubit pair in a random state.

Chapter 4 introduces the basic theoretical elements related to the quantum Hall effect. We start with the notion of Berry curvature and Berry phase, which play a similar role to that of a magnetic field and an Aharonov-Bohm phase. The Hall effect, with its classical form and its quantum counterpart, is then presented. We focus on the case of the cylindrical geometry, related to our experimental realisation of a quantum Hall cylinder. Finally, following Laughlin's argument for the quantisation of the conductivity in a Hall system, we introduce the

notion of topological pumping and relate its properties to those of a higher-dimensional system.

Chapter 5 details our protocol for encoding two synthetic dimensions in the large total angular momentum of a single dysprosium atom. Using spin couplings of different ranges, the internal degrees of freedom are effectively described as a cylinder with a cyclic dimension of three sites. We discuss the validity of this picture and show how it can be used for the implementation of a Hall cylinder.

Chapter 6 reports on our experimental realisation of an atomic Hall cylinder. We characterise the ground band of the system and its first excitations, and then probe the transverse response to a force, typical of a charged particle in a magnetic field. We perform Laughlin's topological charge pump experiment, by controlling the effective magnetic flux that pierces the cylinder, and measure the non-trivial topological invariant associated with the ground band, the first Chern number.

Chapter 7 discusses extensions of our realisation of an atomic Hall cylinder. Initial experimental results on the engineering of a Hall system in four dimensions are presented, which proves our ability to manipulate two independent synthetic dimensions encoded in the spin of the atoms. We then discuss prospects toward many-body states in the presence of interatomic interactions in our quantum Hall cylinder with a synthetic dimension and in real space using an artificial gauge field mediated by the atomic spin.

1 Dysprosium and its interaction with light

In this Chapter, we describe some of the peculiar properties of dysprosium atoms that emerge from their electronic structure, such as the large total angular momentum in the ground state, the large magnetic moment and the dense electronic spectrum. We introduce the light-matter interaction, at the heart of the manipulation of the external and internal degrees of freedom of the atoms with coherent sources of light. We briefly present our laser systems and the spectroscopy techniques adapted to optical transitions with wide linewidths, similar to the D2 lines of rubidium atoms, as well as much narrower linewidths in the $1 - 100\,\mathrm{kHz}$ regime.

1.1 Dysprosium properties

Dysprosium is a rare-earth metal in the lanthanide line of the periodic table, with an atomic number $Z = 66$. Outside of the field of ultracold atoms, dysprosium is used for its magnetic properties in a few applications ranging from permanent magnets to magnetic data storage in a hard disk for example. Its characteristics stem from its complex electronic structure, which we will describe below. At ambient temperature, this metal has a low vapour pressure and oxidises in an air atmosphere. Due to its high melting point of $1412\,^{\circ}\mathrm{C}$, dysprosium requires a high temperature to evaporate into a gaseous sample. Seven stable isotopes exist in nature, with four of them in large and similar abundance: two fermionic and two bosonic ones. This is advantageous for the study of ultracold samples of different quantum statistics but also for the preparation of mixtures. In this thesis, we use the bosonic isotope ^{162}Dy, whose background s-wave scattering length is better suited than that of ^{164}Dy to reach quantum degeneracy.

The electronic structure of dysprosium can be written:

$$[\mathrm{Xe}]4f^{10}6s^2,$$

relative to xenon. This situation, referred to as a submerged shell, means that the $6s$ shell is fully filled with two electrons while the lower-lying $4f$ shell is still partially filled with 10 electrons out of 14 accessible orbitals. The four unpaired electrons result in a net electronic spin $S = 2$ and an orbital angular momentum $L = 6$, and the electronic ground state of dysprosium has a total electronic angular momentum

λ	$\Gamma/2\pi$	T_D	E_{rec}/h
421.3 nm	32.2 MHz	772 µK	6.95 kHz
626.1 nm	135 kHz	3.2 µK	3.14 kHz
696.0 nm	1.4 kHz		2.54 kHz
832.8 nm	11 kHz		1.78 kHz

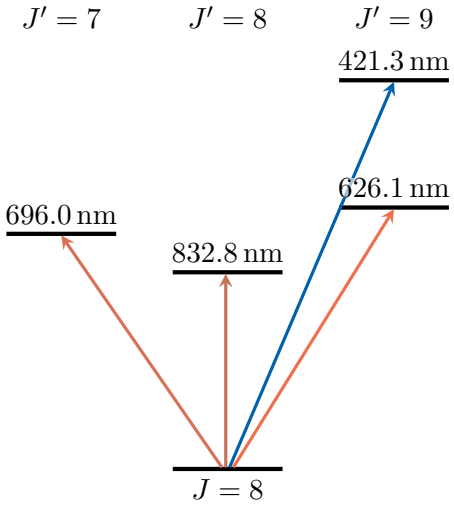

Figure 1.1 – Table: List of transitions of dysprosium atoms with their wavelengths, natural linewidths, Doppler temperatures and recoil energies. Panel: Energy spectrum with the four optical transitions that are used or studied in the work presented in this thesis.

$J = 8$. The bosonic isotopes have a zero nuclear spin and therefore a total atomic angular momentum $F = J = 8$ in the electronic ground state, while the fermionic isotopes have a non-trivial nuclear spin $I = 5/2$, which induces an additional splitting into hyperfine levels ranging from $F = 11/2$ to $F = 21/2$.

1.1.1 Electronic transitions

The electronic structure also leads to a complex structure of excited electronic states, as electrons in both the $6s$ and $4f$ shells are allowed to be promoted to higher orbitals. We show in Fig. 1.1 a tiny fraction of the energy spectrum with the optical transitions that have been exploited during this thesis, as well as some of their characteristics. The difference in nuclear mass between isotopes gives rise to an isotopic shift, proportional to the mass difference, typically of the order of a few GHz for optical transitions.

Two optical transitions, at $\lambda_{\mathrm{blue}} = 421.3\,\mathrm{nm}$ and $\lambda_{\mathrm{red}} = 626.1\,\mathrm{nm}$, respectively called blue and red transitions, are used to laser cool and image dysprosium atoms. Their very different linewidths, $\Gamma_{421} = 2\pi \times 32\,\mathrm{MHz}$ and $\Gamma_{626} = 2\pi \times 136\,\mathrm{kHz}$, make them complementary as they are suitable for different purposes. These transitions correspond to the promotion of an electron from the filled $6s$ orbital to a $6p$ orbital, corresponding to an electronic state of total angular momentum $J' = J + 1 = 9$. The red transition, classified as an intercombination line, has a narrow linewidth and is favourable for the implementation of a cold magneto-optical trap and spin manipulation. The blue transition has a wider linewidth and is more suitable for applications requiring a high cycling rate, such as Zeeman slowing and imaging, due to the short lifetime of the excited level. The three transitions at 696.0 nm, 832.8 nm and 626.1 nm, coupling to excited states with total angular momentum $J' = J - 1$, J and $J + 1$ respectively, have narrow linewidths of the order of 10 kHz and are

favourable for the implementation of spin-dependent light shifts. They are accessible with the lasers available in our experiment and the different total angular momenta J' offer various options for our experimental protocols. Other optical transitions, for example at $\lambda = 741\,\mathrm{nm}$ [48], have been manipulated and studied by other groups.

1.1.2 Magnetic properties

The magnetic properties of dysprosium are also derived from its electronic structure. The magnetic moment μ is given by:

$$\mu = m g_J \mu_B, \tag{1.1}$$

with m the spin projection on the quantisation axis, g_J the Landé g-factor (with $g_J = 1.242$ in the electronic ground state with $J = 8$ [49]) and μ_B the Bohr magneton. The strong magnetic moment of dysprosium atoms comes from the scaling of μ as J, for a fully polarised atom with $m = J$. It reaches $\mu = 9.93\mu_B$ in this case, compared to $\mu = 1\mu_B$ for rubidium (Rb), $\mu = 6.98\mu_B$ for erbium (Er) and $\mu = 9.94\mu_B$ for terbium (Tb), which is the maximum value for a single element.

The presence of an external magnetic field B_z along $\mathbf{z}$ lifts the degeneracy of the magnetic sublevels of a J-manifold. The levels, indexed by their azimuthal angular momentum m along z with an integer $-J \leq m \leq J$, acquire a linear Zeeman shift:

$$E(m) = m g_J \mu_B B_z. \tag{1.2}$$

This relation is valid for all electronic states and the g-factors for the excited states coupled via the blue and red transitions are 1.22 and 1.29 respectively. For the ground state with $g_J = 1.242$, a bias field of 1 G corresponds to a Zeeman splitting of $2\pi \times 1.738\,\mathrm{MHz}$. The difference in g-factors between the ground and excited states plays a role when tuning near-resonant laser beams close to an optical transition, in the presence of a magnetic field.

1.1.3 Interactions

Interactions [50, 51] play a central role in the phenomenology of Bose-Einstein condensates, due to the low kinetic energy of the condensed particles. The interaction between dysprosium atoms results from short-range van der Waals forces proportional to the electronic polarisability of the particles and long-range interactions between magnetic dipoles.

Two atoms located at a distance r feel a weak attractive force known as the van der Waals force, which scales as $-C_6/r^6$, with the van der Waals coefficient C_6. It competes with the strong Coulomb repulsion from the electronic orbitals at smaller distances, which scales as C_{12}/r^{12} with C_{12} a positive coefficient. At low energy, for bosons, the interaction between the particles simplifies to a contact potential[1]:

$$V_\mathrm{s}(\mathbf{r}) = \frac{4\pi\hbar^2 a_\mathrm{s}}{M}\delta(\mathbf{r}), \tag{1.3}$$

[1]This potential leads to a divergence of the scattering amplitude for wavefunctions with a singularity at the origin [52], which is resolved by considering the pseudo-potential $V_\mathrm{pp}(\mathbf{r}) = g_\mathrm{s}\delta(\mathbf{r})\partial_r[r\psi(\mathbf{r})]_{\mathbf{r}=0}$.

with $\mathbf{r}$ the relative position of the two particles, a_s the s-wave scattering length, M the mass of atomic dysprosium and $\delta(\mathbf{r})$ the Dirac delta function. The potential is repulsive (attractive) for a positive (negative) scattering length a_s, with a contact coupling strength defined as $g_\mathrm{s} = 4\pi\hbar^2 a_\mathrm{s}/M$. The background value of the s-wave scattering length is known to date only for two atoms polarised in the same extremal magnetic sublevel $m = -8$ and equals $a_\mathrm{s}^{(bg)} = 126(10)a_0$, with a_0 the Bohr radius. It can be tuned to arbitrary positive and negative values in the vicinity of a Feshbach resonance [53, 54], which occurs when the eigenenergies of the closed and open channels get close and molecular bound states are formed. Due to the difference in spin composition between the two channels, the relative eigenenergies depend on the norm of the magnetic field, which tunes the scattering length as [54]:

$$a_\mathrm{s}(B_z) = a_\mathrm{s}^{(bg)}\left(1 - \frac{\Delta}{B_z - B_0}\right). \tag{1.4}$$

where B_0 is the position of the resonance, at which the scattering length diverges, and Δ is the width of the resonance, such that the scattering length cancels out at $B_z = B_0 + \Delta$. Dysprosium and other lanthanide atoms, such as erbium, exhibit a large choice of Feshbach resonances [55, 56], due to the complexity of their electronic structure. For the bosonic isotope ^{162}Dy, narrow resonances are available for low magnetic fields [56, 57].

Due to the large magnetic moment of dysprosium atoms, the interactions between magnetic dipoles are non-negligible, compared to the s-wave interactions. The dipolar interaction obeys:

$$V_\mathrm{dd}(\mathbf{r}, \theta) = \frac{\mu_0\mu^2}{4\pi}\frac{1 - 3\cos^2\theta}{r^3}, \tag{1.5}$$

with $\mathbf{r}$ the relative position of the two particles and θ the angle between the orientation of the dipoles, set by the quantisation axis, and the vector $\mathbf{r}$. We define the characteristic length $a_\mathrm{dd} = \mu_0\mu^2 M/(12\pi\hbar^2)$ and the coupling strength $g_\mathrm{dd} = 4\pi\hbar^2 a_\mathrm{dd}/M = \mu_0\mu^2/3$, in a similar way to a_s and g_s. Interestingly, this interaction is long-range and anisotropic, which strongly modifies the physics of the interacting particles.

The ratio of the lengths $a_\mathrm{dd}/a_\mathrm{s}$ characterises the interplay between these two types of interactions at low energy. The competition between them is explored in other experiments with lanthanide atoms. Beyond mean-field effects, such as the repulsive Lee-Huang-Yang (LHY) energy [58, 59] resulting from quantum fluctuations, can become dominant if the ratio $a_\mathrm{dd}/a_\mathrm{s}$ is tuned to approximately cancel out the mean-field effects given by the dipolar and contact interactions. This idea is similar to other proposals [60, 61] with binary mixtures of tunable inter- and intra-species interactions for example. At high densities, the LHY energy stabilises the mean-field-induced collapse of the cloud. In recent years, the corresponding phase of matter, called self-bound quantum droplets, has been experimentally studied using dipolar gases [47, 62].

In addition to the elastic collisions described above, the dipole-dipole interaction also induces dipolar relaxation, which is due to inelastic two-body collisions. During a collision, two atoms can decay to lower magnetic sublevels with a release of the corresponding magnetic Zeeman energy, proportional to the strength of the bias

magnetic field. This energy is converted into kinetic energy, which causes heating and possibly losses if it exceeds the trap depth. For bosonic dysprosium, the timescale is of the order of a few ms for a magnetic field of 1 G, and strongly depends on the quantum state of the atoms.

1.2 Light-matter interaction

The manipulation of gaseous samples, as we know it today, has been triggered by the development of lasers [63], emitters of coherent light at high optical powers, and particularly of frequency-adjustable lasers. Initial breakthroughs in this field, making use of the resonant coupling of light with atoms, include the laser cooling of atoms, their trapping in magneto-optical traps and the discovery of sub-Doppler cooling techniques [27, 64, 65]. The ability to reach much lower temperatures, by several orders of magnitude, relies on the use of conservative trapping forces [66], based on the off-resonant coupling with light which does not involve either absorption or spontaneous emission of photons. In its most general form, the coupling between a light field and an atom writes:

$$H = -\mathbf{d} \cdot \mathbf{E} \tag{1.6}$$

where $\mathbf{d}$ is the atomic dipole operator and $\mathbf{E}$ is the light field.

In this Section, we present the basics of the light-matter interaction and derive the formulae and methods that are at the heart of our ability to prepare cold samples of atomic dysprosium and manipulate their internal and external degrees of freedom. We consider resonant fields and then off-resonant fields in a perturbative approach.

1.2.1 Master equation: resonant coupling with light

The resonant coupling of light with a two-level atom (with an energy difference ω_{ge}) can be understood from the following simple picture. An atom, initially in the ground state, absorbs a photon from a light field if the photon angular frequency ω is sufficiently close to the electronic transition at ω_{ge}. The atom is promoted to the excited state and acquires a net momentum kick $\hbar k$ (for a wavevector $k = \omega/c$), due to the conservation of energy and momentum. The Schrödinger equation for a two-level system in the presence of a classical light field predicts that the atom coherently evolves from the ground state to the excited state and then back to the ground state. The latter process can be thought of as a re-emission of a photon coherently with the field, associated with the transition from the excited to the ground state and a net momentum kick $-\hbar k$. This is called a Rabi oscillation, *i.e.* an oscillation of the spin polarisation defined as the difference in occupancy of the ground and excited levels, at the Rabi angular frequency Ω_0 proportional to the light intensity. Starting with an electron fully polarised in the ground state, a π-pulse transfers it to the excited state while a 2π-pulse does not modify the spin state. A $\pi/2$-pulse prepares a coherent superposition of the two levels with equal weight. These three pulses corresponds to pulse times of $T/2$, T and $T/4$ respectively, with $T = 2\pi/\Omega_0$ the period of the Rabi oscillation. This process is fully coherent and the resulting spin state at any time is a pure state, assuming that the initial state is pure. Starting from the ground state, the light field couples it to the excited state,

whose population evolves as:

$$P_e(t) = \frac{\Omega_0^2}{\Omega_R^2} \sin(\Omega_R t)^2 \tag{1.7}$$

with $\Omega_R = \sqrt{\Omega_0^2 + \Delta^2}$ the generalised Rabi angular frequency. On resonance, it is equal to the Rabi angular frequency Ω_0 and the population in the excited state reaches one for a π-pulse, which corresponds to a full population inversion. Rabi oscillations are generalisable to multilevel atoms, by taking into account the effect of the light polarisation and the Clebsch-Gordan coefficients that arise from angular momentum coupling.

In a real system, an electron in an excited state can decay to the ground state in an incoherent process accompanied by the emission of a photon in a random light mode, called spontaneous emission. The rate of occurrence of such an event is given by the linewidth of the excited level Γ, which is inversely related to the average time an electron remains in the excited state. If the linewidth of the electronic level is of the order of or greater than the Rabi frequency, it modifies the Rabi oscillations that are no longer long-lived. This competition is at the heart of the laser cooling techniques. The process of photon absorption is coherent and associated with a net momentum transfer along the propagation axis of the light field, while spontaneous emission is incoherent and accompanied by an isotropic momentum kick. On average (meaning that we consider a large number of photon absorption cycles followed by spontaneous emission), the spontaneous emission does not modify the mean value of the atom momentum. Therefore, the atoms undergo a succession of momentum kicks along the propagation axis of the light field, which promotes them to the excited state before decaying back due to spontaneous emission. Overall, resonant light, together with spontaneous emission acting on a short timescale, affects the external degrees of freedom of an atom. Optical transitions to an excited level with a short lifetime, typically on the order of a few nanoseconds, such as the blue transition at 421.3 nm for dysprosium, are well suited to this application. The effect of the light beam can be effectively rewritten as an external force, called the radiation pressure force [67], exerted on the motion of the atoms as:

$$\mathbf{F}_{\text{rad}}(\mathbf{r}) = \hbar \mathbf{k} \frac{\Gamma}{2} \frac{s}{1 + s + 4\delta(\mathbf{r})^2/\Gamma^2}, \tag{1.8}$$

for a beam of wavevector $\mathbf{k}$. It depends on the natural linewidth Γ, the saturation parameter $s = I/I_s$ (I_s the saturation intensity) and the local detuning:

$$\delta(\mathbf{r}) = \Delta - \mathbf{k} \cdot \mathbf{v}(\mathbf{r}) + \delta_\mu B(\mathbf{r})/\hbar. \tag{1.9}$$

The local detuning contains the absolute laser detuning Δ, the Doppler shift for an atom moving at $\mathbf{v}(\mathbf{r})$ and the Zeeman effect for a local magnetic field $B(\mathbf{r})$, taking into account the difference in the g-factor between the ground and excited states as $\delta_\mu = \mu' - \mu = \mu_B(g_{J'} m_{J'} - g_J m_J)$. For the right choice of parameters, this force is a damping force that slows down the atoms. In the simplest schemes, it requires a negative detuning, while a positive detuning is associated with heating. The limit of laser cooling with resonant light comes from the nature of spontaneous emission.

It acts as a random walk in momentum space, which keeps the average momentum unchanged but increases its variance. This induces a heating of the atoms that competes with the cooling effect. The lowest achievable temperature is called the Doppler limit and is proportional to the linewidth of the optical transition, which favours the use of narrow optical transitions such as the red one at 626.1 nm for dysprosium. This approach with an effective force is valid for two-level atoms, or multi-level atoms with a cycling transition, but it does not describe the internal state of the atoms.

Since spontaneous emission is an incoherent process that cannot be written in a Hamiltonian form, we turn to the framework of the so-called master equation. Lindblad master equation [68, 69] is well suited for the study of open systems [70], with applications in quantum computation [71, 72] for example. It describes the coupling of such systems to their environment, such as spontaneous emission coupling an atom to an infinity of available field modes. The possibly mixed spin states are represented by density matrices and evolve under the effect of a unitary Hamiltonian term and of incoherent processes, represented by the so-called Lindblad operators. Three operators, corresponding to the dimension of the Hilbert space of a photon polarisation, fully describe the spontaneous emission for a multi-level atom, due to the isotropic character of the emission. These operators are sometimes also called jump operators and the optical Bloch equations are a well-known example of the treatment of this problem for two-level systems, where a single jump operator is considered.

In a general case, the master equation in Lindblad form reads as follows:

$$\partial_t \rho = -\frac{\mathrm{i}}{\hbar}[H_0, \rho] + \sum_i \left(C_i \rho C_i^\dagger - \frac{1}{2} C_i^\dagger C_i \rho - \frac{1}{2} \rho C_i^\dagger C_i \right) \tag{1.10}$$

where H_0 is the unitary Hamiltonian term, containing for example the Zeeman field and the light-matter interaction, and the C_i operators are the Lindblad operators corresponding to incoherent processes. The Lindblad operator for spontaneous emission in a two-level system using the Pauli matrix formalism is written $C = \sqrt{\Gamma}\sigma_-$ with Γ the linewidth of the excited state. If we consider only the Hamiltonian part of the evolution, we recover the quantum Liouville equation for a closed system, the generalisation of the Schrödinger equation for density matrices. In the presence of incoherent processes, this type of equation is generally impossible to solve analytically and numerical approaches are required. The usual algorithms for solving sets of coupled differential equations can be used if the Hilbert size is not too large, but we also point out the existence of other numerical methods such as the quantum Monte-Carlo wavefunction method [73, 74]. In our case, the size of the Hilbert space that we will consider with the ground and excited manifolds is of the order of $4J = 32$ (more precisely $(2J+1) + (2J'+1)$ with $J' = J-1$, J or $J+1$), which is tractable.

As an example, we consider a dysprosium atom, initially in its ground state $|J, m = -J\rangle$ in the presence of a bias magnetic field along $\mathbf{z}$, which we subject to resonant light at 626.1 nm (with $J' = J+1$), propagating along $\mathbf{x}$ with linear polarisation along $\mathbf{z}$. The light beam only induces π-transitions that couple spin states in the J- and J'-manifolds with the same azimuthal angular momentum m. Given the initial state, we expect coherent Rabi oscillations between $|J, m = -J\rangle$ and

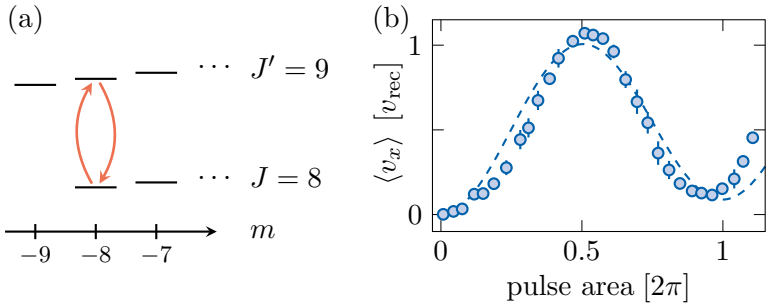

Figure 1.2 – Panel (a): Scheme of the resonant coupling between the J- and J'-manifolds using light at 626.1 nm (with $J' = J + 1$). The relevant transition for atoms initially polarised in $|J, m = -J\rangle$ is highlighted by red arrows. Panel (b): Evolution of the mean velocity of the atoms as a function of the pulse area. The dotted line is obtained by numerically solving the master equation taking into account the spontaneous emission from the excited level.

$|J', m' = -J\rangle$, as sketched in Fig. 1.2(a). For clock transitions with long lifetimes, the atoms in the excited state are shelved for long enough times and are not affected by the imaging light, that couples the ground state to another excited state. The proportion of atoms in the excited states is measured as a change in the number of atoms imaged. However, the lifetime of 1.2 µs in the excited level associated with the transition at 626.1 nm is too short compared to the typical duration of our imaging pulse of the order of tens of microseconds. Instead, we measure the Rabi flops by recording the mean velocity of the atoms, after a time-of-flight expansion of 5.1 ms, which oscillates between zero and the recoil velocity $v_{\mathrm{rec}} = \hbar k/M$.

We choose a high Rabi angular frequency to limit the effect of spontaneous emission during the resonant light pulse. We realise a π-pulse in 62 ns, which is much smaller than the lifetime in the excited state. At such short times, the pulses are at the limit of the rising time of the AOM that shapes the pulse. We account for the non-linear response of the AOM by recording the pulse shape on a fast photodiode[2] with a bandwidth of 600 MHz and measuring the pulse area instead. The full evolution of the mean velocity as a function of the pulse area is presented in Fig. 1.2(b). We observe deviations that can be explained by taking into account spontaneous emission, whose effect is small but not negligible on this timescale. Our numerical simulations are performed by solving the master equation including the coherent resonant light coupling and the incoherent decay of the excited state by spontaneous emission. We treat the external degrees of freedom of the atoms in a semi-classical way. A transition to a metastable state with a longer lifetime would allow for long-lived Rabi oscillations, not limited by spontaneous emission.

[2]FPD610-FS-VIS, Menlo Systems

1.2.2 Light shifts: off-resonant coupling with light

Off-resonant light negligibly populates the excited states, but it still affects the atoms by inducing a dipole force, which derives from a conservative potential proportional to the intensity of the light field. Away from all resonances, only the blues transitions with a wide linewidth significantly contribute and the shift is spin-independent. In the vicinity of a well-separated transition, the dipole force derives mainly from the single transition and is spin-dependent for the correct choice of light polarisation. In this Section, we briefly derive the expression of the AC Stark shift for a multi-level atom, taking into account a single transition, and we highlight the advantages of the electronic structure of lanthanide atoms over alkali species.

According to Eq. 1.6, considering at first a two-level atom (with an energy difference $\hbar\omega_{ge}$) in the presence of a monochromatic light field $\mathbf{E}$ at angular frequency ω, the light-matter potential reads:

$$V_{\mathrm{LS}} = \frac{|E|^2}{4} |\langle e|\mathbf{d}\cdot\boldsymbol{\epsilon}|g\rangle|^2 \frac{1}{\Delta + \mathrm{i}\Gamma/2}, \tag{1.11}$$

where $\boldsymbol{\epsilon}$ is the light polarisation, $\mathbf{d}$ is the electric dipole operator, $\Delta = \omega - \omega_{eg}$ is the detuning from the transition, Γ is the natural linewidth and the light field is written as:

$$\mathbf{E} = \frac{1}{2} E \mathrm{e}^{-\mathrm{i}\omega t} + \mathrm{cc}. \tag{1.12}$$

We have used the second-order perturbation theory and the rotating wave approximation to neglect the fast oscillating terms [75].

The potential has both real and imaginary parts, which have different physical consequences. The real part gives rise to a conservative potential [76]:

$$U_{\mathrm{dip}} = -\,\mathrm{Re}(\alpha(\omega))\frac{|E|^2}{4} = -\,\mathrm{Re}(\alpha(\omega))\frac{I}{2\epsilon_0 c}, \tag{1.13}$$

where we define the frequency-dependent atomic polarisability $\alpha(\omega)$. The potential is attractive or repulsive depending on the sign of the detuning (red or blue detuning, respectively). In the presence of the light field, the atoms feel a force $\mathbf{F} = -\boldsymbol{\nabla} U_{\mathrm{dip}}$. The profile of the light intensity $I(\mathbf{r})$ opens up various possibilities, such as the implementations of optical tweezers with tightly-focused beams or optical lattices with interfering counter-propagating beams. The imaginary part is related to the non-conservative part of the interaction and represents the photon scattering, as the atoms undergo cycles of absorption and spontaneous emission despite the shift from resonance. It is therefore related to the heating of the atoms and its rate reads as follows:

$$\Gamma_{\mathrm{sc}} = \mathrm{Im}(\alpha(\omega))\frac{|E|^2}{2\hbar} = \mathrm{Im}(\alpha(\omega))\frac{I}{\hbar\epsilon_0 c}. \tag{1.14}$$

Away from all resonances, the light-matter interaction for dysprosium atoms reduces to a spin-independent term, which is similar to the case of a two-level system. The corresponding dipole force is associated with a background polarisability, arising mainly from the broad transitions around 400 nm. At infrared frequencies, much lower than the optical transitions, where commercial lasers with high optical powers are available, around 1064 nm, the polarisation $\alpha_s^{1064} = 184.0(24)\,\alpha_0$ [77] (with

J'	$J-1$	J	$J+1$
α_0	$\frac{2J-1}{3(2J+1)} = \frac{5}{17}$	$\frac{1}{3}$	$\frac{2J+3}{3(2J+1)} = \frac{19}{51}$
α_1	$-\frac{2J-1}{2J+1} = -\frac{15}{17}$	$-\frac{1}{J+1} = -\frac{1}{9}$	$\frac{J(2J+3)}{(J+1)(2J+1)} = \frac{152}{153}$
α_2	$-\frac{2J-1}{3(2J+1)} = -\frac{5}{17}$	$\frac{2J-1}{3(J+1)} = \frac{5}{9}$	$-\frac{J(2J-1)}{3(J+1)(2J+1)} = -\frac{40}{153}$

Figure 1.3 – Coefficients α_0, α_1 and α_2, corresponding to the scalar, vector and tensor components of the light shift respectively, for $J = 8$ and $J' = -J+1$, J and $J+1$.

$\alpha_0 = 4\pi\epsilon_0 a_0^3$ the polarisability unit) has a positive real part, which creates an attractive potential. For a Gaussian beam propagating along $\mathbf{z}$, with a focal point at $z = 0$ a beam waist w_0, the intensity profile is given by:

$$I(\mathbf{r}) = I(r,z) = I_0 \left(\frac{w_0}{w(z)}\right)^2 \exp\left(-2\frac{r^2}{w(z)^2}\right), \tag{1.15}$$

where r is the distance from the propagation axis, around which the intensity is cylindrically symmetric. The typical distance for the variation of intensity along r is set by the beam radius:

$$w(z) = w_0\sqrt{1+\left(\frac{z}{z_R}\right)^2}, \tag{1.16}$$

where the Rayleigh range $z_R = \pi w_0^2/\lambda$ defines the scale of intensity variation along z. For beam waists of the order of tens of micrometres and visible or near-infrared light, $z_R \gg w_0$ and the trapping effect is quite loose along the propagation axis. The intensity I_0 at the centre of the beam at the focal point ($\mathbf{r} = \mathbf{0}$) is related to the optical power P as follows:

$$I_0 = \frac{2P}{\pi w_0^2}. \tag{1.17}$$

Using the harmonic approximation around the position of the intensity maximum at $\mathbf{r} = \mathbf{0}$, assuming that the cloud dimensions are much smaller than the typical scales of the beam, the dipole potential reads:

$$U_{\text{dip}}(r,z) \approx -U_0 + \frac{M}{2}(\omega_r^2 r^2 + \omega_z^2 z^2) \quad \text{with} \quad \begin{cases} \omega_r = \sqrt{\dfrac{4U_0}{Mw_0^2}}, \\ \omega_z = \sqrt{\dfrac{2U_0}{Mz_R^2}}, \end{cases} \tag{1.18}$$

where we define the radial and longitudinal trap angular frequencies ω_r and ω_z, using the trap depth $U_0 = -U_{\text{dip}}(\mathbf{r} = \mathbf{0})$.

We now consider a situation where the light field is tuned in the vicinity of an electronic transition, such that the spin-dependent terms are significant. We turn to a framework adapted to a multi-level atom [75]. The AC Stark shift, for a single transition, reduces to a simple formula that we will use throughout this thesis to

derive the spin-dependent Hamiltonian from light-matter interaction:

$$V_{\mathrm{LS}} = \frac{3\pi c^2\Gamma}{2\omega_0^3}\frac{I}{\Delta_0}\left[\alpha_0\hat{\mathbb{1}} - \mathrm{i}\alpha_1(\boldsymbol{\epsilon}^*\times\boldsymbol{\epsilon})\frac{\hat{\mathbf{J}}}{2J} + \alpha_2\frac{3[(\boldsymbol{\epsilon}^*\cdot\hat{\mathbf{J}})(\boldsymbol{\epsilon}\cdot\hat{\mathbf{J}}) + (\boldsymbol{\epsilon}\cdot\hat{\mathbf{J}})(\boldsymbol{\epsilon}^*\cdot\hat{\mathbf{J}})] - 2\hat{\mathbf{J}}^2}{2J(2J-1)}\right], \tag{1.19}$$

with $\boldsymbol{\epsilon}$ the light polarisation, Γ the transition linewidth, ω_0 the laser frequency, Δ_0 the detuning to resonance and I the laser intensity. We introduce the light-shift for Clebsch-Gordan coefficients equal to unity:

$$V_0 = \frac{3\pi c^2\Gamma}{2\omega_0^3}\frac{I}{\Delta_0}. \tag{1.20}$$

The three terms, with prefactors α_0, α_1 and α_2, are called the scalar, vector and tensor, or rank-0, -1 and -2, components of the light shift respectively. The values of the prefactors are given in Fig. 1.3 for the three accessible values of total angular momentum J' with single-photon transitions. Compared to the case of alkali atoms, the vector and tensor contributions are not dominated by the scalar one [78]. The scalar part is spin-independent and is at the heart of the dipole force that we derived above. The vector part is non-zero for circular polarisations only and is associated with rank-1 spin coupling. The tensor part provides rank-2 spin coupling terms and cancels out for a total spin $J = 1/2$, *e.g.* for Rb atoms.

As we have seen in the two-level case, there is also an incoherent scattering of photons due to residual populations of excited states. When working in the vicinity of a narrow transition to induce strong spin-dependent couplings, the photon scattering depends on all components of the polarisability of this transition but also on the scalar polarisability originating from the broad transitions. The advantage of lanthanide atoms over alkali atoms lies in the availability of narrow transitions far from the broad ones (D1 and D2 lines for Rb, and blue transitions around 400 nm for Dy for example). It allows for strong coupling with limited heating, which is essential for the realisation of artificial gauge fields for interacting particles, that typically requires timescales of the order of a few seconds [79].

1.3 Spectroscopy

In this Section, we briefly describe some parts of our laser systems and focus on the spectroscopy of the blue and red transitions. These two transitions are used for applications, such as cooling or imaging, that require frequency tuning close to the optical transition with a precision roughly fixed by the natural linewidth of the excited state. For this purpose, we actively adjust the absolute frequency of our lasers using a feedback loop scheme based on an atomic reference. During this thesis, we modified the frequency locking schemes and used a hollow cathode lamp, instead of the atomic jet.

1.3.1 Blue transition

We briefly describe our blue laser setup. Our commercial source consists of a diode laser at 840 nm whose light is amplified and then frequency doubled using a

non-linear crystal in a bow-tie cavity. Since its initial installation, it has deteriorated and we now only get $\approx 300\,\mathrm{mW}$ at $421.3\,\mathrm{nm}$. This laser, referred to as the master laser in the following, provides blue light at different frequencies for Zeeman slowing, imaging, spectroscopy and transverse cooling. For independent control of the relative frequencies and optical powers of the beams, we use three acousto-optic modulators (AOM) in double-path configuration for transverse cooling, imaging and spectroscopy. To maximise the light power for Zeeman slowing, we use a single-path AOM. The four paths are coupled to fibres for improved stability. The transverse cooling setup, which uses an additional laser diode, seeded by the master laser, will be described in more detail in the next Chapter.

The different uses of the blue laser are all related to the resonant coupling of the light field with the atoms. This requires the frequency of the master laser to be stabilised around the resonance, at the level of the natural linewidth. We use a stable reference for the atomic transition and we apply a feedback loop to a piezo actuator, which finely controls the absolute frequency of the master laser. Possible candidates for stable references are ultra-stable cavities or dysprosium atoms directly. Previously, we used the atomic jet of our experiment as a reference. To decouple the different parts of our setup, we now use a see-through cathode lamp[3], dedicated to frequency locking. The lamp is a small glass cell containing a buffer gas of argon and two electrodes, the cathode of which is made of dysprosium. A current is sent to the anode and cathode and excites a vapour of atoms, which we probe using resonant light.

Our frequency-locking protocol is based on a Doppler-free and background-free technique, called modulation spectroscopy. It derives from the well-known saturated spectroscopy techniques [80] that involve two counter-propagating beams called the probe and pump beams. The probe beam is sent to a photodiode after passing through the atoms and gives almost 100% absorption close to resonance when the pump beam is switched off. Due to the Doppler effect, the width of the transition is significantly broadened, an effect that is even stronger in a cathode lamp than in an atomic jet with a narrow transverse velocity distribution. In saturated spectroscopy, the pump beam is much stronger than the probe beam and promotes atoms to the excited states, when tuned on resonance. Owing to the Doppler shift, which is of opposite sign for counter-propagating beams, the two beams are simultaneously resonant with atoms with zero velocity only. On one side, atoms at zero velocity are not accessible for excitation by the probe beam, which strongly reduces the absorption of this beam. On the other side, atoms with non-zero velocity contribute to the absorption of the probe beam in the same way, regardless of the pump intensity. The absorption spectrum of the probe beam is thus modified by the pump beam with the appearance of a sub-Doppler dip, whose width is given by the natural linewidth of the optical transition and is not limited by the Doppler broadening.

A periodic modulation at frequency $15\,\mathrm{MHz}$ is applied to the pump beam using an electro-optical modulator[4] (EOM) and transferred to the probe beam via a four-wave mixing process. Since this process is mediated by the atoms interacting with both light beams, thus the ones having zero velocity, the modulated component of the

[3] Heraeus hollow cathode lamp
[4] EO-T15T3-VIS, Qubig

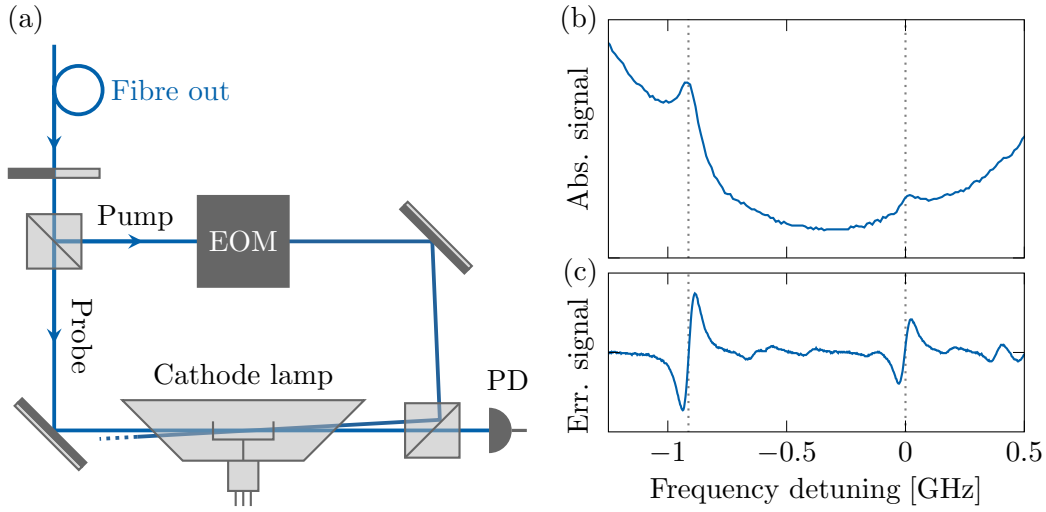

Figure 1.4 – Spectroscopy of the blue transition at 421.3 nm. Panel (a): Scheme of the optical setup for modulation spectroscopy involving two counter-propagating beams, denoted probe and pump beams. A polarising beam splitter, with a half-waveplate, controls the relative intensities of the two paths. The pump beam is phase-modulated by an electro-optical modulator (EOM). The modulation is transferred to the probe beam by a four-wave mixing process, whose signal after the cathode lamp is recorded on a photodiode (PD). Panel (b): Absorption signal of the probe beam in the presence of the pump beam, measured on the PD, as a function of the frequency. Panel (c): Corresponding error signal, after demodulation. The origin of the frequencies is set to the resonance for ^{162}Dy. The transitions for the bosonic isotopes ^{162}Dy and ^{164}Dy are highlighted by vertical grey dotted lines.

signal recorded on the photodiode only contains the sub-Doppler feature of interest. We demodulate the signal using a home-made lock-in amplifier and extract an error signal, which features a zero-crossing at the optical transition and is Doppler-free. In practice, due to the isotopic shifts, we observe a forest of zero-crossing features with widths given by the natural linewidth of the transition, corresponding to the different bosonic isotopes and hyperfine levels of fermionic isotopes. Factors limiting the width of the error signal are the pressure broadening of the cathode lamp due to the buffer gas and the power broadening that occurs at high light intensities. It is advantageous to work with a low current in the lamp and a low power for the probe and pump beams, but this reduces the size of the error signal. We choose our experimental parameters, such as a waist of 0.39 mm and approximately equal powers of the order of 400 µW corresponding to a saturation parameter of 2.9, based on the competition between these effects. In Fig. 1.4, we show the optical setup and the measured saturated spectroscopy as well as the corresponding error signal after demodulation. Two Lamb dips are visible in the absorption signal and correspond to the two most abundant bosonic isotopes, while additional sub-Doppler features appear in the error signal.

1.3.2 Red transition

The resonant light at 626.1 nm, used for the MOT, the Doppler cooling stage and spectroscopy, is generated using a sum-frequency generation setup. Two infrared lasers at 1050 nm and 1550 nm, are amplified using fibre amplifiers. The two beams, both with an optical power of 5 W, are focused onto a non-linear crystal[5], which converts the two photons from each into a single photon at 626.1 nm. The crystal, whose temperature is precisely tuned to meet the phase matching condition, has a maximum conversion efficiency of 75.5 $\mathrm{mW/W^2}$ corresponding to a maximum output power of 1.89 W, but we routinely reach 1 W only. The light is then split into three paths, which are individually controlled by AOMs and are all fibred. Most of the optical power is dedicated to the six MOT beams, after passing through a single-path AOM. The remaining power is used for spectroscopy and Doppler cooling before loading in the crossed dipole traps. The sum-frequency generation setup is duplicated using two other fibre amplifiers with respective powers 10 W and 5 W, which yields an output power of 1.5 W, which is directly fibred. This second laser, whose frequency is simply measured by a wavelength-metre[6], is used for off-resonant light coupling, with a detuning of typically 10 GHz $\approx 10^5\,\Gamma_{\mathrm{red}}$, and does not require frequency stabilisation.

The requirements for the frequency stabilisation of the resonant laser at 626.1 nm are much more difficult to fulfil than those of the laser at 421.3 nm, due to the difference by two orders of magnitude between the natural linewidths of the corresponding excited levels. Other groups have chosen to use ultra-stable cavities in a vacuum environment as a reference. Similarly to the frequency-locking of the blue laser, our current implementation uses the atomic jet of dysprosium atoms as a reference. The narrowness of the natural linewidth has several consequences. The absorption or fluorescence signal when the atoms are illuminated by light is weak. The saturation intensity scales as the inverse of the linewidth and power broadening can be a limiting factor. Electronic noise from the demodulating setup can also affect the laser linewidth. Our current setup is based on saturated absorption spectroscopy, measured on the fluorescence signal instead of the absorption signal, with modulated retro-reflected beams. This is applied to the atomic jet exiting our atomic source because the Doppler broadening is limited in the transverse directions and the optical accesses facilitate the interrogation of a large number of atoms. The beam modulation is performed at 40 kHz and the demodulation is realised by a commercial lock-in amplifier[7]. The error signal has a Doppler-free feature corresponding to the Lamb dip, but has a non-zero background originating from Doppler broadening. It is used to feedback a piezo actuator of the 1050 nm seed laser, which actively stabilises the laser frequency.

Following the same procedure as for the blue laser, we implement a modulation spectroscopy setup on a see-through cathode lamp, which yields an error signal visible in Fig. 1.5(a). The signal is quite faint however, compared to our error signal on the atomic jet. One limitation stems from the geometry of the lamp, which forces us to work with small beam waists and thus large saturation parameters. A

[5]Periodically Poled Lithium Niobate (PPLN) crystal
[6]Highfiness WS6-200 wavelength-metre
[7]SR510 Lock-in amplifier, SRS

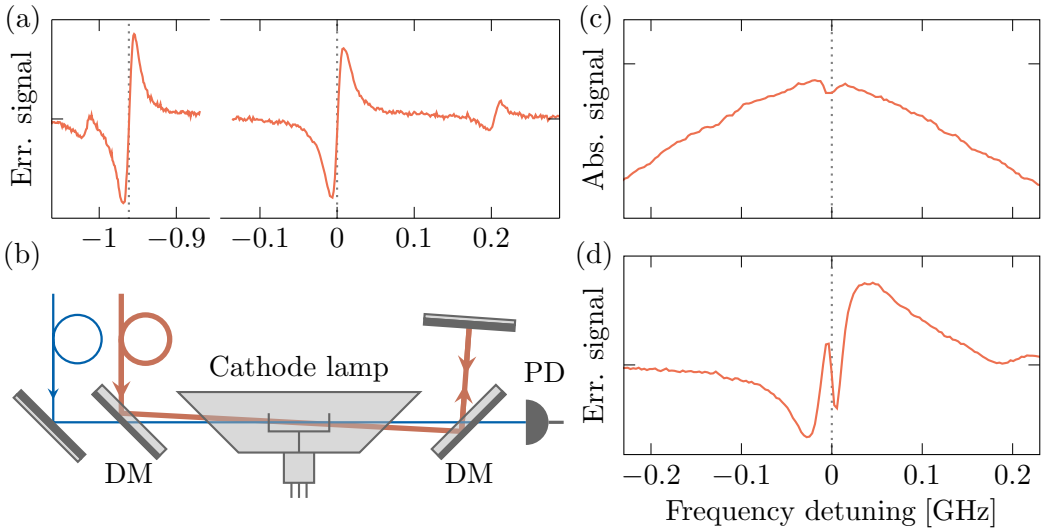

Figure 1.5 – Spectroscopy of the red transition at 626.1 nm. Panel (a): Error signal as a function of the red laser frequency, using modulation spectroscopy with an optical setup similar to Fig. 1.4(a). The origin of the frequencies is set to the resonance for ^{162}Dy and we focus on the two main zero-crossings corresponding to ^{162}Dy and ^{164}Dy, marked by grey dotted lines. Panel (b): Scheme of the optical setup for shelving spectroscopy. It involves a retro-reflected beam at λ_{red} and a beam at λ_{blue} with a single passage through the cathode lamp. The red beam is frequency modulated by an AOM (not represented here) and shelves atoms to the electronic excited state. The blue beam probes the remaining atoms with an increased sensitivity due to its wide linewidth and its absorption signal is recorded on a photodiode (PD). Dichroic mirrors (DM) combine the two paths in the cathode lamp and then separate them. Panel (c,d): Absorption signal of the blue beam in the presence of the retro-reflected red beam and corresponding error signal, as a function of the frequency, around the resonance for ^{162}Dy, using shelving spectroscopy.

possibility to increase the size of the error signal with limited noise is an alternative technique, well-suited for intercombination lines, called shelving spectroscopy [81]. This bichromatic technique benefits from a narrow transition to obtain a sub-Doppler feature, whose width is limited by the natural linewidth, and from a wide transition to maximise the absorption-emission cycles that increase the recorded signal. A modulated retro-reflected beam around 626.1 nm is shined upon the atoms and promotes them in the excited state. A single blue beam, which is resonant with the optical transition at 421.3 nm, passes through the atoms but only part of the atoms contribute to the absorption of the beam as the remaining ones are shelved to a state inaccessible to the red laser. Maximum power of blue light is transmitted when the red laser is close to resonance and efficiently excites the atoms. As with saturated spectroscopy, a sub-Doppler feature is visible on resonance, because of the retro-reflection of the red beam. The gain in signal originates from the interrogation

of whether the atoms have been shelved by the wide transition instead of the narrow transition, and is thus of the order of $\Gamma_{\text{blue}}/\Gamma_{\text{red}}$. A first signal has been observed on the cathode lamp and we show both the absorption signal on the blue transition and the error signal in Fig. 1.5(c,d), while sweeping the frequency of the red laser across the transition, with a blue laser locked on resonance. We observe a zero-crossing corresponding to the ^{162}Dy isotope, surrounded by a Doppler-broadened feature, which is reminiscent of saturated spectroscopy. The corresponding optical setup is sketched in Fig. 1.5(b). Since then, the setup has been replicated on the atomic jet of dysprosium atoms, where the optical access allows for a less constrained optimisation of the beam parameters, but the demodulating setup is not yet completed.

2

Description of the experimental setup

This Chapter describes the successive steps of the experimental cycle which consists of preparing an ultracold sample of dysprosium atoms, carrying out a chosen experiment and probing the atoms destructively. The vast majority of the setup was built by the original students on the experiment [82, 83], with significant contributions from all former members of the group. We present a brief introduction to Bose-Einstein condensation while discussing the tools for reaching low temperatures. We also highlight some selected steps that have been implemented during this thesis. We present the set of experimental techniques that we routinely use for the characterisation of off-resonant light beams.

2.1 Experimental timeline

Each experimental cycle consists of a succession of timesteps with precise objectives, which are achieved through variations in numerous physical parameters. The control over a large number of electronic devices is performed via an interface called Cicero, connected to a chassis. It supplies analog and digital outputs that trigger devices and adjust their parameters. Wave generators are controlled using Python scripts for the preparation of arbitrary waveforms, taking as inputs the variables of the Cicero interface. The sequence cycle lasts about 22 s and is kept constant for stability, regardless of the experiment. The successive steps have timescales ranging from tens of nanoseconds to a few seconds.

To reach temperatures as low as a fraction of µK, the atoms are trapped using light potentials that decouples them from the temperature of the ambient environment. The ultra-high vacuum system, with pressures down to less than 10^{-10} mbar in the final stages of the cycle, reduces the probability of collisions with residual particles and limits collision-induced losses. Differential pumping before the glass cell, where the cold atomic samples are manipulated, significantly improves the lifetime compared to the previous stages. We show the vacuum system in Fig. 2.1, with some indicated stages.

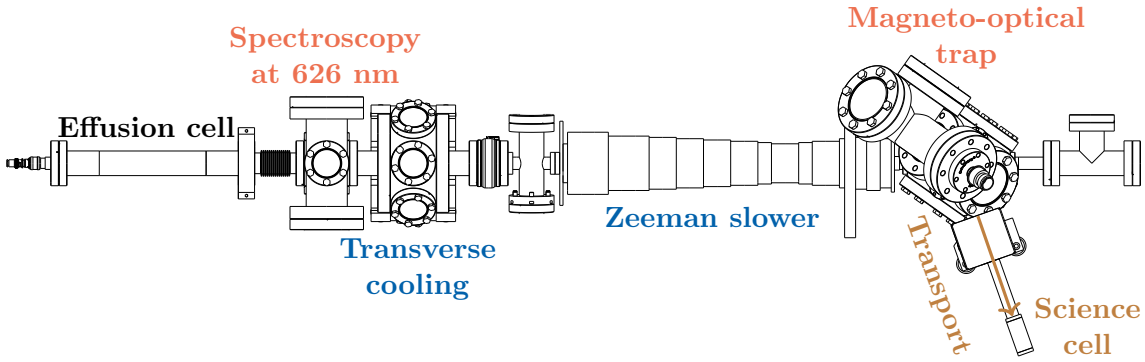

Figure 2.1 – Simplified scheme of the vacuum system. Atoms are emitted by the effusion cell and then cooled and trapped, before transport to the science cell. We focus on the successive parts of the setup that are involved in the experimental sequence. The different stages are described in Section 2.1.

Effusion oven

An evaporation oven[1] heats solid pieces of pure dysprosium to about 1100 °C where a vapour forms inside the oven and exits through a millimetre-sized hole. At this temperature, the atoms have a most probable velocity of about 500 ms^{-1}. Despite several cooling devices, the oven heats surrounding vacuum pieces to almost 100 °C, which is detrimental to the quality of the vacuum. Fortunately, dysprosium atoms exhibit a getter property as they coat the walls of the vacuum system and residual particles stick to them. This counteracts the negative effect of the high temperature and lowers the vacuum pressure.

Transverse cooling

The hole of the oven barely collimates the atomic jet that propagates horizontally. The atoms actually have a fairly wide transverse velocity distribution and a significant proportion of them stick to the walls of the vacuum system. To maximise the number of atoms that will be accessible to laser trapping, we first apply laser cooling of the transverse motion of the atoms, so-called transverse cooling. We use two-dimensional molasses, consisting of two counter-propagating beams, whose frequency is red-detuned from the broad transition at 421.3 nm. We will present this step in detail in Section 2.1.1.

Zeeman slowing

In the next step, we reduce the longitudinal velocity of the atoms down to the capture velocity of our magneto-optical trap of about 8 ms^{-1} in a region of 50 cm using laser cooling. We shine a single circularly-polarised beam at 421.3 nm, with

[1] DFC-40-10-WK-2B, Createc

an optical power of about 60 mW, resonant with the cycling transition between the extremal $|J, m = -J\rangle$ and $|J', m = -J'\rangle$ states. The initial velocity corresponds to a Doppler shift on the blue transition of $\mathbf{k} \cdot \mathbf{v}/(2\pi) \approx 36\,\Gamma_{\text{blue}}$, and the capture velocity of the magneto-optical trap to less than the natural linewidth Γ_{blue}. The laser cooling technique presented in Section 1.2.1 requires the laser beam to be in the vicinity of the optical transition, within Γ_{blue} typically. To maintain this resonant condition as the atoms are slowed down, we add a spatially-varying magnetic field with water-cooled wires carrying large currents. The so-called Zeeman slower is in a spin-flip configuration with the magnetic field crossing zero. It minimises the current through the coils and requires a beam with large detuning $\approx -15\,\Gamma_{\text{blue}}$ from the transition for atoms at rest, which reduces the photon scattering for atoms that have been successfully cooled down.

Magneto-optical trap

Atoms with reduced velocities are then trapped in a magneto-optical trap (MOT), consisting of six beams, counter-propagating in pairs, and two coils in anti-Helmoltz configuration. It operates on the intercombination line at 626.1 nm with a narrow linewidth and thus a low Doppler limit $T_{\text{DL}} = \hbar\Gamma_{\text{red}}/(2k_{\text{B}}) \approx 3.2\,\mu\text{K}$, compared to the D2 lines of rubidium atoms for example with linewidths in the MHz range. The coils create a magnetic gradient whose zero-crossing theoretically gives the position of the trap centre. For dysprosium and other lanthanide species, the large mass of the atoms results in a non-negligible gravitational contribution that competes with the trapping induced by light and magnetic forces. The equilibrium position of the MOT is located below the zero-crossing, where the magnetic field is non-zero and the degeneracy of the ground state manifold is lifted. The MOT equilibrates in this position and is spin-polarised by the laser beams, which has been further studied in our group [84]. The loading of the MOT is realised in two steps: an initial loading with high light intensities and sideband modulation to broaden the laser linewidth, and a compression of the MOT by removing the modulation and decreasing the beam intensities. We load our MOT in 15 s, followed by compression in 400 ms, and trap 5×10^7 atoms at a temperature of $T = 15\,\mu\text{K}$, five times larger than the Doppler limit.

Loading in crossed dipole traps

The atoms are loaded in conservative traps, in which the minimum temperature is no longer limited by the recoil energy associated with the absorption and emission of a photon. We first load the atoms in a single dipole trap at 1070 nm using a 50 W multi-mode laser. The atoms are displaced from the MOT chamber to a glass cell, depicted in Fig. 2.2, with multiple optical accesses, precise magnetic field control and improved vacuum due to differential pumping. The focal point of the laser beam is shifted over a distance of 28 cm using a magnetic-levitating translation stage which varies the length of the optical path [83]. The efficiency of the loading and transport stages is about $1 - 10\%$ and we obtain about 10^6 atoms in the glass cell at a temperature slightly above 100 µK. The limiting factors are here the volume of the optical dipole trap relative to the size of the MOT, the collisional lifetime in the MOT chamber and the low trapping frequency along the transport axis, set by the Rayleigh range ≈ 3.6 mm. Possible alternatives for the transport stage include optical lattices

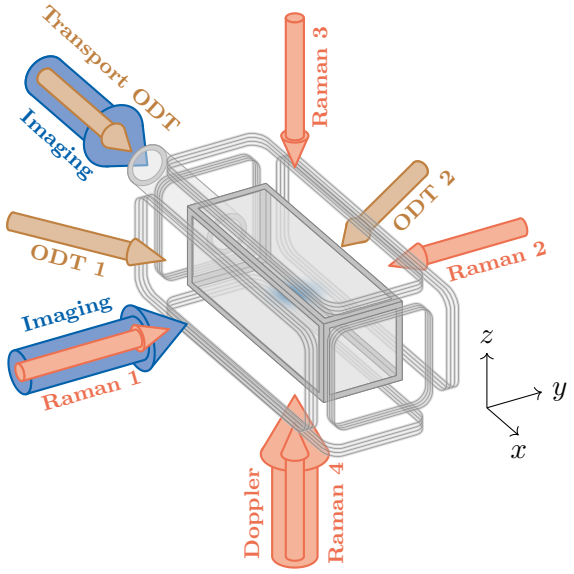

Figure 2.2 – Scheme of the science cell, presenting the multiple axes of the laser beams. The glass cell and a part of the tube that connects it to the MOT chamber are shown in grey, as well as the rectangular magnetic coils surrounding the glass cell. The position of the atoms is indicated by a shaded blue cloud at the centre of the cell. The dipole traps, the imaging beams, the Doppler beam the Raman beams are depicted by small brown, large blue, large red and small red arrows respectively. The Raman beams are tuned out of resonance in the vicinity of the 626.1 nm optical transition. The paths of Raman 1 and Raman 3 have also been used for the implementation of resonant coupling (at 626.1 nm) and spin-dependent light shifts (at 696.0 nm and 832.8 nm) respectively.

with control of the frequency difference of the counter-propagating beams to displace the atoms while taking advantage of the strong axial confinement [85, 86].

After transport, we apply Doppler cooling using a single vertical red-detuned beam at 626.1 nm for a short duration of 40 ms. The parameters of this cooling scheme take into account the difference in polarisabilities between the ground and excited states, which depend on the polarisation and intensity of the optical dipole trap, as previously studied in depth [87]. The temperature of the cloud decreases with some atom losses due to light-assisted inelastic collisions, and we gain a factor of two in the collisional rate, which is more favourable to the evaporation scheme.

We transfer the atoms from the single transport beam to crossed dipole traps (cODTs). A pair of beams, from single-mode lasers at 1064 nm of 45 W and 10 W powers, intersect at the focal point of the transport beam, with waists of about 25 µm. We time modulate the position of one of two dipole traps at a frequency of 50 kHz, much higher than any trap frequency. This effectively increases the width of the beam and thus the overlap with the transport beam, which is quite elongated due to the loose longitudinal confinement in a Gaussian beam. The transfer is achieved by ramping down the power of the transport dipole trap.

Evaporation cooling

We then reduce the trap depths of the crossed dipole traps to perform evaporation cooling towards quantum degeneracy. The principle of forced evaporation is to let the high energy atoms escape the trap while elastic collisions ensure thermalisation of the remaining atoms. It leads to a decrease in the average energy per particle. The timescale of the reduction of the trap depth must be long enough to allow for thermalisation, but it must remain short to limit the effect of background-collisional losses. We compensate for gravity during the evaporation state using a magnetic field gradient. The dipolar relaxation is negligible because the atoms are polarised in the ground state $|m = -J\rangle$, which is ensured by a vertical magnetic field of typically 1 G. The latter sets the magnetic Zeeman energy splitting which remains larger than the thermal energy $k_\mathrm{B}T$ throughout the evaporation, thus minimising population in the first magnetic excited state $|m = -J + 1\rangle$.

The quantitative estimation of the efficiency of the cooling relies on the increase of the phase space density (PSD) [88]. It is related to the ratio of the thermal de Broglie wavelength λ_dB, which characterises the typical width of the individual atomic wavefunction, to the inter-particle distance set by the atomic density n:

$$\mathcal{D} = n\lambda_\mathrm{dB}^3 \quad \text{with} \quad \lambda_\mathrm{dB} = \sqrt{\frac{2\pi\hbar^2}{Mk_\mathrm{B}T}}. \tag{2.1}$$

Quantum effects typically occur when the atomic wavefunctions start to overlap, *i.e.* when the PSD is of the order of unity. In the case of three-dimensional harmonic trapping of average trap frequency $\overline{\omega} = (\omega_x\omega_y\omega_z)^{1/3}$, the PSD reads as follows:

$$\mathcal{D} = N\left(\frac{\hbar\overline{\omega}}{k_\mathrm{B}T}\right)^3. \tag{2.2}$$

In the case of a non-interacting Bose gas, at a fixed atom number, the population of the ground state for the external degrees of freedom becomes macroscopic below a temperature called the critical temperature, as the chemical potential approaches the energy of the lowest energy state. This mechanism [50, 89], called Bose-Einstein condensation, occurs when the PSD increases beyond the limit of $\zeta(3) \approx 1.202$ for harmonic traps (or $\zeta(3/2) \approx 2.612$ in uniform systems). A Bose-Einstein condensate is a phase of particles obeying bosonic statistics with a large fraction of particles occupying the lowest-energy quantum state. It also features long-range coherence throughout the condensate which can be represented by a macroscopic wavefunction. At such a low kinetic energy, the interaction effects cannot be neglected and modify the properties of the quantum state. Interacting Bose gases at zero temperature are well described using the Gross-Pitaeiskii equation in the mean-field regime for weak interactions and Bogoliubov theory to study the elementary excitations of the condensate. Beyond mean-field effects become important at increasing densities.

Bose-Einstein condensation of ^{162}Dy atoms has been achieved in our group [87], and many other experiments have reached the quantum degeneracy regime with various bosonic and fermionic isotopes [90–93]. Currently, we routinely prepare thermal clouds of 5×10^4 atoms at temperatures ranging from 0.2 to 0.5 µK. In this regime, on the timescale of our experiments of less than a few milliseconds, contact

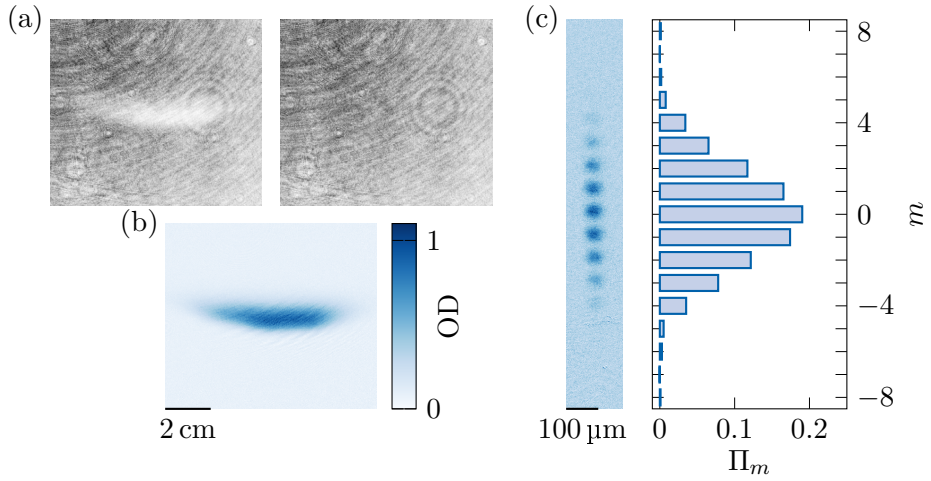

Figure 2.3 – Panels (a,b): Example of a single-shot optical density in (b), reconstructed from the two successive images with and without atoms, on the left and right panel (a) respectively. This optical density is obtained by absorption imaging on a magneto-optical trap. Panel (c): Example of the optical density for a coherent state of magnetisation $\langle \hat{J}_z \rangle \approx 0$ with single-spin resolution, imaged after a time-of-flight expansion with a strong magnetic gradient. We show the corresponding spin distribution Π_m on the Dicke basis, calculated from the optical density.

interactions are negligible and we are working in a regime of single-body physics. The atoms can be considered as simultaneous realisations of the same experiment and only act as an averaging mechanism.

Absorption imaging with single-spin resolution

We perform absorption imaging either *in situ* or after a time-of-flight expansion to record the position distribution or the velocity distribution respectively. We shine resonant light on the atomic sample and measure the light distribution on a CCD camera. The atoms absorb photons by undergoing successive cycles of absorption and spontaneous emission. They appear as a shadow on the image recorded on the camera.

We use the transition at 421.3 nm with a wide natural linewidth to maximise the number of absorption-emission cycles and increase the sensitivity of the detection of the atoms. Due to the short lifetime of 5 ns in the excited state, for a saturation parameter of one, a thousand photons are typically absorbed by a single atom in 40 µs, the typical pulse duration in the experiments presented here. This type of imaging integrates the atomic distribution of the atoms $n(x, y, z)$ along the propagation axis of the imaging beam. Using Beer-Lambert law for an incoming beam propagating along $\mathbf{z}$, of intensity $I_0(x, y)$ in the low-intensity regime, the intensity after passing through the atoms reads:

$$I(x, y) = I_0(x, y) \mathrm{e}^{-\sigma_0 \int \mathrm{d}z\, n(x,y,z)}, \tag{2.3}$$

with σ_0 the effective cross-section which characterises the coupling of the atoms with

the resonant light. This formula can be extended to include saturation effects at higher light intensity [94]. By recording two successive images with and without atoms for the same imaging pulse parameters, we compute the so-called optical depth (OD), proportional to the integrated density distribution:

$$\mathrm{OD}(x,y) = \sigma_0 \int \mathrm{d}z\, n(x,y,z) = \log \frac{I_0(x,y)}{I(x,y)}. \tag{2.4}$$

We then derive various observables such as the atom number or the mean position of the cloud in the (x,y) plane, using the integrated density distribution.

Most of our measurements record the velocity distribution by allowing the cloud to expand for a given time, which maps the velocity distribution of the atoms before their release onto the density distribution probed by absorption imaging. In addition to this expansion, we can apply a strong linear magnetic field gradient of the order of $50\,\mathrm{G/cm^{-1}}$ for a duration of 2.2 ms. This Stern-Gerlach gradient creates a uniform spin-dependent force, whose expression immediately derives from the magnetic Zeeman energy splitting. Each atom in the quantum state $|\psi\rangle$ is projected on a single Zeeman sublevel state $|J,m\rangle$, with integer $-J \leq m \leq J$, with probability $\Pi_m = |\langle\psi|J,m\rangle|^2$. This basis of spin states is also called the Dicke basis. In the absence of interatomic interactions, each atom corresponds to a single realisation of the same experiment and, after projection with the magnetic gradient, we record the spin-resolved velocity distribution, obtained from typically 10^4 simultaneous runs of the same experiment due to the large atom number. We obtain the spin projection distribution Π_m from a single-shot measurement by counting the fraction of atoms in each of the $2J+1 = 17$ resolved velocity distributions.

Observables related to the external degrees of freedom, such as the temperature of the atomic cloud, are also computed from measurements of the density distribution after a time-of-flight expansion. They require a precise calibration of the magnification of the imaging setup, which depends mainly on the choice of lenses and the size of the camera pixels. The magnification is measured in a dedicated experiment using two-photon optical transitions that couple neighbouring spin states with a net momentum kick $\pm 2\hbar k$, with k the laser wavevector. For atoms initially at rest and polarised in $|m=-8, v=0\rangle$, the accessible states are of the form $|m, v=(m+8)\hbar k/M\rangle$ for a Dicke state m ($-J \leq m \leq J$ integer) with a velocity v along the propagation axis of the laser beams. We prepare the atoms in a superposition state with a significant proportion in $|m=0, v=16\hbar k/M\rangle$, obtained by eight successive two-photon transitions, and then switch off the spin coupling. We resolve the $m=0$ component alone by projecting the quantum state on the Dicke basis using a Stern-Gerlach magnetic gradient. We record the centre-of-mass of this component, which is insensitive to residual magnetic gradients in the glass cell, as a function of the expansion time. We deduce the velocity of this state, whose expected value $v = 16\hbar k/M$ allows us to calibrate the imaging setup.

2.1.1 Transverse cooling

In this Section, we further discuss the transverse cooling stage [95, 96] which aims at collimating the atomic jet. It reduces the width of the transverse velocity distribution and increases the number of atoms that pass through the Zeeman slower

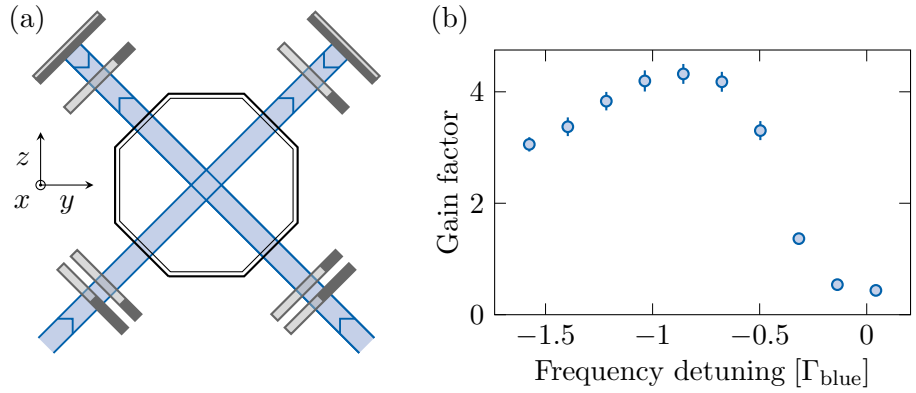

Figure 2.4 – Panel (a): Scheme of the transverse cooling setup with two orthogonal retro-reflected laser beams at 421.3 nm. The beams intersect at the centre of the vacuum system, with eight optical accesses at this position, and affect the transverse velocity distribution of atoms propagating along the axis (axis x on the scheme), orthogonal to the two beams. The polarisations of the forward and backward beams are controlled using a pair of waveplates and a single quarter-waveplate respectively. Panel (b): Gain factor in the number of atoms loaded in the MOT with the transverse cooling stage, compared to without it, as a function of the frequency detuning of the beams. This measurement is performed for a short MOT loading time, in the linear regime. Optimal cooling is achieved at about $-0.8\,\Gamma_{\text{blue}}$, for fixed parameters such as the saturation parameter or the magnetic field.

and reaches the MOT capture region with a finite transverse size of typically 1 cm. A bare collimation is designed at the exit of the effusion oven by a tube of centimetric length and millimetric diameter. The transverse velocity distribution of the hot atoms is still quite wide and a significant part of them is lost on the walls of the vacuum system. A gain factor of typically 5 in the number of atoms loaded in the MOT has been measured in various dysprosium or erbium experiments using two-dimensional optical molasses consisting of two orthogonal retro-reflected laser beams tuned to the red side of the broad transition at 421.3 nm, in the absence of a magnetic field [97–100].

Our group also implemented this cooling stage in the early days of the experiment and achieved a gain factor of 4. For unknown reasons, this has degraded up to the point where the optical setup was completely rebuilt but we did not obtain any significant gain, despite several successive attempts. We therefore decided to try again following the same approach but with more control over the relevant parameters. A first study was performed along a single axis with independent control of the counter-propagating beams, instead of using a single retro-reflected beam. It confirms that transverse cooling, albeit small, is obtained for beams of equal intensity.

We switch to the usual configuration with a pair of orthogonal retro-reflected beams. The optical setup of the blue laser at 421.3 nm is rebuilt such that we can vary the frequency of the transverse cooling beam across the resonance and up to approximately $-1.5\,\Gamma_{\text{blue}}$ from the resonance. We also add three magnetic coils with

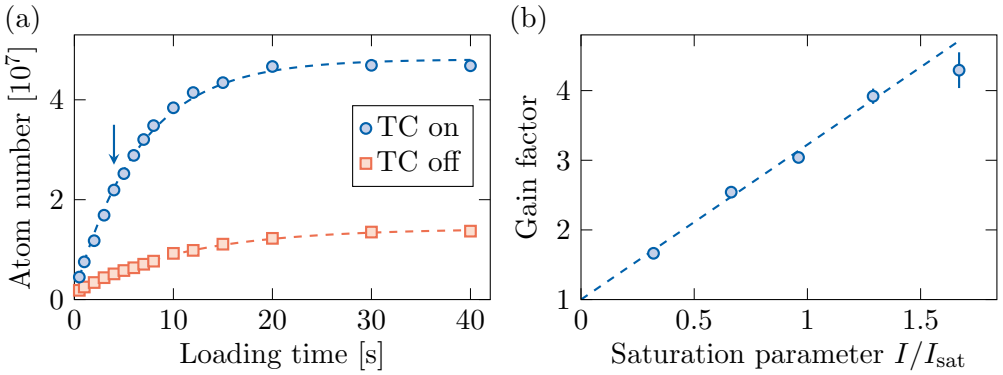

Figure 2.5 – Panel (a): Number of atoms loaded in the MOT after recompression as a function of the loading time, with and without transverse cooling (TC), in blue and red respectively. Exponential fits of the data are represented by dashed lines. A vertical arrow indicates the loading time at which the optimisation of the transverse cooling parameters has been performed, in the linear regime at short times. Panel (b): Gain factor in the number of atoms loaded in the MOT with transverse cooling compared to without it, as a function of the saturation parameter of the beams. The dashed line is a linear fit.

several windings to control the norm and orientation of the magnetic field at the position of the atoms. The coils are made up of 15 turns and are located about 10 cm from the transverse cooling region. They typically produce 1 G for a current of 10 A. A semiconductor laser diode[2], seeded by 5 mW from the master laser at 421.3 nm, provides 100 mW of blue light with a non-Gaussian beam shape, which is coupled into a fibre. The output beam with a waist of 4 mm has an optical power of 50 mW, equally split into two paths. The injection locking of the diode is optimised using the transmission signal on a Fabry-Perot cavity[3] and its stability is improved by automatically adjusting the current through the diode at the beginning of each experimental cycle. The polarisations of the forward beams are independently tuned by a half-waveplate and a quarter-waveplate. After passing through the atoms, the forward beams are reflected off a mirror and go through a quarter-waveplate twice before reaching the atoms again. We geometrically align the forward beams with respect to the optical windows and then the backward beams by coupling them back into the fibre. A scheme of the optical setup is shown in Fig. 2.4(a).

The resonance of the transition is independently calibrated with a beam in a single path, which pushes the atoms away and strongly reduces the number of atoms in the MOT. We measure the number of atoms in the MOT at a short loading time of 4 s to be in the linear regime of the loading curve and compare it in the presence or absence of the transverse cooling beams. We vary the relevant parameters and converge to an optimum atom number at a detuning of $-0.8\,\Gamma_{\text{blue}}$, with a gain factor of 4.25 compared to the same loading time without transverse cooling, as shown in Fig. 2.4(b).

[2]LD-0425-0120-1, Thorlabs
[3]SA210-3B (FSR 10 GHz, finess > 150), Thorlabs

The optimum corresponds to beams in the so-called lin⊥lin configuration, with a saturation parameter of 1.7. The coils create a non-zero magnetic field of about $\mathbf{B} = (0.7, 0.25, 0.75)$G along the three axes defined in Fig. 2.4(a), which does not affect the nearby spectroscopy at 626.1 nm or Zeeman slowing. However, it is possible that the applied magnetic field simply compensates for residual stray fields originating from nearby pumps for example. We study in detail the dependence of the gain factor as a function of the magnetic field and the polarisations of the forward and backward beams around the optimum, in Appendix B.

We compare the loading in the compressed MOT with and without transverse cooling in Fig. 2.5(a). In both cases, the number of atoms increases according to an exponential law that saturates at long times. We deduce that the atom number is multiplied by a factor of 4.5(1) in the linear regime at short times. At long times, the saturated atom number is increased by a factor of 3.4(1). Future improvements include the use of a second laser diode to double the optical power in each beam. To estimate the expected gain in this situation, we measure the atom number in the MOT as a function of the saturation parameter. For the chosen waist, we reach $s = I/I_{\mathrm{sat}} \approx 1.7$ at maximum power and the variation of the atom number is linear and may start being sublinear at the highest optical power. At higher optical power, we should use cylindrical lenses to increase the beam diameter along the propagation axis of the atomic jet only while maintaining the saturation parameter close to one.

2.1.2 Imaging improvement

In this Section, we describe our algorithm for reducing noise and removing fringes in the computed optical densities. We first recall the formula for the calculation of an OD in the low-intensity regime:

$$\mathrm{OD}(x, y) = \log \frac{I_0(x, y)}{I(x, y)}, \tag{2.5}$$

from two images taken with (I) and without (I_0) atoms. In practice, we also record an additional image without imaging light, which we subtract from the two images I_0 and I, in order to remove stray light and electronic background noise. In the following, we assume that this subtraction has been performed for all images.

We notice significant noise in the background of the ODs in the absence of atoms, as well as clear patterns such as fringes or circles whose position and visibility can vary from one shot to another. This is partly due to fluctuations in the light intensity and mechanical instabilities of the imaging setup. This can be prevented by minimising the time interval between the successive snapshots and ensuring that the optics are clean. Fluctuations in the light intensity can be accommodated by rescaling the image I_0 based on a region away from the position of the atomic cloud.

A more general approach to this problem is to construct an alternative image to I_0, denoted $\tilde{I}_0$ in the following, which is as close as possible to the image I, in a region without atoms but close to the atomic cloud. Our algorithm follows the ideas of the so-called best reference image algorithm [101], which considers a set of N_1 images without atoms $\{I_0^{(n)}\}_n$. We distinguish a region R_0 where atoms are expected and a region R_1 in the vicinity. We compute the autocorrelation matrix Ξ of this

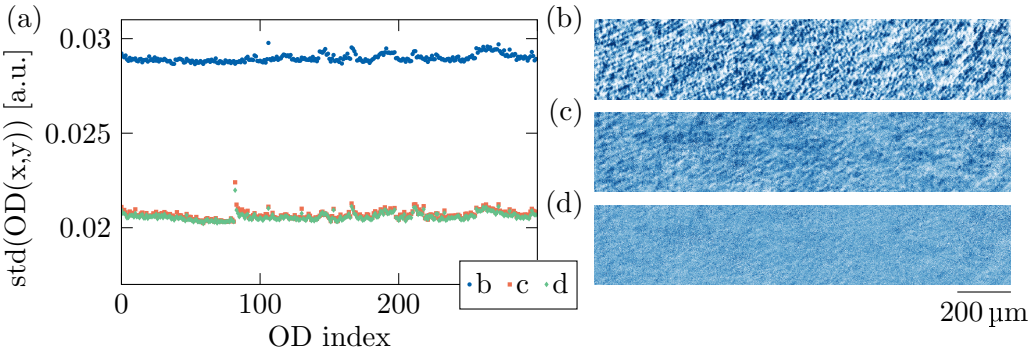

Figure 2.6 – Panel (a): Standard deviation of the optical density pixels, calculated for each of 300 experimental sequences, with the standard computation of the OD based on Eq. 2.4 (blue dots), with the first part of the algorithm presented in Section 2.1.2 only (red squares) and with the full algorithm (green diamonds), labelled with b, c and d respectively. Panels (b,c,d): Average of the ODs of the experimental sequences, corresponding to the three methods to compute ODs used in panel (a). The colour map is identical for all three panels. We use experimental sequences without atoms to highlight the effect of our algorithm on the background noise.

set, based on the region R_1 without atoms, as:

$$\Xi_{n,n'} = \sum_{x,y \in R_1} I_0^{(n)}(x,y) I_0^{(n')}(x,y), \tag{2.6}$$

and invert it. For each image I, we compute its autocorrelation with all images in the set $\{I_0^{(n)}\}_n$ in the region R_1, which forms a column vector C of size N_1. We construct the best reference image $\tilde{I}_0$ corresponding to I, as a linear combination of the $\{I_0^{(n)}\}_n$ images:

$$\tilde{I}_0(x,y) = \sum_{1 \leq n \leq N_1} D_n I_0^{(n)}(x,y), \tag{2.7}$$

with the column vector $D = \Xi^{-1} C$, using the inverse of the autocorrelation matrix. This construction of $\tilde{I}_0$ minimises the least-square distance to the image I in the region R_1.

This algorithm strongly reduces the background noise and the contrast of the fringes. We estimate this quantitatively by computing the standard deviation of each OD for the pixels in the region R_0, using an experimental sequence where we load no atom on purpose, and compare this quantity for the OD calculated with I_0 or $\tilde{I}_0$. We observe a significant reduction in standard deviation using the best reference algorithm in Fig. 2.6(a). Another approach to highlighting residual defects in the ODs, that may be below the noise, is to average them. We obtain an averaged optical density $\overline{\mathrm{OD}}$ and compare it, for ODs computed with and without the best reference algorithm in Fig. 2.6(b,c). The noise reduction is significant but we observe residual patterns, which are problematic in some of our analyses. This is particularly relevant when we extract higher-order moments of the velocity distribution, which are highly sensitive to individual pixel values.

We apply a second algorithm directly to the ODs, to minimise this background. In practice, we construct a set of N_2 ODs without atoms, deliberately performing experimental cycles that do not trap atoms. Then, we follow the basic ideas of the first protocol, applied to the pixels of the ODs in a zone R_2, where atoms are not expected. For each OD with atoms, we construct an optical density $\tilde{S}$ that minimises the least-square distance to the OD in the region R_2 and subtracts it from the OD. The standard deviation of the OD is only slightly reduced after this stage (see Fig. 2.6(a)), but we observe a significant reduction in the patterns that were visible when averaging the ODs. We show the average optical density $\overline{\mathrm{OD}}$ computed with the full algorithm in Fig. 2.6(d) to highlight the reduction of background noise.

For more details about the dependence of these algorithms on certain parameters such as the number of images or the size of the region R_1, we refer to Appendix C, where we also provide a schematic representation of the algorithm.

2.1.3 Magnetic field control

Atoms with large magnetic moments require special care of the magnetic field at all stages, especially for cooling and spin manipulation. We control the magnetic field at each stage of the experimental cycle using several sets of coils. Three sets of coils (coils C) in Helmoltz configuration surround most of the optical table and create a uniform magnetic field over the MOT chamber and the glass cell. They are used for the compensation of stray fields at the position of the atomic cloud in the glass cell. Three other sets of coils (coils A) of smaller size are mounted in a cage around the glass cell and generate the static bias field that the atoms feel, with the surrounding coils compensating for all other components. These coils are shown in grey in Fig. 2.2. Additional coils in anti-Helmholtz configuration create a magnetic gradient along $\mathbf{z}$ to compensate for gravity during evaporation cooling. A single coil under the glass cell produces a strong magnetic gradient for a short time, which allows for the spin-resolved detection of the atoms.

Our procedure for cancelling the ambient static magnetic field, which may originate from the Earth's magnetic field or surrounding fixed magnetic elements, is as follows. We use a three-axis flux-gate probe, with a precision of 1 mG over a range of 1 G, positioned about 10 cm away from the glass cell. First, we roughly cancel out the ambient static field based on the probe signal, using coils C. In the second stage, we cancel the residual stray fields at the position of the atoms using the atomic cloud itself as a probe. We apply a small bias field along $\mathbf{z}$ of norm $B_z = 20\,\mathrm{mG}$, using the coils A. In the presence of residual stray fields along $\mathbf{x}$ or $\mathbf{y}$ at the position of the atoms, the total magnetic field before the measurement is aligned along an axis $\mathbf{n} \neq \mathbf{z}$ and the atoms are polarised in the state $|-J\rangle_{\mathbf{n}}$. At such a weak field, the strong magnetic gradient along $\mathbf{z}$ applied during the time-of-flight expansion defines the quantisation axis and suddenly projects the atoms on the magnetic Zeeman sublevels defined with respect to $\mathbf{z}$. This leads to non-zero populations in the excited Zeeman sublevels $|m > -J\rangle_{\mathbf{z}}$ that we cancel out by tuning the coils C. Once this is done, the magnetic field is aligned with $\mathbf{z}$ and has contributions from the bias field and a possible residual stray field. We estimate this stray field by measuring the norm of the magnetic field using radio-frequency spectroscopy or Ramsey interferometry, and then compensate for it using the coils C.

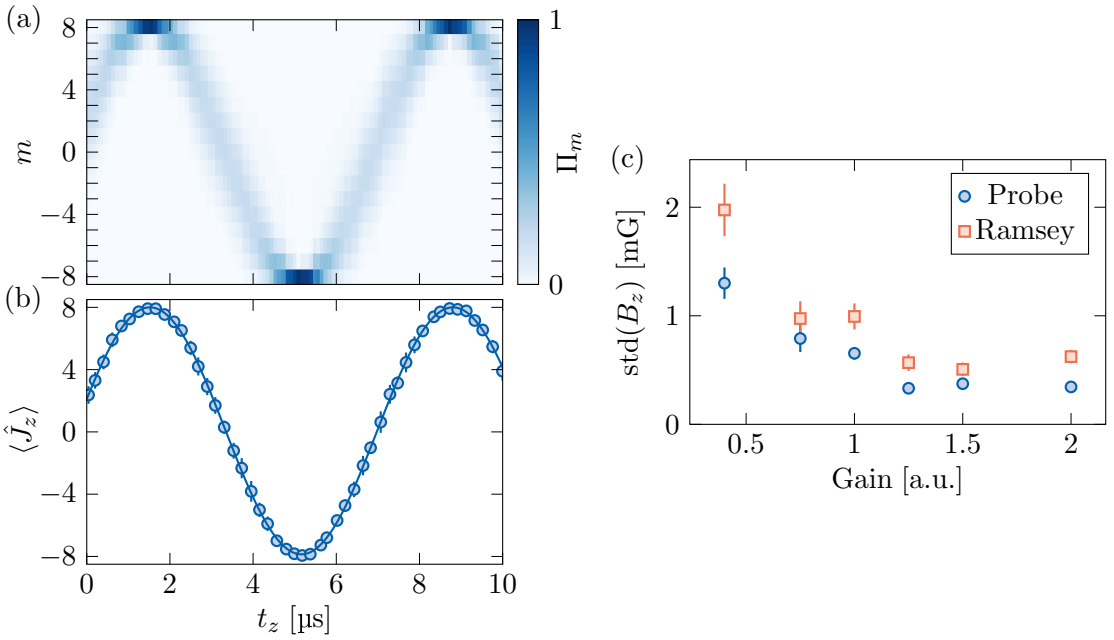

Figure 2.7 – Panel (a,b): Spin distribution Π_m and magnetisation $\langle \hat{J}_z \rangle$ of a coherent state using Ramsey interferometry, as a function of the waiting time t_z between the two $\pi/2$-pulses. The magnetisation oscillates at the Larmor frequency 137.7(4) kHz, corresponding to a bias magnetic field of 79.3(2) mG. The waiting time t_z is corrected based on the signal from a flux-gate probe to account for residual magnetic field fluctuations. Panel (c): Standard deviation of the magnetic field in the glass cell, measured using the magnetic probe in blue dots and the atoms with Ramsey interferometry in red squares, as a function of the gain of the active open-loop compensation scheme.

Ramsey interferometry combines our spin-resolved measurement technique with spin rotations. In a two-level system, the norm of the magnetic field can be measured using a linear combination of the two states with equal weight. In the Bloch sphere representation, such a state is polarised along the equatorial plane. The evolution in the presence of a magnetic field along **z** is a precession of the state around the **z** axis, which leaves the state along the equatorial plane. The angular frequency of the precession is set by the Larmor angular frequency $\delta_z = \mu_B g_J B_z/\hbar$ and provides a direct measurement of the magnetic field norm. Since the rotating states are not distinguishable by spin projection along **z**, we perform a spin rotation which is equivalent to measuring the spin projections along an axis of the equatorial plane. The precession around **z** maps onto oscillation of the magnetisation $\langle \hat{J}_z \rangle$. Our protocol involves the following sequence of rotations:

$$\mathcal{R} = R_y(\pi/2) R_z(\phi) R_y(\pi/2) \tag{2.8}$$

where the operators $R_a(\theta) = \exp(\mathrm{i}\theta J_a)$ are the rotation operators of angle θ around the axis a, with $a = x$, y or z. Starting with atoms polarised in the spin state

$|-J\rangle_{\mathbf{z}}$, the first y-rotation transfers them onto the equatorial plane of the generalised Bloch sphere. The z-rotation corresponds to the precession of angle $\phi = \delta_z t_z$ around the bias field of norm B_z, which is controlled by varying the time t_z. The second y-rotation, followed by a projection of the spin along $\mathbf{z}$, amounts to projecting the spin state along $\mathbf{x}$. We observe oscillations in the magnetisation, which we compute from the spin distribution as:

$$\langle \hat{J}_z \rangle = \sum_m m\Pi_m, \tag{2.9}$$

and show in Fig. 2.7(a,b), along with the full spin projection distribution. The y-rotations are produced by a pulsed magnetic field along $\mathbf{y}$, of duration 5 µs. For a vertical bias field $B_z \approx 79$ mG, the z-rotation occurring during the pulse is not negligible as $\delta_z \approx 2\pi \times 138$ kHz, with a period of 7.2 µs. This simply adds a phase shift to the magnetisation oscillations, unimportant for the determination of the Larmor frequency and independently calibrated. The contrast of the oscillations decreases at long times, with a coherence time of the order of a few hundred microseconds, and is limited by magnetic field fluctuations.

The magnetic field fluctuations are recorded on the magnetic probe along $\mathbf{z}$ with a rms value of 2 mG and a timescale of ≈ 1 s, which are correlated with Ramsey interferometry measurements. The main cause of the magnetic field instability is the nearby Paris metro line. We use an open-loop scheme based on the signal of the magnetic probe along $\mathbf{z}$ and back-action from additional metre-sized coils in Helmoltz configuration along the vertical axis. We adjust the strength of the compensating field by varying a gain factor and minimise the rms value of the fluctuations down to 0.4 mG, which is confirmed by simultaneously recording the probe signal and performing Ramsey interferometry in Fig. 2.7(c). In our protocol using Ramsey interferometry, we fix the waiting time to a time t_z with zero magnetisation, where the derivative of the magnetisation is maximal. A fluctuation ϵ_z of the Larmor angular frequency leads to a linear variation in the magnetisation $\pm J\epsilon_z t_z$, which is amplified at long times. For the data presented in Fig. 2.7(c), we work at 70 mG and choose t_z =13.4 µs, such that a fluctuation of 1 mG maps on a shift of the magnetisation of about 1.2, above our detection noise.

2.2 Preparation of laser beams

The work presented in this thesis involves spin-dependent light shifts produced by laser beams, whose frequency lies in the vicinity of narrow optical transitions. In addition to a laser at 626.1 nm, which is not locked because its detuning from resonance is set to be on the order of a few GHz, we also use a Titanium:Sapphire (Ti-Sapph) laser with a tunable wavelength ranging from 695 nm to 1005 nm, to address transitions at 696.0 nm and 832.8 nm. This allows us to work with spin-dependent light shifts of various relative scalar, vector and tensor contributions, depending on the difference in total angular momenta $J' - J = -1$, 0 or 1. In this Section, we present our techniques to characterise off-resonant laser beams.

All the beams are fibred for better long-term stability. Before the fibre, a laser beam passes through an AOM which controls both its frequency and its power. For

applications requiring particularly short pulses, we focus the beam in the AOM crystal to improve its time response with raising times in the nanosecond range. The first order of the light coming out of the AOM is coupled into a fibre and we control the AOM using radiofrequency signals of controlled intensity and frequency. After the fibre, the polarisation of the collimated beam is cleaned by a polarising beam splitter and a beam sampler sends a tiny fraction of light onto a photodiode for intensity control. The beam waist is magnified by a telescope and a lens with a focal length of around 50 cm focuses the beam on the atomic cloud with a beam waist of approximately 50 µm. The lens is mounted on a single-axis translation stage to tune the focal point of the beam. A two-axis mirror with piezo actuators is positioned after the lens and controls the position of the beam on the atomic plane, with a precision of the order of a fraction of micrometre. A half-waveplate and a quarter-waveplate, before the focusing lens, control the polarisation of the beam. After aligning the beam on the atomic cloud and finely tuning the focal point, we measure the parameters of the beam using a set of experimental techniques, described below.

Two complementary techniques provide information about the trap depth of the beam for a given polarisation $\boldsymbol{\epsilon}$, in the repulsive and attractive regime, for positive and negative detunings respectively. In these experiments, summarised in Fig. 2.8, we consider atoms polarised in $|-J\rangle$ with a vertical magnetic field of norm $> 1\,\mathrm{G}$. It pins the atoms in their initial spin state even when the spin-coupling light is switched on and we measure the expectation value of the light potential $\langle V_{\mathrm{LS}}\rangle$ for a spin state $|-J\rangle$. For red-detuned light, the trapping potential is attractive and we observe oscillations of the centre-of-mass in the transverse plane of the laser beam. The radial angular frequency is given by $\omega_r = (4\langle V_{\mathrm{LS}}\rangle / M w_0^2)^{1/2}$ (see Eq. 1.18) for a beam waist of w_0. For a blue-detuned light, the repulsive potential expels the atoms and the energy conservation implies that the potential energy $\langle V_{\mathrm{LS}}\rangle$ is transformed into kinetic energy $Mv^2/2$ as the atoms leave the light potential. For a well-centred beam, the atoms form a ring whose radius increases linearly in time with a velocity given by the acquired kinetic energy. We measure the distribution with an imaging beam propagating either along the repulsive beam or along an orthogonal axis, depending on the optical access. In the former case, we observe a ring while in the latter case, we observe the transverse projection of a ring that features two main peaks whose half distance is roughly the radius of the ring.

An additional experiment with positive detuning provides further insight into the trap depth and is performed on a much shorter timescale with a pulse duration in the $10 - 100\,\mu\mathrm{s}$ range, compared to a few milliseconds in the previous two experiments. We off-centre the beam by half the waist such that the force $F = -\boldsymbol{\nabla} V_{\mathrm{LS}}$ is maximal and proportional to $\langle V_{\mathrm{LS}}\rangle / w_0$. The atoms acquire a velocity $v = Ft$ with t the pulse duration that we measure after a time-of-flight expansion. By combining the measurements of the trap depth presented above and the measurement of the force, we obtain an estimate of the beam waist, independently of the intensity and polarisation of the beam.

This protocol also provides information on the polarisation $\boldsymbol{\epsilon}$ if we extend it to the case of a coherent state polarised along any direction $\mathbf{n}$. A coherent state with orientation $\mathbf{n}$ parametrised by the spherical angles (θ, ϕ) has significant projection

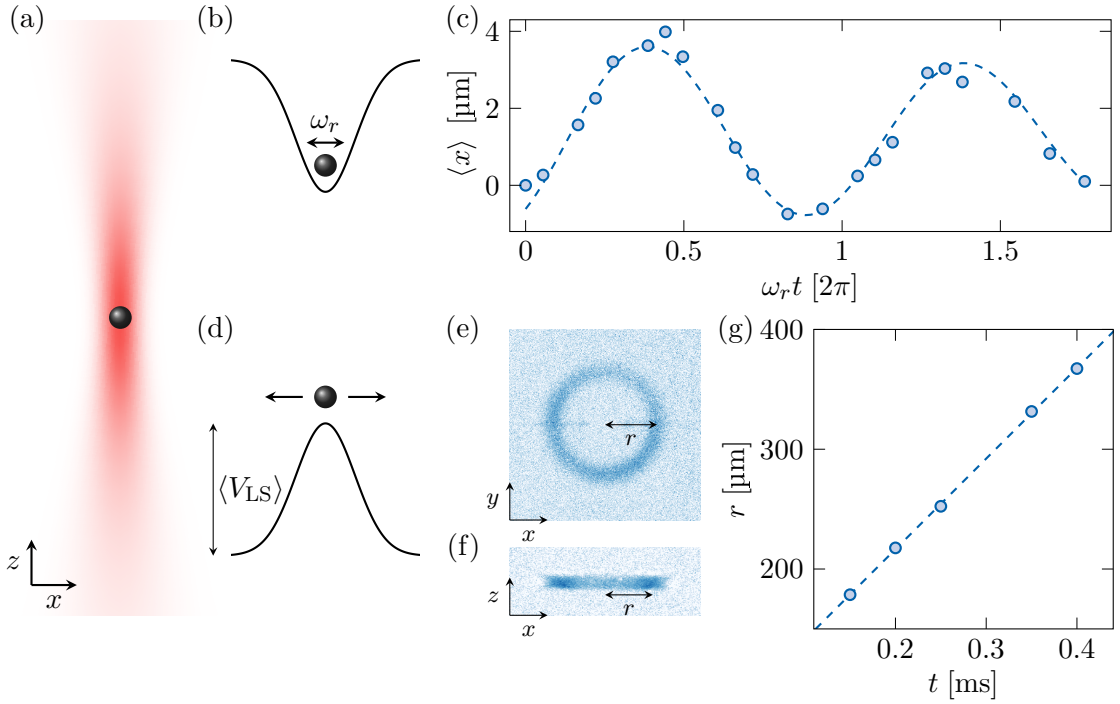

Figure 2.8 – Panel (a): Scheme of a single off-resonant light beam propagating along **z**, centred on an atomic cloud. We distinguish the cases with negative detuning in (b,c) and positive detuning in (d,e,f,g). Panel (b): The red-detuned beam creates an attractive potential with a trapping angular frequency ω_r (see Eq. 1.18) in the (x, y) plane. Panel (c): Oscillation of the centre-of-mass position $\langle x \rangle$ as a function of time, with angular frequency ω_r, and its fit in dashed line. Panel (d): The blue-detuned beam creates a repulsive potential of trap depth $\langle V_{\mathrm{LS}} \rangle$, that repels the atoms radially. Panels (e,f): Examples of atoms subjected to this potential after a time-of-flight expansion, imaged along **z** and **x** respectively. Panel (g): Radius r of the exploded cloud as a function of the expansion time. A linear fit (dashed line) gives the velocity of the expansion, related to the trap depth $\langle V_{\mathrm{LS}} \rangle$ by energy conservation.

probabilities Π_m along magnetic Zeeman sublevels $|m\rangle$, with m close to $J \cos\theta$. We prepare such a state using the magnetic rotations introduced for Ramsey interferometry in Section 2.1.3, with an angle θ ranging from 0 to π. We pulse the repulsive force and measure the velocity distribution, after time-of-flight expansion in the presence of a strong magnetic field. The single-spin resolution allows us to measure the expectation value of the force for each Dicke state $|m\rangle$ independently. From these measurements, we deduce the quantity $Q_m = \langle m|V_{\mathrm{LS}}|m\rangle / V_0$, with V_0 defined in Eq. 1.20, for each integer $-J \leq m \leq J$, which depends on the total angular momentum of the excited level and on the polarisation only. Systematic errors in V_0 can be corrected using the global constraint $\sum_m Q_m = (2J+1)/3$, fixed by the spin algebra. As in all previous experiments in this Section, we maintain a magnetic field large enough to hamper spin dynamics during the light pulse.

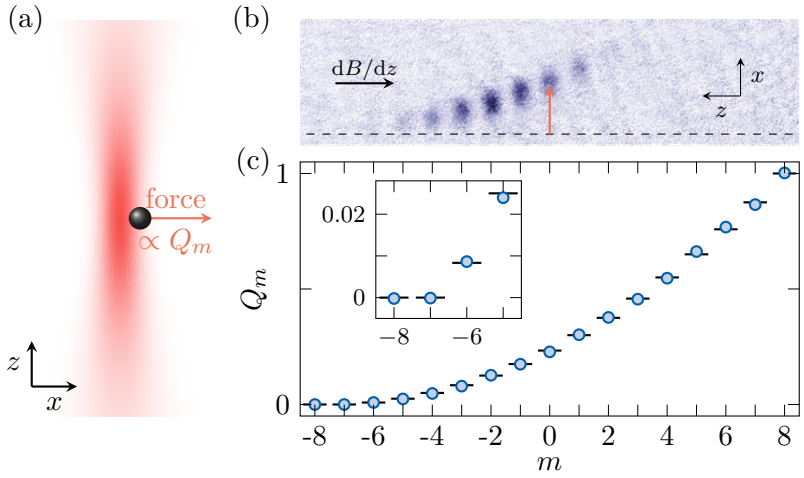

Figure 2.9 – Panel (a): Scheme of a single off-resonant light beam propagating along **z** with negative detuning, off-centred from the position of the atomic cloud by half its waist. The atoms feel the force that derives from the gradient of the repulsive potential. It is related to the coefficients $Q_m = \langle m|V_{\mathrm{LS}}|m\rangle / V_0$ defined for the Dicke basis. We take the example of a circularly-polarised beam with polarisation σ_-. Panel (b): Example of a single image with single-spin resolution after expansion, for a coherent state with polar angle $\theta = 100°$. We measure the displacement of the centre-of-mass of the atoms for each significantly populated spin state m. Panel (c): Q_m coefficients, measured using coherent states spanning all magnetic Zeeman sublevels. In the inset, we highlight the vanishing expectation values of the light shift for $m = -J$ and $-J+1$, which are dark states for the σ_- polarisation.

In Fig. 2.9, we give the example of a circularly-polarised beam propagating along **z** at 696.0 nm, coupling the electronic ground state to an excited state with a total angular momentum $J' = J - 1$. The light shift is diagonal in the Dicke basis defined by the orientation of the bias magnetic field along **z** and has a tensor contribution which is quadratic in $\hat{J}_z$:

$$V_{\mathrm{LS}} = V_0 \left[\left(\alpha_0 + \alpha_2 \frac{J+1}{2(2J-1)} \right) \hat{\mathbb{1}} - \alpha_1 \frac{1}{2J} \hat{J}_z - \alpha_2 \frac{3}{2J(2J-1)} \hat{J}_z^2 \right], \tag{2.10}$$

for a σ_- polarisation $\boldsymbol{\epsilon} = (\mathbf{e}_x - \mathrm{i}\mathbf{e}_y)/\sqrt{2}$. For the transition at 696.0 nm, the light shift reduces to:

$$V_{\mathrm{LS}} = V_0 \frac{(\hat{J}_z + J)(\hat{J}_z + J - 1)}{2J(2J+1)}, \tag{2.11}$$

and cancels out for the two states $|m = -J\rangle$ and $|m = -J+1\rangle$ with vanishing $Q_m = \langle m|V_{\mathrm{LS}}|m\rangle / V_0$ coefficients. These states, called dark states, do not couple to light, which protects them from decoherence by spontaneous emission. Dark states arise for specific choices of optical transition and polarisation and have been considered in a wide range of applications [102, 103], including the implementation of

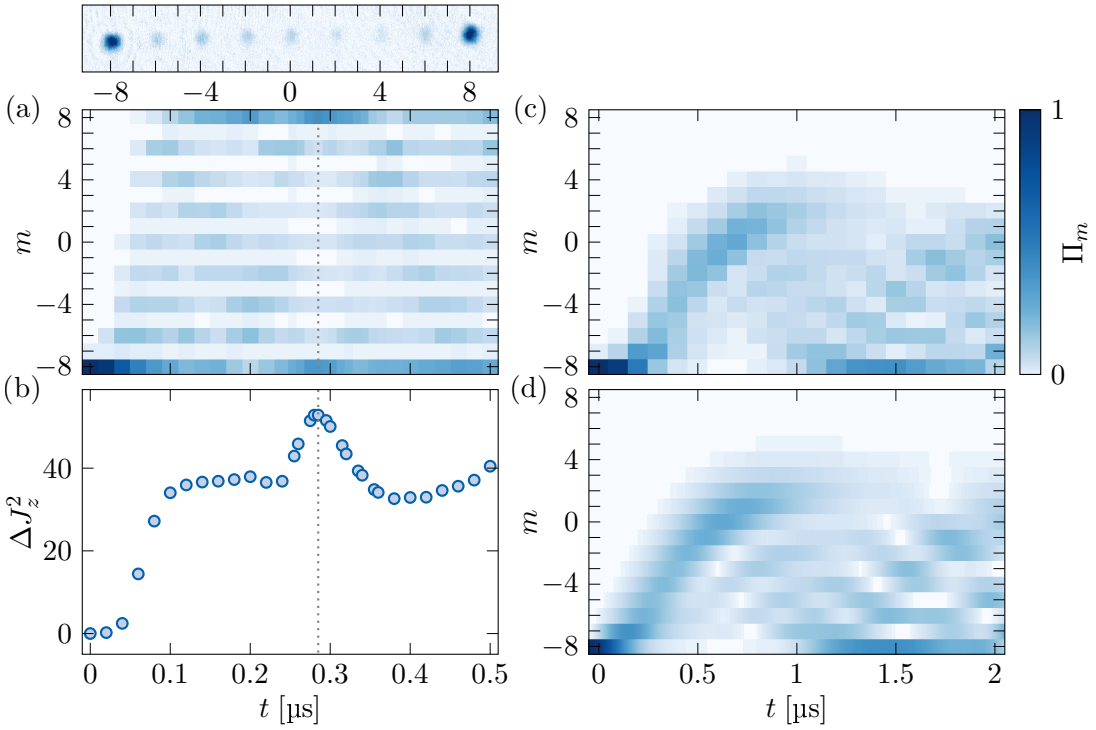

Figure 2.10 – Panel (a): Evolution of the spin distribution Π_m under the one-axis twisting Hamiltonian $\hbar\chi\hat{J}_x^2$, with $\chi \approx 2\pi \times 0.9\,\mathrm{MHz}$, induced by a beam with linear polarisation $\boldsymbol{\epsilon} = \mathbf{e}_x$, in the presence of a bias magnetic field $B_z \approx 50\,\mathrm{mG}$. Panel (b): Corresponding evolution of the spin variance ΔJ_z^2 with a maximum at $t \approx 0.28\,\mu\mathrm{s}$ highlighted by a vertical dotted grey line. The corresponding spin state, a coherent superposition with nearly equal maximum populations in $|m = \pm J\rangle$, is referred to as a cat state and is shown above. Panel (c): Evolution of the spin distribution Π_m as a function of the pulse time t. The light shift is induced by a single beam with polarisation $\boldsymbol{\epsilon} = \cos\theta\,\mathbf{e}_z + \sin\theta\,\mathbf{e}_y$ with fixed θ. Panel (d): Fit of the spin distribution in (c) taking into account defects in the polarisation, notably a deviation of θ or an additional phase between the two linear components that introduces a polarisation ellipticity.

artificial gauge fields [79, 104]. We show a single-shot absorption image for a coherent state of polar angle $\theta \approx 100°$ and the resulting values of Q_m, combining measurements of coherent states with various orientations spanning the whole Bloch sphere. We zoom in on the states close to $m = -J$ and point out that both $|m = -J\rangle$ and $|m = -J + 1\rangle$ have vanishing expectation values of the light shift, as expected for dark states.

Information about the polarisation of the beam can also be obtained in a completely different type of experiment, in the presence of a much weaker bias field of typically 50 mG, which does not dominate the spin-changing couplings. Atoms initially polarised in $|-J\rangle$ are subjected to short pulses of light on the microsecond timescale and their spin state evolves with time. We give some examples:

- A beam at 696.0 nm with linear polarisation $\boldsymbol{\epsilon} = \mathbf{e}_x$, producing a spin-changing light shift:

$$V_{\mathrm{LS}} = V_0 \left[\left(\alpha_0 - \alpha_2 \frac{J+1}{2J-1} \right) \hat{\mathbb{1}} + \alpha_2 \frac{3}{J(2J-1)} \hat{J}_x^2 \right]. \tag{2.12}$$

  The first term is diagonal in the Dicke basis and contributes only to a spin-independent potential. The second term of the form $\hbar\chi \hat{J}_x^2$ realises the so-called one-axis twisting Hamiltonian, well-known for the generation of spin squeezing [105–107]. At short times $\chi t \approx 0.05$, the spin state is squeezed while remaining gaussian, with a reduction of a spin projection quadrature at the expense of an increase in the orthogonal one. At intermediate times, the spin distribution is featureless and these states are referred to as oversqueezed states. At time $\chi t = \pi/2$, the state forms a coherent superposition of the stretched states $|m = \pm J\rangle$, which is called a Schrödinger cat state. We show the spin evolution and the measured cat-like state in Fig. 2.10(a,b), as well as the evolution of the variance ΔJ_z^2. The cat-like state has residual populations in other spin states than the stretched states, due to the non-zero bias magnetic field.

- A beam at 626.1 nm with linear polarisation $\boldsymbol{\epsilon} = \cos\theta\, \mathbf{e}_z + \sin\theta\, \mathbf{e}_y$ with $\theta = \mathrm{acos}\left(1/\sqrt{3}\right) \simeq 55°$, which is used for the implementation of an atomic Hall cylinder. The induced light shift is similar to the case of $\mathbf{e}_x$ polarisation associated with the one-axis twisting Hamiltonian described above, although with the change of operator $\hat{J}_x \to \cos\theta \hat{J}_z + \sin\theta \hat{J}_y$. Due to the bias field and the spin projection along $\mathbf{z}$, we do not record the same spin evolution as for a polarisation $\mathbf{e}_x$ but recognise interference patterns that are typical of coherent state superpositions. The evolution of the measured spin projection distribution is shown in Fig. 2.10(c), together with a fit in (d). We fit the distribution Π_m using the theoretical formula for the spin coupling allowing for a systematic error in the coupling strength V_0 and accounting for defects in the polarisation. We use the more general polarisation $\boldsymbol{\epsilon} = \cos\theta\, \mathbf{e}_z + \mathrm{e}^{\mathrm{i}\phi} \sin\theta\, \mathbf{e}_y$ with an additional phase ϕ between the two linear components, related to the polarisation ellipticity. The three parameters V_0, θ and ϕ are essential to reproduce the experimental data with the numerical simulations.

- A circularly-polarised beam at 696.0 nm propagating along the axis of the bias magnetic field. It induces no spin evolution for an initial spin state $|-J\rangle$ because the light shift is diagonal in the basis of Zeeman sublevels $|m\rangle$, as shown in Eq. 2.10.

This Chapter has described our experimental setup and how it can be used for the manipulation of spin systems. In the next Chapter, we present a project about the notion of entanglement in a large spin system, which relies on the optical coupling to excited levels with different total angular momentum J'. This work illustrates some of the off-resonant light shifts described above.

3

Partitioning dysprosium's electronic spin to reveal entanglement

This Chapter briefly describes our work on the notion of entanglement in non-classical states prepared in the electronic spin of dysprosium atoms. We refer interested readers to the thesis of Tanish Satoor for a more detailed discussion.

This work has been published in the following publication [108]:
Partitioning dysprosium's electronic spin to reveal entanglement in non-classical states
T. Satoor*, A. Fabre*, J.-B. Bouhiron, A. Evrard, R. Lopes, S. Nascimbene
Physical Review Research 3 (1), 043001 (2021)
* These authors contributed equally
The full text of the article is available in Appendix A.

Entanglement is a fundamental property of quantum mechanics, which involves non-classical correlations between the constituents of the total system and expresses non-locality. Schrödinger described entanglement as a "spooky" feature of quantum compounds and a situation where "the best possible knowledge of a whole does not include the best possible knowledge of its parts" [109]. First highlighted in a seminal work by Einstein, Podolsky and Rosen [110], a test of its existence was proposed by Bell [111] with a set of inequalities and has been experimentally realised since then [112]. More recently, the interest in this notion has renewed with developments in quantum technologies, including applications in quantum computing [113, 114], and has been highlighted by the 2022 Nobel Prize.

The notion of entanglement has been extensively studied in the context of many-body systems [115]. Experimental contributions include systems of distinguishable components, such as photonic systems [116], superconductors [117], trapped ions [118] and Rydberg atom arrays [119], producing highly entangled states of tens of qubits. The ability to individually probe and even address the particles facilitates the observation of entanglement. In systems of indistinguishable particles, such as an ensemble of interacting atoms [120], where individual addressing is not possible, entanglement in the many-body quantum state is revealed by global properties, such

as the squeezed spin quadrature [106, 121–123] and the quantum enhancement of metrological sensitivity [107, 124, 125].

In this Section, we describe our study of non-classical correlations and entanglement within dysprosium's large spin $J = 8$, based on its formal equivalence with a system of $N = 2J$ indistinguishable qubits of spin 1/2, symmetric upon particle exchange. Large-spin systems are known to host quantum states with non-classical correlations [126–128]. However, the notion of entanglement is disputable as long as the angular momentum J is conserved, since the set of qubits cannot be partitioned. For this reason, our work contributes to a discussion about non-classicality and entanglement in systems of indistinguishable constituents [129]. We first recall some basic elements about the description of entanglement and its observation. We then develop our protocol to partition our system into subsystems of $2(J-1)$ and 2 qubits, using the optical coupling to an excited state with angular momentum $J' = J - 1$, which encodes the remaining 2 qubits in the photon polarisation. In a complementary set of experiments, starting with a quantum state in an excited level with spin $J' = J + 1$, we study the effect of decoherence and interpret the spontaneous emission of a photon as the loss of a qubit pair in a random state.

3.1 Notion of entanglement

A pure state is said to be entangled if it cannot be expressed as a product state with respect to a partition in subsystems A and B as $|\phi_A\rangle \otimes |\phi_B\rangle$, contrary to the so-called separable states. This definition generalises to the case of mixed states, represented by a density matrix. In general, the determination of the degree of entanglement is challenging because it requires non-linear operations [130]. Interestingly, for a two-qubit system, a measure of entanglement called the concurrence [131] has an explicit form that simplifies its computation. In systems with a larger number of components, an alternative approach relies on simply proving the presence of entanglement. For quantum states close to a known entangled state, an entanglement witness [132] can be constructed by comparison between the two. Another criterion for entanglement is based on the property of separable states that the global state is more disordered than its parts [133]. This translates into a condition on the sign of the conditional entropy defined with respect to a partition. The inequality $S(A|B) \equiv S(A,B) - S(B) < 0$ proves the presence of entanglement for any choice of entropy measure S. In our experiments, we use the Rényi entropy of infinite order [134], or min-entropy, $S_\infty(\rho) = -\log \lambda_{\max}(\rho)$ where $\lambda_{\max}(\rho)$ is the maximum eigenvalue of the density matrix ρ, which corresponds to the maximum possible overlap of ρ with a pure state.

An essential characteristic of multipartite systems arises from the existence of inequivalent classes of entanglement, which exhibit different properties. This was first highlighted in three-qubit systems [135, 136], which host two inequivalent entanglement classes represented by the so-called GHZ state, or N00N state or Schrödinger cat state depending on the context, and the W state [137–139]. These two classes also exist in systems with a larger number $N = 2J$ of compounds, with

the equivalent Schrödinger cat state and W state:

$$\begin{aligned} |W\rangle &= \frac{1}{\sqrt{N}}(\,|\uparrow\downarrow\downarrow\cdots\rangle + |\downarrow\uparrow\downarrow\cdots\rangle + |\downarrow\downarrow\uparrow\cdots\rangle + \cdots) = |J, m=-J+1\rangle \\ |\text{cat}\rangle &= \frac{1}{\sqrt{2}}(\,|\downarrow\downarrow\downarrow\cdots\rangle + |\uparrow\uparrow\uparrow\cdots\rangle) = \frac{1}{\sqrt{2}}(\,|J, m=-J\rangle + |J, m=J\rangle) \end{aligned} \tag{3.1}$$

We used the formal equivalence between the quantum states of $N = 2J$ particles of spin 1/2 with particle-exchange symmetry and those of the Zeeman J-manifold, to represent these two states using the Dicke basis. These paradigmatic states have attracted considerable attention and have been realised in various platforms. On one side, the W state hosts pairwise entanglement and is known for its robustness against decoherence and in particular particle loss. On the other side, the cat state is often described as maximally entangled and features what is referred to as genuine multipartite entanglement, which strongly suffers from decoherence. A hallmark of this state is that any of its subsystems is classical.

3.2 Pair Husimi function

Our protocol to probe entanglement upon partition of the spin J in the electronic ground state relies on its interpretation as a system of $N = 2J$ qubits with spin 1/2 in a state symmetric upon particle exchange. In this analogy, a state of the Dicke basis $|J, m\rangle$ is composed of $J - m$ qubits in $|\downarrow\rangle_{\mathbf{z}}$ and $J + m$ qubits in $|\uparrow\rangle_{\mathbf{z}}$. We perform a $2(J-1) : 2$ partition via the coupling to an excited level of spin $J' = J - 1$. The light polarisation can be represented as a symmetric two-qubit state, with a total angular momentum $L = 1$, via its decomposition on the three usual polarisations $\sigma_\pm$ and π. The coupling to light is polarisation-dependent and proportional to $\langle\boldsymbol{\epsilon}^*|\rho_{\text{pair}}|\boldsymbol{\epsilon}^*\rangle$ with $|\boldsymbol{\epsilon}^*\rangle$ the complex-conjugate of the polarisation state and $\rho_{\text{pair}} = \text{Tr}_{2J'}(\rho)$ the pair density matrix, obtained by tracing out the remaining $2J'$ qubits. This can be understood in the case of resonant light as an annihilation process with the removal of qubit pair in state $|\boldsymbol{\epsilon}^*\rangle$ upon absorption of a photon in state $|\boldsymbol{\epsilon}\rangle$. In practice, our measurements are performed using off-resonant light shifts with a σ_- polarisation, corresponding to $|\boldsymbol{\epsilon}^*\rangle = |\uparrow\uparrow\rangle_{\mathbf{z}}$. For this choice of polarisation, the expectation value ${}_{\mathbf{z}}\langle\boldsymbol{\epsilon}^*|\rho_{\text{pair}}|\boldsymbol{\epsilon}^*\rangle = \langle\uparrow\uparrow|\rho_{\text{pair}}|\uparrow\uparrow\rangle_{\mathbf{z}}$ is also known as the pair Husimi function $Q_{\text{pair}}(\mathbf{z})$ along the direction $\mathbf{z}$, related to the probability of finding two qubits in $|\uparrow\rangle_{\mathbf{z}}$. This function completely characterises the qubit pair state when known along all directions $\mathbf{n}$. In the light shift context, it is simply written $\langle V\rangle / V_0$, with $\langle V\rangle$ the light shift computed for the density matrix ρ and the σ_- polarisation. For a state of the Dicke basis $|J, m\rangle$, we recover the Q_m coefficients introduced in Section 2.2, whose measurements were presented in Fig. 2.9. Since they form a basis of the Hilbert space in the J-manifold, we can deduce the pair Husimi function of any quantum state along an axis $\mathbf{n}$ from the measurements of the spin distribution:

$$Q_{\text{pair}}(\mathbf{n}) = \sum_m Q_m \Pi_m(\mathbf{n}). \tag{3.2}$$

Interestingly, we can compute the tools presented in Section 3.1 using the pair Husimi function only. On one hand, the non-classical character of the qubit pair

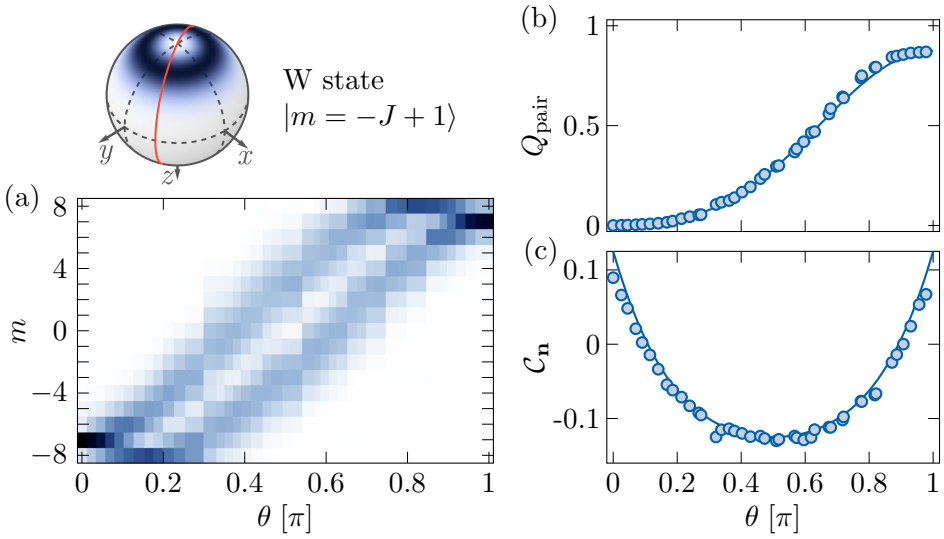

Figure 3.1 – Panel (a): Measured spin projection probabilities Π_m as a function of the polar angle θ, for the W state. The upper panel represents the considered spin-J state on the Bloch sphere, the red circle indicates the spanned measurement projection axis. Panel (b): Pair Husimi function Q_{pair} computed from the data in (a). The line corresponds to the expected function $Q_{\text{pair}}(\theta)$ for the W state. Panel (c): Distribution $\mathcal{C}_{\mathbf{n}}$ of non-classical correlations as a function of the polar angle θ. The points with $\mathcal{C}_{\mathbf{n}} > 0$ evidence the non-classicality of the qubit pairs of the W state.

state is equivalent to finding an orientation $\mathbf{n}$ for which the non-classical measure $\mathcal{C}_{\mathbf{n}} = 1 - \left(\sqrt{Q_{\text{pair}}(\mathbf{n})} + \sqrt{Q_{\text{pair}}(-\mathbf{n})}\right)^2$ is strictly positive, similarly to the bipartite entanglement witness [140]. The concurrence of the qubit pair is then expressed as the maximum of the non-classical measure $\mathcal{C}_{\mathbf{n}}$, measured for all orientations. This relation was conjectured and numerically checked for randomly generated states [141]. On the other hand, the conditional entropy requires the computation of two terms. The entropy of the qubit pair state is deduced from the quantum tomography of the state [142], reconstructed from the pair Husimi function along all possible orientations. The entropy of the state of the total system is estimated by techniques that are suited to the entanglement class to which the quantum state belongs.

3.3 Entanglement in the W and cat states

We focus on two paradigmatic states, the W state and the Schrödinger cat state, for which we first compute the pair Husimi function. The W state is prepared by applying a strong quadratic light shift, diagonal in the Dicke basis and acting on all spin states except the two spin states $|m = -J\rangle$ and $|m = -J + 1\rangle$ as in Eq. 2.11. The resulting energy splitting between neighbouring Dicke states is uneven and increases with m, and we can restrict the dynamics to the two dark states. Starting with atoms polarised in $|m = -J\rangle$, a resonant radio-frequency π-pulse brings the system to $|m = -J + 1\rangle$ with a maximum fidelity with the W state of 0.91(1).

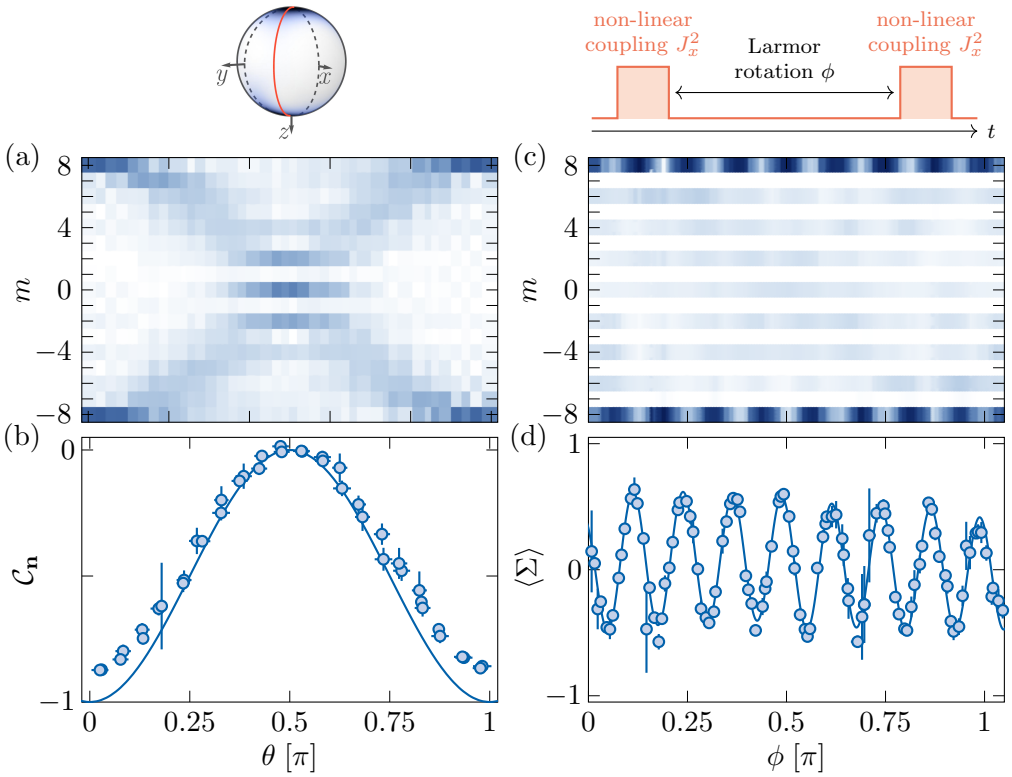

Figure 3.2 – Panel (a): Measured spin projection probabilities Π_m for a cat state, as a function of the polar angle θ. The azimuthal angle $\phi = 0.86(5)$ rad is chosen such that the two coherent state Husimi functions destructively interfere for odd m values around $\theta = \pi/2$. Panel (b): Distribution $\mathcal{C}_\mathbf{n}$ inferred from the probabilities shown in (a). The solid line is the expected variation for a perfect cat state. Panel (c): Projection probabilities Π_m measured after a Larmor rotation of angle ϕ followed by a second non-linear evolution. Panel (d): Evolution of the mean sign of even projections $\langle\Sigma\rangle$ deduced from (c). The solid line is a fit with a Fourier series.

The cat state is prepared using the one-axis twisting Hamiltonian in Eq. 2.12, with parameters similar to the example of Fig. 2.10(c,d). We confirm dominant population of the stretched states $\Pi_{-J} = 0.38(2)$ and $\Pi_J = 0.42(2)$.

The prepared W state features a measured concurrence of its qubit pairs of $\mathcal{C} = 0.089(5)$, smaller than the maximal value of $1/J = 0.125$ due to experimental defects in the state preparation. The strictly positive value of the concurrence demonstrates the non-classicality of a qubit pair of the W state that highly breaks the symmetry between the basis states $|\uparrow\rangle_\mathbf{z}$ and $|\downarrow\rangle_\mathbf{z}$. The measurement of the spin distribution along all axes $\mathbf{n}$ and the resulting non-classical measure $\mathcal{C}_\mathbf{n}$ are presented in Fig. 3.1. Using the projection probability $\Pi_{-J+1} = 0.91(1)$ with the Dicke state $|m = -J+1\rangle$ as a lower bound on the maximum overlap $\lambda_{\max}(\rho)$ with a pure state and state tomography for the estimation of $\lambda_{\max}(\rho_{\text{pair}})$, we deduce the conditional entropy $S_\infty(2J'|2) < -0.03(1)$, a proof of the entanglement of the W state.

For the prepared cat state, the non-classical measure $\mathcal{C}_\mathbf{n}$ remains negative for all

orientations $\mathbf{n}$ and its pair density matrix does not exhibit a non-classical behaviour, which is a characteristic feature of genuine multipartite entanglement. The calculation of the conditional entropy requires an estimate of the maximum eigenvalue $\lambda_{\max}(\rho)$, for which a lower bound follows from the overlap with a perfect cat state $\mathcal{O} = (\Pi_{-J} + \Pi_J + 2|\rho_{-J,J}|)/2$. The extremal coherence $|\rho_{-J,J}|$ can be measured from any observable upon Larmor rotation around z. The Fourier coefficient at the frequency $2J$ times the Larmor frequency contains the information about the extremal coherence, independently from other coherences [143]. We consider an observable based on repeating a non-linear operation, the one-axis twisting evolution used to produce a cat state. We choose the operator Σ defined as the sign of the spin projection on even states as an observable, benefiting from the parity symmetry of the one-axis twisting Hamiltonian. It gives a lower bound of 0.247(5) on $\lambda_{\max}(\rho)$, which leads to a condition entropy $S_\infty(2J'|2) < -0.12(3)$ when combined with the tomography of the pair density matrix. This proves entanglement more evidently than for the W state.

3.4 Decoherence via qubit pair loss

In a complementary set of experiments, we consider the effect of decoherence on the entanglement of the total system and the non-classical character of the pair density matrix. We focus on decoherence upon qubit pair loss that naturally appears in our system via spontaneous emission from an electronic excited level of spin $J' = J + 1$ to the ground level of spin J, with two virtual qubits missing. For an entangled quantum state ρ' in the excited level, taking into account the three polarisation components $\mathbf{e}_-$, $\mathbf{e}_z$ and $\mathbf{e}_+$, corresponding to σ_-, π and σ_+ respectively, the state after spontaneous emission reads:

$$\rho = \sum_{\mathbf{e}_u = \mathbf{e}_-, \mathbf{e}_z, \mathbf{e}_+} \langle \mathbf{e}_u | \rho' | \mathbf{e}_u \rangle = \mathrm{Tr}_2\, \rho', \tag{3.3}$$

corresponding to the loss of an arbitrary qubit pair. The spontaneously emitted photon has an arbitrary polarisation which encodes the state of the removed qubit pair. We do not retrieve the photon but record the spin state ρ after decay.

The preparation of quantum states in the excited level relies on the resonant optical coupling to the transition at 626.1 nm, for a given choice of initial quantum state in the ground level and light polarisation. We perform a π-pulse that promotes the atoms to the electronic level with a fidelity of 0.98, which we check by measuring the mean velocity along the propagation axis of the resonant field as a function of the pulse duration. An example of Rabi oscillation monitored via the atom recoil upon light absorption is shown in Chapter 1, in Fig. 1.2, in the case of atoms initially polarised in $|J, m = -J\rangle$ with π-polarised resonant light. This protocol prepares a W state in the excited level $|J', m' = -J' + 1\rangle$, which we probe via measurements of the spin state in the ground level, after waiting for spontaneous emission to occur. We mainly measure populations in the two states $|J, m = -J\rangle$ and $|J, m = -J + 1\rangle$, as expected from the selection rule $|m' - m| \leq 1$ for single-photon processes, with a larger population in the W state. We compare our measurements with the expected spin state after decay and take into account the defects in the state preparation due to spontaneous emission during the resonant pulse, by solving

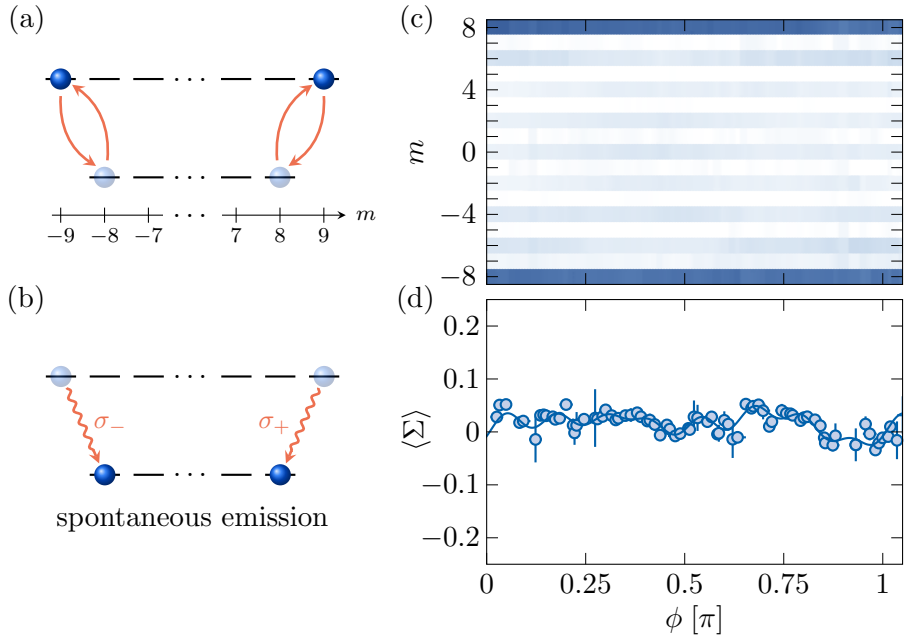

Figure 3.3 – Panel (a): Scheme of the preparation of the Schrödinger cat state in the excited electronic level. Given the small values of their Clebsch-Gordan coefficients, we neglect the couplings between $|m = \pm 8\rangle$ to $|m' = \pm 7\rangle$. Panel (b): Scheme of the subsequent spontaneous emission. Panel (c): Spin projection probabilities, as a function of the phase ϕ of the Larmor rotation before the second non-linear evolution. Panel (d): Evolution of the corresponding sign observable $\langle\Sigma\rangle$, together with a fit with a Fourier series.

the master equation for the two electronic levels following the treatment in Section 1.2.1. We quantify the non-classical character of qubit pairs by measuring the pair Husimi function and computing the non-classical measure along $\mathbf{z}$. This gives a lower bound on the concurrence $\mathcal{C} = 0.104(3)$, to be compared to the expected concurrence $\mathcal{C} = 1/(J+1) \approx 0.111$ in the initial state. This highlights the robustness of the pairwise non-classical behaviour of the W state.

We now contrast this property with the fragility of coherent superpositions of distant states in phase space [144]. The preparation of a cat state consists of producing a cat state in the ground manifold and then applying resonant light with a linear polarisation along x, which predominantly couples the stretched states $|m = \pm J\rangle$ to the states $|m' = \pm J'\rangle$. Using the non-linear protocol with the sign observable Σ, we estimate the extremal coherence $|\rho_{-J,J}|$ to be 0.006(10), indicating an absence of coherence. Associated with the populations measured in the stretched states, the conditional entropy is positive and does not demonstrate entanglement. The complete loss of coherence can be interpreted by the spontaneous emission from $|m' = -J'\rangle$ or $|m' = J'\rangle$ by a photon with σ_- or σ_+ polarisation respectively. Since these polarisations are orthogonal, the photon polarisation holds complete 'which path' information [145, 146] about the spin state, which destroys the coherence

between the two paths.

A natural extension of this work involves the retrieval of the spontaneously emitted photon whose polarisation is entangled with the quantum state in the ground level. The photon can be sent over large distances and used as a resource for entanglement manipulation and quantum communication [147, 148]. This Chapter has demonstrated an application of spin-dependent light shifts to manipulate a purely spin system. In the following Chapters, we will discuss the emerging physics when the spin degree of freedom is coupled to a spatial dimension, which effectively engineers an artificial gauge field for neutral particles.

4

Theory of the two-dimensional quantum Hall effect

Quantum Hall systems belong to a class of topological insulators that break the time-reversal symmetry. Their central position stems from the early experimental discovery of the quantised conductivity in metals [2]. The problem of charged particles subjected to a magnetic field has been investigated extensively in experiments and with various theoretical approaches. The effect of a magnetic field can be reformulated in terms of a complex phase for the particle wavefunction with physical consequences, the so-called Aharonov-Bohm phase [149]. Its effect is observable in interference experiments such as the well-known case of a double-slit experiment with charged particles passing around an infinite solenoid, where this phase cannot be gauged away. In modern physics, it is reinterpreted as a geometric phase over a closed contour, referred to as a Berry phase, a more general concept for periodically-driven systems [150].

In the first Section, we derive the Berry phase from the evolution of a wavefunction under a time-periodic Hamiltonian. This geometric phase, analogous to the Aharonov-Bohm phase for a charged particle, opens the way toward the implementation of gauge fields for neutral particles using the adiabatic following of a dressed state. We will discuss this approach from an experimental point of view in Chapter 7. In the second Section, we describe the physics of a Hall system, in the classical and quantum cases. We focus on the quantised transverse response, at the source of the integer quantum Hall effect. Arguments supporting the quantisation and its robustness arise from different approaches. The third Section treats this problem in cylindrical geometry, which connects to our implementation of an atomic Hall cylinder. The fourth Section is dedicated to topological pumps, where a quantised current is observed under periodic driving of an external parameter. We relate this concept to topological insulators in higher dimensions, where the quantisation of the bulk response is protected by the topology of the system. We conclude this Chapter with a brief presentation of the fractional quantum Hall states, in the presence of repulsive interactions.

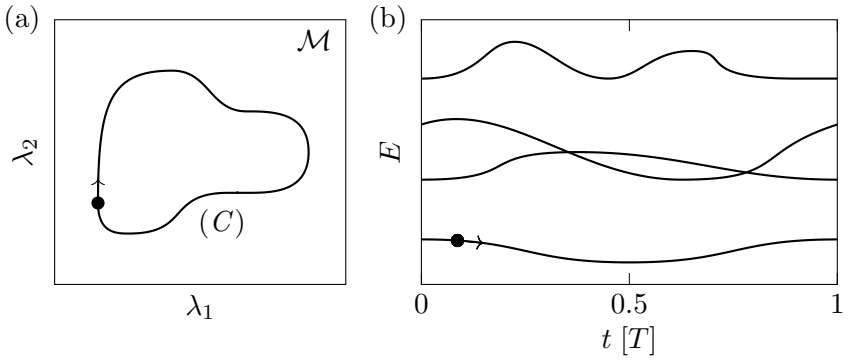

Figure 4.1 – Panel (a): A closed loop (C) in parameter space $\mathcal{M}$, represented as a two-dimensional space parametrised as (λ_1, λ_2). The direction of the evolution of the parameter in time is represented by an arrow. Panel (b): The spectrum of the Hamiltonian $H_{\boldsymbol{\lambda}}$ along the closed loop depicted in panel (a), parametrised by time varying from 0 to the cycle duration T. Due to the time periodicity ($\boldsymbol{\lambda}(T) = \boldsymbol{\lambda}(0)$), the eigenenergies at $t = 0$ and $t = T$ are equal. The adiabatic theorem requires the absence of energy crossing for the band where the particle is initialised, as is depicted for the lowest band here.

4.1 Geometric phase

We first introduce the notion of the geometric phase, generally referred to as Berry phase [150]. This notion is related to the description of the adiabatic evolution of a quantum system under a time-periodic Hamiltonian. Briefly, a quantum system in a given eigenstate $\psi_n(t)$ (with label n and associated energy $E_n(t)$) of a time-dependent Hamiltonian $H(t)$ remains in this eigenstate under adiabatic evolution, while acquiring a complex phase. The first contribution to this phase is trivial and comes from the time integration of the energy (divided by $\hbar$) of the instantaneous eigenstate; it is the so-called dynamical phase as it directly depends on the time evolution. The second contribution is the Berry phase and cannot be gauged out for a closed-loop evolution. It is a gauge-invariant property of the system, which is thus physical and measurable. This phase is also called the geometric phase because it depends on the path followed in the parameter space, but not on the time-dependence of the evolution.

4.1.1 Adiabatic theorem

We consider an Hamiltonian $H_{\boldsymbol{\lambda}}$, parametrised by the (possibly multidimensional) parameter $\boldsymbol{\lambda}$ that lives in a parameter space $\mathcal{M}$, as represented in Fig. 4.1(a). We study the evolution of quantum states under a time-variation of the parameter $\boldsymbol{\lambda}(t)$. In particular, we focus on an evolution of the parameter which is arbitrarily slow and follows a closed loop in the space $\mathcal{M}$ with a period T: $\boldsymbol{\lambda}(T) = \boldsymbol{\lambda}(0)$.

The evolution under a time-dependent Hamiltonian is generally non-trivial. However, due to the slow variation in parameter space, the quantum adiabatic theorem describes it simply: if the system is initiated in an eigenstate of the Hamiltonian at

time $t = 0$, the quantum state remains in the corresponding instantaneous eigenstate of the Hamiltonian $H_{\boldsymbol{\lambda}(t)}$, under the assumption that there is no gap closing during the evolution. This requires that the eigenstate remains non-degenerate at all times t during the evolution.

Now, in the case of cyclic evolution, if the quantum state is initially an eigenstate of $H_{\boldsymbol{\lambda}(0)}$, the adiabatic theorem implies that the final quantum state must be the same as the initial quantum state, up to a phase:

$$|\psi(T)\rangle = \mathrm{e}^{\mathrm{i}\Phi} |\psi(0)\rangle . \tag{4.1}$$

As mentioned previously, two terms contribute to the accumulated phase Φ, as we will calculate in the following. An explicit condition for the validity of the adiabatic theorem will be derived. We follow a standard derivation using the adiabatic theorem [151, 152]. We explicitly define the eigenstates of the Hamiltonian $H_{\boldsymbol{\lambda}}$: $\psi_{\boldsymbol{\lambda}}^{(n)}$, associated with the eigenenergies $E_{\boldsymbol{\lambda}}^{(n)}$, labelled by the integer n (see Fig. 4.1(b)). At each time t, we decompose the quantum state on the basis of instantaneous eigenstates:

$$|\psi(t)\rangle = \sum_n c_n(t) \, |\psi_{\boldsymbol{\lambda}(t)}^{(n)}\rangle . \tag{4.2}$$

The quantum state evolves according to the Schrödinger equation:

$$\mathrm{i}\hbar \frac{\mathrm{d} \, |\psi(t)\rangle}{\mathrm{d}t} = H_{\boldsymbol{\lambda}(t)} \, |\psi(t)\rangle . \tag{4.3}$$

In the following, for simplicity, we do not explicitly indicate the time-dependences. By projecting onto the instantaneous eigenstates $\langle \psi_{\boldsymbol{\lambda}}^{(m)}| \cdot$, for integers m, we obtain the equations:

$$\mathrm{i}\hbar \left(\dot{c}_n + \hbar \sum_m \dot{\boldsymbol{\lambda}} \, \langle \psi_{\boldsymbol{\lambda}}^{(m)} | \boldsymbol{\nabla}_{\boldsymbol{\lambda}} \psi_{\boldsymbol{\lambda}}^{(n)} \rangle \, c_m \right) = E_{\boldsymbol{\lambda}}^{(n)} c_n . \tag{4.4}$$

We rewrite it as a system of coupled linear differential equations of the coefficients $c_n(t)$:

$$\mathrm{i}\hbar \dot{c}_n = E_{\boldsymbol{\lambda}}^{(n)} c_n - \hbar \sum_m \alpha_{\boldsymbol{\lambda}}^{(n,m)} c_m \quad \text{with} \quad \alpha_{\boldsymbol{\lambda}}^{(n,m)} = \mathrm{i} \dot{\boldsymbol{\lambda}} \, \langle \psi_{\boldsymbol{\lambda}}^{(m)} | \boldsymbol{\nabla}_{\boldsymbol{\lambda}} \psi_{\boldsymbol{\lambda}}^{(n)} \rangle , \tag{4.5}$$

where $|\boldsymbol{\nabla}_{\boldsymbol{\lambda}} \psi_{\boldsymbol{\lambda}}^{(n)}\rangle \equiv \left(\partial_{\lambda_1} |\psi_{\boldsymbol{\lambda}}^{(n)}\rangle , \partial_{\lambda_2} |\psi_{\boldsymbol{\lambda}}^{(n)}\rangle , \ldots \right)$. For simplicity, we also use the following compact form, which should be understood as a shortcut for the complete expression written above: $\alpha_{\boldsymbol{\lambda}}^{(n,m)} = \mathrm{i} \, \langle \psi_{\boldsymbol{\lambda}}^{(m)} | \partial_t \psi_{\boldsymbol{\lambda}}^{(n)} \rangle$.

Intuitively, $|\partial_t \psi_{\boldsymbol{\lambda}}^{(n)}\rangle$ corresponds to the modified eigenstate labelled n, under the effect of an infinitesimal time variation of the parameter $\boldsymbol{\lambda}(t)$. Its inner product $\langle \psi_{\boldsymbol{\lambda}}^{(m)} | \partial_t \psi_{\boldsymbol{\lambda}}^{(n)} \rangle$ with the eigenstate labelled m characterizes the coupling between the two eigenstates due to the time-dependence of the Hamiltonian. This coupling strength must be compared to other natural scales of the system such as the energy difference between eigenstates. The smallest energy scale is given by the smallest energy difference between the energy level n and all the others: $\hbar \omega_{\boldsymbol{\lambda}}^{(n,\min)} = \min_m |E_{\boldsymbol{\lambda}}^{(n)} - E_{\boldsymbol{\lambda}}^{(m)}|$. At zeroth order, the adiabatic approximation consists in neglecting the coupling

between the different eigenstates under the condition: $\max_m |\alpha_{\boldsymbol{\lambda}}^{(n,m)}| \ll \omega_{\boldsymbol{\lambda}}^{(n,\min)}$. The system of coupled differential equations significantly simplifies:

$$\begin{aligned} \mathrm{i}\hbar\dot{c}_n(t) &= \left(E_{\boldsymbol{\lambda}}^{(n)} - \hbar\alpha_{\boldsymbol{\lambda}}^{(n,n)}\right) c_n(t), \\ \dot{c}_m(t) &= 0 \quad \text{for} \quad m \neq n. \end{aligned} \tag{4.6}$$

As we neglect all couplings between the eigenstates, only one eigenstate is populated during the time evolution. Now, by integrating Eq. 4.6, we get two phases that contribute to the evolution:

$$\dot{c}_n(t) = \mathrm{e}^{\mathrm{i}\Phi_{\mathrm{dyn}}}\mathrm{e}^{\mathrm{i}\Phi_{\mathrm{geo}}}c_n(0) \quad \text{with} \quad \begin{cases} \Phi_{\mathrm{dyn}} &= \dfrac{1}{\hbar}\displaystyle\int_C E_{\boldsymbol{\lambda}}^{(n)}\mathrm{d}t, \\ \Phi_{\mathrm{geo}} &= \displaystyle\int_{\boldsymbol{\lambda}(0)}^{\boldsymbol{\lambda}(t)} \mathcal{A}_{\boldsymbol{\lambda}}^{(n)}\mathrm{d}\boldsymbol{\lambda}, \end{cases} \tag{4.7}$$

where we introduced the so-called Berry connection:

$$\mathcal{A}_{\boldsymbol{\lambda}}^{(n)} = \mathrm{i}\,\langle\psi_{\boldsymbol{\lambda}}^{(n)}|\boldsymbol{\nabla}_{\boldsymbol{\lambda}}\psi_{\boldsymbol{\lambda}}^{(n)}\rangle\,. \tag{4.8}$$

The state after a time t is modified with respect to the initial state only by a phase factor with two distinct contributions. The dynamic phase Φ_{dyn} comes from the time integration of the energy of the instantaneous eigenstate along the parameter path, and as a consequence, it depends on the time evolution along the path. The geometric phase Φ_{geo} does not, however, depend on time, but only on the path in parameter space. At a given time t, these phases could be cancelled out by the right choice of gauge transformation. However, for a closed path in parameter space, the accumulated phase cannot be gauged out. The expression for the geometric phase along a closed loop can be rewritten using Stokes theorem:

$$\Phi_{\mathrm{geo}} = \oint_C \mathcal{A}_{\boldsymbol{\lambda}}^{(n)}\mathrm{d}\boldsymbol{\lambda} = \iint_\Sigma \boldsymbol{\Omega}_{\boldsymbol{\lambda}}^{(n)}\mathrm{d}\mathbf{n}, \tag{4.9}$$

where we have defined the so-called Berry curvature (for a three-dimensional parameter space):

$$\begin{aligned} \boldsymbol{\Omega}_{\boldsymbol{\lambda}}^{(n)} &= \boldsymbol{\nabla}_{\boldsymbol{\lambda}} \times \mathcal{A}_{\boldsymbol{\lambda}}^{(n)} \\ &= \mathrm{i}\,\langle\boldsymbol{\nabla}_{\boldsymbol{\lambda}}\psi_{\boldsymbol{\lambda}}^{(n)}| \times |\boldsymbol{\nabla}_{\boldsymbol{\lambda}}\psi_{\boldsymbol{\lambda}}^{(n)}\rangle\,. \end{aligned} \tag{4.10}$$

An alternative formulation of the Berry curvature is based on a summation over all other eigenstates which is numerically more tractable. As such, the Berry curvature can be seen as a local description of the residual effect of the eigenstates that have been projected out in the quantum adiabatic theorem. Using the closure relation $\sum_n |\psi_{\boldsymbol{\lambda}}^{(n)}\rangle\langle\psi_{\boldsymbol{\lambda}}^{(n)}| = \mathbb{1}$ and the eigenvalue equation $H_{\boldsymbol{\lambda}}|\psi_{\boldsymbol{\lambda}}^{(n)}\rangle = E_{\boldsymbol{\lambda}}^{(n)}|\psi_{\boldsymbol{\lambda}}^{(n)}\rangle$, the Berry curvature between two coordinates μ and ν of the multidimensional parameter space reads as follows:

$$\Omega_{\boldsymbol{\lambda},\mu\nu}^{(n)} = \mathrm{i}\sum_{n'\neq n} \frac{\langle\psi_{\boldsymbol{\lambda}}^{(n)}|\partial_{\lambda_\mu}H_{\boldsymbol{\lambda}}|\psi_{\boldsymbol{\lambda}}^{(n')}\rangle\,\langle\psi_{\boldsymbol{\lambda}}^{(n')}|\partial_{\lambda_\nu}H_{\boldsymbol{\lambda}}|\psi_{\boldsymbol{\lambda}}^{(n)}\rangle + (\mu \leftrightarrow \nu)}{\left(E_{\boldsymbol{\lambda}}^{(n')} - E_{\boldsymbol{\lambda}}^{(n)}\right)^2} \tag{4.11}$$

The Berry connection $\mathcal{A}_{\boldsymbol{\lambda}}^{(n)}$ is a gauge-dependent quantity as, under a gauge transformation of the form $|\psi_{\boldsymbol{\lambda}}^{(n)}\rangle \to \mathrm{e}^{\mathrm{i}\zeta(\boldsymbol{\lambda})/\hbar}|\psi_{\boldsymbol{\lambda}}^{(n)}\rangle$ with $\zeta(\boldsymbol{\lambda})$ an arbitrary smooth function, it is replaced by:

$$\mathcal{A}_{\boldsymbol{\lambda}}^{(n)} \to \mathcal{A}_{\boldsymbol{\lambda}}^{(n)} - \boldsymbol{\nabla}_{\boldsymbol{\lambda}}\zeta(\boldsymbol{\lambda}). \tag{4.12}$$

Considering the rotational of this equation, we immediately obtain that the Berry curvature $\boldsymbol{\Omega}_{\boldsymbol{\lambda}}^{(n)}$ is gauge-invariant. Then, along a given path C from $\boldsymbol{\lambda}_i$ to $\boldsymbol{\lambda}_f$, the geometric phase changes as: $\Phi_{\text{geo}} \to \Phi_{\text{geo}} + \zeta(\boldsymbol{\lambda}_i) - \zeta(\boldsymbol{\lambda}_f)$. For a closed loop $\boldsymbol{\lambda}_i = \boldsymbol{\lambda}_f$, since a quantum-mechanical wavefunction must be single-valued, we get that $\zeta(\boldsymbol{\lambda}_i) - \zeta(\boldsymbol{\lambda}_f)$ has to be an integer multiple of 2π. This reasoning demonstrates that the geometric phase along a closed loop, or Berry phase, Φ_{geo} is a gauge-invariant physical quantity. This phase can also be related to the model of charged particles (of charge q) in the presence of a magnetic field $\mathbf{B}(\mathbf{r})$, deriving from a vector potential $\mathbf{A}(\mathbf{r})$. The particle wavefunction has a conserved norm, but accumulates a phase along a closed loop, called the Aharonov-Bohm phase:

$$\Phi_{\text{AB}} = \frac{q}{\hbar}\oint_C \mathbf{A}(\mathbf{r})\mathrm{d}\mathbf{r} = \frac{q}{\hbar}\iint_\Sigma \mathbf{B}(\mathbf{r})\mathrm{d}\mathbf{n}. \tag{4.13}$$

This analogy with the physics of a charged particle in a magnetic field extends to the Berry connection and curvature. In particular, in the case where the parameter $\boldsymbol{\lambda}$ is the particle position $\mathbf{r}$, we have the direct correspondence between the Berry connection and a vector potential and between the Berry curvature and the associated magnetic field, up to a factor q, the particle charge, as we will see in the next Section.

In the derivation above, we have assumed that there is no energy crossing between the eigenstate of interest and any of the other eigenstates of the Hamiltonian. In Eq. 4.11, we notice that terms of the summation diverge at energy crossings. An extension of this approach is to consider sets of degenerate eigenstates. In this case, the dynamic is no longer restricted to a single eigenstate, but to a subspace spanned by these degenerate eigenstates. This naturally leads to non-abelian Berry curvatures [151].

4.1.2 Adiabatic following of a dressed state

This approach has been extensively used in the context of artificial gauge fields with the notion of adiabatic following of a dressed state [153–155]. The light-matter interaction mediates an effective Hamiltonian of the motion of neutral particles that mimics the effect of a magnetic field on charged particles. The Berry phase acquired along a given path is associated with a gauge field with a scalar potential $\mathcal{W}$ and a vector potential $\mathbf{A}$, such that, in the limit of slow dynamics of the external degrees of freedom, the Hamiltonian for the centre-of-mass reads:

$$H_{\text{c.o.m.}} = \frac{(\mathbf{p} - \mathbf{A}(\mathbf{r}))^2}{2M} + \mathcal{W}(\mathbf{r}) + E_0(\mathbf{r}) + V_{\text{ext}}(\mathbf{r}), \tag{4.14}$$

where M is the atomic mass, $q = 1$ is the effective charge of the particle, E_0 is the energy of the spin part of the Hamiltonian and V_{ext} is a spin-independent potential. In experiments with neutral particles, in the presence of interactions, vortex lattices have

been observed in cold atoms [37] and spin-orbit coupling has been engineered [156] using dressed states. We will revisit this approach in Chapter 7 where we will discuss a possible implementation in our experiment. The strength of the artificial magnetic field, which increases with J, benefits from the large spin $J = 8$ of dysprosium atoms in their electronic ground state, especially compared to past implementations of a similar protocol with alkali atoms.

Here we derive how the Berry phase leads to an artificial gauge [79, 153, 157]. The treatment that we perform follows the adiabatic approximation where we explicitly separate the internal and external degrees of freedom. We assume a time-independent but spatially-varying external field $U(\mathbf{r})$ that couples the internal states, such that we parametrise the Hamiltonian by the position $\boldsymbol{\lambda} = \mathbf{r}$.

$$H = \left(\frac{\mathbf{p}^2}{2M} + V_{\text{ext}}(\mathbf{r})\right)\hat{\mathbb{1}} + U(\mathbf{r}), \tag{4.15}$$

with $\hat{\mathbb{1}}$ the identity operator acting on the internal Hilbert space only and V_{ext} a potential that does not depend on the internal state. We describe the wavefunction of an atom $|\psi(\mathbf{r},t)\rangle$ as a spinor and the Schrödinger equation projected on a single internal state becomes:

$$\mathrm{i}\hbar\partial_t\phi_l = \sum_n \langle\chi_l| \frac{\mathbf{p}^2}{2M} |\chi_n\rangle + E_l\phi_l + V_{\text{ext}} \quad \text{with} \quad |\psi(\mathbf{r},t)\rangle = \sum_l \phi_l(\mathbf{r},t)\,|\chi_l(\mathbf{r})\rangle\,, \tag{4.16}$$

where $|\chi_l(\mathbf{r})\rangle$ is the local eigenstate (indexed by an integer l) of the potential $U(\mathbf{r})$ acting on the internal states only, taken at the position $\mathbf{r}$, associated with the energy $E_l(\mathbf{r})$, and $\phi_l(\mathbf{r},t)$ is the time-dependent probability amplitude of an atom to be in the internal state indexed l, at the position $\mathbf{r}$. We obtain a system of coupled differential equations of the probability amplitudes $\phi_l(\mathbf{r},t)$, which we solve using the adiabatic approximation for an atom initialised in an eigenstate indexed by l. This approximation is valid in the case of a sufficiently slow motion of the atom such that the coupling with the other internal eigenstates is negligible. Under this assumption, only the eigenstate labelled by the integer l is populated: $\phi_l(\mathbf{r},t) \neq 0$. Our problem reduces from a system of coupled differential equations to a single differential equation where we simply need to compute the kinetic term $\langle\chi_l|\,\mathbf{p}^2(\phi_l\,|\chi_l\rangle)/(2M)$. The Hamiltonian for the amplitude $\phi_l(\mathbf{r},t)$ in the internal state l has the compact form:

$$H_l = \frac{(\mathbf{p}-\mathbf{A}_l)^2}{2M} + \mathcal{W}_l + E_l + V_{\text{ext}}, \quad \text{with} \quad \begin{cases} \mathbf{A}_l &= \mathrm{i}\hbar\,\langle\chi_l|\boldsymbol{\nabla}\chi_l\rangle\,, \\ \mathcal{W}_l &= \dfrac{\hbar^2}{2M}\displaystyle\sum_{n\neq l} |\,\langle\boldsymbol{\nabla}\chi_n|\chi_l\rangle|^2. \end{cases} \tag{4.17}$$

The vector $\mathbf{A}_l$ is the Berry connection, playing the role of a vector potential for a particle of charge $q = 1$. The energy $\mathcal{W}_l$ is an additional potential, called scalar potential, which accounts for the kinetic energy of the micromotion induced by the presence of all the other eigenstates, although not populated. This interpretation is reminiscent of the one we provided for the adiabatic theorem. Indeed, even when the adiabatic condition is well satisfied and only one eigenstate of the internal

Hamiltonian is populated, the structure of the spectrum created by the spatially-varying potential manifests itself in the dynamics of the particle through the vector potential, with a phase accumulation along a given path, and through the scalar potential, with a spatially-varying energy term.

In particular, proposals have studied the case of a dark state that is not coupled to light, such that $E_l = 0$. Dark states are experimentally favourable as the internal energy term can be energetically dominant otherwise and it suppresses light-induced heating for implementations using light-matter coupling. Here, we focused on the case of non-degenerate states, where abelian vector potentials appear. As stated earlier, extending the discussion to a set of degenerate states, which have to be treated on equal footing, non-abelian gauge fields can be designed [157].

4.2 Hall effect

Quantum Hall systems are considered as archetypal examples of topological insulators, which break the time-reversal symmetry, and their study could provide a better understanding of the physics of topological insulators. Part of the peculiarity of Hall physics derives from its (apparent) simplicity, as the problem is easily formulated. Interest in this topic has not faded over the decades, as open questions remain in the description of the behaviour of strongly-interacting particles in the presence of a strong magnetic field. Key properties of these systems include quantised transverse responses [158] and the occurrence of chiral edge modes protected from backscattering [7], which have been both predicted and experimentally observed in various platforms ranging from solid-state physics to photonics, or cold atoms [159–163].

In the following, we start with a description of the classical Hall effect and then move on to the quantum Hall effect, with a brief reminder of the textbook treatment of the problem in the Landau gauge. We give arguments supporting the quantisation of the conductivity. We mention that the extension of our arguments to realistic situations, such as in metallic samples, is however not straightforward, and we refer to theoretical approaches that demonstrate the quantisation of the Hall conductivity in the presence of edges and disorder, for non-interacting electrons. This Section is significantly inspired by the following references [164–167].

4.2.1 Classical Hall system

We now describe the classical motion of an electron as a point-like particle of mass M and charge $q = -e$, with e the elementary charge, whose position is constrained to evolve in a (x, y) plane. A magnetic field $\mathbf{B} = B\mathbf{e}_z$ and a uniform electric field $\boldsymbol{\mathcal{E}} = \mathcal{E}\mathbf{e}_y$ are applied. The classical trajectory immediately derives from the equation of motion of the electron, with the Lorenz force:

$$M\dot{\mathbf{v}} = q(\mathbf{v} \times \mathbf{B} + \boldsymbol{\mathcal{E}}). \tag{4.18}$$

The particle motion, represented in Fig. 4.2, is a superposition of a cyclotron oscillation, set by the cyclotron angular frequency $\omega_c = e|B|/M$, and a velocity drift along

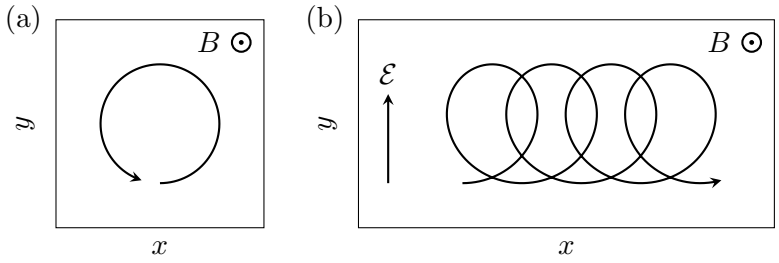

Figure 4.2 – Cyclotron orbit of a negatively charged particle in the presence of a magnetic field B, in the absence of an electric field in panel (a) and the presence of an electric field pointing along y in panel (b). The orbits are computed using the classical equations of motion, for arbitrarily chosen initial velocities, phase and radius. The cyclotron motion shows no net drift when averaging it over a period of $2\pi/\omega_c$, while a uniform electric field induces a linear drift of the position along the direction orthogonal to the electric and magnetic fields.

$\mathbf{v}_{\text{drift}} = \boldsymbol{\mathcal{E}} \times \mathbf{B}/B^2 = \mathcal{E}/B\mathbf{x}$:

$$\begin{aligned} x(t) &= x_0 - R\sin(\omega_c t + \phi) + \mathcal{E}t/B, \\ y(t) &= y_0 + R\cos(\omega_c t + \phi), \end{aligned} \tag{4.19}$$

where the initial position (x_0, y_0), the oscillation radius R and the phase ϕ can take any value a priori.

Although in the absence of a magnetic field, the electric field accelerates a charged particle along its direction, we note that the drift occurs along an axis that is orthogonal to both the magnetic and electric fields. On average, in the absence of impurities, there is no net position drift induced by the cyclotron motion (by averaging its contribution over a period of the cyclotron angular frequency). Then the only contribution is the transverse drift induced by the electric field in combination with the magnetic field, and the electronic current density, for a system with a uniform electronic density n_e, reads: $\mathbf{j} = n_e q\mathbf{v} = n_e q\mathcal{E}/B\mathbf{x}$. The conductivity describes the (linear) conversion of an electric field into a current density $\mathbf{j} = \sigma\boldsymbol{\mathcal{E}}$, such that we obtain zero longitudinal conductivity and $\sigma_{xy} = n_e q/B$. This formula does not indicate the formation of conductivity plateaus.

4.2.2 Quantum Hall system

The Hamiltonian in quantum mechanics, when considering only its orbital part and not the spin part of the electron, is given by:

$$H = \frac{(\mathbf{p} - q\mathbf{A}(\mathbf{r}))^2}{2M} \tag{4.20}$$

where $\mathbf{A}(\mathbf{r})$ is a vector potential associated with the magnetic field $\mathbf{B} = \boldsymbol{\nabla} \times \mathbf{A}(\mathbf{r})$. The velocity operator is derived from the Heisenberg equation of motion $\mathbf{v} = \mathrm{i}/\hbar[H, \mathbf{r}] = (\mathbf{p} - q\mathbf{A}(\mathbf{r}))/M$, and we define the kinetic momentum $\boldsymbol{\pi} = M\mathbf{v}$. Compared to the

canonical momentum $\mathbf{p}$, its components do not commute: $[\pi_x, \pi_y] = \mathrm{i}\hbar qB = -\mathrm{i}\hbar^2/\ell_m^2$ with $\ell_m = \sqrt{\hbar/(e|B|)}$ the so-called magnetic length.

In the absence of a magnetic field, the translations are generated by the momentum operator, whose components commute. Now, in the presence of a uniform magnetic field, the system is still translationally invariant, which imposes that the translation operator commutes with the Hamiltonian. The two natural momentum operators that have appeared so far, namely the canonical one $\mathbf{p}$ and the kinetic one $\boldsymbol{\pi}$, do not commute with the Hamiltonian. The correct generator of magnetic translations, which commutes with the Hamiltonian of Eq. 4.20, has been introduced by Brown and Zak [168, 169] for the symmetric gauge, and then extended to any gauge [170]:

$$\boldsymbol{\kappa} = \mathbf{p} - q(\mathbf{A} - \mathbf{B} \times \mathbf{r}) = \boldsymbol{\pi} + q\mathbf{B} \times \mathbf{r}. \tag{4.21}$$

It is also referred to as the pseudomomentum and defines the magnetic translation operator $T(\boldsymbol{\delta}) = \exp(-\mathrm{i}\boldsymbol{\delta} \cdot \boldsymbol{\kappa}/\hbar)$, for a position vector $\boldsymbol{\delta}$. To prove that the pseudomomentum does generate the magnetic translation group, we check that the operators $T(\boldsymbol{\delta})$ commute with the Hamiltonian. Using the usual commutation relations of the position and momentum operators[1], we show that the two components of the pseudomomentum do not commute $[\kappa_x, \kappa_y] = -\mathrm{i}\hbar qB$ and that the commutators for the three components of the kinetic momentum and pseudomomentum verify $[\pi_i, \kappa_j] = 0$ $(i, j = x, y, z)$. As a consequence, the pseudomomentum $\boldsymbol{\kappa}$ and the generated translation operators commute with the Hamiltonian.

These commutation relations imply the non-commutation of the translation operators of vectors $\mathbf{r}_i$ $(i = 1,2)$ if these vectors are not collinear:

$$T(\mathbf{r}_1)T(\mathbf{r}_2) = T(\mathbf{r}_2)T(\mathbf{r}_1)\exp\Big(-\mathrm{i}(\mathbf{r}_1 \times \mathbf{r}_2)_z/\ell_m^2\Big), \tag{4.22}$$

using the Baker–Campbell–Hausdorff formula. Now, if we consider a parallelepipedic path that forms a closed loop $T(-\mathbf{r}_1)T(-\mathbf{r}_2)T(\mathbf{r}_1)T(\mathbf{r}_2)$, using the commutation relation, we simply get a phase term $\exp(-\mathrm{i}(\mathbf{r}_1 \times \mathbf{r}_2)_z/\ell_m^2)$, which is analogous to an Aharonov-Bohm phase accumulated along a closed loop.

4.2.3 Landau gauge

The Hamiltonian of Eq. 4.20 can be diagonalised in different choices of gauge that are all related to the same physical properties. In this Section, we recall a well-known treatment of the quantum Hall effect, while the next Section will present an approach that is less frequently found in textbooks and directly connects to our implementation of an atomic Hall cylinder. Here, we consider this system in the so-called Landau gauge, where the vector potential is oriented along y and varies linearly as a function of x, as $\mathbf{A}(\mathbf{r}) = Bx\mathbf{e}_y$:

$$H = \frac{p_x^2}{2M} + \frac{(p_y - qBx)^2}{2M}. \tag{4.23}$$

In this gauge choice, the magnetic translation operators along x and y reduce to the following expressions:

$$T_{x_0} = \exp\left(-\mathrm{i}\frac{x_0(p_x - qBy)}{\hbar}\right) \quad \text{and} \quad T_{y_0} = \exp\left(-\mathrm{i}\frac{y_0 p_y}{\hbar}\right), \tag{4.24}$$

[1] $[r_i, f(\mathbf{p})] = \mathrm{i}\hbar\partial_{p_i} f$, $[p_i, f(\mathbf{r})] = -\mathrm{i}\hbar\partial_{r_i} f$

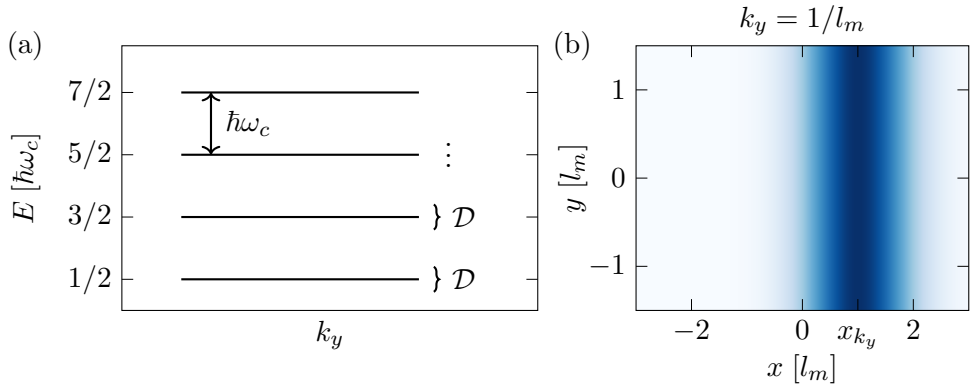

Figure 4.3 – Panel (a): Landau levels whose energies correspond to a one-dimensional oscillator of angular frequency ω_c. The macroscopic degeneracy $\mathcal{D}$ of each level is indicated. Panels (b): Density distribution of the ground state, computed in the Landau gauge as an eigenstate of κ_y, indexed by its wavevector $k_y = 1/\ell_m$. The state is extended along y and peaked along x at the position $x_{k_y} = k_y \ell_m^2$.

associated with $\kappa_x = p_x - qBy$ and $\kappa_y = p_y$ respectively.

We can now look for eigenstates of the Hamiltonian as common eigenstates of either κ_x or κ_y (but not of the two since they do not commute). In the following, we start by using the translation invariance along y, *i.e.* of the commutation of the Hamiltonian with $p_y = \kappa_y$. We look for eigenstates that are plane waves along y, characterised by a momentum k_y, times a function of the position x only: $\Psi_{k_y}(\mathbf{r}) = \mathrm{e}^{\mathrm{i}k_y y}\psi_{k_y}(x)$. Using this ansatz in Eq. 4.23, the function $\psi_{k_y}(x)$ is a solution of the eigenvalue equation of the one-dimensional harmonic oscillator of angular frequency ω_c, the cyclotron angular frequency that we have already introduced in the classical case, and centre $x_{k_y} = k_y \ell_m^2$.

The density distribution of the ground state is translationally invariant along y as expected for a plane wave, but shows a peak along x at the position x_{k_y}, as shown in Fig. 4.3(b) for $k_y = 1/\ell_m$. We notice that no kinetic energy is associated with the momentum k_y and that the effect of k_y is simply to shift the centre position of the one-dimensional oscillator. We can compute the $\Psi_{k_y}^{(n)}(\mathbf{r})$ eigenfunctions, associated to the n-th Landau level, using the n-th Hermite polynomials H_n, and in particular for the lowest Landau level (LLL) for $n = 0$:

$$\begin{aligned}\Psi_{k_y}^{(n)}(\mathbf{r}) &\propto \mathrm{e}^{\mathrm{i}k_y y} H_n(x - x_{k_y}) \exp\left(-\frac{(x - x_{k_y})^2}{2\ell_m^2}\right),\\ \Psi_{k_y}^{(0)}(\mathbf{r}) &\propto \mathrm{e}^{\mathrm{i}k_y y} \exp\left(-\frac{(x - x_{k_y})^2}{2\ell_m^2}\right).\end{aligned} \tag{4.25}$$

The energy spectrum does not vary as a function of k_y, which is related to the fact that a change in k_y simply shifts the wavefunction along x. It is composed of equally spaced bands of energies $E_n = \hbar\omega_c(n + 1/2)$ with integer $n \geq 0$. These energy levels are called Landau levels and are represented in Fig. 4.3(a). The energy gap between

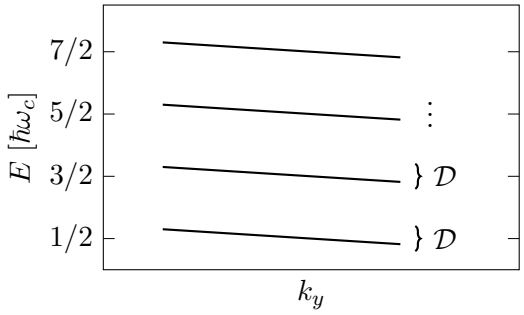

Figure 4.4 – Landau levels in the presence of an electric field along x which induces a linear slope of the bands as a function of momentum k_y.

successive levels is equal to $\hbar$ times the cyclotron angular frequency. A key feature of Hall physics appears in the reduction from a two-dimensional Hamiltonian to a one-dimensional harmonic oscillator, which leads to flat bands and to a macroscopic degeneracy of each Landau level.

To estimate this degeneracy, we temporally consider a particle in a rectangular box of size $L_x \times L_y$. Assuming periodic conditions along y, the momentum k_y can only take discrete values $k_y = n2\pi/L_y$ with integer n. We note that this implies that the distance between neighbouring oscillators is $2\pi\ell_m^2/L_y$, which becomes arbitrarily small as the sample size L_y is increased. Now the box constrains the centre of the oscillators to the bounds $0 \leq x_{k_y} \leq L_x$, which leads to $0 \leq k_y \leq L_x/\ell_m^2$. Since the momentum k_y takes only discrete values, we compute the degeneracy:

$$\mathcal{D} \approx \frac{L_x L_y}{2\pi\ell_m^2} = \frac{SB}{\Phi_0}, \tag{4.26}$$

where $S = L_x L_y$ is the area of the sample and $2\pi\ell_m^2$ is the area of the disk that is threaded by a flux quantum $\Phi_0 = h/e$, for the magnetic field B. Consequently, the degeneracy is the number of flux quanta Φ_0 threaded by a magnetic field B through the sample of surface S. In other words, there is exactly one electronic state per flux quantum in the sample.

4.2.4 Effect of a uniform electric field

We consider an additional force $q\mathcal{E}\mathbf{x}$ via an electric field along x. The ansatz with a plane wave along y for the eigenfunction is still valid. From the classical case, we expect a position drift along an axis that is orthogonal to the magnetic and electric fields. We diagonalise the Hamiltonian and compute the expectation value of the velocity along y from the derivative of the energy with respect to k_y, up to a factor of $1/\hbar$. In the presence of a uniform electric field along x, the total energy acquires a k_y-linear dependence with the additional terms: $q\mathcal{E}k_y\ell_m^2 - M\mathcal{E}^2/(2B^2)$, as shown in Fig. 4.4(a). This is related to the fact that the effect of the force is to shift the centre of the harmonic oscillator along x: $x \to x + M\mathcal{E}/(qB^2)$ in the Hermite polynomial. We obtain a velocity drift $\langle v_y \rangle_{n,k_y} = \partial_{\hbar k_y} \langle H \rangle = \mathrm{sgn}(q)\mathcal{E}/B$, whose orientation is given by the sign of the particle charge. We assume that the ν lowest Landau levels are filled and sum up the contributions for all wavevectors k_y.

Since the contributions are independent of both the band index n and the wavevector k_y, we simply count the number of states that participate in the conductivity:

$$I_y = \nu \mathcal{D} \frac{q \langle v_y \rangle}{L_y}, \tag{4.27}$$

where we again consider a rectangular box of size $L_x \times L_y$ to make sense of the degeneracy, but we do not consider edge effects. The electric voltage drop across the sample along x being $V_x = \mathcal{E} L_x$, we finally get the transverse conductivity:

$$\sigma_{xy} = \frac{I_y}{V_x} = \nu \frac{q^2}{h}, \tag{4.28}$$

and the longitudinal conductivities σ_{xx} and σ_{yy} are zero. The transverse conductivity is quantised in units of q^2/h and this corresponds to the quantum Hall plateaus first observed in metals [171], which is generally referred to as the integer quantum Hall effect.

4.3 Quantum Hall effect in cylindrical geometry

4.3.1 Landau gauge revisited

In the previous Section, we have followed the most common approach in the literature to treat the quantum Hall effect in the Landau gauge $(0, Bx, 0)$. We codiagonalised the Hamiltonian and the momentum $\kappa_y = p_y$, taking advantage of the translation invariance of the system along x. However, as we pointed out, an alternative approach allows us to look for eigenstates as common eigenstates of the Hamiltonian and of the other component of the pseudomomentum $\kappa_x = p_x - qBy = p_x + \hbar y/\ell_m^2$. Similarly to the approach in the previous Section, the ground state wavefunctions are characterised by a wavevector k_x:

$$\Psi_{k_x}^{(0)}(\mathbf{r}) \propto \mathrm{e}^{\mathrm{i}(k_x + y/\ell_m^2)x} \exp\left(-\frac{(y - y_{k_x})^2}{2\ell_m^2}\right), \tag{4.29}$$

with $y_{k_x} = -k_x \ell_m^2$. The density profile of these states is extended along x and peaked along y at the position y_{k_x}, and is represented in Fig. 4.5(a) for $k_x = 0$. We also recover the energy spectrum composed of Landau levels, with a macroscopic degeneracy, which stems from the y-translation of the eigenfunction when the wavevector k_x is changed.

The reason why we prefer this basis of eigenstates is related to our implementation of a quantum Hall cylinder with atomic dysprosium and will become clearer with the following argument. We consider the effect of an additional term in the Hamiltonian, which couples states $|\Psi_{k_x}\rangle$ and $|\Psi_{k_x+K}\rangle$, for a given pseudomomentum difference K. Such a coupling can be realised by a periodic potential of spatial periodicity $2\pi/K$ along the axis defined by the translation generator κ_x. Due to the flatness of the ground band, related to the macroscopic degeneracy of the Landau levels, states of the ground band with momenta differing by K are strongly coupled by this periodic potential. Its effect is similar to that of the textbook example of a sinusoidal lattice on the band structure of a free electron. Using the Bloch theorem,

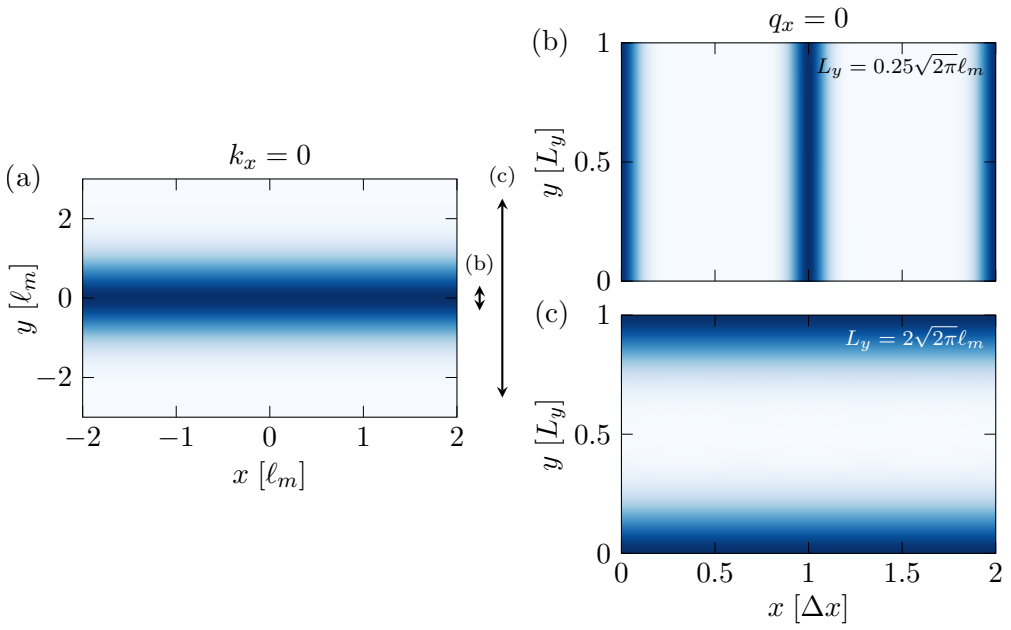

Figure 4.5 – Panel (a): Density distribution of an eigenstate Ψ_{k_x} of the system with open boundary conditions along y, with infinite y dimension, at $k_x = 0$ such that the state is extended along x and peaked at $y = -k_x\ell_m^2 = 0$. Panels (b,c): Density distribution of a state ϕ_{q_x} for the system with periodic boundary conditions along y, for the two extreme regimes $L_y \ll \ell_m$ in (b) and $L_y \gg \ell_m$ in (c). The circumferences $L_y = 0.25\sqrt{2\pi}\ell_m$ and $2\sqrt{2\pi}\ell_m$ are compared to the density distribution of $\Psi_{k_x}$of typical width ℓ_m, in panel (a) with two arrows labelled (b) and (c) respectively. The density distributions are periodic along x of period Δx and we show two unit cells only.

the relevant quantum number is a quasimomentum q_x defined on a Brillouin zone of size K. The initially infinite flat ground band is folded inside the Brillouin zone and the periodic potential opens energy gaps which lift the degeneracy. This splits the folded ground band into a succession of flat bands, whose energy differences are set by the coupling strength. The eigenstates of the lowest energy band inherit from the discrete translation invariance of the periodic potential and are therefore linear combinations of an infinite number of eigenstates $|\Psi_{k_x}\rangle$ of the Hamiltonian without $2\pi/K$-periodic potential, with equal real weights: $|\phi_{q_x}\rangle \propto \sum_n |\Psi_{k_x=q_x+nK}\rangle$. Here, we consider only the lowest Landau level and drop the $\cdot^{(0)}$ notation. The summation involves states that are peaked along y at positions $y_{k_x} = -q_x\ell_m^2 - nK/\ell_m^2$ (with integers n), such that they are equally spaced with inter-distance $L_y = K/\ell_m^2$. The regular spacing and the infinite number of eigenstates involved in the summation dictate that these states are y-periodic of period L_y. They can be represented on a cylinder of circumference L_y, with y playing the role of the cyclic dimension.

To make the analogy with a cylindrical geometry explicit, we do not consider the term coupling states with different pseudomomenta, but add periodic boundary conditions along y instead. As we have already noticed when computing the degeneracy of the Landau levels, this leads to discrete values of the wavevector k_x, set by the

circumference of the cylinder that we call L_y. Since the eigenstates $|\Psi_{k_x}\rangle$ are peaked along y at positions that linearly depend on k_x, they are located at equally-spaced positions along y. Now, the eigenvectors of κ_x are not periodic functions of y, but we can easily propose a family of L_y-periodic functions along y as a linear combination of the eigenstates $\Psi^{(0)}_{k_x}$:

$$|\phi_{q_x}\rangle \propto \sum_n |\Psi_{k_x=q_x+nL_y/\ell_m^2}\rangle\,, \tag{4.30}$$

for the lowest Landau level only. We stress that we recover the wavefunction defined on a plane for a Landau Hamiltonian with an additional term coupling the eigenstates with a pseudomomentum varying by $K = L_y/\ell_m^2$. The difference in pseudomomentum $K = L_y/\ell_m^2$ defines the size of the Brillouin zone, on which the conserved quasimomentum q_x is defined. We check that we have constructed the correct number of eigenstates by calculating the degeneracy of the ground band. We consider a finite size L_x along x which imposes that the momentum is a multiple of $2\pi/L_x$. The constraint given by the size of the Brillouin zone leads to the relation involving the degeneracy: $\mathcal{D}2\pi/L_x = L_y/\ell_m^2$, which is consistent with our result in Eq. 4.26.

We discuss the properties of this family of quantum states. We first investigate their density profiles $n_{q_x}(x,y)$, which are both x- and y-periodic with periods $\Delta x = 2\pi/K$ and L_y respectively. The two-dimensional plane is thus paved by a unit cell of area $\Delta x L_y = 2\pi\ell_m^2$ which corresponds to the area threaded by exactly one flux quantum. The effect of varying q_x is simply to translate the density profile at $q_x = 0$ along y by a quantity $-q_x\ell_m^2$ such that: $n_{q_x}(x,y) = n_0(x, y + q_x\ell_m^2)$.

The states Ψ_{k_x} involved in the definition of the $|\phi_{q_x}\rangle$ wavefunctions in Eq. 4.30 have different momenta $k_x = q_x + nK$, with n integer, regularly spaced by K. These states are infinite along x and peaked at y_{k_x}, which vary by exactly the circumference of the cylinder L_y for neighbouring indices n. They also have phases that depend on k_x. In the limit of large $L_y \gg \ell_m$, the y-spacing L_y between the states Ψ_{k_x} is much larger than the typical size of the wavefunctions, so that they do not overlap. Therefore, there is no interference from the phase differences and the density of the states $|\phi_{q_x}\rangle$ is extended along x and reaches its maximum along y at the positions $y_{q_x} = -q_x\ell_m^2 \,(\mathrm{mod}\, L_y)$, as expected from the connection to an infinite system with open boundary conditions. In the opposite limit, called the thin-torus limit, with $L_y \ll \ell_m$, the states Ψ_{k_x} significantly overlap and the phase differences matter. In the system with periodic boundary conditions, the states are extended along y and x-periodic of period Δx with localised density peaks at positions that are integer multiples of Δx. Indeed, at these positions $x_s = s\Delta x$ with s integer, the interferences are constructive because $\mathrm{e}^{\mathrm{i}nKx_s} = \mathrm{e}^{\mathrm{i}ns2\pi} = 1$ while, at other x-positions, the contributions destructively interfere. Deep in the thin-torus limit, the orbitals are well separated along x. The density distributions of the $|\phi_{q_x=0}\rangle$ state in the two limits are displayed in Fig. 4.5(b,c).

We now focus on the intermediate regime $L_y = \sqrt{2\pi}\ell_m$, where the cylinder circumference is on the order of the magnetic length that sets the extent of the Ψ_{k_x} along y. The density distributions are represented in Fig. 4.6(a) for two values of the quasimomentum $q_x = 0$ and $0.25K$. A change of q_x shifts all $\Psi_{k_x=q_x+nK}$ states by the same displacement along y, which thus also translates the density distribution of

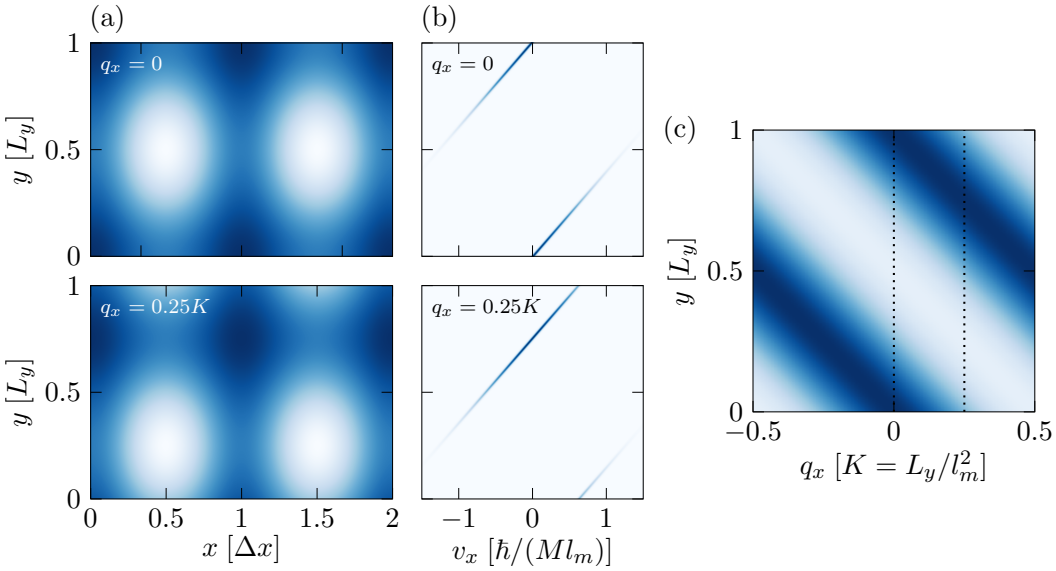

Figure 4.6 – Panel (a): Density distributions of the $|\phi_{q_x}\rangle$ state, for $q_x = 0$ and $0.25K$ (top and bottom panels respectively), for the circumference $L_y = \sqrt{2\pi}\ell_m$. Panel (b): Velocity distributions $\rho_{q_x}(v_x, y)$ for the same states. Panel (c): y-distribution as a function of the quasimomentum q_x in the first Brillouin zone. The black dots indicate the two q_x states whose density and velocity distributions are displayed in the left panels. The y-distribution winds once around the cyclic coordinate y, as the quasimomentum q_x is tuned from one side of the Brillouin zone to the other, which is typical of the transverse response of a charged particle in a quantum Hall system.

$|\phi_{q_x}\rangle$ by the same amount. This is visible in the density distributions of Fig. 4.6(a). We also show in Fig. 4.6(b) the velocity distributions $\rho_{q_x}(v_x, y)$ for the same states, given by the formula:

$$\rho_{q_x}(v_x, y) = \sum_n \delta\left[v_x - \frac{M\ell_m}{\hbar}\left(q_x + \frac{y + nL_y}{\ell_m^2}\right)\right] \exp\left[-\frac{1}{2}\left(v_x \frac{M\ell_m}{\hbar}\right)^2\right], \qquad (4.31)$$

which simply derives from the conservation of quasimomentum, where δ is the delta function. We see that the velocity is bounded along x and its mean value remains zero.

Using the density distributions, we reconstruct the y-distribution as a function of the quasimomentum, which we plot in Fig. 4.6(c). We observe a transverse response of the system as the y-distribution winds exactly once around the circumference of the y axis when q_x is tuned from one side of the Brillouin zone to the other, which is equivalent to applying a force along x. This transverse response is characteristic of the presence of electric and magnetic fields for charged particles.

4.3.2 Laughlin's argument

Historically, the cylindrical geometry was first investigated by Laughlin to justify the quantisation of the Hall conductivity. His argument relies on the gauge invariance

of quantum mechanics, in this geometry. Compared to the situation in the previous Section, we consider edges along x ($0 \leq x \leq L_x$). The system is a cylinder of circumference L_y, whose surface is pierced by an orthogonal magnetic field of norm B, in the presence of a driving electric field along x. We remind that the vector potential is written $\mathbf{A} = (0, Bx, 0)$ in the Landau gauge. We add a solenoid that passes through the hole of the cylinder. We assume that it is of infinite length so that no magnetic field leaks out of the solenoid. A scheme of the cylinder with an infinite solenoid is depicted in Fig. 4.7. Since the magnetic field at the surface of the cylinder is unchanged, the threading of a magnetic flux Φ in the solenoid inside the cylinder can be incorporated as an additional vector potential $(0, -\Phi/L_y, 0)$. We verify that this additional vector potential preserves the gauge-invariant electric and magnetic fields. Nevertheless, it contributes to the physics of the system similarly to an Aharonov-Bohm phase as we consider a closed loop that winds around the cylinder. We also notice that the total vector potential can be rewritten as $(0, B(x - \Phi/(L_y B)), 0)$, which immediately highlights that the flux Φ is equivalent to a translation along x. If one were to adiabatically thread a flux quantum $\Phi_0 = h/e$, the wavefunctions would be displaced by $\Phi_0/(L_y B)$, which equals the x-period Δx of the density distributions of the $|\phi_{q_x}\rangle$ states. This means that it maps the density distribution onto itself and that the electrons occupying each orbital have been pumped to the neighbouring orbital.

From an alternative point of view, a change in flux $\Delta\Phi$ modifies the vector potential and can be seen as a gauge transformation, which in turn changes the wavefunction only up to a phase. Let us make this explicit:

$$\begin{aligned} |\psi(\mathbf{r})\rangle &\to \mathrm{e}^{\mathrm{i}q\zeta(\mathbf{r})/\hbar}\,|\psi(\mathbf{r})\rangle\,, \quad \text{with} \quad \zeta(\mathbf{r}) = y\Delta\Phi/L_y \\ \mathcal{A}(\mathbf{r}) &\to \mathcal{A}(\mathbf{r}) - \boldsymbol{\nabla}_{\mathbf{r}}\zeta(\mathbf{r}) = \mathcal{A}(\mathbf{r}) - \Delta\Phi/(2\pi R)\mathbf{y} \\ \Phi &\to \Phi + \Delta\Phi \end{aligned} \tag{4.32}$$

An interesting consequence of the additional phase in the wavefunction above appears when we consider a cyclic dimension y. The wavefunction satisfies $\psi(x, y + L_y) = \psi(x, y)$, and this condition must also hold after the gauge transformation $\psi(x, y + L_y)\exp(\mathrm{i}q\zeta(x, y + L_y)/\hbar) = \psi(x, y)\exp(\mathrm{i}q\zeta(x, y)/\hbar)$. Moreover, the wavefunctions at y and $y + L_y$ are necessarily equal up to a phase factor that is an integer multiple of 2π. As a consequence, if the phase change $\Delta\Phi$ is an integer multiple of Φ_0, it can be gauged away by an appropriate gauge transform and the wavefunction is not modified, except for a complex phase. This is consistent with our statement above that each orbital is shifted onto the next one, whenever a flux Φ_0 is inserted. The single-particle spectrum is also invariant under this operation.

Considering the Hamiltonian H_Φ, with its ground state ϕ_Φ of energy E_Φ, where Φ is a smoothly varied external parameter, we get that the total current I_y is the expectation value of the derivative of the total Hamiltonian with respect to Φ, following Laughlin's derivation. Using the Hellman-Feynman theorem[2], we obtain that $I_y = \langle \partial_\Phi H_\Phi \rangle = \partial_\Phi E_\Phi$. This assumes that the evolution is slow enough and that there is no gap closing, as in the adiabatic theorem (see Section 4.1), and it

[2]The Hellman-Feynman theorem states that the variation of the total energy of a system, induced by the variation of a parameter λ of the Hamiltonian H_λ, is given by $\partial_\lambda E_\lambda = \langle \psi_\lambda | \partial_\lambda H_\lambda | \psi_\lambda \rangle$, for an eigenstate $|\psi_\lambda\rangle$.

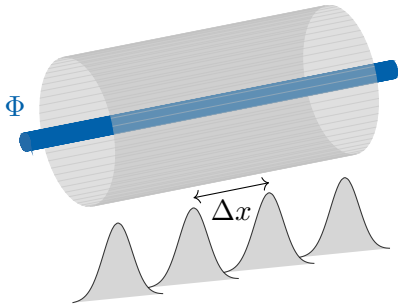

Figure 4.7 – The cylindrical version of a two-dimensional Hall system, as first envisioned by Laughlin in his seminal paper [18]. The cylinder is pierced by an infinite solenoid which controls an axial flux Φ. The x-periodicity, of period Δx, of the electronic wavefunction (with orbitals being represented by filled Gaussians) is indicated.

corresponds to the effect of an electromotive force around the cylinder. Then, we replace the derivative by a differential (which is equivalent to an average over all possible boundary conditions [172]), considering a finite flux difference $\Delta\Phi = h/q$ and ν filled Landau levels. If there is a voltage difference V_x between the two edges along x, the energy cost of the pumping is $q\nu V_x$, by simply counting the number of pumped particles (one per occupied Landau level, as we saw above whenever a flux Φ_0 is threaded). We recover the expression of the conductivity of Eq. 4.28:

$$\sigma_{xy} = \frac{I_y}{V_x} = \nu \frac{q^2}{h}. \tag{4.33}$$

In the next Section, we introduce the concept of Thouless pump, which is a generalisation of the charge pump that we described above with the control over an axial magnetic flux. It naturally relates the quantisation in Laughlin's argument to a topological invariant of the system, the so-called first Chern number in two-dimensional systems.

As a side note, we point out that we did not provide a definite proof of the quantisation of the conductivity for arbitrary geometry and boundary conditions, nor treat the case of disorder and interactions. Arguments, based on the mobility gap for bulk states and on the chirality of the edge states, justify the partial insensitivity of the integer quantum Hall effect against these variations [172]. We mention the existence of a mathematical proof in the non-interacting case, using the framework of noncommutative geometry [173].

4.4 Topological pumping

The concept of topological pumping originated from a seminal paper in 1983 [19], in the context of the quantum Hall effect, and was first experimentally explored in quantum dots [22, 23]. It has been extended to a wider class of pumps that are characterised by a topological invariant. Thouless considers an electron gas subjected to a magnetic field, placed in a spatially-periodic potential, and the slow

and periodic modulation in time of the potential induces a quantised transport, even in the absence of an electric field. This situation is reminiscent of the Archimedes screw, a spiral tube, which pumps water from one side of the screw to the other by continuously rotating it. However, this effect is based solely on classical physics and no quantisation is derived from the topology of the system [174]. In the case of a Thouless pump, the amount of pumped particles is protected from small changes in the pumping parameters or even disorder, as it is bound to a topological invariant. This quantisation follows from arguments similar to those of the integer quantum Hall effect. There is a correspondence between a topological pump in low dimensions and a higher-dimensional non-trivial topological system, where the time-modulated parameters of the low-dimensional system play the role of artificial dimensions. Topological pumps thus realise dynamical implementations of higher-dimensional topological systems. This connection, called dimensional extension [17], has been experimentally investigated first in the case of one-dimensional topological pumping, related to the two-dimensional quantum Hall effect [21, 24, 25].

This correspondence can be recovered from different points of view. A common one is based on the Bloch theorem, such that one can define localised Wannier functions from the delocalised Bloch functions. This allows one to compute a position shift of the Wannier wavefunctions when varying an external parameter, which is closely related to the concept of electric polarisation in crystalline solids [175, 176]. However, we decide to follow a treatment based on the adiabatic theorem taken at a higher order with respect to Section 4.1 [151, 152, 177]. For simplicity, we will show this correspondence for a topological charge pump in a one-dimensional system, whose quantisation is analogous to the quantised response to a force in a two-dimensional system.

4.4.1 Quantised charge pumping in a one-dimensional system

We consider a gas of electrons in a one-dimensional lattice potential, of period a along x, that will be subjected to a time-periodic modulation. The Bloch theorem decomposes the eigenfunction into a plane wave with wavevector q_x defined in a Brillouin zone of size $2\pi/a$ and a x-periodic function with same period a as the potential: $|\psi_{q_x}^{(n)}\rangle = \mathrm{e}^{\mathrm{i}q_x x}\,|u_{q_x}^{(n)}\rangle$. The $|u_{q_x}^{(n)}\rangle$ wavefunctions are eigenstates of the q_x-representation of the Hamiltonian. Up to the first order in the rate of change of the Hamiltonian, the wavefunctions are:

$$|\phi_{q_x}^{(n)}\rangle = |u_{q_x}^{(n)}\rangle - \mathrm{i}\hbar \sum_{n'\neq n} \frac{\langle u_{q_x}^{(n')}|\partial_t u_{q_x}^{(n)}\rangle}{E_{q_x}^{(n)} - E_{q_x}^{(n')}}\,|u_{q_x}^{(n')}\rangle\,, \tag{4.34}$$

where we used the compact notation $|\partial_t u_{q_x}^{(n)}\rangle$, previously defined in Eq. 4.5. We then compute the average velocity of a state of wavevector q_x in the n-th band, still up to first order in the adiabatic approximation:

$$\begin{aligned} v_{q_x}^{(n)} &= \partial_{\hbar q} E_{q_x}^{(n)} - \mathrm{i}\left(\langle \partial_{q_x} u_{q_x}^{(n)}|\partial_t u_{q_x}^{(n)}\rangle - \langle \partial_t u_{q_x}^{(n)}|\partial_{q_x} u_{q_x}^{(n)}\rangle\right), \\ &= \partial_{\hbar q_x} E_{q_x}^{(n)} - \Omega_{q_x,t}^{(n)}. \end{aligned} \tag{4.35}$$

We used successively the definition of the velocity operator as the commutator of the Hamiltonian operator with the position operator, the effect of the momentum

operator on the Bloch wavefunctions, the completeness relation for the basis of states $\{|u_{q_x}^{(n')}\rangle\}_{n'}$ and the definition of the Berry curvature $\Omega_{q_x,t}^{(n)}$ defined in a parameter space (q_x, t). We obtain two contributions to the velocity: the velocity due to the variation of the energy in a single band, which is simply the group velocity, and the so-called anomalous velocity [178, 179]. It is interesting to note that, when averaged over a Brillouin zone (which is equivalent to uniformly filling the band), the contribution of the group velocity cancels out, owing to the periodicity of the band spectrum. The induced adiabatic velocity is then only given by the first-order term in the adiabatic theorem, and we immediately deduce the mean displacement over a full cycle (of duration T) of the time-periodic modulation of the external parameter:

$$\begin{aligned} \overline{v}^{(n)} &= -\frac{a}{2\pi}\int_{BZ} \mathrm{d}q_x \Omega_{q_x,t}^{(n)}, \\ \Delta x^{(n)} &= -\frac{a}{2\pi}\int_0^T \mathrm{d}t \int_{BZ} \mathrm{d}q_x \Omega_{q_x,t}^{(n)}. \end{aligned} \tag{4.36}$$

We have found an expression for the particle transport for the n-th band over a modulation cycle, which depends on a gauge-invariant quantity that is well defined for all parameters spanning the parameter space. The Gauss-Bonnet-Chern theorem states that the integral of the adiabatic curvature over a two-torus is quantised (*i.e.* an multiple integer of an integration factor determined by the boundary limits of the parameter space). Here, the two-torus parameter space is parametrised by the wavevector q_x defined over a Brillouin zone of size $2\pi/a$ and by time with a periodicity of T. This way, we define the so-called first Chern number $\mathcal{C} \in \mathbb{Z}$, a topological invariant that originates from the mathematics of fibre bundles:

$$\Delta x^{(n)} = -a\mathcal{C}. \tag{4.37}$$

Experimentally, however, the measurement of the Berry curvature, a local gauge-invariant property of the system, may be of interest as it contains more information than its average over the Brillouin zone, the Chern number [180]. Actually, a non-zero Berry curvature can have significant consequences even when the Chern number is trivial (equal to zero), because of the anomalous velocity. This type of pumping is generally referred to as geometrical pumping and no quantisation of topological origin is expected.

Topological pumping is directly related to the integer quantum Hall effect, whose robustness also relies on the non-trivial Chern number characterising the Landau levels. Interestingly, at the interface between two systems with different Chern numbers, for example between a Hall system and vacuum (which is topologically trivial $\mathcal{C} = 0$), the Chern number exhibits a discontinuity since it only takes integer values. This discontinuity occurs when there is a gap closing at the interface, which leads to a singularity in the Berry curvature. As a consequence, there are gapless states at the edges, whose main features are their chirality and the absence of states for backscattering: states on opposite edges of a sample propagate along the boundary in opposite directions, even in the presence of small disorder. We also mention that this topological notion has also been explored with two-dimensional periodic systems. The single-particle spectrum is organised in successive bands, similar to the Landau levels, and a topological invariant, called the TKNN invariant in this context [3], is

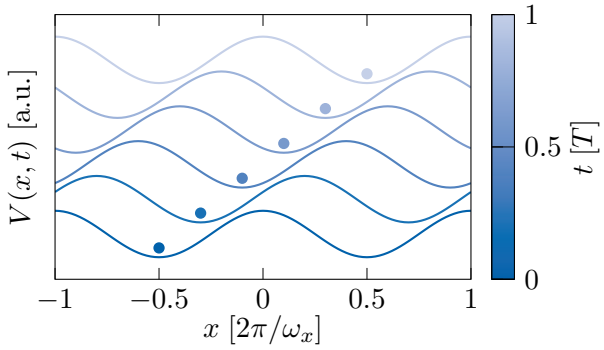

Figure 4.8 – A sliding potential, as imagined by Thouless in its seminal paper, along **x**. The different coloured lines represent the variations of the potential as a function of time. The potentials at different times are lifted up for better visibility. A wavepacket, represented by a blue dot, is initialised at the bottom of a well of the potential and is dragged towards the right as the potential slides. After the period T, the potential returns to its initial shape, but the wavepacket position has shifted from one well to the next.

associated with the response of the system when the Berry curvature is averaged over the two-dimensional Brillouin zone.

The simplest example of a pumping process is a sliding potential, which is related to Laughlin's pump experiment, where the flux insertion through the cylinder tunes the position of the electronic orbitals. The intuition is that, when the periodic potential is sliding, while keeping its shape unchanged, the electrons follow the potential adiabatically. Since there is exactly one state per unit cell for each occupied Landau level, the particle transport over one cycle of the sliding process amount to the number of occupied Landau level, which corresponds to a Chern number of +1 for each Landau level. The quantisation relies on the adiabaticity criterion, assumed in the adiabatic theorem, which is given by the smallest gap to the other bands during the time evolution. The deviations to the quantisation are exponentially small in the cycle period T [181, 182].

This differs from the classical case of a sliding potential, where the particle motion obeys the equation $M\ddot{x} = -\partial_x V_{\text{sliding}}(x,t) = V_0\omega_x \sin(\omega_t t - \omega_x x)$, where the potential V_{sliding} has a period $d = 2\pi/\omega_x$ in space and $T = 2\pi/\omega_t$ in time. This evolution is easily solved in the reference frame moving at $v = \omega_t/\omega_x$, where the equation of motion simplifies to a pendulum equation $\ddot{\theta} + \omega_0^2 \sin(\theta) = 0$ for the variable $\theta = \omega_x x - \omega_t t$, with $\omega_0^2 = V_0\omega_x^2/M$. The drift x of the particle position is written as a sum of a linear drift term, which is quantised at multiples of the cycle time T, and of an oscillation governed by θ. This oscillation does not necessarily reach zero at multiples of the cycle time. However, for a slow evolution $\omega_t \ll \omega_0$, the oscillation of θ becomes small and the oscillation amplitude scales as $1/T$, which is to be compared to the exponentially small correction in the quantum case due to the presence of an energy gap. For more complicated periodic and periodically-driven potentials (*e.g.* a superlattice where a double well is contained in a single unit cell), the pumping expected from a classical evolution may differ from the quantum case

in an even more striking way [174].

4.4.2 Quantised response to a force in a two-dimensional system

We now want to highlight the similarity of a topological pump, as illustrated above, with a higher-dimensional system. We consider a particle evolving in a two-dimensional periodic potential, such that the single-particle spectrum consists of a succession of bands according to Bloch theorem. This can be easily generalised in the presence of a magnetic field by considering magnetic translation operators such that the spectrum is composed of the so-called magnetic Bloch bands [183]. The particle is initially prepared in a Bloch wavefunction at quasimomentum $\mathbf{q}_0$ in the n-th band. We now apply a force $\mathbf{F} = F\mathbf{e}_x$, similarly to applying an electric field in a Hall system. We want to derive the evolution of the particle velocity. To do so, the same argument as in the case of topological pumping, namely the adiabatic approximation up to first order, applies. We write the wavefunction at a time t using Eq. 4.34 and first need to compute the term $|\partial_t u^{(n)}_{\mathbf{q}}\rangle$ (where we have just replaced q_x by $\mathbf{q}$ as a generalisation to higher dimensions). Using a unitary transformation to incorporate the effect of the force as an effective vector potential, we can show that the instantaneous eigenstates are Bloch states at all times, and we find that the wavevector $\mathbf{q}$ evolves as:

$$\hbar \frac{\mathrm{d}\mathbf{q}}{\mathrm{d}t} = \mathbf{F}. \tag{4.38}$$

This is known as Bloch oscillations: the quasimomentum $\mathbf{q}$ uniformly spans the Brillouin zone along x for a uniform and time-independent force $\mathbf{F} = F\mathbf{e}_x$ and its evolution is periodic. We immediately deduce that $\hbar\,|\partial_t u^{(n)}_{\mathbf{q}}\rangle = F\,|\partial_{q_x} u^{(n)}_{\mathbf{q}}\rangle$. We do not provide the full derivation after this stage, for it relies on the same arguments as in the case of the topological pump. We again obtain that the velocity has two components [184], the group velocity and the anomalous velocity:

$$\mathbf{v}^{(n)}_{\mathbf{q}} = \boldsymbol{\nabla}_{\hbar\mathbf{q}} E^{(n)}_k - \frac{1}{\hbar}\boldsymbol{\Omega}^{(n)}_{\mathbf{q}} \times \mathbf{F}. \tag{4.39}$$

The expression of the anomalous velocity highlights the analogy between the Berry curvature and a magnetic field on charged particles. We now consider particles uniformly filling the ground band (*e.g.* fermions accumulating in the ground state with the Fermi energy lying in the gap between the ground and the first excited band), such that the relevant velocity is obtained after averaging over the Brillouin zone. The contribution of the group velocity cancels out as mentioned earlier. We obtain a current along y proportional to the force applied along x and define the conductivity as the transverse response to the force:

$$\tilde{\sigma}_{xy} = \frac{J_y}{F_x} = \frac{1}{h}\frac{1}{2\pi}\iint_{BZ} \Omega_{\mathbf{q}} \mathrm{d}^2 q. = \frac{1}{h}\mathcal{C}, \tag{4.40}$$

with $\mathcal{C}$ the Chern number associated to the topology of the ground band.

4.5 Fractional quantum Hall effect

The so-called fractional quantum Hall effect was discovered in 1982 [185], in an attempt to reproduce the initial observation of the integer quantum Hall effect. Conductivity plateaus were observed at fractional fillings of Landau levels [186], in addition to integer fillings. These observations were realised at high magnetic fields such that the energy scale related to the magnetic field is very high. This induces an accumulation of electrons in the lowest Landau level only, and the Fermi energy lies within this level. The presence of conductivity plateaus indicates some protection from energy gaps, as we have already seen in the case of the integer quantum Hall effect. However, at partial filling of a single Landau level, due to the macroscopic degeneracy, the system is gapless, unless electron-electron interaction plays a role. Because of the flatness of the bands, the interactions are necessarily non-perturbative and their effect is crucial in the description of the quantum states. An energy gap arises from the Coulomb interaction between charged particles in the same Landau level, and the fractional quantum Hall effect corresponds to a problem of strongly-correlated fermions, which is challenging to solve.

Theoretical works [187–189] have addressed the issue of describing such phases of matter and have shown that a fractional quantum Hall state is an incompressible electron liquid, with gapped collective excitations in the bulk, and gapless edge modes. The excitations, called abelian anyons, have fractional particle numbers and statistics [190]. The problem has been particularly studied in the case of small rational filling fractions. An ansatz solution was proposed by Laughlin [191] for the specific case of the lowest Landau level with a partial filling fraction $\nu = 1/3$, which is generalisable to a filling fraction $\nu = 1/m$ with odd integer m for fermionic particles. In the symmetric gauge, the so-called Laughlin wavefunction is written:

$$\Psi_{\nu=1/m}(\{z_j\}_{j=1\ldots N}) = \prod_{j<k}(z_j - z_k)^m \exp\left(-\frac{1}{4}\sum_{i=1}^{N}|z_i|^2\right). \tag{4.41}$$

The exponential part in the expression of the wavefunction simply derives from the solution of the one-body wavefunction in the ground band. The polynomial term was proposed following some prescriptions such as the anti-symmetry of the wavefunction for fermions under the exchange of two particles, the Pauli exclusion principle and the fluid incompressibility. It corresponds to a state of uniform density in the bulk, up to a radius at which the density smoothly goes to zero. This state contains vortices that are not localised.

For other filling fractions, other *ex-nihilo* constructions have proven successful in describing certain conductivity plateaus, such as the composit fermion construction [192] or the Moore-Read wavefunction (or Pfaffian state) [193]. The Read-Rezayi wavefunction [194] is relevant for the filling fraction 5/2 and well suited for topological computing where the system is topologically protected from decoherence. Such a state is also interesting for the study of non-abelian phases because its quasiparticle excitations obey non-abelian statistics [195].

Experimental observation of these strongly-correlated phases of matter has been a challenge in recent decades and some proposals have focused on cold atoms using spin-orbit coupled internal states. These systems naturally realise synthetic

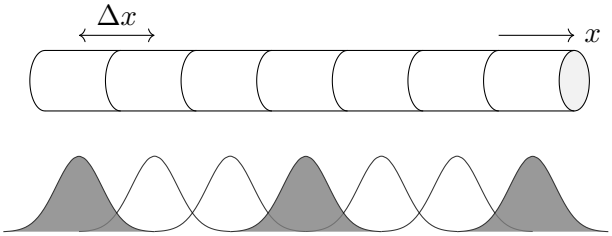

Figure 4.9 – Fractional state at filling 1/3, in a cylindrical geometry with circumference L_y. The orbitals are peaked at discrete positions along x with a distance between neighbouring orbitals $\Delta x = 2\pi\ell_m^2/L_y$. The presence of repulsive interaction, such as Coulomb interaction for electrons, leads to the filling of one every three orbitals, as depicted by the filled Gaussians in grey.

ladders of connected one-dimensional wires with complex phases that play the role of Aharonov-Bohm phases. The mimimal example of this approach is a two-leg ladder system using two coupled internal states, which is a quasi-one-dimensional version of a two-dimensional quantum Hall system. This particular configuration can also be realised in experiments with superlattices. The connection between strongly-correlated states in these geometries and fractional quantum Hall states has been theoretically investigated [196–198]. The treatment of these systems simplify when considering a cylindrical geometry, such as a system infinite along x and periodic of length L_y along y [199].

The case of an infinitely small circumference L_y is solvable even in the presence of interactions and is referred to as Tao-Thouless limit [200]. As we saw in the Landau gauge in Section 4.2.3, the eigenstates, parametrised by the wavevector k_y, are extended along y and localised along x. In the thin-torus limit where $L_y \ll \ell_m$, corresponding to a vanishing periodic dimension, the orbitals are well-separated along x and the system can be reinterpreted as a one-dimensional lattice. A basis for the many-body wavefunctions is given by simply counting whether or not there is a particle on each orbital $\{|n_1, ..., n_N\rangle\}_{n_i\in\{0,1\}}$ for N accessible orbitals in the system. We now consider the effect of interactions such as Coulomb interaction for electrons. Such a two-body interaction can be written as a combination of terms that act on lattice sites at different distances, with or without hopping and exchange of position. In the thin torus limit, only one component contributes and the interaction simplifies to an electrostatic repulsive interaction. It has been shown that the eigenstates are simply states of the basis given above, where the number of filled orbitals is given by the filling ratio [199, 201]. In particular, it is easy to explicit the ground state for a filling fraction $\nu = 1/m$: it amounts to placing one particle every m sites, which obviously minimises the repulsive interaction. This situation is depicted in Fig. 4.9 for $m = 3$. This construction generates three-fold degenerate states, with broken translational symmetry along x, which are usually referred to as charge-density waves. Such a state is a precursor of the Laughlin state at filling fraction 1/3, in a system of finite size. A connection between the two states is expected at increasing circumference L_y, as the cylindrical system approaches a

two-dimensional Hall system.

Signatures of fractional quantum Hall states could be accessible from their chiral currents on the edges or topological fractional pumping [202–204]. Recent works have started to investigate the role of interactions in Thouless pumps [205–208], and in particular with synthetic dimensions [209, 210].

In this Chapter, we have seen that topological pumping is a relevant tool for probing the global properties of a topological insulator in higher dimensions. The historical thought experiment developed by Laughlin to explain the integer quantum Hall effect has not, however, been experimentally realised as it requires the engineering of a cyclic dimension and the control of a magnetic flux threaded through the cylinder. In the next Chapter, we describe our approach to simulating a quantum Hall system in a cylindrical geometry, by coupling the internal and external degrees of freedom of ultracold atoms.

5 Synthetic dimensions encoded in a single large spin

In this Chapter, we will introduce the concept of synthetic dimensions, namely the use of the internal degrees of freedom of a system as an effective additional dimension. It has attracted interest over the past decade in a variety of experimental platforms, in particular in the context of spin-orbit coupling and quantum Hall physics. After reviewing some proposals on different platforms, we focus on the experiments with cold atoms that exploit the electronic total angular momentum of an atom as an effective dimension. We present in detail our recent proposal to encode two dimensions in the spin of a single atom, including a cyclic one. This paves the way for our realisation of an atomic Hall cylinder and for the study of quantum Hall physics in higher dimensions.

This proposal has been published in the following article [211]:
Simulating two-dimensional dynamics within a large-size atomic spin
A. Fabre, J.-B. Bouhiron, T. Satoor, R. Lopes, S. Nascimbene
Physical Review A 105, 013301 (2022)

5.1 Definition and motivation

Synthetic dimensions have developed as widespread tools to address open questions about topological insulators. Limitations in reaching arbitrary geometries and dimensions appear when considering spatial dimensions only [212], which has slowed down experimental investigations of physics in dimensions higher than three or non-planar geometries. A strength of the synthetic dimensions approach lies in the facilitated engineering of gauge fields. The Spielman group has provided evidence of this flexibility by implementing gauge fields in a two-dimensional system consisting of a spatial dimension and a synthetic dimensions [44] or of spatial dimensions only, with the gauge field being mediated by the spin [37].

A synthetic dimension is a non-spatial dimension that is treated similarly to usual spatial ones. Spatial dimensions are naturally continuous ones when considering a particle moving along an axis. But the dynamics of particles can be effectively

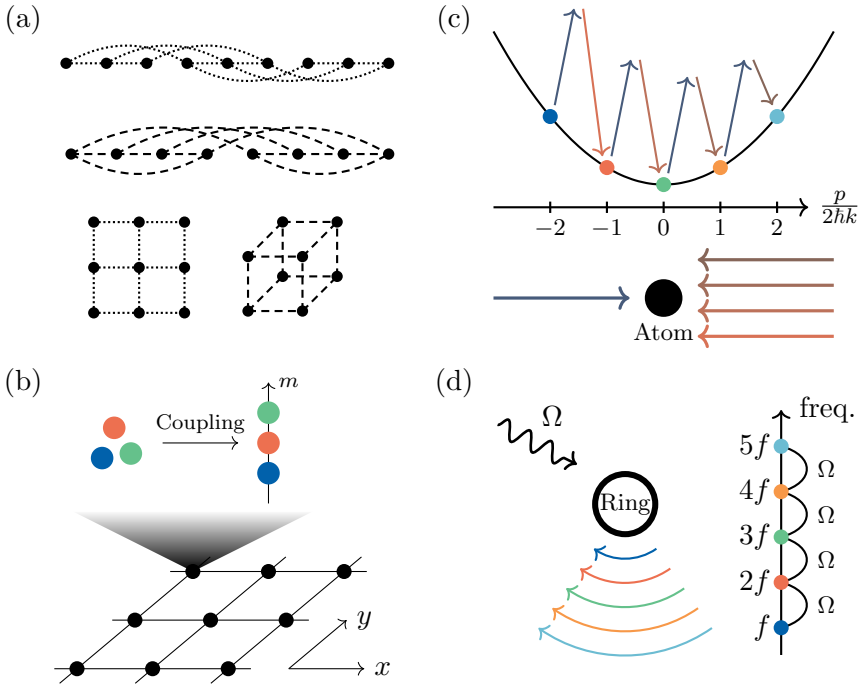

Figure 5.1 – Panels (a,b): Constructing a synthetic dimension from a set of states. The upper panel represents the connectivity approach: adequate physical connections of sites effectively engineer two- or three-dimensional lattices. The lower panel represents the encoding of an additional dimension on each site of a lattice by coupling internal degrees of freedom. Panels (c,d): Examples of synthetic dimensions. The upper panel represents the coupling of momentum states $n2\hbar k$ labelled by integers n, with laser wavevector k, by two-photon optical transitions. The lower panel depicts a single photonic ring resonator, which hosts discrete frequency modes propagating along the same direction (coloured arrows) with equally-spaced frequencies nf labelled by integers $n > 0$, with f the smallest frequency mode. An external perturbation Ω couples the neighbouring modes.

restricted to discrete positions by the use of lattices, such that spatial dimensions can also be deemed discrete. This naturally arises in many models that are effective descriptions of complicated Hamiltonians, such as the Hubbard model. In condensed-matter physics, the crystalline structure of atomic nuclei generates a periodic potential for electrons, which, in the so-called tight-binding limit, can be reinterpreted as a discrete lattice with an on-site interaction and a hopping process between sites. In most proposals, the synthetic dimensions are additional discrete dimensions.

Two paths are generally followed to define a synthetic dimension. They have in common the idea of connectivity: a lattice is simply a set of states that are connected according to a geometrical rule. The first approach considers that any set of states can be reinterpreted as a D-dimensional lattice, with arbitrary D, regardless of their position in space, if they are properly connected [213–215]. Theoretically, any dimension and any geometry are accessible with this approach, which however

requires a large amount of engineering. Indeed, the number of links in the D-dimensional lattice scales as N^D with N the number of sites per axis. To achieve complex geometries, these N^D connections must be individually realised. The second strategy considers nodes as lattice sites according to natural labelling. This labelling becomes relevant when a coupling between them is implemented. What we mean by "natural" is that coupling schemes, usually involving nearest- or next-nearest-neighbours, exist and that they affect all nodes at once. Typical examples are spin states which are readily coupled using vector light shifts, or ring resonators positioned in line such that tunnelling is only allowed between neighbours. The geometry of the synthetic space arises directly from the coupling scheme and complex structures which involve novel topological states can be realised under the right choice of coupling [45, 216]. Interestingly, some key features of quantum Hall systems, *e.g.* spatially-dependent hopping phases for the implementation of artificial gauge fields, are naturally implemented along synthetic dimensions, because the coupling between states is externally applied. More generally, the flexibility in the external coupling facilitates the engineering of topological systems [212, 217]. We schematically represent these two approaches in Fig. 5.1(a,b).

An alternative route, that we already mentioned in Section 4.4, studies high-dimensional physics in a lower-dimensional space, considering parameters of the Hamiltonian as coordinates along an additional axis. There is a deep connection between topological pumps in low dimensions and higher-dimensional models through the procedures of dimensional reduction or extension. The pump parameters can be interpreted as momenta along fictitious dimensions, thus effectively increasing the dimensionality of the problem. This approach has been the subject of extensive theoretical analysis, in particular for quantum Hall systems [19, 218]. However, in the mathematical mapping between the two systems of different dimensions, the dynamic along the parameter dimensions is effectively frozen, such that the full dynamics of the high-dimensional system cannot be accessed.

5.2 Short review

The concept of synthetic dimension has a rich history, with key contributions from theory and experiments in the last ten years. In this Section, we describe some proposals and experimental realisations in different fields of physics. We focus on photonic systems, which have been strikingly successful, and on cold atom systems, as they are the closest to the approach of our group. Two examples of experimental techniques are shown in Fig. 5.1(c,d).

5.2.1 Photonics

In photonics, several proposals have paved the way toward the implementation of synthetic dimensions. For example, the frequency modes of light propagating in a cavity, the orbital angular momentum states of light circulating in a ring resonator, or the arrival times of multiple pulses are candidate sets of states to engineer a synthetic dimension [217, 219, 220].

We will briefly discuss the case of frequency modes in a multi-mode cavity, *e.g.* a ring resonator. In a ring geometry, the resonance conditions give rise to

frequency eigenmodes that form an almost equally spaced frequency comb. Temporal modulation of the resonator refractive index, at the frequency corresponding to the mode spacing, effectively induces hopping processes between the modes, interpreted as sites of a discrete lattice. This constitutes a building block in experiments where many ring resonators are coupled together, via spatial tunnelling of light in a given frequency mode between neighbouring resonators. By constructing spatial D-dimensional lattices of such resonators, with $0 \leq D \leq 3$, exploiting the cavity modes of each resonator as a synthetic dimension leads to simulating a $(D+1)$-dimensional lattice. Further control of the modulation phases of the resonators induces hopping along the synthetic lattice with complex phases that are spatially dependent, which is a key feature of many topological systems. Such a property leads naturally to gauge fields and to the exploration of the physics of particles subjected to a magnetic field in lattices, *e.g.* the 2D Harper-Hofstadter model using a $(1+1)$-dimensional system. In Fig. 5.1(d), we schematically show a resonator ring with frequency modes of light circulating clock-wise. An external time-dependent perturbation of strength Ω modulates the refractive index of the resonator and induces coupling between neighbouring frequency modes. Modulation at higher integer multiples of the spacing between the frequency modes leads to the simulation of models with higher dimensionality [221].

5.2.2 Cold atoms

The use of internal degrees of freedom as sites along a synthetic axis was first introduced in the context of cold atoms [41], with extensions towards the realisation of quantum Hall systems [42] and complex geometries [45]. A common approach is to consider a set of electronic states and couple them with single- or two-photon transitions, whether these states are clock states or hyperfine states. Another approach relies on the coupling of external degrees of freedom, considering for example momentum states or harmonic modes as sites of a synthetic lattice.

A momentum-space lattice is created by selecting momentum states using counter-propagating laser beams with well-chosen frequency differences. Semi-classically, the atoms experience the absorption of a photon in a beam, followed by the re-emission of a photon in a counter-propagating beam. This process leaves the electronic state of the atom unchanged, but induces a momentum shift of $2\hbar\mathbf{k}$ for beams of wavevectors $\pm\mathbf{k}$. Starting from atoms at rest, it couples a discrete set of momentum states $\mathbf{p}_n = 2n\hbar\mathbf{k}$, with an integer n, with nearest-neighbour hopping only. Since the energy dispersion is quadratic in the momentum $\mathbf{p}$ of the atoms, the energy difference between coupled momentum states does not vary linearly as a function of n. Each transition can be individually addressed, which provides additional flexibility in the coupling strength and relative phases of the two-photon processes. This approach is depicted in Fig. 5.1(c) where two-photon processes, addressing each transition $n \leftrightarrow n+1$ independently, are driven by laser fields with adjusted frequency differences. Several synthetic dimensions can be created with this protocol by adding beams along orthogonal directions. However, the number of frequency components to connect all the states in a D-dimensional lattice scales as L^D, with L the number of sites per axis. This greatly complicates experimental realisations of large-size and high-dimensional lattices, but recent realisations have managed to realise one- and

two-dimensional momentum-space lattices [222, 223].

Alternative approaches have been developed, including the eigenmodes of a harmonic oscillator [224–226] or the orbitals of a lattice [227]. The former uses the eigenmodes $|n\rangle$ (labelled by integers $n \geq 0$) of a quantum harmonic oscillator along x, of angular frequency ω. The nearest-neighbour harmonic eigenmodes, with equally-spaced eigenenergies, can be coupled by a temporally-modulated perturbation along the axis of the harmonic trap. The latter involves the orbital degree of freedom of an optical lattice, where the orbital states are coupled by two-photon Raman transitions. Under appropriate conditions, the spatially-modulated hopping phases engineer a non-zero effective magnetic flux per unit cell of the lattice.

Finally, the implementation of synthetic dimensions within the total angular momentum J of an atom generally relies on the interpretation of each Zeeman sublevel $|J, m\rangle$ as a site of a one-dimensional lattice of total size $2J + 1$ with open boundary conditions. The coupling of nearest or next-nearest neighbouring sites can easily be achieved using the vector or tensor parts of the light-matter coupling. This is facilitated if the energy spacing between neighbouring states does not vary (which is true in the absence of a quadratic Zeeman term for example). However, due to variations in the matrix elements of the light shift, the couplings are not uniform across the whole synthetic dimension. Another approach, which is reminiscent of the momentum state protocol, considers a few isolated states among all the available electronic states and couples them by pair independently. This requires lifting the energies of the unused states away from resonance with the driving fields and also adjusting the energy difference between coupled states to avoid any crosstalk. After properly shaping the electronic landscape, a finite lattice can be designed with independent control of the coupling strengths and relative hopping phases. This also opens the way toward less conventional geometries, such as periodic boundary conditions by coupling extremal sites of the lattice. Initial experimental realisations include two- and three-leg ladder systems, consisting of a small discrete synthetic dimension and an infinite spatial dimension [43, 44, 228, 229], before a generalisation to a larger synthetic dimension [46].

5.3 Protocol for encoding two independent dimensions in a single spin

5.3.1 Introduction

We now describe a different protocol that applies to atoms with a large spin J, in which we encode two synthetic dimensions. A combination of low-rank spin couplings, up to rank 2, effectively decouples the dynamics of the spin projection m and the remainder r of its Euclidian division by 3. These two coordinates act as the two orthogonal coordinates describing the surface of a cylinder with a discrete axis of finite size with open boundary conditions and a discrete cyclic dimension composed of three sites. To do this, let us consider the following Hamiltonian:

$$H = -U_a \frac{\hat{J}_+}{J} - U_b \frac{\hat{J}_-^2}{J(J-1/2)} + \text{hc}. \tag{5.1}$$

The two terms, which we will refer to as process (a) and process (b) in the following, couple the nearest- and next-nearest neighbours respectively with strengths U_a and U_b.

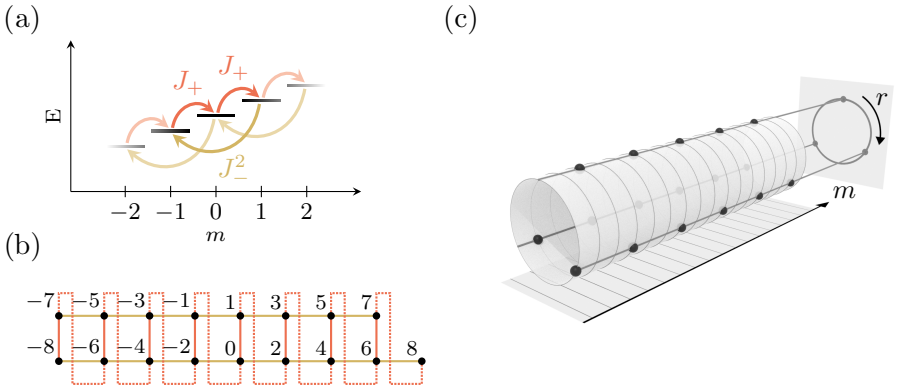

Figure 5.2 – Panel (a): Nearest- and next-nearest-neighbour couplings for some spin projection m states, from Eq. 5.1. Panel (b): Representation of the connected sites m as a two-dimensional lattice with additional connections between the edge sites. Panel (c): Representation of the Dicke states $|m\rangle$ on a cylinder with coordinates (m, r).

The other coefficients in their expressions are relevant only to simplify calculations. For $|m| \leq J - 2$, both processes act as discrete translations along the m states, whereas near the extremal states $m = \pm J$, they cannot induce hopping as no spin state exists beyond. Nevertheless, even for states close to $m = 0$, the ladder operators have m-dependent hopping amplitudes, owing to the Clebsch-Gordan coefficients. This variation is however small enough to preserve the interpretation of the spin ladder operators as discrete translations. The effect of the Clebsch-Gordan coefficients manifests itself by favouring states that minimise the Hamiltonian of Eq. 5.1, in our system, states with a zero mean magnetic projection along z. This effectively restricts the dynamics to spin states close to $m = 0$, thus suppressing the effect of the finite edges.

The two processes act differently on the two coordinates: both $\hat{J}_+$ and $\hat{J}_-^2$ increase r by 1, while the former increases m by 1 and the latter decreases m by 2. Based on this, the resulting dynamic does not show an obvious decoupling between m and r. However, the combination of the processes induces transitions between magnetic levels $|m\rangle$ with non-trivial cycles $m \to m+1 \to m+2 \to m$ which wind once around r. These cycles are thus independent of the magnetic projection m, within the range of populated spin states close to $m = 0$, and are encoded in the division remainder r modulo 3. Here, we already have an intuition of the dynamics of the system: the coordinate r encodes the evolution along these cycles and the dynamic along m is constrained by the variation of energy as the energy is minimal when the mean magnetisation is zero.

A condition for independent dynamics along both axes does not naturally arise from this picture. Here, we first provide a hand-waving argument, treating m and r

as continuous variables and approximating the action of the two processes as follows:

$$\begin{aligned}\frac{\hat{J}_+ + \hat{J}_-}{J}\psi(m,r) &\simeq \psi(m+1,r+1) + \psi(m-1,r-1)\\ &\simeq (2 + \partial_m^2 + 2\partial_m\partial_r + \partial_r^2)\psi(m,r),\\ \frac{\hat{J}_+^2 + \hat{J}_-^2}{J(J-1/2)}\psi(m,r) &\simeq \psi(m+2,r-1) + \psi(m-2,r+1)\\ &\simeq (2 + 4\partial_m^2 - 4\partial_m\partial_r + \partial_r^2)\psi(m,r).\end{aligned} \tag{5.2}$$

We have Taylor-expanded the two-variable quantities $\psi(m,r)$ up to second-order. In each process, the first-order terms have cancelled out such that we end up with a combination of zero- and second-order terms only. The full Hamiltonian is then expressed as:

$$H = -2(U_a + U_b) - (U_a + 4U_b)\partial_m^2 - (U_a + U_b)\partial_r^2 - 2(U_a - 2U_b)\partial_m\partial_r. \tag{5.3}$$

Decoupled dynamics along the two directions m and r are obtained for the specific ratio $U_b/U_a = 1/2$, since the $\partial_m\partial_r$ term vanishes, and these two dimensions can be considered orthogonal. For this ratio, denoting $U = U_a = 2U_b$, the total Hamiltonian is then written:

$$\frac{H}{U} = -6 - 9\partial_m^2 - 3\partial_r^2. \tag{5.4}$$

The dynamic associated with this Hamiltonian is that of a particle on a cylinder parametrised by an axial coordinate m and a cyclic azimuthal coordinate r. Two effective masses, inversely proportional to the coupling strength U, characterise the motion along these two axes. In the following sections, we will assume that the coupling ratio is fixed to $1/2$ and denote $U = U_a = 2U_b$. The effect of a deviation of the coupling ratio from this condition will be regularly revisited.

5.3.2 Semi-classical treatment

We now perform a precise treatment of the dynamic. For a sufficiently large total spin $J \gg 1$, it is well reproduced by a semi-classical analysis of the problem. We restrict the accessible states to the linear combinations of coherent spin states. The coherent spin states that we denote $|\theta,\phi\rangle$ are maximally polarised along an axis parametrised by spherical angles (θ,ϕ). In this approach, we replace the spin operators by their classical counterparts $(\hat{J}_x, \hat{J}_y, \hat{J}_z) = (J\sin\theta\cos\phi, J\sin\theta\sin\phi, J\cos\theta)$.

The associated energy functional, plotted in Fig. 5.3(a), is therefore:

$$\begin{aligned}E(\theta,\phi) &= \langle\theta,\phi|H|\theta,\phi\rangle\\ &= -2U\sin\theta\cos\phi - U\sin^2\theta\cos(2\phi).\end{aligned} \tag{5.5}$$

It features three extrema oriented along the equatorial plane of the Bloch sphere ($\theta = \pi/2$), with a zero mean magnetic projection along z, confirming the intuitive picture derived in the previous section. They are pointing along maximally distant axis: $\phi = 0, 2\pi/3$ and $4\pi/3$. For a large enough total spin J, the overlap between these states decreases to almost zero and the three states can be viewed as orthogonal states,

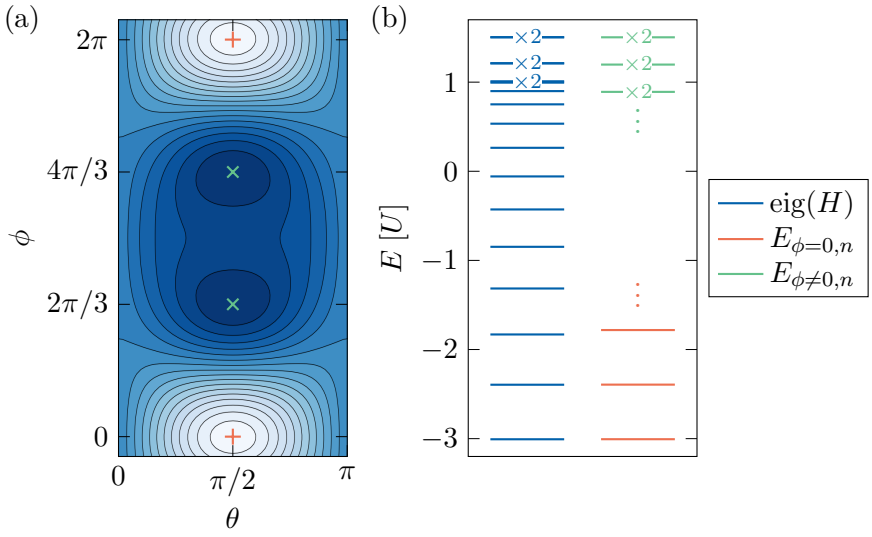

Figure 5.3 – Panel (a): We show the energy functional calculated for a coupling ratio $U_b/U_a = 1/2$. We identify its extrema by three marks: the red + sign for the single minimum at $\phi = 0$ and the green crosses for the two maxima at $\phi = 2\pi/3$ and $4\pi/3$. Panel (b): We compare the energy spectrum obtained from the diagonalisation of the potential of Eq. 5.1 (blue solid lines) and the predictions from the effective harmonic spectra $E_{\phi,n}$ (red and green solid lines, corresponding to panel (a)). We denote ×2 the eigenvalues that are degenerate or almost degenerate, for more clarity.

although, strictly speaking, they are not. Among the three states, $|\theta = \pi/2, \phi = 0\rangle$, oriented along x, is the unique minimum of the energy functional.

We now expand the Hamiltonian in the vicinity of an extremum of the energy functional. To treat the three states in a similar way, we consider spin operators in a rotated basis $(\tilde{J}_x, \tilde{J}_y, \tilde{J}_z)$, where $\tilde{J}_i = U^\dagger \hat{J}_i U$ with $U = \exp\left(\mathrm{i}\phi \hat{J}_z\right)$, a spin rotation of angle ϕ around z. In this way, each state $|\theta = \pi/2, \phi\rangle$ is oriented along $\tilde{J}_x$ in the corresponding rotated basis. Assuming that the spin states remain highly polarised along $\tilde{J}_x$ when varying the state energy by a small amount only, one can approximate $\tilde{J}_x \simeq J$ such that the commutator $\left[\tilde{J}_z, \tilde{J}_y\right]$ becomes:

$$\left[\hbar\tilde{J}_z, -\frac{\hbar\tilde{J}_y}{J}\right] = \mathrm{i}\hbar\frac{\tilde{J}_x}{J} \simeq \mathrm{i}\hbar. \tag{5.6}$$

The operators $\hbar\tilde{J}_z$ and $(-\hbar\tilde{J}_y/J)$ are canonically conjugated and we interpret the former as a position operator along the spin projection ladder and the latter as its associated momentum operator.

Now that we have some intuition about the problem, we follow a treatment making use of a bosonic Holfstein-Primakoff transformation [230] to express the spin operators in terms of a bosonic degree of freedom. For simplicity, we only consider the expansion around the minimum $|\theta = \pi/2, \phi = 0\rangle$, which points along $\hat{J}_x$. By introducing a bosonic annihilation operator a and considering spins highly polarised

along $\hat{J}_x$:

$$\begin{aligned}\hat{J}_x &= J - a^\dagger a,\\ \hat{J}_z - \mathrm{i}\hat{J}_y &= \sqrt{2J - a^\dagger a}\, a,\\ \hat{J}_z + \mathrm{i}\hat{J}_y &= a^\dagger \sqrt{2J - a^\dagger a}.\end{aligned} \tag{5.7}$$

Then at the lowest order in $1/J$, the two operators

$$\hbar\hat{J}_z = \hbar\sqrt{\frac{J}{2}}(a + a^\dagger) \quad \text{and} \quad -\frac{\hbar\tilde{J}_y}{J} = \mathrm{i}\hbar\sqrt{\frac{1}{2J}}(a^\dagger - a) \tag{5.8}$$

map to the position and momentum operators of the harmonic oscillator associated with the annihilation operator a. We find back the same commutator as in Eq. 5.6. Compared to the simple approach where we would expand the Hamiltonian in terms of two canonically-conjugated operators $\hbar\hat{J}_z$ and $(-\hbar\hat{J}_y/J)$, the advantage of the Holfstein-Primakoff transformation is that it can be written at higher orders in $1/J$. We now expand the Hamiltonian in power series of $1/J$ up to the first order. We get for the two processes:

$$\begin{aligned}H_a/U &= -2 + \frac{2}{J}a^\dagger a,\\ H_b/U &= -\frac{1}{2}\frac{1}{J(J-1/2)}\left[2J(J-1/2) + J(-6a^\dagger a + a^{\dagger 2} + a^2) + 2(a^\dagger a)^2\right]\\ &\simeq -1 + \frac{1}{2J}(6(a^\dagger a) - a^{\dagger 2} - a^2).\end{aligned} \tag{5.9}$$

Overall, we obtain at first order:

$$H/U \simeq -3 + \frac{10(a^\dagger a) - a^2 - a^{\dagger 2}}{J}. \tag{5.10}$$

Such a quadratic Hamiltonian can be diagonalised using a Bogoliubov transformation, by defining new bosonic operators:

$$b = ua + va^\dagger \quad \text{and} \quad b^\dagger = v^* a + u^* a^\dagger, \tag{5.11}$$

with $u^2 - v^2 = 1$ to satisfy the correct normalisation. The Hamiltonian has the canonical form for the choice: $u = (1/2 + 5/(4\sqrt{6}))^{1/2}$ and $v = -\sqrt{u^2 - 1}$.

$$H = E_0 + \hbar\omega b^\dagger b \quad \text{with} \quad \begin{cases} E_0 &= \left(-3 + \dfrac{2\sqrt{6} - 5}{2J}\right)U,\\ \hbar\omega &= \dfrac{2\sqrt{6}}{J}U.\end{cases} \tag{5.12}$$

The treatment of the Hamiltonian in the vicinity of the two maxima ($\phi = 2\pi/3$ and $4\pi/3$) is similar, up to a rotation of the spin operators basis as described above. The difference only stems from an additional factor -0.5 in the final expression of the energy for the two maxima. Noticing that $\cos\phi$ equals -0.5 for the two extrema and 1 for the minimum, the effective Hamiltonian can be recast into a single expression:

$$H_\phi = (E_0 + \hbar\omega b^\dagger b)\cos\phi. \tag{5.13}$$

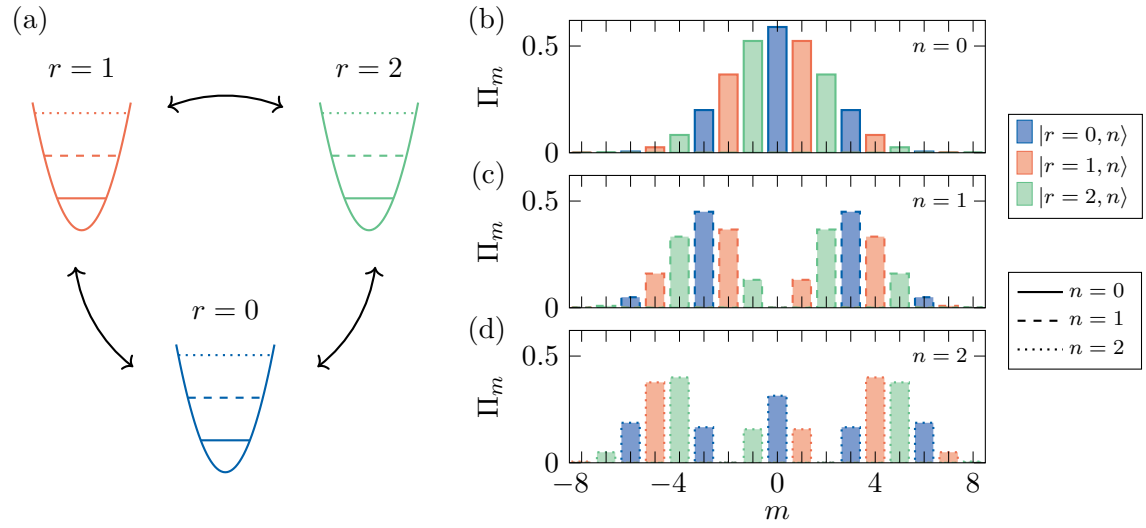

Figure 5.4 – Panel (a): Effective system consisting of three coupled sites $|r\rangle$ with an additional harmonic degree of freedom n (represented up to $n = 2$ for simplicity). Right panels: spin projection Π_m for the three states $r = 0, 1, 2$, for $n = 0$ (b), $n = 1$ (c) and $n = 2$ (d). The states $r = 0, 1, 2$ are encoded in the colors (blue, red and green respectively), while the quantum numbers $n = 0, 1, 2$ are encoded in the lineshape (solid, dashed, dotted lines respectively).

It is diagonal in the basis of Fock states $|\phi, n\rangle$ with the associated harmonic spectra: $E_{\phi,n} = (E_0 + \hbar\omega n)\cos\phi$. The eigenstates are easily constructed from the ground states $|\phi, n = 0\rangle$ by applying the raising operator n times: $|\phi, n\rangle = b^{\dagger n}|\phi, n = 0\rangle$.

This harmonic spectrum is only relevant to describe the dynamics of the system at low and high energies, but not in the intermediate energy regime. This approach is slightly unconventional since we are treating the low- and high-energy regimes similarly, which is not physical. However, this will become justified when we couple the internal states to a spatial degree of freedom such that all three $|\phi, n = 0\rangle$ states are involved in the low-energy dynamics. For now, restricting the spin dynamics to the semi-classical spectrum, we interpret it as the spectrum of a particle in a two-dimensional space.

For a given angle ϕ, the $E_0 + \hbar\omega n$ part describes a one-dimensional motion with harmonic trapping along the m coordinate, with an energy minimum for a spin pointing along $\tilde{J}_x$ in the corresponding rotated basis. Then, for a fixed n, the $\cos\phi$ term is reminiscent of the dispersion relation $E(q) \sim -2t\cos(qa)$ of a particle evolving on a one-dimensional ring lattice of length L, where t is the tunnelling strength and a is the lattice constant. The quasi-momentum q takes the discrete values $2\pi j/L$, with $0 \leq j < L/a$ an integer. By analogy, in our system, the three discrete angles ϕ play the role of the momenta conjugated to a cyclic dimension of length $L/a = 3$. For a fixed value of n, this motivates the definition of a basis of three position states $\{|r, n\rangle\}_{r=0,1,2}$, which are related to the momentum states by

inverse Fourier transform:

$$|r,n\rangle = \frac{1}{\sqrt{3}} \sum_{\phi=0,\frac{2\pi}{3},\frac{4\pi}{3}} \mathrm{e}^{-\mathrm{i}\phi r} \, |\phi,n\rangle \, . \tag{5.14}$$

The variable r represents the position along the cyclic dimension. This notation is justified and consistent with the initial definition of the coordinate r from the remainder of m modulo 3. Indeed, the three states $|r,n\rangle$ have a peculiar form when projected along the z axis. Their spin projection probabilities Π_m only involve spin projections m such that $m = r \,(\mathrm{mod}\, 3)$. This arises from the structure of the three states $|\phi,n\rangle$, which are obtained from $|\phi = 0, n\rangle$ by a spin rotation around z of angle ϕ. Projecting $|r,n\rangle$ on an arbitrary spin state $|m\rangle$ ($-8 \leq m \leq 8$), which is an eigenstate of $\hat{J}_z$, we obtain:

$$\langle m|r,n\rangle = \frac{1}{\sqrt{3}} \left(\sum_{\phi=0,\frac{2\pi}{3},\frac{4\pi}{3}} \mathrm{e}^{-\mathrm{i}\phi(r-m)} \right) \langle m|\phi = 0, n\rangle \, , \tag{5.15}$$

where $\sum_\phi (\mathrm{e}^{-\mathrm{i}\phi})^{(r-m)}$ equals 3 when $m = r \,(\mathrm{mod}\, 3)$ and 0 when $m \neq r \,(\mathrm{mod}\, 3)$. The projection of the coherent state $|\phi = 0, n\rangle$ on the Dicke basis gives the envelope for the spin projection probabilities of the three $|r,n\rangle$ states, with maximal probabilities close to $m = 0$.

In Fig. 5.4, we show the spin projection probabilities Π_m for the states $|r,n\rangle$ for the three positions $r = 0, 1, 2$ and the smallest values of n. The intuition we have developed in this Section is summarised in this graph: the $|r,n\rangle$ states involve only spin projections m such that $m = r \,(\mathrm{mod}\, 3)$ and we recognise the typical shape of the lowest energy eigenstates of a one-dimensional harmonic oscillator, labelled by the positive integer n.

We can recast the diagonal Hamiltonian of Eq. 5.13 in terms of the position states:

$$\begin{aligned} H_\phi &= \sum_{\phi=0,\frac{2\pi}{3},\frac{4\pi}{3}} (E_0 + \hbar\omega b^\dagger b) \cos\phi \, |\phi\rangle \langle\phi| \\ &= \sum_{n\geq 0} \sum_{\phi=0,\frac{2\pi}{3},\frac{4\pi}{3}} (E_0 + n\hbar\omega) \cos\phi \, |\phi,n\rangle \langle\phi,n| \\ &= \sum_{n\geq 0} \sum_{r=0}^{2} \frac{E_0 + n\hbar\omega}{2} \, |r+1,n\rangle \langle r,n| + \mathrm{hc} \end{aligned} \tag{5.16}$$

This Hamiltonian describes a particle on a cylinder, with harmonic trapping along the axis m and free dynamics along the azimuthal direction r (albeit with a coupling that depends on the quantum number n of the harmonic trapping).

5.3.3 Excitations

We now provide examples of decoupled dynamics along the two coordinates m and r. We start in the ground state of the Hamiltonian and apply a perturbation that induces a non-zero velocity along one of the two directions. The velocities along the two axes are defined as follows.

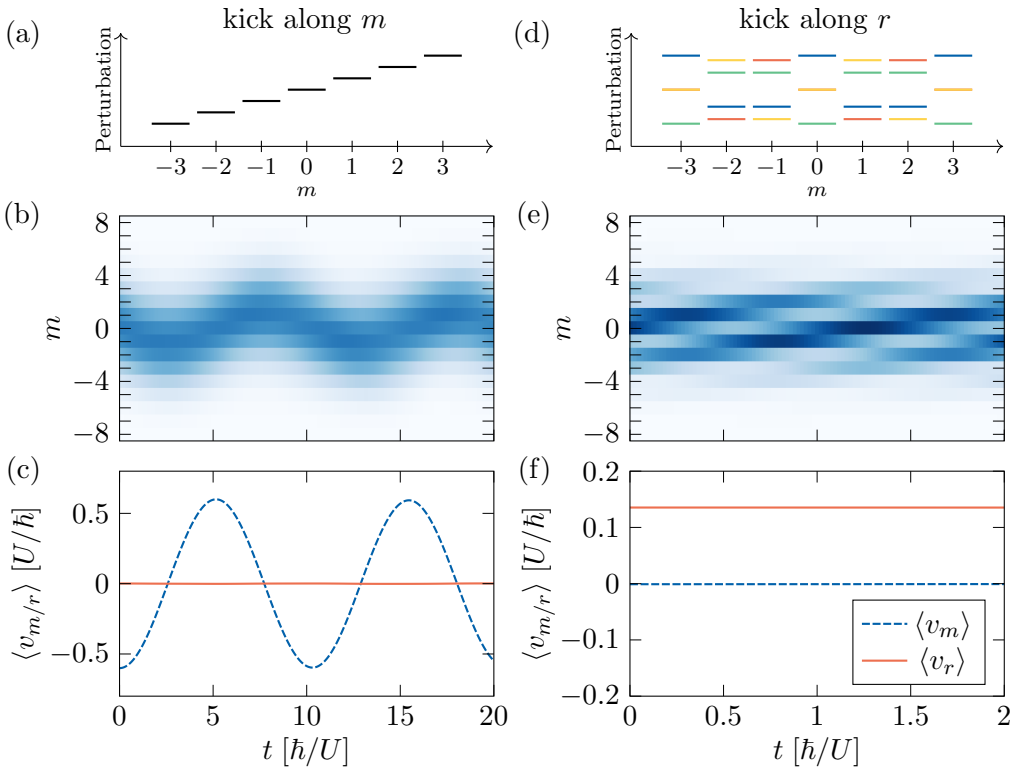

Figure 5.5 – We study the effect of perturbations along one of the two axes m (left column) and r (right column). The upper panels are representations of the applied perturbation in the $|m\rangle_z$ basis. In panel (d), the different colours represent the time-dependent perturbation at different times $-\alpha t = 0$, $\pi/2$, π and $3\pi/2$, in blue, red, green and yellow respectively. It highlights the temporal periodicity of the perturbation and also its m-periodicity at each time. We then present the spin dynamics following the application of a perturbation. The middle panels show the spin distribution Π_m as a function of time. The lower panels show the evolution of the mean velocities $\langle v_m \rangle$ (dashed blue lines) and $\langle v_r \rangle$ (solid red lines) for the same dynamics.

As usual, the velocity operator along m can be constructed from the position operator along this axis, which is simply $\hat{J}_z$, and is defined, using the Heisenberg picture, as:

$$\begin{aligned} v_m &\equiv \frac{\mathrm{i}}{\hbar}\left[H, \hat{J}_z\right] \\ &= U_a \frac{\mathrm{i}\hat{J}_+}{J} + U_b \frac{-2\mathrm{i}\hat{J}_-^2}{J(J-1/2)} + \mathrm{hc}. \end{aligned} \tag{5.17}$$

The case of the coordinate r is not so trivial. Since it is cyclic, it can be viewed as an angular variable, which cannot be expressed in terms of a Hermitian operator [231, 232]. However, the velocity operator along r is well defined. We give here qualitative arguments for its construction. Following the usual derivation of a velocity operator, we compute the commutator of the Hamiltonian with a position operator along the synthetic axis, such as $\exp\left(\mathrm{i}\frac{2\pi}{3}\hat{J}_z\right)$ which is indeed cyclic in r. However, this term is

not Hermitian, so we consider its anticommutator with the Hermitian conjugate of the position operator along r:

$$\begin{aligned} v_r &\equiv \frac{\mathrm{i}}{\hbar}\frac{1}{\sqrt{3}}\left\{\exp\left(-\mathrm{i}\frac{2\pi}{3}\hat{J}_z\right), \left[H, \exp\left(\mathrm{i}\frac{2\pi}{3}\hat{J}_z\right)\right]\right\} \\ &= U_a\frac{\mathrm{i}\hat{J}_+}{J} + U_b\frac{\mathrm{i}\hat{J}_-^2}{J(J-1/2)} + \mathrm{hc}. \end{aligned} \tag{5.18}$$

Intuitively, one can understand the final formula by first looking at the velocity along m and then replacing the i coefficients based on the effect of the spin operators on the coordinate r, instead of m. $\hat{J}_+$ and $\hat{J}_-^2$ both increase r by 1, such that we associate them with i. However, $\hat{J}_-^2$ decreases m by 2, which explains the $-2\mathrm{i}$ coefficient in the expression for the velocity v_m along m.

Let us start with an excitation along the m coordinate only, applied on the ground state of the Hamiltonian $|\phi = 0, n = 0\rangle$. A Zeeman field pointing along z, $V_{\mathrm{pert}}^{(m)} = V_z\hat{J}_z$ corresponds to a linear potential in m. In the perturbative regime with $V_z \ll 1$, since it is a low-rank spin operator, we expect no coupling with the two other $|\phi, n = 0\rangle$ states, and thus no dynamics along r. If we apply a perturbation of this form on $|\phi = 0, n = 0\rangle$, it will rotate the spin state along z, thus retaining θ but slightly changing ϕ toward a state of the form $|\phi \propto V_z, n = 0\rangle$. This is equivalent to pulling a particle in a harmonic trap away from the stationary position. This results in an oscillation of the position along the m coordinate, *i.e.* the magnetisation $\langle\hat{J}_z\rangle$, and an out-of-phase oscillation of the velocity along this axis, *i.e.* $\langle v_m\rangle$. If we apply an instantaneous kick along m, we observe the spin dynamics depicted in Fig. 5.5(a,b). As anticipated, no dynamic along r is observed.

Now, as for the definition of v_r, finding a perturbation along r that conserves m is more challenging, especially from an experimental point of view where we mostly consider spin couplings of rank less than 2. Due to the distance between the three $|\phi, n = 0\rangle$ states in phase space, we consider a high-order coupling operator, such as:

$$V_{\mathrm{pert}}^{(r)}(t) = V_r\cos(2\pi r/3 - \alpha t). \tag{5.19}$$

It corresponds to a perturbation in r at the speed $3\alpha/(2\pi)$, which is diagonal in the $|m\rangle_z$ projection state basis. It drives the system to a non-zero velocity $\langle v_r\rangle \neq 0$. The three $|\phi, n = 0\rangle$ states are coupled by the perturbation and a modulation of the spin distribution Π_m modulo 3 is visible. In Fig. 5.5(c,d), we show the spin dynamics following the perturbation. The non-zero velocity $\langle v_r\rangle$ is conserved, which is compatible with the absence of trapping along this axis, and the velocity along m remains negligible.

5.3.4 Uncoupled dynamics

We study the effect of varying the coupling ratio away from the decoupling value 1/2. We seek to understand more deeply the interpretation of our system as a cylinder with harmonic trapping along the longitudinal axis.

We vary the coupling ratio and simulate the dynamics under the effect of a perturbation along either m or r. In Fig. 5.6(a), we show how the velocity along the unperturbed axis is modified as a function of the coupling ratio. For the case

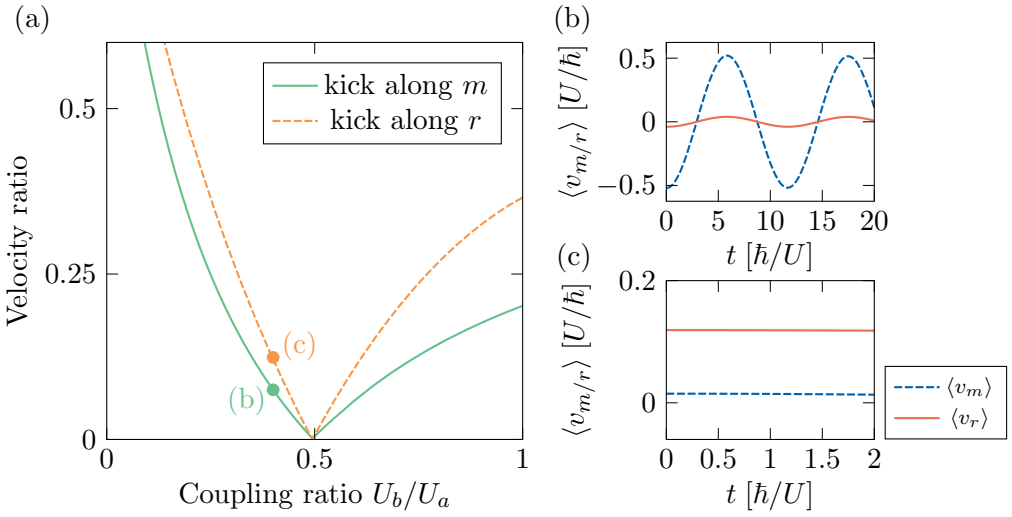

Figure 5.6 – Panel (a): For the two types of kick described in the main text, we show a quantity related to the dynamics along the axis that is not excited. For a kick along m, we plot the ratio of the amplitude of the oscillations of $\langle v_r\rangle$ and of the amplitude of those of $\langle v_m\rangle$. For a kick along r, we plot the ratio of the mean value of $\langle v_m\rangle$ and of the mean value of $\langle v_r\rangle$ after the perturbation is turned off. Panels (b,c): We show the mean velocities during the spin dynamics after a perturbation along m and r, in the upper and lower panels respectively, for a coupling ratio $U_b/U_a = 0.4 \neq 1/2$.

of a perturbation along m, since we expect velocity oscillations due to the trapping along m, we present the ratio of the oscillation amplitudes of $\langle v_r\rangle$ and $\langle v_m\rangle$. For the case of a perturbation along r, we show the ratio of $\langle v_m\rangle$ and of $\langle v_r\rangle$, averaged over a short period just after switching off the perturbation. We observe in both situations a minimum around the coupling ratio of 1/2. As we move away from it, the interpretation of uncoupled dynamics along the two axes no longer holds. This matches our hand-waving approach, treating m and r as continuous variables, where we have stated that the independence of the dynamics along these two axes is ensured at a coupling ratio of 1/2. We also interpret this as the result of the peculiar treatment of low- and high-energy regimes on an equal footing. We will contrast this behaviour with that in the presence of a coupling between the internal states and a spatial dimension in Section 5.4, where the low-energy picture is preserved.

In the following Section, we present our proposal to engineer a quantum Hall system by coupling the internal and external degrees of freedom of an atom. We engineer a Hall cylinder, made of a spatial dimension and of the cyclic coordinate r, while the coordinate m remains frozen.

5.4 Application: A two-dimensional Hall cylinder

The dynamics presented in Section 5.3, characteristic of a particle on a cylinder, can be enriched by coupling to a spatial dimension. Raman processes, involving two beams with opposite wavevectors $\pm\mathbf{k}$, induce spin transitions together with a

momentum kick $\pm 2\mathbf{k}$, leading to a one-dimensional spin-orbit coupling.

Consider two laser beams counter-propagating along a spatial axis x, driving two-photon optical transitions. The couplings inherit a spatially-dependent phase $\mathrm{e}^{\pm \mathrm{i}2kx}$ from the laser beam interference and the Hamiltonian of the system reads:

$$\begin{aligned} H &= \frac{M v_x^2}{2} + V, \\ V &= -\left[U_a \frac{\hat{J}_+}{J} + U_b \frac{\hat{J}_-^2}{J(J-1/2)} \right] \mathrm{e}^{\mathrm{i}2kx} + \mathrm{hc}, \end{aligned} \tag{5.20}$$

where v_x is the velocity along the x axis, k is the norm of the laser wavevector $\mathbf{k}$ and M is the atomic mass. We define the corresponding recoil velocity $v_{\mathrm{rec}} = \hbar k/M$ and the recoil energy $E_{\mathrm{rec}} = \hbar^2 k^2/(2M)$.

As in Section 5.3, let us see the effect of the two processes on the two synthetic axes m and r. The two processes increasing the remainder r are commonly associated with a phase accumulation $-2kx$, proportional to the position x, leading to an effective gauge field in the (x, r) plane. Conversely, the wavefunction acquires phases of opposite sign $\pm 2kx$ under the effect of the two processes increasing m, such that it is not clear at this stage whether there can be a gauge field in the (x, m) plane. We note however that, at vanishing coupling strength for one of the two processes, we expect a magnetic field in the (x, m) plane [46], indicating a relation between the presence of a magnetic field and the coupling strength ratio.

Following the semi-classical treatment in the purely spin case, we derive the energy functional as a function of the real position x:

$$E(x, \theta, \phi) = -2U \sin\theta \cos(\phi - 2kx) - U \sin^2\theta \cos(2\phi + 2kx). \tag{5.21}$$

Interestingly, at the coupling ratio $1/2$, for all positions x, it still features three extrema for $\theta = \pi/2$ and $\phi = 0, 2\pi/3$ and $4\pi/3$. The energy functional is x-periodic with a period $\lambda/2$ (with $\lambda = 2\pi/k$ the laser wavelength) and the $|\phi = 0, 2\pi/3, 4\pi/3\rangle$ states are minima for the positions $x = 0, \lambda/6, \lambda/3$ respectively, reaching equal minimum energy. Contrary to the purely spin case, the three spin states $|\phi\rangle$ play equivalent roles at low energy, within a cell of size $\lambda/2$.

By expanding the spin operators around the three extrema, at a given position x, we obtain the effective Hamiltonian:

$$\begin{aligned} V_{\mathrm{eff}} &= \sum_{\phi = 0, \frac{2\pi}{3}, \frac{4\pi}{3}} (E_0 + \hbar\omega b^\dagger b) \cos(\phi - 2kx) \\ &= \sum_{n \geq 0} \sum_{\phi = 0, \frac{2\pi}{3}, \frac{4\pi}{3}} (E_0 + n\hbar\omega) \cos(\phi - 2kx) \, |\phi, n\rangle \langle \phi, n| \\ &= \sum_{n \geq 0} \sum_{r=0}^{2} \frac{E_0 + n\hbar\omega}{2} \mathrm{e}^{-\mathrm{i}2kx} \, |r+1, n\rangle \langle r, n| + \mathrm{hc} \end{aligned} \tag{5.22}$$

where we have defined the $|r, n\rangle$ position states, as conjugated to the momentum states $|\phi, n\rangle$.

The energy spectrum $E_{\phi,n} = (E_0 + n\hbar\omega)\cos(\phi - 2kx)$ has two parts: a harmonic degree of freedom, defined by n, and a cosine term which plays the role of a lattice

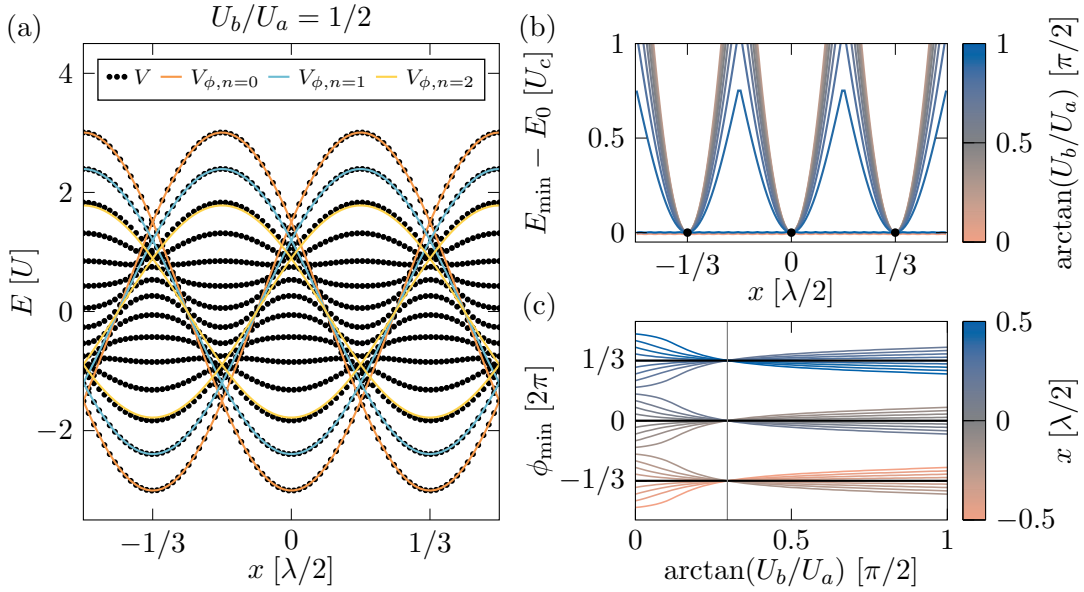

Figure 5.7 – Panel (a): Spectra as a function of position x for the coupling ratio $U_b/U_a = 1/2$, in black dots for the total potential $V(x)$ and in solid lines for the effective potentials $V_{\phi,n}(x)$ ($n = 0, 1, 2$ in orange, cyan and yellow respectively), for $\phi = 0, 2\pi/3$ and $4\pi/3$. Panels (b,c): Study of the deviation from the coupling ratio 1/2 in the semi-classical picture, keeping $U_c = \sqrt{U_a U_b}$ constant. The extremal cases $U_b = 0$ and $U_a = 0$ correspond to $\arctan(U_b/U_a)/(\pi/2)$ equal to 0 and 1 respectively. The upper panel show the variation of the minimum of the energy functional $E(\theta, \phi)$ as a function of position x and coupling ratio U_b/U_a. The common energy minima, at positions x that are integer multiples of $\lambda/6$, are marked with black dots. In the lower panel, we plot the angle $\phi_{\min}$ at which the minimum of the energy functional is reached as a function of both the coupling ratio and the position. The black lines correspond to the three positions marked by black dots in the upper panel. The vertical grey line marks the coupling ratio $U_b/U_a = 1/2$.

potential. The angle ϕ defines the position of the energy minima along x, as mentioned earlier. The potential in Eq. 5.22 describes the hopping dynamics along r, with a x-dependent complex phase that mimics the Aharonov-Bohm phase associated with a magnetic field in the xr plane. This interpretation becomes explicit when deriving the energy spectrum at first order in $\phi - 2kx$, with $|E_0| \gg \hbar\omega$. The full atom dynamics, described by the effective Hamiltonian $H_{\text{eff}} = p_x^2/2M + V_{\text{eff}}$, then maps to the motion of a charged particle on a Hall cylinder along x and r, with an additional harmonic degree of freedom n. In Fig. 5.7(a), we compare the position-dependent spectra obtained from the diagonalisation of the exact coupling operator in Eq. 5.20 and the effective model V_{eff} given by Eq. 5.22, at $U_b/U_a = 1/2$. The two lowest energy bands of the exact spectrum are well reproduced by the effective model and some deviations are visible for n higher than 2.

Let us now consider a departure from the coupling ratio $U_b/U_a = 1/2$. The

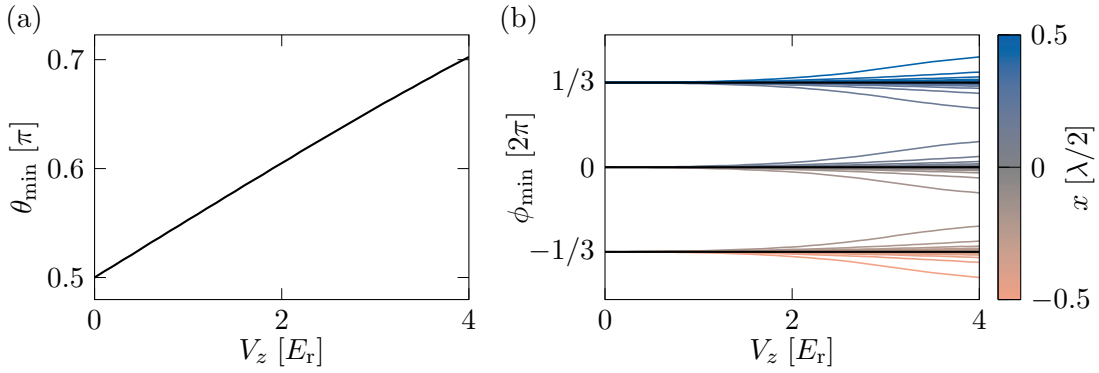

Figure 5.8 – Study of the effect of an additional term $V_z\hat{J}_z$. We numerically determine the functional energy minimum as a function of position x and field strength V_z, and the angle $(\theta_{\min}, \phi_{\min})$ for which the minimum is reached. For all field strengths, the minimum of the functional energy minima is reached for the positions $x_j = j\lambda/6$, with integers j. Panel (a): Angle $\theta_{\min}$ as a function of V_z. Panel (b): Angle $\phi_{\min}$ as a function of V_z and x. In both panels, the solid lines are obtained at the positions x_j.

purely spin case taught us that the dynamics along the two synthetic axes are no longer decoupled. In Fig. 5.7(b,c), we see that, whatever the ratio, the energy functional always has global minima at the positions $x_j = j\lambda/6$, with integers j (marked by black dots). For these positions, the energy functional minimum is always reached, at $\theta = \pi/2$, for the same angle $\phi_j = j2\pi/3 \,(\mathrm{mod}\, 2\pi)$. Overall, the lowest energy states are reached at positions that are integer multiples of $\lambda/6$, for the three angles $\phi = 0, 2\pi/3, 4\pi/3$, whatever the coupling ratio. We conclude that the low-energy physics is unchanged, for coupling ratios deviating from 1/2, and that the interpretation with three sites r remains valid, although the picture with an additional independent harmonic degree of freedom n partially breaks down.

We also point out that the two extreme cases $U_a = 0$ or $U_b = 0$ are also visible in Fig. 5.7(b). There, the energy of the ground state does not vary with the x-position, which is related to the absence of breaking of the continuous translation symmetry. Indeed, when only one of the two processes is present, the spatial dependence of the hopping phases can be gauged out with an appropriate unitary transformation.

The robustness of the interpretation at low energy goes hand in hand with the robustness against magnetic field fluctuations. We consider an additional term in the Hamiltonian $V_z\hat{J}_z$, a Zeeman term corresponding to a magnetic field along $\mathbf{z}$. We only study the effect of magnetic fluctuations along the z axis because, in the rotating wave approximation (see Section 6.2 for details on our implementation of processes (a) and (b) using light-matter coupling within the rotating wave approximation), the contributions from magnetic fields along the x and y axes oscillate rapidly and average out to zero. In Fig. 5.8, we show the angles $(\theta_{\min}, \phi_{\min})$ for which the functional energy minima are reached, as a function of the position x and the field strength V_z. We note that, again, the physics at low energy always occurs in the vicinity of positions that are integer multiples of $\lambda/6$, for the three angles $\phi = 0, 2\pi/3, 4\pi/3$.

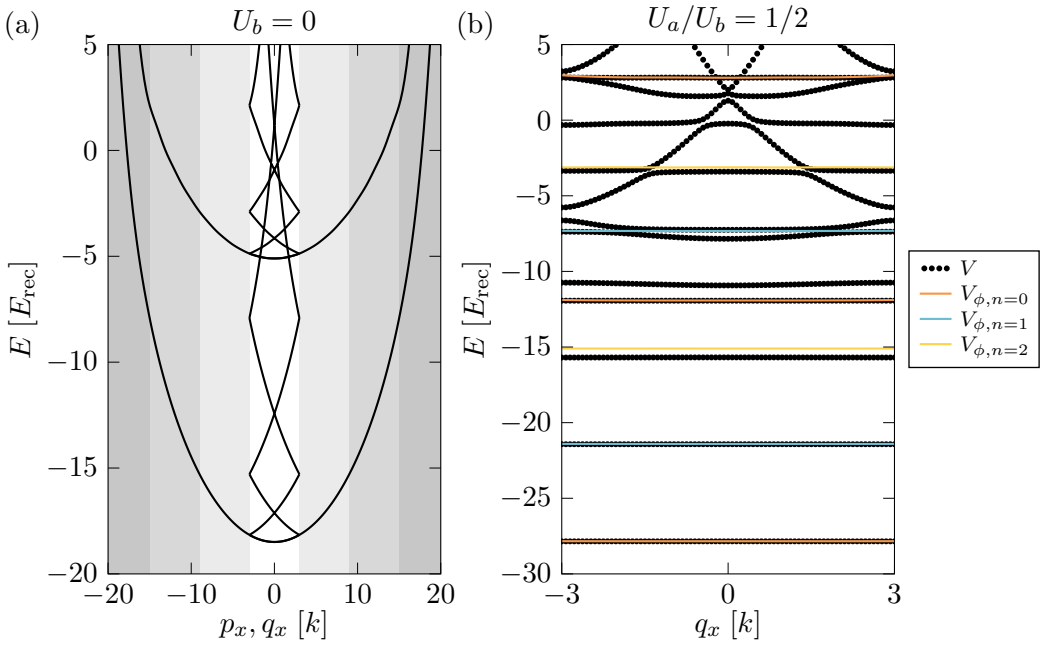

Figure 5.9 – Panel (a): Band structure for $U_b = 0$. The spatially-dependent phases of $\hat{J}_+ \mathrm{e}^{-\mathrm{i}2kx} + \mathrm{hc}$ can be incorporated as a vector potential with the unitary transformation $U = \mathrm{e}^{\mathrm{i}2k\hat{x}\hat{J}_z}$, such that p_x is a conserved quantum number. We show the unfolded band structure and the folded band structure in the first Brillouin zone of size $6k$ (defined from the magnetic translation symmetry of the full Hamiltonian with non-zero U_b). The shaded areas highlight the successive Brillouin zones. Panel (b): Band structures calculated using the actual potential $V(x)$ (black dots) and the effective ones $V_{\phi,n}(x)$, with $n = 0, 1, 2$ (orange, cyan and yellow lines), at $U_b/U_a = 1/2$. The process (b) induces coupling between momentum states with spacing $6k$, such that a gap opens in the folded picture at increasing U_b and a band structure with quasi-flat bands appears.

However, we observe a departure from the angle $\theta = \pi/2$ as the $V_z\hat{J}_z$ term tends to polarise the spin along the z axis, *i.e.* towards $\theta = 0$ or π depending on the sign of V_z. For reasonable values of V_z, typically of the order of E_{rec}, as shown in Fig. 5.8, the picture at low energy holds and we expect only a shift of the mean spin projection along z, which does not endanger the interpretation of the system as a cylinder.

We validate the description of our system as a quantum Hall cylinder, by comparing the band structure of the exact Hamiltonian of Eq. 5.20 and the effective model of Eq. 5.22. Both models are invariant under the discrete magnetic translation:

$$T_{\mathrm{mag}} = T_x(\lambda/6)R_z(-2\pi/3), \tag{5.23}$$

which combines a $\lambda/6$-translation along x and a rotation of the spin around z of angle $-2\pi/3$. This symmetry leads to the conservation of the quasi-momentum:

$$q_x \equiv \frac{Mv_x}{\hbar} + 2k\hat{J}_z \,(\mathrm{mod}\, 6k), \tag{5.24}$$

defined over the magnetic Brillouin zone $-3k \leq q_x < 3k$, of size $6k$. The Hamiltonian spectra are organised in magnetic Bloch bands, illustrated in Fig. 5.9(b), for a coupling strength $U = 12E_{\text{rec}}$. This Hamiltonian can be understood starting from the Hamiltonian with kinetic energy and process (a) only. The application of the unitary transformation $U = \mathrm{e}^{\mathrm{i}2k\hat{x}\hat{J}_z}$ incorporates the x-dependent phase in the kinetic energy as a non-zero vector potential $2\hbar k\hat{J}_z$, such that the momentum $p_x = Mv_x/\hbar + 2k\hat{J}_z$ is a conserved quantity. We show in Fig. 5.9(a) the resulting band structure. The effect of process (b), in this gauge choice, is to couple momentum states in a given band that are distant by $6k$. To make this more transparent, we fold the band structure for $U_b = 0$, in a Brillouin zone of size $6k$, centred on $p_x = 0$ (successive Brillouin zones are represented by the grey shaded areas in Fig. 5.9(a)). Crossings at the edges of the Brillouin zone, involving momentum states with a momentum difference of $6k$, are avoided in the presence of process (b). As U_b is increased, the gaps are opened and the ground band splits into a succession of bands that flattens. The large number of crossings for the ground band, at energies below the first excited band, for $U_b = 0$, leads to a large number of quasi-flat bands in the resulting spectrum for the total Hamiltonian.

We compare this spectrum with that of the effective model in Fig. 5.9(b), which reproduces well the very flat lowest bands for $n = 0, 1, 2$. This confirms the relevance of the description of low-energy dynamics as that of a quantum Hall cylinder.

Generalisations

The above protocol can be generalised to a cylinder with a different number of sites along the cyclic dimension. For example, using only vector light shifts, one can design a two-leg system, albeit without spatially-dependent hopping phase. A less trivial example is to replace the rank-2 spin coupling with a higher-rank spin operator to obtain a cylinder with a larger circumference. Spin coupling of rank strictly higher than 2 cannot be produced by simply applying a DC light shift, but they can be engineered by temporal modulation for example [233]. Periodically-driven systems, at a high frequency compared to all the relevant energies, can be described by an effective Hamiltonian with possibly non-trivial spin couplings, albeit associated with a micromotion. The most natural extension is to prepare a cylinder with 4 sites along the cyclic coordinate, using a $\hat{J}_+^3$ coupling. Interestingly, this system could be a building block to study two-dimensional models of topological insulators that do not break the time-reversal symmetry, characterised by a non-trivial $\mathbb{Z}_2$ invariant [16]. These topological insulators require an even number of states, and the smallest non-trivial case can be realised with only 4 sites, coupled together. In this Section, we consider couplings of general rank $f \geq 1$.

We consider the Hamiltonian $H = Mv_x^2/2 + V$ with a spatially-dependent potential V:

$$V = -\left[U_a \frac{\hat{J}_+}{J} - U_b \frac{\hat{J}_-^f}{J^{f-1}(J-1/2)}\right] \mathrm{e}^{\mathrm{i}2kx} + \mathrm{hc}. \tag{5.25}$$

In a semi-classical approach, the generalisation of Eq. 5.21 to an energy functional for a spin coupling of rank f and a coupling ratio $U_b/U_a = 1/f$, is:

$$E(\theta, \phi) = -2U \sin\theta \cos(\phi - 2kx) - 2U \frac{1}{f} \sin^f(\theta) \cos(f\phi + 2kx), \tag{5.26}$$

with $U = U_a = fU_b$.

The local extrema of the energy functional are obtained for the $f+1$ coherent states pointing along the equatorial plane ($\theta = \pi/2$) of azimuthal angle $\phi = k2\pi/(f+1)$ with integer $0 \leq k \leq f$. By expanding the Hamiltonian in the vicinity of these states, we obtain an equivalent of the effective picture presented in the previous Section: our system maps to the motion of a charged particle on a Hall cylinder defined by the coordinates x and r, of circumference $f+1$.

Let us consider two extremal cases. On the one hand, the highest non-trivial order of the spin coupling is reached at $f = 2J$, where the $\hat{J}_{\pm}^{f}$ terms couple the two edge states of the Zeeman manifold $|J, \pm J\rangle$ only. This produces a Hall cylinder with the largest cyclic dimension composed of $2J+1$ sites. In this configuration, the sites of the cylinder are the Dicke states, highly non-classical states, and the semi-classical approach obviously breaks down. On the other hand, we expect very few modifications to our scheme (with $f = 2$) when we simply consider $f = 3$, for which we obtain a cylinder with 4 sites. Intuitively, this arises from the ratio between the coupling rank and the total spin f/J, which varies very little and remains much less than one.

5.5 Interactions in synthetic dimensions

We mentioned earlier that synthetic dimensions are treated on an equal footing with spatial dimensions, but we must point out an important difference between them. In hybrid systems based on internal degrees of freedom such as electronic states of atoms, the interactions are typically infinite-range along the synthetic dimension, while being generally short-range along spatial coordinates. Indeed, spin-changing collisions $m_1, m_2 \rightarrow m_3, m_4$ are allowed for a priori arbitrary spin states m_i ($i = 1, 2, 3, 4$). The peculiar nature of interactions in hybrid systems, in particular its strong anisotropy, leads to exotic phases of matter [217]. It complicates the analogy with standard models, for which analogue simulation is much awaited. For example, it is still a debate whether fractional quantum Hall states could be observed in systems with synthetic dimensions [234]. Still, some implementations of synthetic dimensions may feature finite-range interaction. For example, in the approach based on eigenmodes of a harmonic quantum oscillator, interactions decay algebraically [224] with distance along the synthetic axis. Another approach rather tunes the range of the interaction along a synthetic dimension. For example, in the case of a Hall ribbon where the dimension with edges is encoded in the Zeeman manifold of the electronic ground state of an atom [46], the addition of a magnetic field gradient can spatially separate the different Zeeman states. Compensated by a harmonic trap along the direction of the gradient, the atoms remain confined and the spatial distributions of the different Zeeman sublevels are shifted, thus effectively ensuring short-range interactions along the synthetic axis. More generally, interactions along synthetic dimensions can be shaped by mixing trotterisation techniques and multiple Feshbach resonances [235].

Even if the range of the interactions is a limitation in reaching strongly-interacting phases of matter in quantum Hall systems and requires specific protocols to circumvent it, it can be favourable to study other systems. Among possible candidates for the

implementation of synthetic dimensions, alkaline-earth-like fermionic atoms, such as strontium or ytterbium, with SU(N) symmetric interactions in their ground state with pure nuclear spin [236], have attracted attention recently, following successes in bringing them to quantum degeneracy [237, 238]. This symmetry is connected to high-energy physics for the description of quarks and to condensed-matter physics with unconventional magnetic states, for example. In the latter, an emblematic model, the Fermi-Hubbard model, has a generalisation to interactions with SU(N) symmetry [239, 240], originally studied for transition-metal oxides and recently studied using ultracold atoms [241, 242].

The variety of implementations of synthetic dimensions thus leads to a wide range of types of interactions, and we will revisit this topic in further detail in Chapter 7 for our implementation of a Hall cylinder.

We have shown how two synthetic dimensions can be encoded in the spin of a single atom using a combination of spin couplings of different ranges. In the next Chapter, we present our implementation of an atomic Hall cylinder using a cyclic synthetic dimension coupled with a spatial one and probe its topology. We extend our protocol to realise a four-dimensional Hall system in Chapter 7, benefiting from the two synthetic dimensions encoded in the large spin of dysprosium atoms.

6

Realisation of Laughlin's topological charge pump

This Chapter is dedicated to the experimental realisation of topological pumping in an atomic Hall cylinder, engineered using the approach described in Chapter 5.

This work has been published in the following article [243]:
Laughlin's Topological Charge Pump in an Atomic Hall Cylinder
A. Fabre, J.-B. Bouhiron, T. Satoor, R. Lopes, S. Nascimbene
Physical Review Letters 128, 173202 (2022)

The Hall cylinder, first envisioned by Laughlin in his argument for the quantisation of the integer quantum Hall effect, consists of a radial magnetic field $\mathbf{B}_\perp$, yielding the Hall effect, and an axial field $\mathbf{B}_\parallel$ along $\mathbf{x}$, which threads the cylinder with a flux $\Phi_\parallel$. As presented in Section 4.2.3, the electronic states are localised along the longitudinal axis and there is one accessible state per magnetic flux quantum Φ_0. This defines the length ℓ_{mag} of the magnetic unit cell, with each cell being filled with exactly one electron for a filled ground band. Laughlin's thought experiment consists of performing an adiabatic cycle by threading one flux quantum $\Delta\Phi_\parallel = \Phi_0$ through the cylinder. The full cycle shifts the electronic occupations by exactly ℓ_{mag} and maps the final electronic state back onto the initial state. A single electron is pumped from one edge to the other, or equivalently the centre-of-mass position is displaced by ℓ_{mag}. The topology of the system protects the quantised electronic motion along the cylinder from perturbations that do not close the energy gap between the ground band and the excited ones.

In recent years, there have been a few realisations of cylindrical geometry using the internal states of cold atoms to encode a cyclic dimension. Li *et al* [244] exploits four internal levels, assembled in two pairs that form two minimal planar two-dimensional Hall systems using two-photon Raman transitions. Microwave fields connect the edges of the two planar systems, synthesising a Hall cylinder, with a plaquette size of half the length associated with the net momentum transfer of the Raman transitions. An axial field is tunable in this implementation. Han *et al* [245] considers a fermionic one-dimensional lattice, coherently manipulating three hyperfine levels while the

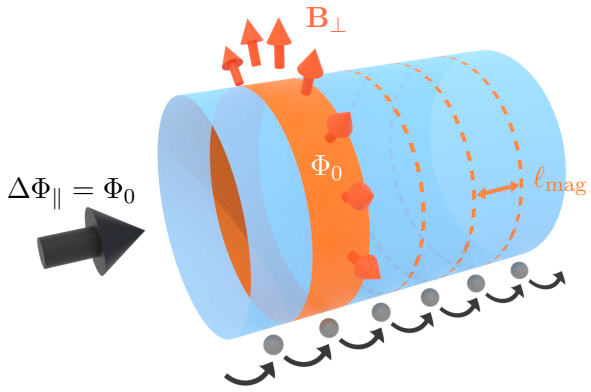

Figure 6.1 – Scheme of a two-dimensional electronic system in a cylindrical geometry, with a radial $\mathbf{B}_\perp$ magnetic field, yielding a quantum Hall effect, and a longitudinal $\mathbf{B}_\parallel$ magnetic field, producing a magnetic flux $\Phi_\parallel$ threading the cylinder. The orange area, pierced by one magnetic flux quantum Φ_0, defines the length ℓ_{mag} separating localised electronic states. The threading of one flux quantum $\Delta\Phi_\parallel = \Phi_0$ shifts electron occupations, causing electrons to be pumped from one edge to the other.

other levels are kept far off-resonant. The implementation of the radial magnetic field also derives from two-photon transitions that couple the three states with individual control of the phases and coupling strengths. The momentum transfer of the Raman processes is adjusted to induce a uniform phase per plaquette that is commensurate with the lattice spacing. The properties of the system are probed via quench dynamics. Liang *et al* [246] also considers a one-dimensional lattice and implements a synthetic cylinder using the three levels of the electronic ground state manifold of rubidium atoms in $|F = 1\rangle$, rendered insensitive to fluctuations of the magnetic field by continuous dynamical decoupling [247]. The commensurability of the acquired phase per plaquette is controlled by the net momentum transfer of the Raman transitions through the use of a tunable laser.

Similarly to some of these experiments, we first imagined using three cyclically-coupled magnetic sublevels ($m = -J$, $-J+1$ and $-J+2$, for example) of the electronic ground state manifold of dysprosium atoms. In this configuration, two-photon optical transitions induce hopping between the three states with spatially-varying phases, thus implementing a radial magnetic field in a cylindrical system, infinite along a spatial dimension and cyclic along a synthetic dimension of three sites. The other magnetic sublevels are lifted away from resonance using a non-linear light shift, induced by an off-resonant circularly-polarised beam. However, in the absence of a technique such as continuous dynamical decoupling, numerical simulations for experimentally reasonable parameters predict that the magnetic fluctuations on the order of 0.4 mG on our experiment substantially alter the band structure and the spin composition of the states of the ground band. The ground band is not flat and becomes asymmetric. Even if the topological invariant of the ground band protects the quantisation of transport, we expect significant fluctuations of local

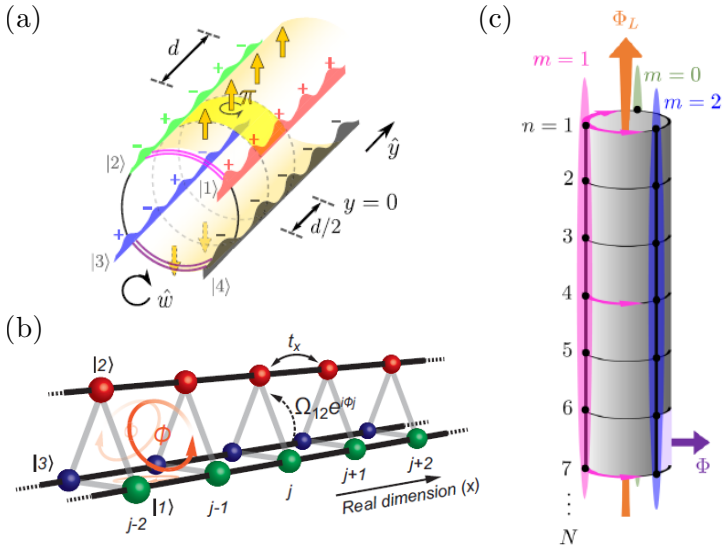

Figure 6.2 – Previous realisations of Hall cylinders using internal states to engineer both the cyclic dimension consisting of three or four coupled sites and the artificial gauge field. Figures extracted from Li *et al* [244] (a), Han *et al* [245] (b) and Liang *et al* [246] (c).

properties such as the Berry curvature, which complicates our understanding of Bloch oscillations or geometrical pumping. From a technical point of view, the coupling of the three magnetic sublevels is very asymmetric due to the Clebsch-Gordan coefficients. More specifically, it requires a high laser intensity to couple the states $|-J\rangle$ and $|-J+2\rangle$, which increases the trapping (or anti-trapping) effect of the beam. Unwanted transitions, that are however favoured by the Clebsch-Gordan coefficients, can affect the atoms for large coupling strengths. For these reasons, we turned to another scheme, whose basic idea has been presented in Chapter 5. The observables of interest are insensitive to magnetic field fluctuations and the band structure is favourable with a flat ground band and large energy gaps, for reasonable coupling strengths.

We first describe the laser configuration that produces the required spin-changing processes. We remind the form of the Hamiltonian at low energy. Following the approach to topological pumping described in Section 4.4, we describe the topological properties of the system and how to access them in our experimental realisation. We present the parameters that control the quantum state. In addition, we show bandgap measurements that probe the first excitations of our system and highlight the peculiar properties of the engineered Hall cylinder. We then perform a series of experiments to measure the transverse response of the system and probe the topology of the system from different points of view. On one hand, under the application of a force along the spatial dimension, we observe a winding along the cyclic synthetic dimension in two related experiments. On the other hand, we study the response to the threading of an axial flux, equivalent to an electromotive force along the synthetic dimension, which realises the thought experiment first envisioned

by Laughlin. Our observations are consistent with the non-trivial quantisation of the topological invariant of the ground band, the first Chern number. We also access local properties of the system via geometrical pumping, related to the Berry curvature. Finally, these measurements are validated by a study of the adiabaticity of the responses when the parameters are changed.

6.1 Experimental setup

For the experiments presented in this Chapter, we use a thermal gas of about 4×10^4 atoms, at a temperature of $T = 0.54(3)\,\mu\text{K}$. We emphasise that the large number of atoms acts only as an averaging mechanism and we remain in a regime of single-body physics. Indeed, the interactions between atoms are negligible for the corresponding atomic density on the timescale of our measurements. A magnetic field is aligned along $\mathbf{z}$, with a norm of $231(1)\,\text{mG}$, and induces a linear Zeeman splitting $\delta_z = 2\pi \times 401(2)\,\text{kHz}$ that lifts the degeneracy between the magnetic sublevels m (with integer m with $-J \leq m \leq J$) of the electronic ground state manifold. Spin transitions of first and second order, coupling nearest- and next-nearest-neighbour magnetic sublevels, as required in the protocol of Chapter 5, are implemented with two-photon optical transitions, using a pair of laser beams, counter-propagating along $\mathbf{x}$, as depicted in Fig. 6.4(a). The atoms evolve in three dimensions, but the spin-orbit coupled dynamics, induced by the net momentum kick associated with spin-changing transitions, are limited to the x-direction. The dynamics along the two other axes are governed by the trapping (or anti-trapping) effect induced by the focused laser beams and by gravity only and are separable from the spin-orbit coupled dynamic along $\mathbf{x}$. As a consequence, we can consider our physical system as a one-dimensional one.

Each beam is linearly polarised along $\mathbf{e}_1 = \cos\theta\,\mathbf{e}_z + \sin\theta\,\mathbf{e}_y$ and $\mathbf{e}_2 = \cos\theta\,\mathbf{e}_z - \sin\theta\,\mathbf{e}_y$ for the laser beams 1 and 2, which propagate along $\mathbf{x}$ and $-\mathbf{x}$ respectively. They are represented in Fig. 6.4(b). Their waist $w \simeq 60\,\mu\text{m}$ is much larger than the rms size $\sigma \simeq 3\,\mu\text{m}$ of the atomic gas, such that the light intensity can be considered uniform. The laser frequencies are set in the vicinity of the atomic resonance of wavelength $\lambda = 626.1\,\text{nm}$, with the associated wavevector $k = 2\pi/\lambda$, coupling the electronic ground state to an excited level with total angular momentum $J' = J + 1$. We note at this point that the bias magnetic field along $\mathbf{z}$ is large enough to prevent Bragg processes, that couple different momentum states while keeping the spin state unchanged. More precisely, the magnetic Zeeman splitting verifies the condition $\delta_z \simeq 128 E_{\text{rec}}/\hbar \gg \hbar(2k)^2/(2M) = 4E_{\text{rec}}/\hbar$, the right term being the kinetic energy difference between an atom at rest and an atom with shifted momentum $\pm 2k$ in the same spin state.

6.1.1 From a Hall ribbon...

This set of laser beams has been used in our group to realise a Hall ribbon [46], before the work presented here. We briefly describe the experiment that probed the topology of a two-dimensional system of coordinates (x, m) with sharp edges along the synthetic axis at $m = \pm J$. Two-photon Raman transitions are resonant with processes coupling nearest-neighbour spin states $m \to m + 1$, with a net momentum

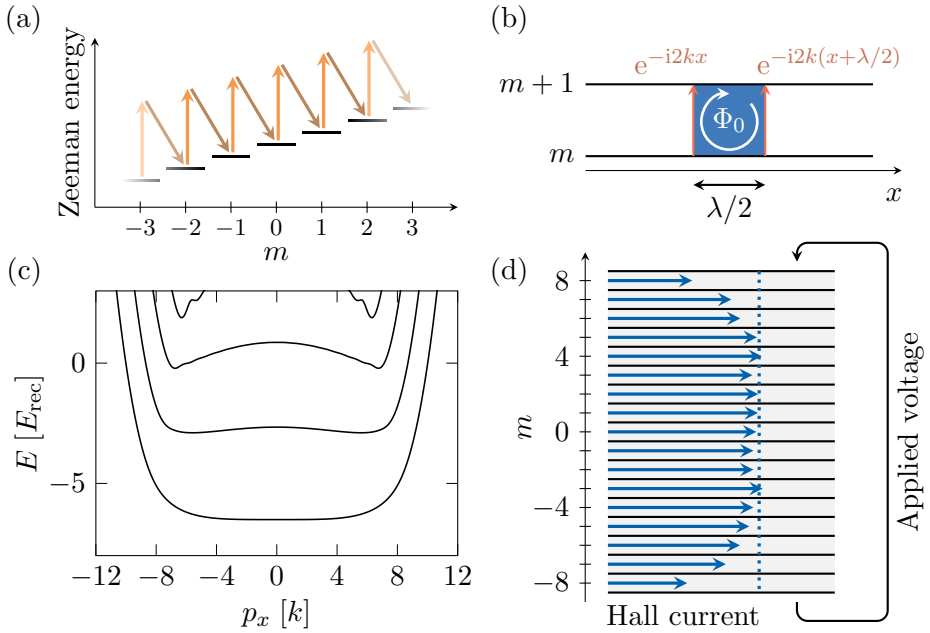

Figure 6.3 – Realisation of an atomic Hall ribbon. Panel (a): Two-photon optical transitions induced by the interference of two counter-propagating laser beams, coupling all neighbouring spin states. Panel (b): Resulting Hall ribbon with (x, m) coordinates. We focus on two m states and show the unit cell pierced by a magnetic flux quantum Φ_0 in blue. Spatially-dependent hopping phases associated with the process $m \to m+1$ are indicated in red. Panel (c): Energy spectrum of the synthetic Hall ribbon. Panel (d): Measured local Hall currents along x under the effect of a potential along the synthetic axis. We observe a transverse response, consistent with a quantised Hall response in the bulk of the system, close to $m = 0$, indicated by a vertical dashed blue line.

kick $-2k$, as shown in Fig. 6.3(a). The resulting spatially-varying hopping phases, highlighted in Fig. 6.3(b), are equivalent to Aharonov-Bohm phases associated with an artificial gauge field. They define a unit cell of shape $\Delta x \times \Delta m = \lambda/2 \times 1$ which is pieced by a magnetic flux quantum. Using a succession of unitary transformations and approximations that we will derive in detail in the following Sections for the atomic Hall cylinder, the total Hamiltonian reads:

$$\begin{aligned} H =& \frac{\hbar^2(p_x - 2k\hat{J}_z)^2}{2M} + V(x) + B_z\frac{\hat{J}_z^2}{J^2}, \\ V(x) =& -t\left[\frac{\hat{J}_+}{J} + \text{hc}\right]. \end{aligned} \tag{6.1}$$

We define the coupling strength t from the intensities of the two laser beams and the strength B_z of the quadratic $\hat{J}_z^2$ term, which stems from the angle of linear polarisation θ. A key feature of this Hamiltonian is that the momentum $p_x = Mv_x/\hbar + 2k\hat{J}_z$ is a conserved quantity, that originates from the correlation between kicks along x and

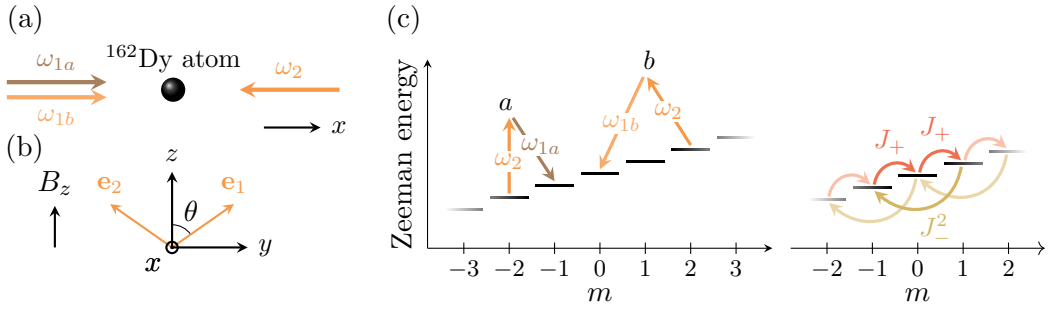

Figure 6.4 – Description of the laser setup and spin couplings. Panel (a): Scheme of an atom subjected to two laser beams, counter-propagating along **x**. The frequencies of the beams are detuned from the optical transition at 626.1 nm. The beam propagating along +**x** contains two frequency components, that interfere with the second beam, such that they are resonant with processes changing the spin by ±1 and ±2 respectively. Panel (b): Representation of the linear polarisation angles of the two laser beams, parametrised by an angle θ from the z axis defined as the direction of the bias magnetic field B_z (aligned with the gravity axis). Panel (c): Optical transitions induced by the two-photon processes involving either of the two sets of counter-propagating laser beams. They induce $\hat{J}_\pm$ and $\hat{J}_\pm^2$ transitions between all nearest- and next-nearest-neighbour spin states.

hopping along m. For the choice of linear polarisation angle $\theta = 45°$ and a positive detuning from the transition, the quadratic term compensates the curvature of the ground band, which becomes quasi-flat. The band structure, shown in Fig. 6.3(c), strongly resembles Landau levels in the presence of edges.

The topology of the system can be probed by applying a force along the synthetic dimension m by adjusting the laser frequency difference and measuring the transverse response along the real dimension x. In the presence of gapless edges, the topological character of the ground band cannot be probed as it is a global quantity, but key signatures are observable away from the edges, in the gapped bulk region. In this realisation of an atomic Hall ribbon, a central region hosts bulk physics due to the large size of the synthetic dimension, which derives from the large total angular momentum $J = 8$. The local topology can be probed by measuring Hall currents that characterises the local response to a force, as shown in Fig. 6.3(d). It depends on the local properties of the system as it is not a topologically-protected quantity like the Chern number. Still, we observe that the Hall current approaches its quantised value over a region centred around $m = 0$, far from the edges at $m = \pm J$. As we have seen in Chapter 4, the study of bulk physics with a transverse response characterised by a topological invariant is facilitated in the cylindrical geometry where edges are absent. In this case, it is possible to measure the Chern number of the ground band by probing the global transverse response to a force.

6.1.2 ...to a Hall cylinder

We consider a modification of the optical setup presented for the Hall ribbon, to engineer an atomic Hall cylinder. The configuration of laser frequencies now ensures that the atoms undergo a momentum kick $-2k$ upon either resonant process $m \to m+1$ or $m \to m-2$. We immediately see that the momentum p_x is no longer a conserved quantity, compared to the case of a Hall ribbon, where we have the first process only. However, both processes conserve the quantity $Mv_x/\hbar + 2kr$ with $r \equiv m \,(\mathrm{mod}\, 3)$, which defines a quasi-momentum with a periodicity $6k$ and is at the heart of our implementation of a Hall cylinder.

The laser 2 is monochromatic at frequency ω_2 while the laser 1 has two frequency components ω_{1a} and ω_{2a}, close to $\omega_2 - \delta_z$ and $\omega_2 + 2\delta_z$, that induce first- and second-order spin couplings respectively. The resonant processes induced by the laser beams are shown in Fig. 6.4(c). The laser beams are red detuned from the resonance by $\Delta_0 \simeq -2\pi \times 22\,\mathrm{GHz}$. The two beams and the two frequency components contribute to a spin-independent light shift, that tends to confine the atoms in high-intensity regions, and to a quadratic light shift of the magnetic sublevels proportional to $(3\cos^2\theta - 1)m^2$, which we cancel by setting the polarization angle to $\theta = \mathrm{acos}\left(1/\sqrt{3}\right) \simeq 55°$. The detailed derivation of the Hamiltonian is given in the next Section.

6.2 Derivation of the Hamiltonian

The Hamiltonian that determines the dynamics of an atom has the expression:

$$H = H_0 + V_{\mathrm{LS}}, \tag{6.2}$$

where H_0 contains the kinetic and Zeeman terms and V_{LS} describes the light-matter interaction. Using the general formula for off-resonant light in Eq. 1.19, these terms take the form:

$$\begin{aligned} H_0 &= \frac{M\mathbf{v}^2}{2} + \hbar\delta_z \hat{J}_z, \\ V_{\mathrm{LS}} &= \gamma \left[\alpha_0 |\mathbf{E}|^2 \hat{\mathbb{1}} - \mathrm{i}\alpha_1 (\mathbf{E}^* \times \mathbf{E}) \frac{\hat{\mathbf{J}}}{2J} \right. \\ &\qquad \left. + \alpha_2 \frac{3[(\mathbf{E}^* \cdot \hat{\mathbf{J}})(\mathbf{E} \cdot \hat{\mathbf{J}}) + (\mathbf{E} \cdot \hat{\mathbf{J}})(\mathbf{E}^* \cdot \hat{\mathbf{J}})] - 2|\mathbf{E}|^2 \hat{\mathbf{J}}^2}{2J(2J-1)} \right], \end{aligned} \tag{6.3}$$

where δ_z is the magnetic Zeeman angular frequency, $\mathbf{E}$ is the light field amplitude, and γ is the coefficient that converts light intensity in light coupling amplitude, based on the characteristics of the optical transition and of the detuning of the laser from resonance:

$$V_0 = \gamma I = \frac{3\pi c^2 \Gamma}{2\omega_0^3} \frac{I}{\Delta_0}, \tag{6.4}$$

with Γ the transition linewidth, ω_0 the laser frequency, Δ_0 the detuning to resonance and I the laser intensity. The total light field amplitude is the sum of the contributions of the three laser beams:

$$\begin{aligned} \mathbf{E}_{1a} &= E_{1a} \mathrm{e}^{\mathrm{i}(kx - \omega_{1a}t + \varphi_{1a})} \mathbf{e}_1, \\ \mathbf{E}_{1b} &= E_{1b} \mathrm{e}^{\mathrm{i}(kx - \omega_{1b}t + \varphi_{1b})} \mathbf{e}_1, \\ \mathbf{E}_2 &= E_2 \mathrm{e}^{\mathrm{i}(-kx - \omega_2 t + \varphi_2)} \mathbf{e}_2, \end{aligned} \tag{6.5}$$

where E_s, ω_s, φ_s are the field amplitude, angular frequency and phase for laser beam s (with $s = 1a$, $1b$ or 2). The relative detunings of the beams are chosen such that the interferences of beam 2 with beam $1a$ and $1b$ are close to resonance with two-photon optical transitions changing the spin m by ± 1 and ± 2 respectively. They are defined as:

$$\begin{aligned} \omega_{1a} - \omega_2 &= -\delta_z + \delta_a, \\ \omega_{1b} - \omega_2 &= 2\delta_z + \delta_b, \end{aligned} \tag{6.6}$$

with δ_a and δ_b the detunings from the two resonances.

The explicit derivation of the Hamiltonian is rather cumbersome. For clarity, we identify different contributions that are treated separately. The terms in the Hamiltonian originate either from each beam independently (in which case they are proportional to the beam intensity and there is no spatial or time dependence) or from the interference between two of the three beams. Among these terms, we separately treat the diagonal terms in m, involving spin operators that are multiples of $\hat{J}_z$, and the off-diagonal terms. We first apply a unitary transformation

$$U = \mathrm{e}^{\mathrm{i}\delta_z t \hat{J}_z}, \tag{6.7}$$

which amounts to considering the spin states in a basis that rotates at the angular frequency δ_z around z. This cancels out the Zeeman term in the total Hamiltonian and the Hamiltonian is transformed as:

$$H \to UHU^\dagger, \tag{6.8}$$

which only affects off-diagonal terms because all diagonal terms commute with $\hat{J}_z$ and thus with U. All off-diagonal operators that appear in the light-matter Hamiltonian can be written as linear combinations of powers of the spin ladder operators $\hat{J}_\pm$, possibly multiplied by powers of $\hat{J}_z$ that anyway commutes with U. The ladder operators transform as:

$$\hat{J}_\pm \to \mathrm{e}^{\pm \mathrm{i}\delta_z t} \hat{J}_\pm. \tag{6.9}$$

We then apply the rotating wave approximation (RWA), which neglects the fast oscillating terms that appear in this rotating frame. This approximation is valid as long as $|\delta_s| \ll \delta_z$ ($s = a$ or b) and $|V_s/\hbar| \ll \delta_z$ ($s = 1a$, $1b$ or 2). We set $\delta_z \simeq 128 E_{\mathrm{rec}}/\hbar$ and we choose the potentials on the order of a few times the recoil energy and vary the detunings from resonance up to a dozen times the recoil angular frequency, which fulfils the criteria of the RWA. For the diagonal terms, which are not modified under the unitary transformation, we neglect all time-dependent terms. We are left with three terms that originate from each beam independently:

$$\begin{aligned} V_{\mathrm{diag}} &= (V_{1a} + V_{1b} + V_2) \left[\left(\alpha_0 + \alpha_2 \frac{J+1}{2J-1} \frac{3\sin^2\theta - 1}{2} \right) \hat{\mathbb{1}} \right. \\ &\qquad \left. + \alpha_2 \frac{3}{2J(2J-1)} (3\cos^2\theta - 1) \hat{J}_z^2 \right] \\ &= (V_{1a} + V_{1b} + V_2) \alpha_0 \hat{\mathbb{1}}, \end{aligned} \tag{6.10}$$

where V_s is the light coupling amplitude for beam s ($s = 1a$, $1b$ or 2), from Eq. 6.4. The simplification from the first equality to the second assumes a polarisation angle

$\theta = \mathrm{acos}\left(1/\sqrt{3}\right)$, which cancels out the $\hat{J}_z^2$ term. The scalar polarisability α_0 for the optical transition at 626 nm, from J to $J{+}1$, equals $\alpha_0 = (2J{+}3)/(3(2J{+}1)) = 19/51$. For red detuned laser beams ($\Delta_0 < 0$), given the sign of α_0, the diagonal part of the potential is attractive.

For the non-diagonal terms, we keep only two types of terms: those that come from the interference of laser $1a$ and 2 and change the spin m by ± 1 and those that originate from the interference of laser $1b$ and 2 and modify the spin m by ± 2. Indeed, after the unitary transform, the other terms necessarily oscillate at an angular frequency multiple of δ_z and vanishes in the RWA. Among the remaining terms, we neglect the fast oscillating terms at angular frequencies $\simeq 2\delta_z$ (from the process (a)) or $\simeq 4\delta_z$ (from the process (b)) and obtain:

$$\begin{aligned} V_{\text{non-diag}} = &- t_a \left[\frac{\hat{J}_+}{J} \mathrm{e}^{-\mathrm{i}2kx} \mathrm{e}^{\mathrm{i}\delta_a t} \mathrm{e}^{\mathrm{i}(\varphi_{1a} - \varphi_2 + \pi/2)} + \mathrm{hc} \right] \\ &- t_b \left[\frac{\hat{J}_-^2}{J^2} \mathrm{e}^{-\mathrm{i}2kx} \mathrm{e}^{\mathrm{i}\delta_b t} \mathrm{e}^{\mathrm{i}(\varphi_{1b} - \varphi_2)} + \mathrm{hc} \right]. \end{aligned} \tag{6.11}$$

The phase difference between the two processes can be gauged away such that we retain hereafter a single phase $\varphi \equiv \varphi_{1a} - \varphi_2 + \pi/2 = \varphi_{1b} - \varphi_2$. The coupling strengths t_a and t_b are given by:

$$\begin{aligned} t_a &= \sqrt{V_{1a} V_2} \frac{J(2J+3)}{4(J+1)(2J+1)} \sin(2\theta), \\ t_b &= \sqrt{V_{1b} V_2} \frac{J^2}{4(J+1)(2J+1)} \sin^2\theta. \end{aligned} \tag{6.12}$$

The time dependence of the non-diagonal part of the Hamiltonian can be suppressed with the right choice of transformations. First, we consider the motion of the atoms in a reference frame moving at velocity v^* relative to the laboratory frame. Then, we apply a second gauge transformation defined by the unitary operator:

$$U = \mathrm{e}^{-\mathrm{i}\Delta t J_z}. \tag{6.13}$$

The non-diagonal terms are transformed as follows:

$$\begin{aligned} V_{\text{non-diag}} = &- t_a \left[\frac{\hat{J}_+}{J} \mathrm{e}^{-\mathrm{i}2kx} \mathrm{e}^{\mathrm{i}\delta_a t} \mathrm{e}^{\mathrm{i}\varphi} \mathrm{e}^{-\mathrm{i}\Delta t} \mathrm{e}^{-\mathrm{i}2kv^* t} + \mathrm{hc} \right] \\ &- t_b \left[\frac{\hat{J}_-^2}{J^2} \mathrm{e}^{-\mathrm{i}2kx} \mathrm{e}^{\mathrm{i}\delta_b t} \mathrm{e}^{\mathrm{i}\varphi} \mathrm{e}^{\mathrm{i}2\Delta t} \mathrm{e}^{-\mathrm{i}2kv^* t} + \mathrm{hc} \right]. \end{aligned} \tag{6.14}$$

The time-dependence of the two terms is cancelled out by the choice of parameters:

$$\begin{aligned} v^* &= \frac{2\delta_a + \delta_b}{6k}, \\ \Delta &= \frac{\delta_a - \delta_b}{3}, \end{aligned} \tag{6.15}$$

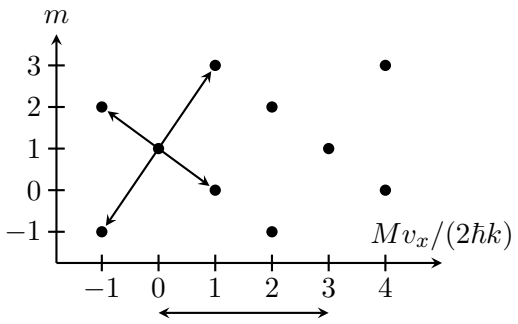

Figure 6.5 – Spin-velocity distribution in the laboratory frame. Accessible states via the processes (a) and (b), in a two-dimensional parameter space, defined by the spin state m (with $-J \leq m \leq J$ integer) and the velocity v_x along $\mathbf{x}$. We show the coupling transitions that are induced by the processes (a) and (b), for the spin-momentum state $|m = 1, Mv_x = 0\rangle$ that corresponds to $n_a = -n_b = 3$.

and the total Hamiltonian in the moving frame becomes:

$$\begin{aligned} H =& \frac{Mv_x^2}{2} + V(x) + \hbar\Delta\hat{J}_z, \\ V(x) =& -t_a\left[\frac{\hat{J}_+}{J}\mathrm{e}^{-\mathrm{i}2kx}\mathrm{e}^{\mathrm{i}\varphi} + \mathrm{hc}\right] \\ & -t_b\left[\frac{\hat{J}_-^2}{J^2}\mathrm{e}^{-\mathrm{i}2kx}\mathrm{e}^{\mathrm{i}\varphi} + \mathrm{hc}\right], \end{aligned} \tag{6.16}$$

where we have removed the momentum components along y and z from the kinetic energy term, because of the separable dynamics along these axes. In the moving frame, with this unitary transformation, the potential $V(x)$ does not depend on time and contains the spin-changing transitions with x-dependent hopping phases. The two parameters (v^*, Δ) can be controlled by varying the relative frequencies of the three laser beams. The parameter Δ plays the role of a Zeeman field. When Δ is set to zero, this Hamiltonian reduces to the one of Eq. 5.20 in Section 5.4. We recall that this Hamiltonian is invariant under the discrete magnetic translation, which leads to the conservation of the quasi-momentum: $q_x \equiv Mv_x/\hbar + 2k\hat{J}_z \,(\mathrm{mod}\, 6k)$, defined over the magnetic Brillouin zone $-3k \leq q_x < 3k$ of size $6k$.

A time-dependent frame velocity v^* results in an inertial force $F_x = M\partial_t v^*$ along the real dimension x, in the moving frame. We also notice that, in this picture, fluctuations in the magnetic field along z translate into fluctuations in the Zeeman field Δ only, but do not affect v^*.

The potential $V(x)$ of the Hamiltonian in the laboratory frame couples together spin states whose spin projection m varies by ± 1 (process (a)) or ± 2 (process (b)) and whose momentum differs by $\pm 2k$. As a consequence, for atoms initially at rest and polarised in $|m = -J\rangle$, the available states under these couplings are the spin-momentum states $\{|m, Mv_x\rangle\}$ satisfying $m = -J + n_a - 2n_b$ and $Mv_x = -2\hbar k(n_a + n_b)$, with n_a, n_b integers and $-J \leq -J + n_a - 2n_b \leq J$. We note

that this is valid in the laboratory frame, whatever the frequency detunings, and thus whatever the parameters (v^*, Δ). Indeed, the set of available states derives from the spin-orbit coupling and the restriction to the processes (a) and (b) in the RWA. As a consequence, we expect the observation of peaks in the spin-velocity distributions, at fixed positions in the laboratory frame. The pattern of these peaks is displayed in Fig. 6.5, along with the allowed transitions for the spin-momentum state $|m = 1, Mv_x = 0\rangle$.

Throughout this chapter, numerical simulations of the band structure and of the dynamics of the atoms are performed for comparison with experimental observations. For that purpose, we consider the Hamiltonian of Eq. 6.16 after making a gauge transformation acting on position instead of time:

$$U = \mathrm{e}^{\mathrm{i}2kx\hat{J}_z}. \tag{6.17}$$

This gauge transformation transfers the momentum kick associated with a spin change as an artificial vector potential that depends on the spin projection along z. We obtain the spin-orbit coupled Hamiltonian:

$$\begin{aligned} H =& \frac{\hbar^2(p_x - 2k\hat{J}_z)^2}{2M} + V(x) + \hbar\Delta\hat{J}_z, \\ V(x) =& -t_a\left[\frac{\hat{J}_+}{J}\mathrm{e}^{\mathrm{i}\varphi} + \mathrm{hc}\right] \\ & - t_b\left[\frac{\hat{J}_-^2}{J^2}\mathrm{e}^{-\mathrm{i}6kx}\mathrm{e}^{\mathrm{i}\varphi} + \mathrm{hc}\right]. \end{aligned} \tag{6.18}$$

The spatially-dependent hopping phase involved in the process (a) is suppressed, while the process (b) couples spin states $m \leftrightarrow m \pm 2$ with a momentum kick $\pm 6k$. By setting the coupling t_b to zero, we recover the Hamiltonian corresponding to the Hall ribbon with coordinates (x, m) and an orthogonal magnetic field $2\hbar k$ for a particle of effective charge $q = 1$. In this picture, the process (b) term couples momentum states with momentum difference $K = \pm 6k$, which is reminiscent of the approach developed in Section 4.3.1. We expect this coupling term to induce a periodicity of the wavefunctions along m of period $L_r = 3$, at the origin of our implementation of a cylinder with a radial magnetic field.

The potential $V(x)$ is periodic along x, with a period $\lambda/6$. Using Bloch theorem, we write the wavefunction in real space as:

$$\psi_{q_x}(x) = \mathrm{e}^{\mathrm{i}q_x x}u_{q_x}(x), \tag{6.19}$$

indexed by the quasimomentum q_x defined on a Brillouin zone of size $6k$, with $u_{q_x}(x)$ a x-periodic function of period $2\pi/(6k)$. We carry out a Fourier series development of the periodic function u_{q_x} which gives:

$$\psi_{q_x}(x) = \sum_n \mathrm{e}^{\mathrm{i}(q_x + n6k)x}c_{q_x,n}, \tag{6.20}$$

with complex coefficients $c_{q_x,n}$, indexed by integers n. In fact, these terms are also indexed by the spin state m as we have only considered the spatial dependence

of the state in the above expression of the wavefunction. Writing the Schrödinger equation associated with the total Hamiltonian from Eq. 6.18 for a quasimomentum q_x, we obtain a set of coupled linear equations for the coefficients $c_{q_x,n,m}$. The kinetic term with spin-orbit coupling and the diagonal terms of the light-matter interaction are diagonal in both n and m. The terms of the process (a) do not modify the Fourier index n because they are not associated with a net momentum kick in this picture, and they are diagonal in n. Process (b) is associated with a net momentum kick $\pm 6k$, which amounts to changing the index n by ± 1. The $\hat{J}_\pm^2$ terms appear in off-diagonal terms, close to the diagonal blocks. Overall, the set of differential equations governing the $c_{q_x,n,m}$ coefficients is written as a matrix:

$$\begin{array}{c} \vdots \\ \left[\begin{array}{c|c|c} E(q_x,n-1,\hat{J}_z)\hat{\mathbb{1}} & -t_b\dfrac{\hat{J}_-^2}{J^2}\mathrm{e}^{\mathrm{i}\varphi} & 0 \\ -t_a\left(\dfrac{\hat{J}_+}{J}\mathrm{e}^{\mathrm{i}\varphi}+\mathrm{hc}\right) & & \\ \hline -t_b\dfrac{\hat{J}_+^2}{J^2}\mathrm{e}^{-\mathrm{i}\varphi} & E(q_x,n,\hat{J}_z)\hat{\mathbb{1}} & -t_b\dfrac{\hat{J}_-^2}{J^2}\mathrm{e}^{\mathrm{i}\varphi} \\ & -t_a\left(\dfrac{\hat{J}_+}{J}\mathrm{e}^{\mathrm{i}\varphi}+\mathrm{hc}\right) & \\ \hline 0 & -t_b\dfrac{\hat{J}_+^2}{J^2}\mathrm{e}^{-\mathrm{i}\varphi} & E(q_x,n+1,\hat{J}_z)\hat{\mathbb{1}} \\ & & -t_a\left(\dfrac{\hat{J}_+}{J}\mathrm{e}^{\mathrm{i}\varphi}+\mathrm{hc}\right) \end{array}\right] \\ \vdots \end{array} \begin{array}{c} \\ n-1 \\ \\ n \\ \\ n+1 \\ \\ \end{array} \tag{6.21}$$

where we have only represented the Hilbert space for three indices $n-1$, n and $n+1$. Each block has a size $(2J+1)\times(2J+1)$ as, for a given quasimomentum q_x and index n, there are $2J+1$ coefficients $c_{q_x,n,m}$ that correspond to the different spin states $-J \leq m \leq J$. The diagonal of the matrix contains the kinetic terms:

$$E(q_x,n,\hat{J}_z) = \frac{\hbar^2(q_x+6kn-2k\hat{J}_z)^2}{2M}. \tag{6.22}$$

The matrix is infinite as the index n can a priori take any value. However, for realistic states, only some indices contribute significantly. In practice, we truncate the number of indices to $n_{\max}=11$ and the size of the Hilbert space is then $n_{\max}\times(2J+1)=187$. We check that increasing $n_{\max}$ does not modify the band spectrum and the dynamics.

As a side remark, the simulation of the dynamics of the atoms beyond RWA requires other theoretical tools, such as Floquet theory, which treats time-oscillating terms in a similar way to the Bloch theorem for spatially-periodic potentials.

6.3 Low-energy approximation

We briefly remind the form of the low-energy dynamics, restricting the system to the three coherent states $|\theta,\phi\rangle$ pointing along the equator ($\theta=\pi/2$) at angles

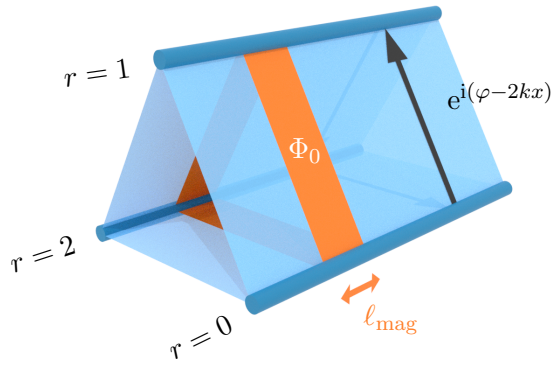

Figure 6.6 – Low-energy emergent cyclic dimension. Three sites $r = 0$, 1 and 2 are cyclically coupled with x-dependent hopping phases $\varphi - 2kx$. The spatially-dependent hopping phases are equivalent to an Aharonov-Bohm phase that is acquired when a particle evolves on a cylinder, and correspond to an artificial radial magnetic field $\mathbf{B}_\perp$. The length ℓ_{mag} is defined as the x-distance that delimits a slice of the cylinder whose radial surface is pierced by one flux quantum Φ_0.

$\phi = 0$, $2\pi/3$ and $4\pi/3$. We follow the treatment in Section 5.4 and get the effective potential:

$$V_{\text{eff}}(x) = -2t \sum_{\phi=0,\frac{2\pi}{3},\frac{4\pi}{3}} \cos(2kx - \phi) \langle\phi|\phi\rangle \,, \tag{6.23}$$

where $t = t_a + t_b(1 - 1/(2J))$. As already pointed out, this is reminiscent of the potential involved in the Harper equation when solving the Hofstadter model of a charged particle evolving on a square lattice pierced by a magnetic field. The similarity allows us to identify the angle ϕ with the quasi-momentum q_r along a synthetic dimension denoted r. This leads to the definition of the $|r\rangle$ position states by inverse Fourier transform of the $|\phi\rangle$ states, as:

$$|r\rangle = \frac{1}{\sqrt{3}} \sum_{\phi=0,\frac{2\pi}{3},\frac{4\pi}{3}} e^{-i\phi r} |\phi\rangle \,. \tag{6.24}$$

Writing the potential using these states, the Hamiltonian contains hopping terms between neighbouring sites $|r\rangle$, with a complex x-dependent hopping phase, that simulates a radial magnetic field $B_\perp = 2\hbar k$ for a unit particle charge:

$$V_{\text{eff}}(x) = -t \sum_{r=0}^{2} \left(e^{i(\varphi-2kx)} |r+1\rangle\langle r| + \text{hc} \right) . \tag{6.25}$$

Together with the kinetic energy term $Mv_x^2/2$, it describes the motion of a particle on a cylinder discretised along its circumference, as schematically represented in Fig. 6.6. The radial magnetic field defines a length $\ell_{\text{mag}} = \lambda/6$, such that the magnetic flux

$\Phi_\perp = \ell_{\mathrm{mag}} L_r B_\perp$ through a portion of cylinder of length ℓ_{mag} equals the flux quantum $\Phi_0 = h$, for a particle of effective charge $q = 1$.

In Fig. 5.7(a), in Section 5.4, the position spectrum of the potential exhibits a periodic subwavelength modulation [248]. Within a cell of size $\lambda/2$, three energy minima are equally spaced, at a distance of $\ell_{\mathrm{mag}} = \lambda/6$, and each minimum is reached for a corresponding $|\phi\rangle$ state. This translates into modulations of the in-situ density profiles of states in the ground band. We note, that in a continuous Hall cylinder, already described in Chapter 4, the Bloch states exhibit a periodic pattern of x-period $\Delta x = L_r/\ell_m^2$ along $\mathbf{x}$. The centre-of-mass of the distribution along r is controlled by the quasimomentum q_x and the x-positions are fixed. In our system, owing to the discretisation of the synthetic dimension r, we expect dips in the density profiles and cancellations of the density only when the vortices are exactly located at a site r. Given our effective radial magnetic field, we obtain the following correspondence with the variables defined in Section 4.3:

$$\begin{aligned} B_\perp &= 2\hbar k, & K &= 6k, \\ q &= 1, & L_r &\equiv K\ell_m^2 = 3, \\ \ell_m &= \sqrt{\frac{1}{2k}}, & \ell_{\mathrm{mag}} &\equiv \Delta x = \frac{2\pi}{K} = \frac{\lambda}{6}. \end{aligned} \tag{6.26}$$

6.4 Topology of the ground band

The total Hamiltonian in Eq. 6.16 has a conserved quantity, the quasimomentum $q_x \equiv Mv_x/\hbar + 2k\hat{J}_z \,(\mathrm{mod}\, 6k)$, defined over the magnetic Brillouin zone $-3k \leq q_x < 3k$. The dynamics can thus be reduced to a Hamiltonian $H(q_x, \varphi)$ parametrised by the couple (q_x, φ) which varies on the torus $[-3k, 3k[\times[0, 2\pi/3[$. The conserved quantities q_x and φ play the role of conjugate variables to the positions along x and r respectively. As we have shown in Chapter 4, the topological character of the ground band is determined by the value of the Chern number:

$$\mathcal{C} = \frac{1}{2\pi} \int_{-3k}^{3k} \mathrm{d}q_x \int_0^{2\pi/3} \Omega_{q_x,\varphi} \mathrm{d}\varphi, \tag{6.27}$$

where we introduce the Berry curvature which characterises the local properties of the band:

$$\Omega_{q_x,\varphi} = \mathrm{i} \sum_{n\geq 1} \frac{\langle \psi^{(0)}_{q_x,\varphi} | v_x | \psi^{(n)}_{q_x,\varphi} \rangle \, \langle \psi^{(n)}_{q_x,\varphi} | v_r | \psi^{(0)}_{q_x,\varphi} \rangle - \mathrm{hc}}{(E^{(0)}_{q_x,\varphi} - E^{(n)}_{q_x,\varphi})^2}. \tag{6.28}$$

We define the velocities $v_x = \partial_{q_x} H$ and $v_r = \partial_\varphi H$ and the Bloch states $|\psi^{(n)}_{q_x,\varphi}\rangle$ of the band n, of energy $E^{(n)}_{q_x,\varphi}$. In our system, Bloch states of the same band n and quasimomentum q_x, but different φ, can be mapped on each other by a spatial translation. Hence, they share the same Berry curvature, which thus only depends on q_x. Integrating over φ, we obtain:

$$\mathcal{C} = \frac{1}{L_r} \int_{-3k}^{3k} \Omega_{q_x} \mathrm{d}q_x, \tag{6.29}$$

with $L_r = 3$ the circumference of the cylinder. For the coupling strengths t_a and t_b used in our experiments, the Berry curvature is extremely flat, equal to $1/(2k)$ for all

quasimomenta with a relative variation less than 10^{-4}. Its integral yields a non-trivial Chern number $\mathcal{C} = 1$. The flatness of the Berry curvature is a consequence of the continuous translation symmetry along x, making our system similar to continuous two-dimensional systems with flat Landau levels. In contrast, discrete lattice systems, such as Hofsdtater and Haldane models [249, 250], or previous implementations of synthetic Hall cylinders [244–246], exhibit dispersive bands with inhomogeneous Berry curvatures.

Our realisation of Laughlin's thought experiment follows the idea behind the derivation of the Chern number. We plan on performing geometric pumping with a periodic driving of φ for states of all quasimomenta q_x, prepared in the ground band, thus measuring the Berry curvature. The average of this local quantity over the magnetic Brillouin zone characterises the topological character of the ground band.

6.5 Ground state preparation

Our experimental protocols all start with the preparation of the ground state of the Hamiltonian with $t_a^{(\mathrm{exp})} = 11.5(3)E_{\mathrm{rec}}$ and $t_b^{(\mathrm{exp})} = 7.1(2)E_{\mathrm{rec}}$, at the Zeeman field $\Delta = 0$. The final coupling strengths are chosen as a compromise that originates from the experimental constraints. Their ratio t_b/t_a is close enough to the ratio $1/2$, highlighted in Chapter 5, to facilitate the interpretation of our experiments with independent dynamics along the m and r dimensions. The topological character of the ground band does not depend strongly on the coupling ratio, except for extreme situations where either of the two processes has vanishing a coupling strength, as can be seen in Fig. 6.7(a,b). However, we point out that the interpretation of some measurements using the effective model requires $t_b/t_a \simeq 1/2$. For example, spectroscopic measurements, involving not only the ground band but also the excited ones, are sensitive to the coupling ratio. In Fig. 6.7(b), we observe that the effective model predicts well the energy spectrum of the exact Hamiltonian for sufficiently large coupling t_b.

The coupling strengths are large enough to obtain flat bands, characterised by small bandwidths, which resemble the Landau levels of an infinite continuous system. Fig. 6.7(a) shows the band structure for three values of t_b. At zero coupling strength $t_b = 0$, the spin-distribution has no q_x-periodicity, which can be deduced from Eq. 6.18. The equation has no spatial periodicity as the spatially-dependent hopping phases have been included as an artificial vector potential proportional to the spin projection along z by a suitable unitary transform. It corresponds to the physics of a Hall ribbon, that we briefly presented in Section 6.1.1. In the opposite limit with a large coupling t_b, we observe that the spin structure of the ground band becomes less sharp, which complicates the measurement of the occupancy of each r state. This translates into smaller visibility of the oscillations of the populations of the r states in the lower panels. Experimentally, the flatness of the ground band facilitates the measurement of the anomalous velocity, as the group velocity cancels out. Large coupling strengths also ensure large gaps to the excited bands, which set the minimum timescale of variations of parameters to be adiabatic and thus facilitate the dynamic manipulation of quantum states. Our choice of coupling strengths derives from these competing effects. We also check that the band structure is

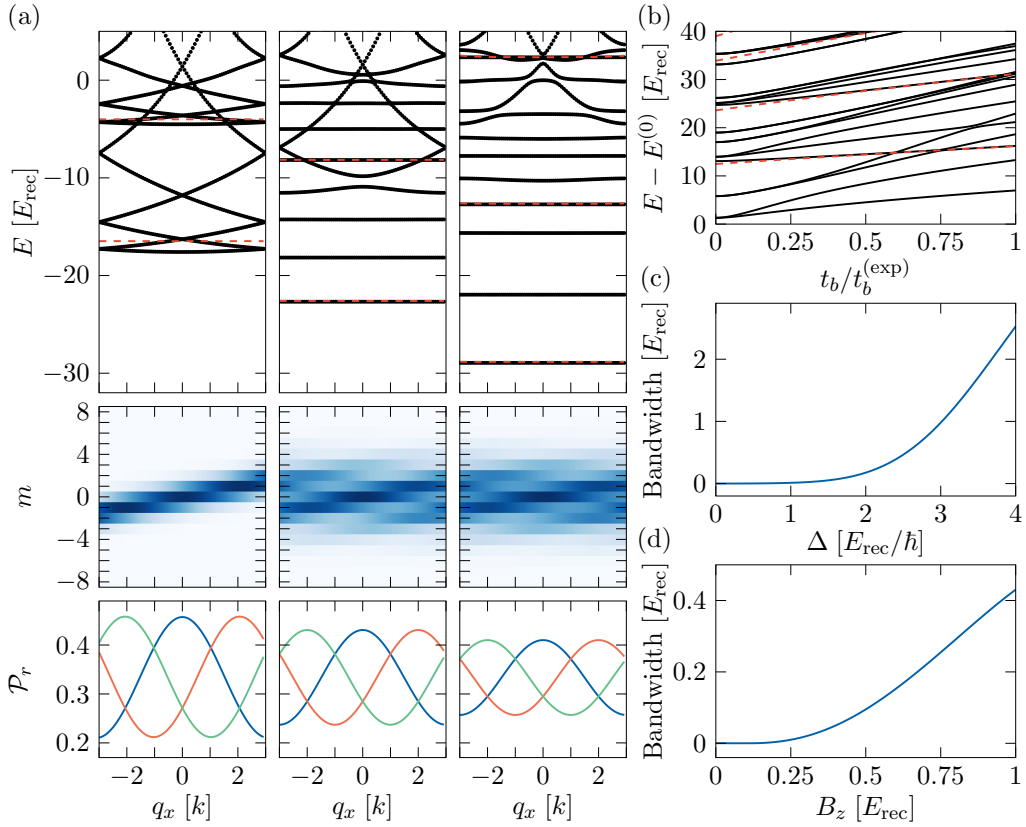

Figure 6.7 – Panel (a): Band structure (upper panels) and ground band properties (m- and r-distributions in the middle and lower panels respectively, with the states $r = 0$, 1 and 2 represented by blue, red and green lines respectively) for three values of coupling strength $t_b/t_b^{(\mathrm{exp})} = 0$, 0.5 and 1, from left to right. Panel (b): Gaps to the excited states at quasimomentum $q_x = 0$, as a function of $t_b/t_b^{(\mathrm{exp})}$. The black and dashed red lines are computed from the total Hamiltonian and the effective model respectively. Panels (c,d): Bandwidth of the ground band as a function of the Zeeman field Δ and of the strength B_z of a quadratic spin term $\hat{J}_z^2$ respectively.

only slightly modified under magnetic fluctuations along **z**, which translates into fluctuations of the Zeeman field Δ only. As an example, we show the variation of the bandwidth of the ground band as a function of the Zeeman field in Fig. 6.7(c). Typical magnetic fluctuations are below 0.4 mG, which corresponds to a Zeeman field below $0.5E_{\mathrm{rec}}/\hbar$ and marginally affects the band structure. As a final check, we consider a deviation of the linear polarisations of the beams from the angle $\mathrm{acos}\left(1/\sqrt{3}\right)$, which translates into a non-zero quadratic spin term $\hat{J}_z^2$ within RWA. In Fig. 6.7(d), we plot the bandwidth as a function of the strength B_z of this diagonal spin term. Given our precision on the estimation of the polarisation angles and the zero derivative of the bandwidth around $B_z = 0$, we assume that the quadratic term $\hat{J}_z^2$ cancels out in the following.

Initially, the atoms have a zero mean velocity $\langle v_x \rangle = 0$ in the laboratory frame.

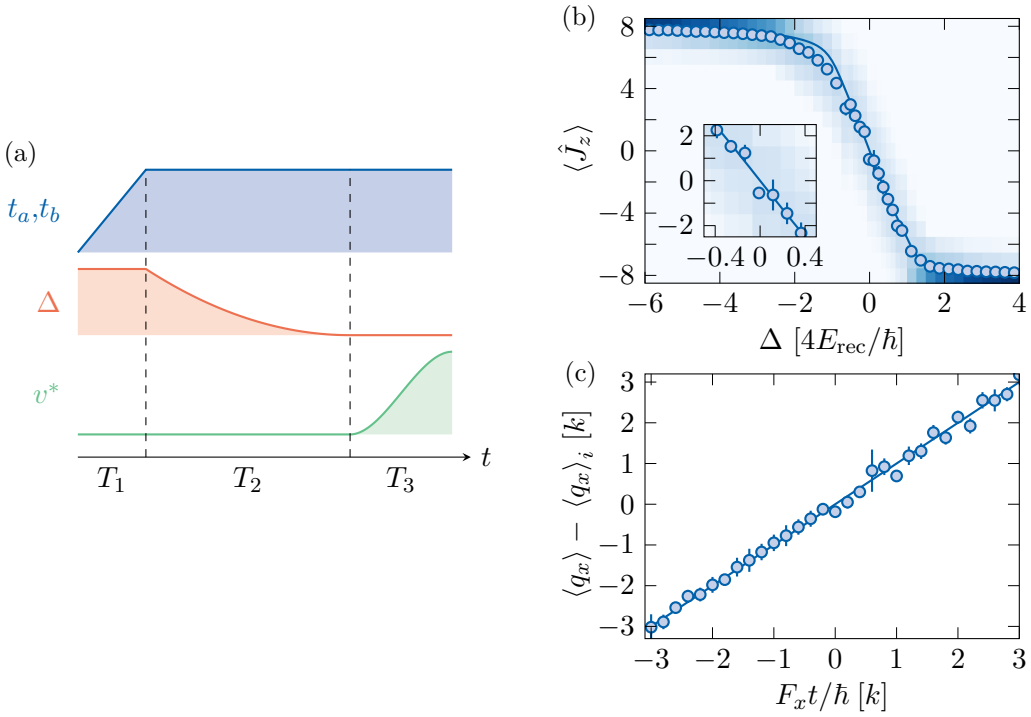

Figure 6.8 – Panel (a): Scheme of the dynamic control of the parameters (t_a, t_b, Δ, v^*) to adiabatically prepare a quasimomentum state in the ground band of the total Hamiltonian. Three steps of lengths T_1, T_2 and T_3 consist of successive ramps of the coupling strengths, then of the Zeeman field and finally of the velocity of the moving frame. Panel (b): Spin distribution Π_m and magnetisation $\langle \hat{J}_z \rangle$ as a function of the Zeeman field Δ for a fixed quasi-momentum $\langle q_x \rangle_i \simeq 2k$. The solid line represents the expected magnetisation for the ground state of the Hamiltonian of Eq. 6.16. The inset highlights the central region around $\Delta = 0$, where the relation is linear and independent of the quasimomentum. Panel (c): Evolution of the mean quasi-momentum $\langle q_x \rangle$ during a Bloch oscillation, compared to the expected law $\langle q_x \rangle (t) = \langle q_x \rangle_i + F_x t/\hbar \,(\mathrm{mod}\, 6k)$.

We set the initial laser frequencies such that the frame velocity v^* cancels, and the Zeeman field is set to $\Delta = 16E_{\mathrm{rec}}/\hbar$. Thus, the mean quasi-momentum reads $\langle q_x \rangle_i = M \langle v_x \rangle_i /\hbar + 2k \langle \hat{J}_z \rangle_i \,(\mathrm{mod}\, 6k) = 2k$. For the initial set of parameters $(v^*, \Delta) = (0, 16E_{\mathrm{rec}}/\hbar)$, the system is gapped and the theoretical ground state remains almost fully polarised in $|m = -J\rangle$ for coupling strengths ranging from zero to their final values. We first adiabatically dress the atoms by the spin couplings and increase the light intensities to their final values in $T_1 = 100\,\mu\mathrm{s}$, following a linear ramp. We then ramp the Zeeman field Δ towards zero in $T_2 = 480\,\mu\mathrm{s}$, following a quadratic profile that reaches $\Delta = 0$ with a zero slope which reduces diabatic effects. This ramp duration is a compromise to ensure adiabaticity while minimising spin-changing collisions occurring on the timescale of a few milliseconds. The minimum value of the gap to the first excited band $\Delta E_{\mathrm{min}} \simeq 5E_{\mathrm{rec}}$ sets the timescale for

adiabaticity $\tau = \hbar/\Delta E_{\min} \simeq 10\,\mu s$, much shorter than the chosen ramp duration. We confirm the adiabaticity of the successive ramps using a numerical simulation of the atomic dynamics, which predicts an overlap with the ground band after the ramp above 97%. The sequence is summarised in Fig. 6.8(a).

The adiabatic loading is experimentally verified by probing the system as a function of Δ, for a fixed reference frame $v^* = 0$. For $\Delta \neq 0$, we expect the system to exhibit a non-zero magnetisation $\langle \hat{J}_z \rangle$. Its measurement, shown in Fig. 6.8(b), is in agreement with the theory. For $\Delta = 0$, the residual fluctuations of the magnetisations are measured from shot to shot and are correlated to the signal on a magnetic probe close to the atomic gas. A deviation from the expected magnetic field translates into a contribution to the Zeeman field Δ, which linearly controls the magnetisation in the region close to $\Delta = 0$.

At this stage, the gas is loaded in the ground band of the Hamiltonian with $\Delta = 0$, with $v^* = 0$, corresponding to a mean quasimomentum $\langle q_x \rangle_i = 2k$. The final step of the state preparation is to reach the desired quasimomentum state in the ground band. We use the approach that we originally described in Section 4.4 and apply a force F_x along $\mathbf{x}$ to induce Bloch oscillations, using the laser frequencies. The dynamic control of the velocity v^* induces an inertial force in the accelerated reference frame $F_x = M\partial_t v^*$. Therefore, the mean quasimomentum evolves as $\langle q_x \rangle (t) = \langle q_x \rangle_i + F_x t/\hbar \,(\mathrm{mod}\, 6k)$, which we use to prepare the desired quasimomentum state. We prepare states with quasimomenta spanning the Brillouin zone of size $6k$, centred on the initial quasimomentum $q_x = 2k$, in order to limit the duration of this step. We use an s-shaped ramp of quasimomentum which smoothly turns the force on and off and as a consequence minimises diabatic effects. The maximal ramp duration, used to reach the edges of the Brillouin zone centred on $q_x = 2k$, is set to $T_3^{(\max)} = 200\,\mu s$. We show in Fig. 6.8(c) the measured values of mean quasimomentum, as the velocity v^* is tuned, which agrees well with the expected variation.

6.6 First excitations of the system

We study the low-energy excitations of the system, which are of two types: the excitations described by the effective Hall cylinder model, which assume that the spin states remain in the $|r\rangle$-manifold with three sites, and the excitations leaving this subspace.

To probe the excitations of the effective Hall cylinder model, we apply a kick along x using a short pulse of the force F_x. In practice, we abruptly tune the laser frequencies to change v^* while keeping $\Delta = 0$. As shown in Fig. 6.9(a), we measure an oscillation of the mean velocity $\langle v_x \rangle$, associated with an energy gap of $16.1(1) E_{\mathrm{rec}}$. This value is close to the expected $15.7 E_{\mathrm{rec}}$, corresponding to the gap to the third excited band of the full model. We recall that this band is well approximated by the effective model, as shown in the band structures of Fig. 6.7(a,b) computed for the experimental coupling strengths. The abrupt change of v^* by v_{rec} ensures that the kick remains perturbative and that no other band is significantly populated, which is confirmed by numerical simulations. During this evolution, the magnetization $\langle \hat{J}_z \rangle$ remains close to zero, as expected for an excitation within the $|r\rangle$ spin states.

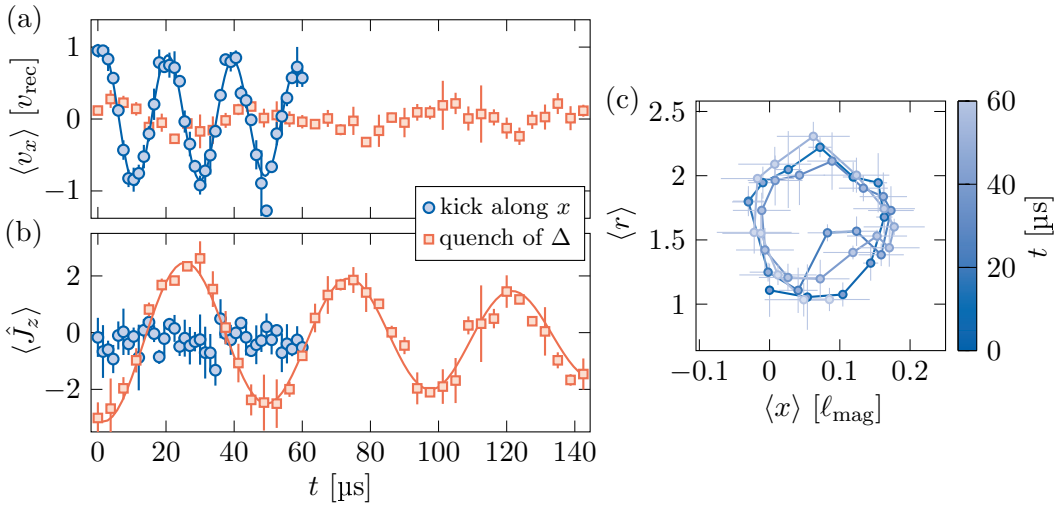

Figure 6.9 – First excitations of the system, induced by a kick along **x** (blue dots) or by a quench of the Zeeman field Δ (red dots). Panels (a,b): Mean velocity along **x** and mean magnetisation $\langle \hat{J}_z \rangle$ as a function of time after the perturbation. The solid lines are obtained from fitting experimental data. Panel (c): Cyclotron orbit, induced by a kick along **x**, plotted in the (x, r) plane. We compute the mean position $\langle x \rangle$ by numerically integrating the mean velocity along **x** and the mean position $\langle r \rangle$ from the spin distributions. The colour of the dots encodes the time variation.

Moreover, we can integrate the x-velocity to obtain the mean position along the physical dimension x and compute the mean position along r, obtained from the spin distributions by summing up the contributions of spin states $m = r \,(\mathrm{mod}\, 3)$. We plot the evolution of these quantities as a function of time in Fig. 6.9(c) and obtain a closed circular orbit on the surface of the cylinder parametrised by (x, r), which is similar to a cyclotron orbit in the bulk of a quantum Hall system.

We also study the excitation to the first excited band, which involves spin states outside the $|r\rangle$-manifold and is well reproduced by the ground state of the effective model for the harmonic quantum number $n = 1$. To promote the atoms to this band, we prepare a state in the ground band with a non-zero Zeeman field Δ, such that it exhibits a non-zero magnetization $\langle \hat{J}_z \rangle$. We then quench the Zeeman field to zero and measure the subsequent evolution of the x-velocity and magnetisation. We quench the Zeeman field by $0.4 E_{\mathrm{rec}}/\hbar$ to remain in the perturbative regime. We measure an oscillation of the magnetisation with a longer period, as well as a modulation of the amplitude of the oscillations, in Fig. 6.9(a,b). We interpret this as a beat note between two oscillations of frequencies set by two energy gaps. Such a feature is visible if the residual population in another excited band is not small enough. We fit the evolution of the x-velocity using a sum of two oscillations, and the component of the largest amplitude corresponds to an energy gap of $6.7(1) E_{\mathrm{rec}}$, close to the expected value of $6.2 E_{\mathrm{rec}}$.

Despite residual evolutions of magnetisation and x-velocity, in the first and second experiments respectively, we observe experimentally the decoupling between the

dimension r, coupled to the physical dimension x, and the dimension m. Residual effects may arise from the excitations that are not strictly perturbative or from the small deviation of the coupling strength ratio from $t_b/t_a = 1/2$. The example of the kick along the real dimension, which triggers oscillations of the mean position along the synthetic dimension r, also demonstrates how the coupling to a physical dimension simplifies the manipulation of the cyclic dimension, compared to the purely spin case that requires highly non-linear spin couplings (see Section 5.3.3).

These excitations can also be understood from a simple model of the dynamics of the effective Hall cylinder model. We define the velocity operators along x, r and m (generalising the formula for the two synthetic dimensions in Section 5.3.3):

$$\begin{aligned} v_x &= \frac{p_x}{M}, \\ v_r &= \frac{t_a}{\hbar}\left(\mathrm{i}\mathrm{e}^{-\mathrm{i}2kx}\frac{\hat{J}_+}{J} + \mathrm{hc}\right) + \frac{t_b}{\hbar}\left(\mathrm{i}\mathrm{e}^{-\mathrm{i}2kx}\frac{\hat{J}_-^2}{J^2} + \mathrm{hc}\right), \\ v_m &= \frac{t_a}{\hbar}\left(\mathrm{i}\mathrm{e}^{-\mathrm{i}2kx}\frac{\hat{J}_+}{J} + \mathrm{hc}\right) + \frac{t_b}{\hbar}\left(-2\mathrm{i}\mathrm{e}^{-\mathrm{i}2kx}\frac{\hat{J}_-^2}{J^2} + \mathrm{hc}\right). \end{aligned} \tag{6.30}$$

The evolution of the expectation value of an operator $\mathcal{O}$ is governed by the Ehrenfest theorem: $\partial_t \langle \mathcal{O} \rangle = \langle [\mathcal{O}, H] \rangle / (\mathrm{i}\hbar)$. As a consequence of this theorem, the velocity along $\mathbf{x}$ follows the simple relation:

$$\partial_t \langle v_x \rangle = -2 v_{\mathrm{rec}} \langle v_r \rangle , \tag{6.31}$$

while the velocities along the synthetic dimensions r and m evolve according to:

$$\begin{aligned} \partial_t \langle v_r \rangle &\simeq \frac{2kt_a}{\hbar}\left\langle \mathrm{e}^{-\mathrm{i}2kx}\frac{\hat{J}_+}{J} + \mathrm{hc}\right\rangle + \frac{2kt_b}{\hbar}\left\langle \mathrm{e}^{-\mathrm{i}2kx}\frac{\hat{J}_-^2}{J^2} + \mathrm{hc}\right\rangle, \\ \partial_t \langle v_m \rangle &\simeq \frac{2kt_a}{\hbar}\left\langle \mathrm{e}^{-\mathrm{i}2kx}\frac{\hat{J}_+}{J} + \mathrm{hc}\right\rangle - 2\frac{2kt_b}{\hbar}\left\langle \mathrm{e}^{-\mathrm{i}2kx}\frac{\hat{J}_-^2}{J^2} + \mathrm{hc}\right\rangle. \end{aligned} \tag{6.32}$$

where we neglected the mean values of the spin operators scaling as $1/J$ at most. We restrict the discussion to the spin states in the $|r\rangle$ manifold. Since the states of the ground band with a Zeeman field $\Delta = 0$ minimise energy with $\mathrm{e}^{-\mathrm{i}2kx}\hat{J}_+/J + \mathrm{hc} \simeq \mathrm{e}^{-\mathrm{i}2kx}\hat{J}_-^2/J^2 + \mathrm{hc} \simeq 2$, we obtain the following approximate dynamics along r and m:

$$\begin{aligned} \partial_t \langle v_r \rangle &\simeq \frac{4k}{\hbar}(t_a + t_b)\langle v_x \rangle , \\ \partial_t \langle v_m \rangle &\simeq \frac{4k}{\hbar}(t_a - 2t_b)\langle v_x \rangle . \end{aligned} \tag{6.33}$$

As a consequence, the coupling ratio $t_b/t_a = 1/2$ cancels out the dynamics along m, when we apply a perturbation that couples the states within the subspace spanned by the three $|r\rangle$ states only. We also recover oscillations of $\langle v_x \rangle$ at angular frequency $4\sqrt{E_{\mathrm{rec}}(t_a + t_b)/\hbar^2} \simeq 17.3 E_{\mathrm{rec}}/\hbar$, which is compatible with the calculated spectrum and our measurements. The oscillations of the velocities along the two dimensions are in quadrature, and the coupled differential equations predict cyclotron orbits in the (x, r) plane, as observed in Fig. 6.9(c).

6.7 Transverse response to a real force

In this Section, we study the transverse response of the system to a force along the physical dimension x. Two sets of experiments are conducted: the first one probes the properties of the ground band, indicating a winding along the synthetic dimension when a force along x is applied, and the second one measures the velocity along r, as a response to a force for different quasimomentum states.

6.7.1 Measurement of the mean position along r

The first experiments measure the velocity and spin distributions for ground states whose quasimomenta span a whole Brillouin zone. These states are prepared using the protocol presented in Section 6.5, using Bloch oscillations. The quasimomentum varies through the Brillouin zone, as the time-dependent velocity v^* induces an inertial force along $\mathbf{x}$ in the reference frame. The force is adiabatically turned on and off to maximise the overlap with the ground state of the system at all times.

Our analysis of the recorded data for various quasimomenta obeys the following procedure. We filter the experimental runs based on the signal on the magnetic probe close to atoms, which reduces the noise on the Zeeman field Δ. The optical densities of this set of experiments are computed using our protocol that reduces imaging defects and background patterns, described in Section 2.1.2. We split the velocity distribution recorded for each quasimomentum $\langle q_x \rangle$ in 17 stripes, corresponding to the 17 magnetic sublevels, thanks to the spatial separation induced by the Stern-Gerlach magnetic gradient along the gravity axis during the free expansion of the cloud. The velocity distribution along the gravity axis $\mathbf{z}$ is not relevant, as the dynamic along this axis is separable from the spin-orbit coupling along $\mathbf{x}$. The decoupling of the horizontal and vertical distributions authorises to average the pixels of the ODs along the vertical axis, with any weighting function, for each of the 17 distributions. Since the distribution along $\mathbf{z}$ is that of a thermal cloud, we choose a Gaussian function, centred on the mean vertical velocity, to maximise the signal-to-noise ratio. We obtain a set of 17 one-dimensional velocity distributions for each mean quasimomentum $\langle q_x \rangle$. An example is shown in Fig. 6.10(a).

Our measurements of the spin-velocity distribution, with varying parameters (v^*, Δ), are consistent with peaks located at fixed positions in the laboratory frame, as expected in Fig. 6.5. The peaks are broadened due to the finite initial temperature of the cloud of 0.54(3) µK, corresponding to a thermal momentum width $\sigma_{q_x} \simeq 1.3k$. We shift the velocity distributions by the velocity v^*, which corresponds to $\langle q_x \rangle$, to consider the distributions in their reference frame. This operation requires precise control of the laser frequencies and the calibration of the imaging setup (see Section 2.1) to convert pixel positions in the recorded ODs into velocities in the moving frame. The frequency differences, between the beams $1a$ and 2 and the beams $1b$ and 2, are dynamically generated by signal generators and checked using an optical beating, recorded on a fast photodiode. Typical deviations and shot-to-shot variations from the desired frequency differences are less than a few kHz, a small fraction of the recoil frequency associated with the wavevector $2k$. The spin-averaged velocity distributions are all centred around $v_x = 0$.

In the moving frame, the diffraction peaks are shifted from the fixed positions in the laboratory frame by v^*, which is not restricted to discrete values. Three examples

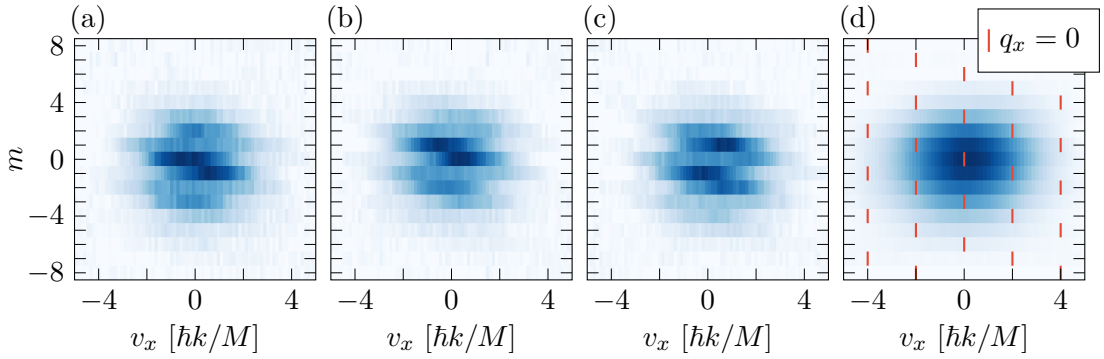

Figure 6.10 – Averaging and deconvolution of velocity distributions. Panels (a,b,c): Spin-resolved velocity distributions measured for $\langle q_x \rangle \simeq -2k, 0, 2k$ (a, b, c respectively), in the moving frame. Panel (d): Velocity distribution averaged over all $\langle q_x \rangle$ uniformly spanning a Brillouin zone. The contribution for a given q_x can be extracted by selecting the velocity components given by Eq. 6.34 (example of $q_x = 0$ shown as red lines).

of spin-velocity distributions in the moving frame for different quasimomentum state are given in Fig. 6.10(a,b,c). As a consequence, when averaging the distributions, the pattern of peaks disappears, as in Fig. 6.10(d). We point out that the pattern of peaks is identical in the moving frame when we consider states with v^* differing by multiples of $6v_{\mathrm{rec}}$ exactly, that have the same quasimomenta.

For a Bloch state of quasimomentum q_x, we recall that the velocity takes discrete values only, at:

$$v_x = \frac{\hbar}{M}(q_x - 2km + 6ks), \tag{6.34}$$

with s integer, for each spin projection m, a consequence of the conservation of the quasimomentum. In our system, the thermal broadening of momentum leads to a continuous spin-resolved velocity distribution. Importantly, Eq. 6.34 shows that different quasimomentum states contribute to distinct velocities in the spin-resolved velocity distribution. First, this means that each experimental shot contains information about states whose quasimomentum lies in a range close to $\langle q_x \rangle$. Second, the thermal broadening can be deconvolved, leading to velocity and spin distributions resolved in quasimomentum. In practice, to treat all quasimomenta equally, we average the spin-resolved velocity distribution for various values of $\langle q_x \rangle$ uniformly spanning the first Brillouin zone. We then deconvolve the data by selecting the velocity components for a given q_x from the averaged spin-resolved distribution, according to Eq. 6.34. The selection of velocity components associated to each spin state is represented in Fig. 6.10(d) for the quasimomentum state with $q_x = 0$. From this procedure, we obtain the deconvolved velocity and spin distributions as a function of the quasimomentum q_x for $\Delta = 0$.

The velocity distribution, plotted in Fig. 6.11(b) as a function of q_x, exhibits a period $2k$, similar to the case of a simple $\lambda/2$-periodic lattice. The mean velocity $\langle v_x \rangle$, shown as a red line, remains close to zero. Since it is related to the slope of the ground-band energy $\partial_{q_x} E_0(q_x) = \hbar \langle v_x \rangle$, this shows that the band is quasi-flat.

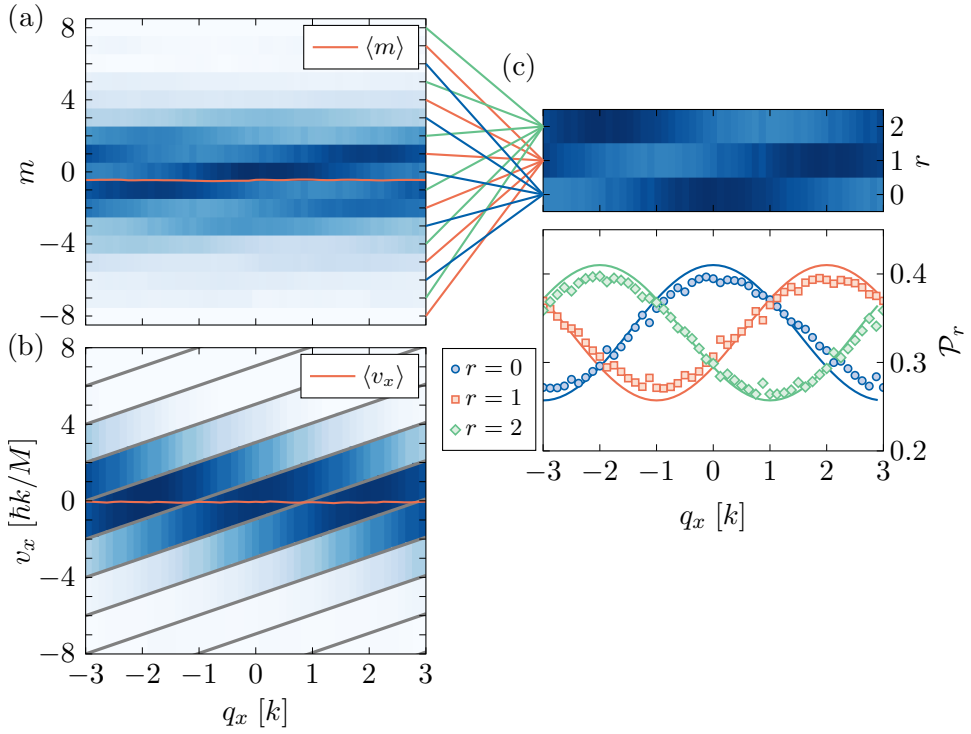

Figure 6.11 – Ground band characterisation. Panel (a): Spin projection probabilities Π_m measured as a function of q_x. The red solid line stands for the mean spin projection $\langle \hat{J}_z \rangle$. Panel (b): Distribution of discrete velocity components $v_x = \hbar(q_x + 2ks)/M$ (with integer s) for states of quasi-momentum q_x. The red solid line shows the mean velocity $\langle v_x \rangle$. Panel (c): Probabilities $\mathcal{P}_r$ of projection on $r = m \,(\mathrm{mod}\, 3)$. The blue circles, red squares and green diamonds correspond to $r = 0$, 1 and 2 respectively. The statistical error bars, computed from a bootstrap random sampling analysis, are smaller than the symbols. The lines are calculated from the expected band structure.

In fact, the band flatness is protected from perturbations, such as external magnetic field fluctuations, by the zero net magnetisation of the $|r\rangle$ spin states. A similar effect has been used in another implementation of a Hall cylinder using dynamical decoupling techniques [246].

The probabilities Π_m of projection on each sublevel m, in Fig. 6.11(a), reveal a longer periodicity $6k$, corresponding to the full extent of the magnetic Brillouin zone. This experimentally confirms the spatial separation of the magnetic orbitals $\ell_{\mathrm{mag}} = 2\pi/(6k) = \lambda/6$. The Π_m measurements also give access to the probabilities $\mathcal{P}_r$ of projection on the synthetic coordinate r, by summing the Π_m distributions with $m = r \,(\mathrm{mod}\, 3)$. The summation is schematically represented using coloured links between the distributions in m and r in Fig. 6.11(a,c). The q_x-variation of these distributions reveals a chirality, typical of the Hall effect: when increasing the momentum by $2k$, the $\mathcal{P}_r$ distributions cycle along the synthetic dimension in a directional manner, as $\mathcal{P}_r \to \mathcal{P}_{r+1}$ [248, 251]. We stress that such a drift does not

occur on the mean spin projection $\langle \hat{J}_z \rangle$, represented as a red line in Fig. 6.11(a), which remains uniform and close to zero. Our measurements reveal features that we have already highlighted in Section 4.3.1, in Fig. 4.6. In particular, we observe that a change of quasimomentum q_x is associated with a global shift of the r-distribution, while the shape of the distribution is not modified.

6.7.2 Measurement of the mean velocity along r

The adiabatic r-drift occurring during Bloch oscillations provides a first insight into the topological character of the lowest energy band, similar to the quantized flow of the Wannier function charge centres in Chern insulators [158]. To quantify this drift, one cannot rely on the mean r position, which is ill-defined for a cyclic dimension [232]. Experimentally, the problem of reconstructing the mean position along the cyclic dimension also stems from the reduced visibility of the oscillation of $\mathcal{P}_r$ for increasing coupling strengths. This is a consequence of the small size of the cyclic dimension, which leads to density distributions that wind around the cylinder as in Fig. 4.6. Instead, in a complementary set of experiments, the r-drift is reconstructed by integrating the anomalous velocity $\langle v_r \rangle$ induced by the force F_x driving the Bloch oscillations. In the weak force limit, the mean velocity $\langle v_r \rangle$ is expected to be proportional to the force and to the local Berry curvature Ω_{q_x}, as follows:

$$\langle v_r \rangle = \frac{1}{\hbar} \Omega_{q_x} F_x. \tag{6.35}$$

The operator v_r is well-defined, but the measurement of its expectation value is not as straightforward as for the mean r-position. For this purpose, we conduct a separate experiment, in which we adiabatically induce a large force along x. We use a cubic-shaped quasimomentum ramp, set by the reference frame velocity v^*, that corresponds to a quadratic ramp of the force, with a zero slope at the beginning to minimise diabatic effects. We vary the shape of the ramp to prepare quasimomentum states spanning a whole Brillouin zone while keeping the final force $F_x = 0.18\,\hbar 2k/\mu\text{s}$ constant. The duration of the ramp varies from 25 µs to 75 µs and, during the ramp of the force which induces a drift of quasimomentum, we span between 0.5 and 1.5 times the size of the Brillouin zone. We suddenly switch off the force F_x, and the centre-of-mass undergoes a cyclotron oscillation, with the x- and r-velocities oscillating in quadrature. More precisely, the rate of change of the x-velocity gives access to the r-velocity, via the exact relation:

$$\partial_t \langle v_x \rangle = -2 v_{\text{rec}} \langle v_r \rangle , \tag{6.36}$$

that we have already derived with the Ehrenfest theorem in Eq. 6.31. Hence, the velocity $\langle v_r \rangle$ induced by the force F_x is given by the initial slope of $\langle v_x \rangle$. The reconstruction of $\langle v_r \rangle$ from our measurements of the oscillations of the velocity after abruptly turning off the force is shown in Fig. 6.12(a). We show in Fig. 6.12(b) the measured Berry curvature for different values of the mean quasi-momentum $\langle q_x \rangle$. The measurements are consistent with a flat Berry curvature. The error bars are dominated by the differentiation operation used to extract the velocity $\langle v_r \rangle$ from the x-velocity oscillations.

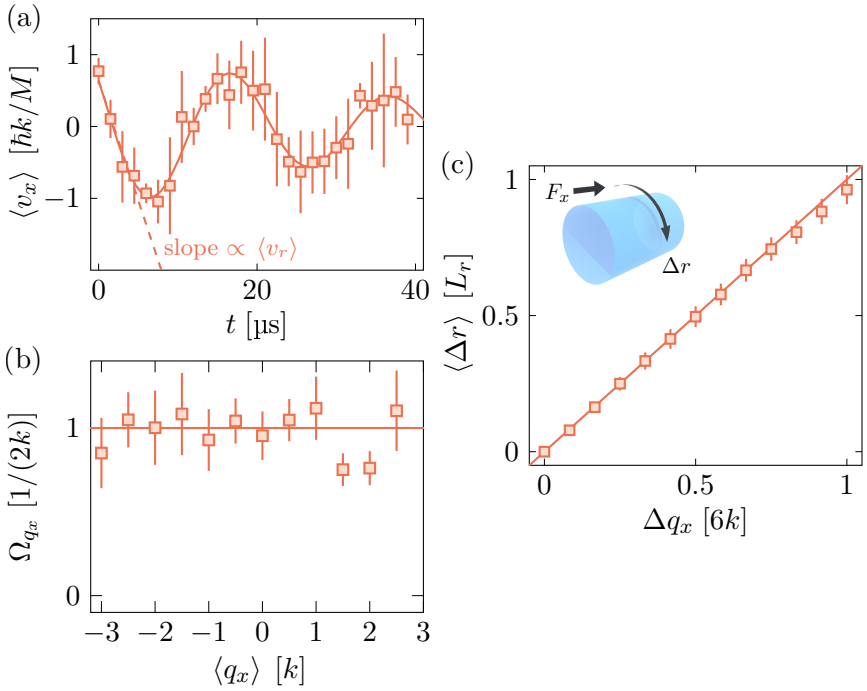

Figure 6.12 – Panel (a): Evolution of the mean velocity $\langle v_x \rangle$ immediately after switching off the force F_x (red squares), fitted with a damped sine (solid line). The velocity $\langle v_r \rangle$ is obtained from the initial slope of the fit (dashed line). Panel (b): Berry curvature measured from the r-velocity induced by a force F_x (red squares), compared to the expected value $\Omega_{q_x} = 1/(2k)$ (solid line). Panel (c): Centre-of-mass displacement $\langle \Delta r \rangle$ as a function of the quasi-momentum shift Δq_x induced by a force F_x (red squares), together with a linear fit (red line).

The adiabatic r-drift acquired for a duration T reads as follows:

$$\begin{aligned} \langle \Delta r \rangle (T) &= \int_0^T \mathrm{d}t \, \langle v_r \rangle (t) \\ &= \int_{q_x(0)}^{q_x(T)} \Omega_{q_x} \mathrm{d}q_x, \end{aligned} \tag{6.37}$$

where we used the equation of variation of the quasimomentum during a Bloch oscillation with a fixed force F_x: $q_x(t) = q_x(0) + F_x t/\hbar$. Hence, the drift accumulated over a period simply equals $\mathcal{C}L_r$, using the expression of the Chern number as an integral of the Berry curvature in Eq. 6.29. This expression links the quantisation of the winding along r during a Bloch oscillation to the Chern number characterising the ground-band topology.

We reconstruct the centre-of-mass drift $\langle \Delta r \rangle$, upon integration of our measurements of $\langle v_r \rangle$ for quasimomenta spanning the Brillouin zone for a constant force F_x, and show that it indeed varies linearly with the quasi-momentum variation Δq_x,

in Fig. 6.12(c). Now the drift accumulated over a Brillouin zone reads:

$$\frac{\langle \Delta r \rangle}{L_r} = 0.97(5), \tag{6.38}$$

compatible with a unit winding around the cylinder of circumference $L_r = 3$. The displacement along r occurring over a Bloch oscillation cycle is thus quantised, providing a first manifestation of the non-trivial band topology.

6.8 Laughlin's topological charge pump

We now characterise the global band topology by implementing Laughlin's charge pump experiment and extend the protocol to reveal the local geometrical properties. To simulate the axial magnetic field used to drive the pump, we interpret the complex phase φ involved in the r-hoppings in Eq. 6.16 as the Peierls phase associated with a field $\mathbf{B}_\parallel$ threading the cylinder with a flux:

$$\Phi_\parallel = \frac{3\varphi}{2\pi}\Phi_0. \tag{6.39}$$

The importance of the axial flux in cylindrical geometries has also been highlighted in the context of localisation measurements [252]. We vary $\Phi_\parallel$ by adjusting the phase difference φ between the laser electric fields involved in the spin transitions. The flux is increased linearly in time at a rate $\dot{\Phi}_\parallel = 0.41\,\Phi_0/\mu\text{s}$, corresponding to a fixed non-zero velocity v^* according to the simple formula: $\dot{\Phi}_\parallel/\Phi_0 = 6kv^*/(2\pi)$. This step is preceded and followed by ramp-up and ramp-down phases of the rate using s-shaped profiles of duration T. This duration is long enough to ensure the adiabaticity of the process.

We drive the pump by slowly ramping the phase φ, and measure the induced shift of the centre-of-mass along the real dimension x. *In situ* density distributions, from which the centre of mass is extracted, are shown in Fig. 6.13(a). The recorded distribution corresponds to the convolution of the position distribution with the point spread function of our imaging system, which significantly magnifies the distribution. We count the threading of phase $\Phi_\parallel$ during the phase of linear flux insertion only, such that the overall drift during the ramp-up and ramp-down steps is unimportant. We also perform an independent verification by implementing the same experimental sequence with $\dot{\Phi}_\parallel = 0$, which consists in keeping the reference frame velocity fixed to its initial value $v^* = 0$ during the three steps. We confirm that there is no visible drift in this case.

The experiment is performed for various values of the quasi-momentum $\langle q_x \rangle$ uniformly spanning the magnetic Brillouin zone. The q_x-averaged drift, shown in Fig. 6.13(c), is consistent with a linear variation:

$$\frac{\langle \Delta x \rangle}{\ell_{\text{mag}}} = \mathcal{C}\frac{\Phi_\parallel}{\Phi_0} \quad \text{with} \quad \mathcal{C} = 1.00(4), \tag{6.40}$$

in agreement with the expected quantisation of transport characterised by the Chern number $\mathcal{C} = 1$. Our experiments also give access to the anomalous drift of individual

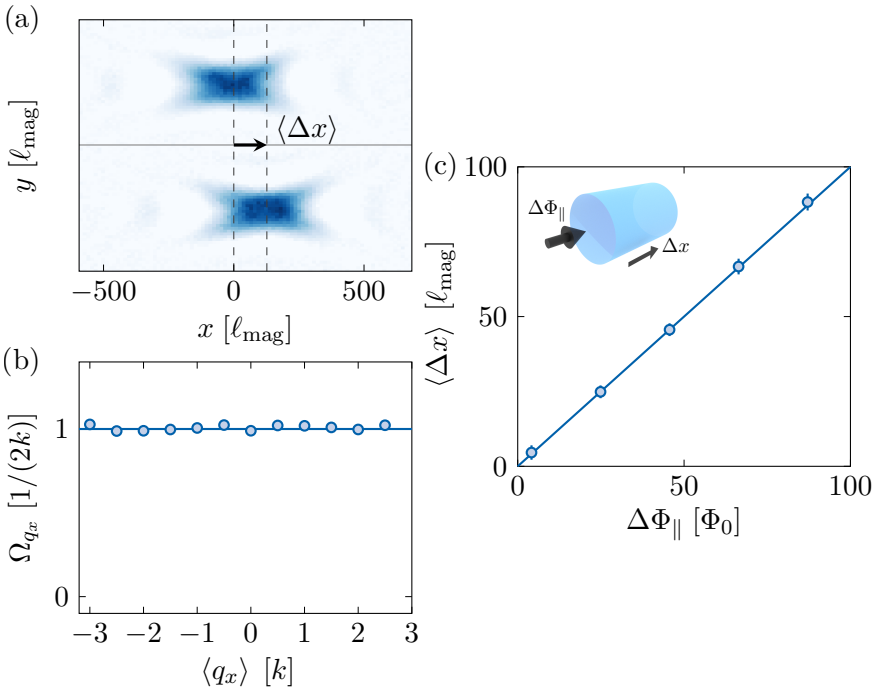

Figure 6.13 – Panel (a): *In situ* density distributions with and without pumping, in the lower and upper panels respectively. The centre-of-mass without pumping is used as a reference and we measure the displacement $\langle\Delta x\rangle$ induced by the pumping process. Panel (b): Berry curvature Ω_{q_x} measured as a function of the mean quasi-momentum $\langle q_x\rangle$ (blue circles). The solid line is the expected Berry curvature, which is not distinguishable from the constant value $\Omega_{q_x} = 1/(2k)$. Panel (c): Displacement of the centre of mass $\langle\Delta x\rangle$ induced by an axial magnetic flux $\Phi_\parallel$ and averaged over the magnetic Brillouin zone (blue cicles). The blue line is a linear fit.

quasimomentum states, proportional to the Berry curvature Ω_{q_x} that quantifies the local geometrical properties of quantum states [180]. As shown in Fig. 6.13(b), the measured Berry curvature is flat within error bars, consistent with theory, which predicts $\Omega_{q_x} = 1/(2k)$ with negligible q_x-variation.

6.9 Adiabaticity of the pumps

The quantisation of topological pumps is protected by an energy gap separating the ground and excited bands and requires only a slow variation of the pump control parameters. In this Section, we present a study of the adiabaticity of the two topological pumps considered in the previous Sections.

6.9.1 Adiabaticity of the pump with a force along x

The first topological pump studied in our work consists of a motion along the synthetic dimension r induced by a force F_x along the real dimension x. We numerically study how the adiabaticity of the ramp of the force depends on the

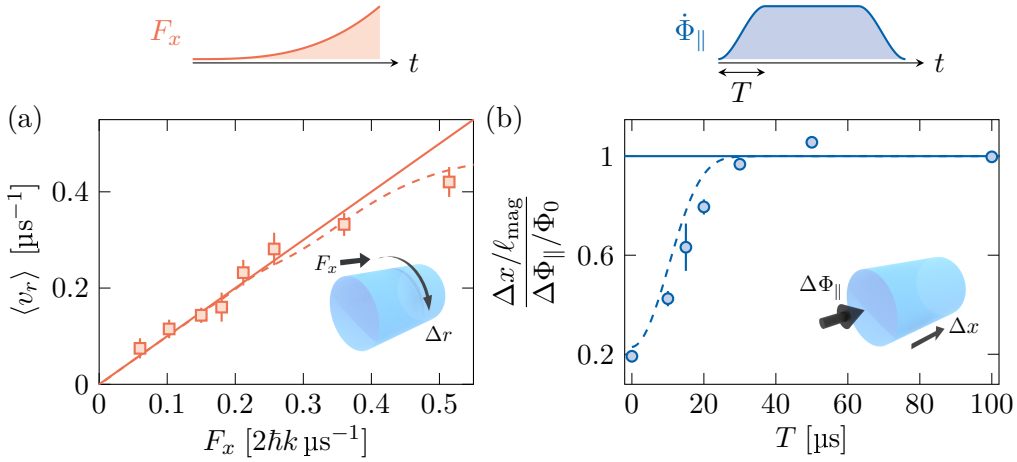

Figure 6.14 – Adiabaticity of topological pumps. Panel (a): Velocity $\langle v_r \rangle$ along the synthetic dimension measured as a function of the applied force F_x. The solid line is the expected linear relation expected for small forces, and the dashed line is obtained by a numerical simulation of the atom dynamics. Panel (b): Drift of the atomic cloud induced by a flux insertion $\Delta\Phi_\parallel \simeq 83\,\Phi_0$ as a function of the duration T. The flux insertion rate is set to $\dot{\Phi}_\parallel = 0.41\,\Phi_0/\mu\mathrm{s}$, with ramp-up and ramp-down steps of duration T. The solid line is the displacement expected in the adiabatic regime for geometrical pumping with $\Omega_{q_x} = 1/(2k)$ and the dashed line is obtained by a numerical simulation.

parameters of the ramp, which include its shape, its duration and the final value of v^*. We choose a quadratic ramp of the force, realised by a cubic ramp of the parameter v^*. We fix the final quasimomentum q_x and vary the duration of the ramp only, which sets the final force. We measure the velocity $\langle v_y \rangle$ induced by the force F_x via the initial slope of $\langle v_x \rangle$, as in Fig. 6.12(a). We show in Fig. 6.14(a) the mean velocity $\langle v_r \rangle$ as a function of F_x. For $F_x \leq 0.25\,\hbar 2k/\mu\mathrm{s}$, the r-velocity varies linearly with F_x, in agreement with the expected adiabatic response. The deviations observed for larger forces are well accounted for by a numerical simulation of the atomic dynamics. The measurements shown in Fig. 6.12 use a force $F_x = 0.18\,\hbar 2k/\mu\mathrm{s}$, well within the adiabatic regime.

6.9.2 Adiabaticity in Laughlin's topological charge pump

Laughlin's topological charge pump, as realised in this work, is driven by inserting a longitudinal magnetic flux $\Phi_\parallel$. The flux insertion rate $\dot{\Phi}_\parallel$ is set by the parameter v^*. It is first ramped up according to an s-shaped profile of duration T, then kept at a fixed value for a controlled duration such that the longitudinal magnetic flux varies linearly in time, and finally ramped down according to an s-shaped profile of the same duration T. This sequence and the shape of the ramping profile are chosen to minimise diabatic effects and maximise the overlap of the quantum state with the ground state of the total Hamiltonian at all times, based on numerical simulations. We experimentally study the effect of the duration T of the ramp profiles. We show

in Fig. 6.14(b) the ratio of the mean atom displacement $\langle \Delta x \rangle$ and of the longitudinal magnetic flux $\Phi_{\parallel}$, as a function of the ramp time T. For slow ramps $T \geq 50\,\mu s$, the displacement is compatible with the value given by the Berry curvature $\Omega_{q_x} \simeq 1/(2k)$. Deviations are observed for faster ramps in agreement with a numerical simulation of the atom dynamics. The measurements shown in Fig. 6.13 are performed with a ramp duration $T = 100\,\mu s$, in the adiabatic regime.

Our implementation of a quantum Hall cylinder and the subsequent realisation of Laughlin's charge pump experiment by periodic driving of the longitudinal magnetic flux provide a new experimental perspective on the integer quantum Hall effect. Measurements along the synthetic cyclic dimension highlight the peculiar geometry of our system. The cylindrical geometry constrains our system to bulk physics only, facilitating the measurement of the topological invariant of the system, the first Chern number. In the next Chapter, we will benefit from the large spin of dysprosium atoms to exploit the two synthetic dimensions described in Chapter 5 and engineer a four-dimensional system. It exhibits global properties associated with another topological invariant called the second Chern number.

The work presented here is restricted to the single-atom regime, where the role of interactions is negligible over the timescale of our experiments. We will discuss the role of interactions in the next Chapter, on systems with synthetic and spatial dimensions.

7

Beyond the non-interacting atomic Hall cylinder

This Chapter explores extensions of our study of the integer quantum Hall effect in an atomic Hall system. We present a generalisation to a four-dimensional space benefiting from the encoding of two synthetic dimensions in the large spin of dysprosium atoms in their electronic ground state. The two synthetic dimensions m and r are coupled to two spatial dimensions with two-photon Raman transitions, which engineer a four-dimensional topological system. We experimentally probe the ground band parametrised by a two-dimensional quasimomentum and reveal some characteristic bulk and edge properties. The second part of this Chapter is dedicated to the theoretical study of Hall systems with interacting particles. We first discuss the role of interactions in the atomic Hall cylinder with the synthetic dimension r. We then turn to possible future implementations of a Hall system in spatial dimensions with an artificial gauge field mediated by the internal degree of freedom of the atoms and enhanced by the large spin $J = 8$.

7.1 A quantum Hall system in four dimensions

Systems of dimensionality higher than three have first been under scrutiny by theorists to understand the fundamental interactions [253, 254] or quantum gravity [255, 256]. They are also involved in the description of the two-dimensional quasicrystals, non-periodic structures with long-range order [21]. Possible applications, such as one-way fibre or optical isolator, have emerged in photonics from the robust and directional edge modes that appear in topological systems and are protected by topological invariants such as the first or second Chern numbers [161, 257, 258]. The topic of topological insulators has also motivated research toward high dimensions. Dimensionality plays a prominent role in their classification [259] and novel phases of matter are expected in systems with more than three dimensions, whose realisation should be facilitated by the combination of synthetic dimensions and spatial ones.

Recently, alternative approaches have tackled specific questions in high-dimensional systems using synthetic dimensions only. On one side, multiterminal Josephson junctions [260] with n leads are related to phenomena in $n-1$ dimensions. They have

been used to study Weyl points [261–264], where a semimetal bandstructure exhibits an energy gap closing with a linear dispersion relation. These conic structures, similar to the Dirac points in graphene [265], are topologically protected from a gap opening. On the other side, atoms using four internal states [266], superconducting qubits coupled to a cavity [267] or NV centres in diamond with a triplet ground state [268] have been used to study gauge theories from high-energy physics, without the need for spatial dimensions. Following Dirac's seminal work on monopoles [269], some gauge field theories have been linked to the existence of monopole solutions in high-dimensional spaces. The modern interpretation of monopoles is connected to Berry curvature and Berry phase and their topological nature is related to invariants, such as the first Chern number for a Dirac monopole or the second Chern number for a Yang monopole [270].

Our approach with atomic dysprosium focuses on quantum Hall systems, *i.e.* topological insulators with explicit time-reversal symmetry breaking via the presence of a magnetic field. The first natural extension of our atomic Hall cylinder is the three-dimensional quantum Hall effect [271–273], which has been recently realised in a condensed-matter system [274]. It involves three first Chern numbers, associated with each of the three orthogonal planes of the material, such that the topology is essentially related to only two dimensions. Novel phenomena appear when adding a pair of dimensions to a two-dimensional Hall system, and this keeps being true whenever a pair is added. Four-dimensional [255, 275, 276] and six-dimensional [277, 278] Hall effects have been predicted. The former has been explored in two-dimensional pumps using dimensional reduction [279, 280] and a small instance has been realised using electronic circuits [281]. The topology of a $d = 2n$-dimensional Hall system is classified by one or more m-th Chern numbers with $m \leq n$, which characterise the m-th order perturbative response to an electromagnetic perturbation, and is associated with the presence of conducting hyperedges. In four dimensions, the second Chern number is a topological invariant that cannot be reduced to that of a two-dimensional system and the conducting modes are three-dimensional. In this Section, we describe our implementation of a four-dimensional Hall system using two synthetic dimensions encoded in the spin of dysprosium atoms and our characterisation of its ground band.

7.1.1 Experimental setup

Our experimental protocol closely follows our implementation of an atomic Hall cylinder with the coupling to an additional spatial dimension. We consider two pairs of counter-propagating beams at 626.1 nm, aligned along the orthogonal axes x and z. The first pair of beams is involved in the process (a) coupling $m \to m+1$ and the second one in process (b) coupling $m \to m-2$, with net momentum kicks $-2k\mathbf{e}_x$ and $-2k\mathbf{e}_z$ respectively. Here, m is the spin projection along z ($-J \leq m \leq J$, m integer). The non-trivial cycle on the coordinate $r \equiv m \,(\mathrm{mod}\, 3)$ now involves the successive processes $r \xrightarrow{x} r+1 \xrightarrow{x} r+2 \xrightarrow{z} r+3 = r$, associated with a total momentum kick $-2k(2\mathbf{e}_x + \mathbf{e}_z)$ and the absence of drift along m. A force along $2\mathbf{e}_x + \mathbf{e}_z$ thus performs periodic Bloch oscillations with a chiral behaviour of the coordinate r while a force oriented along $\mathbf{e}_x - \mathbf{e}_z$ creates a Hall drift along m only, as the increase in velocity is compensated by light-induced momentum kicks. These behaviours can be interpreted

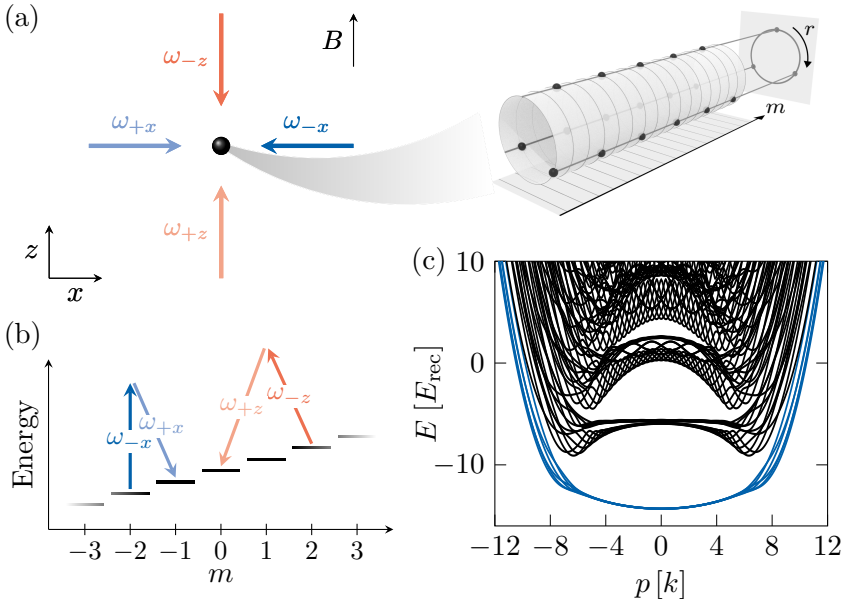

Figure 7.1 – Panel (a): Scheme of an atom subjected to a pair of counter-propagating laser beams in the (x, z) plane, which couples its motion with its internal degrees of freedom. The total angular momentum $J = 8$ encodes two synthetic dimensions given by the magnetic projection m and its remainder $r = m \,(\mathrm{mod}\, 3)$, leading to a synthetic space of cylindrical geometry. The magnetic field is oriented along z. Panel (b): Spin-changing transitions induced by the four laser beams. The pair of counter-propagating beams along x (z) couple nearest-neighbour (next-nearest-neighbour) spin states, with a net momentum kick along its propagation axis. Panel (c): Dispersion relation plotted as a function of the momentum p, for six values of the quasimomentum q. The ground band is represented by blue lines.

as the effect of two magnetic fields coupling two pairs of axes of a four-dimensional system defined by the coordinates (x, z, m, r).

In our implementation, a non-zero bias field is oriented along $\mathbf{z}$. The process (a) is produced by the same beams as in the Hall cylinder described in Section 6.1 with only one frequency component per beam. We recall that the two polarisations are $\mathbf{e}_1 = \cos\theta\,\mathbf{e}_z + \sin\theta\,\mathbf{e}_y$ and $\mathbf{e}_2 = \cos\theta\,\mathbf{e}_z - \sin\theta\,\mathbf{e}_y$ for the laser beams propagating along $\mathbf{x}$ and $-\mathbf{x}$ respectively, with $\theta = \mathrm{acos}\left(1/\sqrt{3}\right) \simeq 55°$. The choice of this angle θ cancels the quadratic $\hat{J}_z^2$ term imparting from the tensor polarisability. The vertical beams are aligned with the magnetic field and realise the process (b). They have opposite circular polarisations, $\mathbf{e}_\pm$ for the beam propagating along $\pm\mathbf{z}$. Since the processes (a) and (b) respectively involve rank-1 and -2 spin couplings, we choose the relative frequencies of the two pairs of beams as:

$$\begin{aligned} \omega_{+x} - \omega_{-x} &= -\delta_z + \epsilon_x, \\ \omega_{+z} - \omega_{-z} &= 2\delta_z + \epsilon_z, \end{aligned} \tag{7.1}$$

with ω_s the absolute frequency of the beam s ($s = \pm x$ or $\pm z$) and ϵ_x and ϵ_z the

detunings from the two resonances.

We apply the rotating wave approximation and discard all fast oscillating terms. The light shifts induced by the two pairs read as follows:

$$\begin{aligned} V_{\mathrm{LS}}^{(x)} &= (V_{+x}+V_{-x})\left(\alpha_0-\alpha_2\frac{J+1}{2J-1}\right)\hat{\mathbb{1}}-t_x\left(\mathrm{e}^{-\mathrm{i}2kx}\mathrm{e}^{\mathrm{i}\epsilon_x t}\mathrm{e}^{\mathrm{i}\phi_x}\frac{\hat{J}_+}{J}+\mathrm{hc}\right), \\ V_{\mathrm{LS}}^{(z)} &= (V_{+z}+V_{-z})\left[\left(\alpha_0+\alpha_2\frac{J+1}{2(2J-1)}\right)\hat{\mathbb{1}}-\alpha_2\frac{3}{2J(2J-1)}\hat{J}_z^2\right] \\ &\quad -t_z\left(\mathrm{e}^{-\mathrm{i}2kz}\mathrm{e}^{\mathrm{i}\epsilon_z t}\mathrm{e}^{\mathrm{i}\phi_z}\frac{\hat{J}_-^2}{J^2}+\mathrm{hc}\right)+(V_{+z}-V_{-z})\alpha_1\frac{1}{2J}\hat{J}_z, \end{aligned} \tag{7.2}$$

where V_s is the light coupling amplitude for beam s ($s=\pm x$ or $\pm z$), from Eq. 6.4 with a detuning Δ_0 from the optical transition. We use red-detuned beams with $\Delta_0=-2\pi\times 8\,\mathrm{GHz}$. The spin-independent contributions are dominated by the scalar terms that create an attractive potential. A scalar term and a quadratic term $\hat{J}_z^2$ in $V_{\mathrm{LS}}^{(x)}$ cancel for our choice of polarisation angle $\theta=\mathrm{acos}\left(1/\sqrt{3}\right)$. We choose $V_z\equiv V_{+z}=V_{-z}$ to suppress the additional linear Zeeman term from $V_{\mathrm{LS}}^{(z)}$. The coupling strengths t_x and t_z are given by:

$$\begin{aligned} t_x &= \sqrt{|V_{+x}V_{-x}|}\frac{J(2J+3)}{4(J+1)(2J+1)}\sin(2\theta), \\ t_z &= \sqrt{|V_{+z}V_{-z}|}\frac{J^2}{2(J+1)(2J+1)}. \end{aligned} \tag{7.3}$$

The quadratic term in $V_{\mathrm{LS}}^{(z)}$ reads $q_z\hat{J}_z^2/J^2$ with $q_z=\mathrm{sgn}(\Delta_0)2t_x$.

We consider the atomic dynamics in a moving frame at velocity $\mathbf{v}^*$ defined as $\mathbf{v}^*=(\epsilon_x\mathbf{e}_x+\epsilon_z\mathbf{e}_z)/2k$. The Hamiltonian becomes time-independent and strongly resembles that of the atomic Hall cylinder in Eq. 6.16, except for the spatially-dependent phases that depend on both x and z:

$$\begin{aligned} H &= \frac{M\mathbf{v}^2}{2}+V(\mathbf{r})+q_z\frac{\hat{J}_z^2}{J^2}+V_1\hat{\mathbb{1}}, \\ V(\mathbf{r}) &= -t_x\left[\frac{\hat{J}_+}{J}\mathrm{e}^{\mathrm{i}\phi_x}+\mathrm{hc}\right]-t_z\left[\frac{\hat{J}_-^2}{J^2}\mathrm{e}^{\mathrm{i}\phi_z}+\mathrm{hc}\right], \end{aligned} \tag{7.4}$$

where $\mathbf{v}$ is the atomic velocity in the moving frame at $\mathbf{v}^*$ and $\phi_s=-2ks$ is the relative phase of the two laser beams involved in each Raman process $s=x$ or z. The energy V_1 is the spin-independent potential created by the four beams. The optical transitions induce correlated dynamics in spin and velocity such that the canonical momentum is conserved $\mathbf{p}=M\mathbf{v}/\hbar+2km\mathbf{e}_x\,(\mathrm{mod}\,\mathbf{K})$. The reciprocal lattice vector $\mathbf{K}=2k(2\mathbf{e}_x+\mathbf{e}_z)$ is the opposite of the momentum kick imparted in the non-trivial cycle described earlier $r\xrightarrow{x}r+1\xrightarrow{x}r+2\xrightarrow{z}r+3=r$. In the following, we decompose the momentum as $\mathbf{P}=p\mathbf{X}+q\mathbf{Y}$ with $\mathbf{Y}\parallel\mathbf{K}$, such that the first Brillouin zone is defined by $|q|<K/2$, p arbitrary. More precisely, we define the vectors of the orthonormal basis $\mathbf{X}=(\mathbf{e}_x-2\mathbf{e}_z)/\sqrt{5}$ and $\mathbf{Y}=(2\mathbf{e}_x+\mathbf{e}_z)/\sqrt{5}$.

7.1.2 Ground band characterisation

We start with atoms at rest in the laboratory frame, initially polarised in $|m = -J\rangle$, the ground state in the presence of the magnetic field oriented along $\mathbf{z}$ with a norm of 223 mG, corresponding to a Larmor angular frequency $\delta_z = 2\pi \times 388\,\mathrm{kHz}$. We adiabatically ramp up the laser intensities to generate the spin couplings, with initial detunings $\epsilon_x = -7.15E_{\mathrm{rec}}/\hbar$ and $\epsilon_z = 14.3E_{\mathrm{rec}}/\hbar$, in 100 µs. In the corresponding moving frame at $\mathbf{v}^* = -8v_{\mathrm{rec}}\mathbf{X}$, the atoms initially at rest are loaded in the quasimomentum state with $p = -15.16k$ and $q = -0.89k$, such that the atoms essentially remain in $|-J\rangle$.

We then proceed to a ramp of frequencies that amounts to applying an inertial force in the moving frame and tuning the quasimomentum. To reduce the duration of the ramp and maintain adiabaticity, the ramp follows a trajectory that avoids the parts of the spectrum where the gap to the first excited state shrinks, as shown in Fig. 7.2(b). These regions are located at the edges along m and correspond to Bragg reflections when a force is applied along $\mathbf{Y}$. We apply forces along $\mathbf{X}$, then $\mathbf{Y}$ and finally $\mathbf{X}$ again, and the successive steps of the ramp have zero slopes of the velocity of the moving frame at their edges to turn the force on and off with minimal diabatic effects. When the desired quasimomentum state is reached, we reduce the coupling strengths by a factor of 0.7 and reach the final values $t_x^{(exp)} = 5.69(6)E_{\mathrm{rec}}$ and $t_z^{(exp)} = 5.1(2)E_{\mathrm{rec}}$ in 200 µs. The preparation protocol lasts up to 1.5 ms, limited by the energy gap on the order of $4.5E_{\mathrm{rec}}$ in the bulk.

We first check that the measured mean quasi-momentum follows the ramp of the force. This allows us to perform the deconvolution of the signal, similarly to our procedure for the atomic Hall cylinder. The main difference stems from the two-dimensional dynamic of the atoms, which complicates the image analysis. In particular, the spin separation using the magnetic gradient and the z-dynamics are recorded on the same axis of the camera, so we independently calibrate the effect of the Stern-Gerlach gradient for all Dicke states $|m\rangle$. We also perform independent experiments to estimate the directions of the propagation axes of the two pairs of beams on our imaging system.

More complexity arises from the position drifts that occur in the lab frame during the application of the inertial forces. This effect is small for the data presented in Chapter 6. Indeed, for the spin-velocity distribution measurements during Bloch oscillations in the Hall cylinder, we prepare a quasimomentum state $\langle q_x \rangle = 2k$ with zero velocity in both the moving and laboratory frames. The states at the edge of the first Brillouin zone are reached in 200 µs and have acquired a velocity of $1.5v_{\mathrm{rec}}$ in the laboratory frame. The ramp leads to a position drift of typically 0.5 µm along the propagation axis of the Raman beams, corresponding to $0.06v_{\mathrm{rec}}$ in the velocity distribution, since it is measured after a 2.3 ms-long expansion. However, in our four-dimensional Hall system, depending on the prepared quasimomentum state, the position drifts range from 5 µm to 50 µm, *i.e.* a shift of $0.5 - 5.5v_{\mathrm{rec}}$ in the velocity distribution measurements. We take these drifts into account by measuring the centre-of-mass at a short expansion time of 0.1 ms, to subtract it from the spin-resolved velocity distribution measurements. Moreover, the position drifts are not negligible compared to the waists of the Raman beams and occur in the (x, z) plane where the laser beams give rise to transverse confinements, of

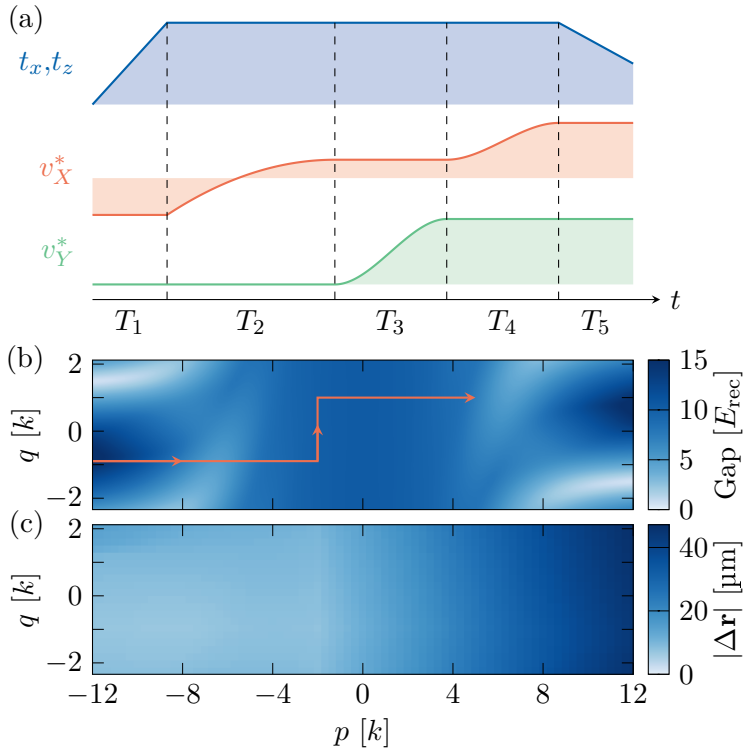

Figure 7.2 – Panel (a): Scheme of the dynamic control of the parameters (t_x, t_z, v_X^*, v_Y^*) to adiabatically prepare a quasimomentum state in the ground band of the total Hamiltonian. Five steps of lengths T_i with integer $1 \leq i \leq 5$, consist of successive ramps of the parameters. Panel (b): Energy gap from the ground state to the first excited state, numerically computed for the maximal values of the coupling strengths during the ramp. We show the paths followed in parameter space to reach a given quasimomentum state without crossing regions with small gaps. Panel (c): Absolute value of the position drifts that occur during the loading protocol, as a function of the final quasimomentum state, numerically computed based on the experimental ramps.

frequencies $\omega_x^{\mathrm{trap}} = 2\pi \times 78\,\mathrm{Hz}$ and $\omega_z^{\mathrm{trap}} = 2\pi \times 163\,\mathrm{Hz}$, measured for atoms polarised in $|m = -J\rangle$. The trapping potentials induce a force as the atoms leave the centre of the beams, as well as gravity along the z axis only. Both forces are of the order of $10^{-3}\hbar k/\mu\mathrm{s}$ and are a small correction to the force that we apply, typically in the range of $10^{-2} - 10^{-1}\hbar k/\mu\mathrm{s}$.

Similarly to the Hall cylinder, we apply a deconvolution algorithm to measure the properties of the ground band. In this set of measurements, the atomic cloud has an initial temperature of 0.26 µK, corresponding to a momentum width $\sigma_p \simeq 0.6k$. For a Bloch state with a quasimomentum $\mathbf{P}$, the velocity belongs to an infinite set of discrete values:

$$\mathbf{v} = \frac{\hbar}{M}(\mathbf{P} - 2km\mathbf{e}_x + s\mathbf{K}), \tag{7.5}$$

with s an integer. States with different quasimomenta (modulo $\mathbf{K}$) have velocities

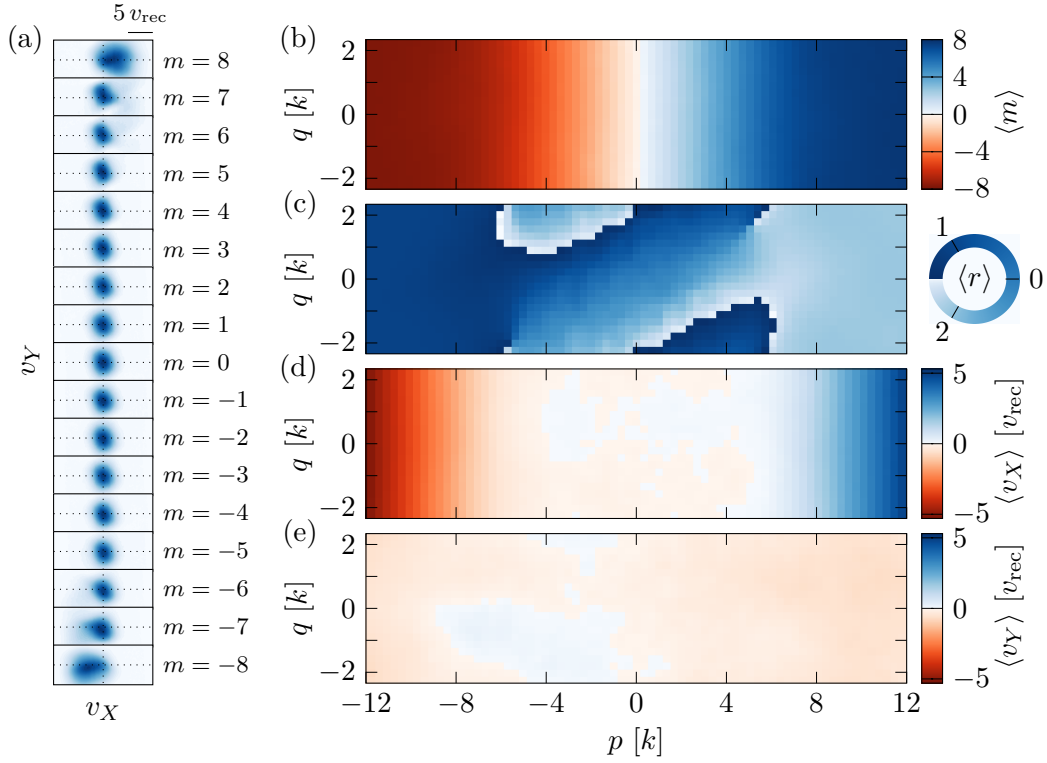

Figure 7.3 – Panel (a): Velocity distributions for each spin projection states, averaged over all prepared mean quasimomentum states. Deconvolution is performed on these images by exploiting the quasimomentum conservation. Panels (b,c,d,e): Distribution of the magnetisation $\langle m \rangle = \langle \hat{J}_z \rangle$, the mean position along the r axis using the formula $\langle r \rangle = 3/(2\pi) \arg \langle \exp(\mathrm{i}2\pi m/3) \rangle$ and the mean velocities along the two orthogonal axes $\mathbf{X}$ and $\mathbf{Y}$, as a function of the quasimomentum $\mathbf{P} = M\mathbf{v}/\hbar + 2km\mathbf{e}_x \,(\mathrm{mod}\,\mathbf{K})$.

at different values, which authorises the deconvolution of the signal. We average the spin-resolved velocity distributions measured for mean quasimomentum states spanning the whole Brillouin zone and interpreted in their reference frame. We obtain a set of $2J + 1 = 17$ two-dimensional distributions from which we reconstruct the properties of each quasimomentum state. In Fig. 7.3(a), we plot these distributions $P(m, v_X, v_Y)$ with coordinates v_X and v_Y. We observe that the velocities are always bounded along Y. The velocities along X are bounded in the bulk of the system for m close to zero, while a ballistic motion is visible on the both edges near $m \approx \pm J$ with a chirality typical of Hall systems.

We show our measurements of the mean positions $\langle m \rangle$ and $\langle r \rangle$ along the synthetic axes and of the mean velocities along the $\mathbf{X}$ and $\mathbf{Y}$ axes in Fig. 7.3(b-e). For a force oriented along $\mathbf{e}_x - \mathbf{e}_z \propto \mathbf{X}$, the increase of velocity due to the force is compensated by light-induced momentum kicks, which come together with an increase in the mean spin projection $\langle m \rangle$. This corresponds to a Hall drift along m. This behaviour contrasts with the case of a force along $2\mathbf{e}_x + \mathbf{e}_z \propto \mathbf{Y}$, the direction of the reciprocal lattice vector $\mathbf{K}$, with a winding along the cyclic axis r and a constant magnetisation.

In the bulk, the mean velocity remains much lower than the recoil velocity, which underlines the quasi-flatness of the ground band. At the edges of the system where the stretched states $|\pm J\rangle$ are predominantly populated, we recover a non-zero mean velocity, whose $\mathbf{X}$ component linearly increases with p, while the $\mathbf{Y}$ velocity remains low. This behaviour is characteristic of an anisotropic edge mode of a four-dimensional quantum Hall system, which can be viewed as a collection of one-dimensional conduction channels oriented along $\mathbf{X}$.

Our characterisation of the ground band contains the response to a force applied in any direction in the (x, z) plane. It is possible to reconstruct the components of the Berry curvature defined on the four-dimensional space [184, 282], which represents the local response of the system to a force. Due to the presence of gapless edge modes, the topology of the ground band appears when considering the bulk of the system only. Similarly to the two-dimensional Hall effect with edges [46], we can define a quantity that locally probes the topology of the system and coincides with the second Chern number for a system of infinite size. The quantisation of the second Chern number can also be directly checked from the non-linear response to both an electric force and a magnetic perturbation. These complementary studies will be the subject of a dedicated publication.

7.2 Interactions in an atomic Hall cylinder

In this Section, we discuss the role of interactions in our implementation of an atomic Hall cylinder with a synthetic cyclic dimension. We first briefly describe the interactions in a spinor Bose-Einstein condensate from a general point of view. We then restrict ourselves to a simplified model of the interactions based on the characteristic of the ground band of our system. We then analyse the ground state for interacting particles using a tight-binding model that approximates the Hamiltonian of our system and using numerical simulations of the Gross-Pitaevskii equation valid for pure Bose-Einstein condensates. For well-chosen parameters, we observe that the ground state is a one-dimensional precursor of vortex lattices.

7.2.1 Spinor Bose-Einstein condensates

Our description of short-range interactions, such as van der Waals interactions, in Section 1.1.3 focuses on the case of spinless particles or, equivalently, of spin-polarised particles in an extremal coherent spin state, such as $|m = -J\rangle$, in binary collisions owing to the small density of the atomic gas. In general, colliding atoms can be found in any spin state and the states of the atoms after interacting are obtained from symmetry considerations. The inclusion of internal degrees of freedom in the scattering process enriches the phenomenology of ultracold atoms with the occurrence of exotic phases mixing superfluidity and magnetism [283, 284] for example. Such ultracold gases are referred to as spinor Bose-Einstein condensates [285, 286] and the general form of their scattering potential reads as follows:

$$V_s(\mathbf{r}) = V_{\text{spin}} \otimes \delta(\mathbf{r}), \tag{7.6}$$

where we simplify the writing of the pseudo-potential to the Dirac function. We still restrict ourselves to the low-energy regime where rotationally-symmetric s-wave scattering dominates and imposes the conservation of the total angular momentum $\mathcal{F}$ of the colliding pair. The exchange symmetry for indistinguishable bosons in the case of s-wave scattering constrains the total angular momentum to even values only. Therefore, the colliding atoms interact through independent spin-$\mathcal{F}$ channels (with $0 \leq \mathcal{F} \leq 2J$ even) and we decompose the interaction term on these channels as:

$$V_{\text{spin}} = \sum_{\substack{\mathcal{F}=0 \\ \text{even}}}^{2J} g_{\mathcal{F}} \mathcal{P}_{\mathcal{F}}, \tag{7.7}$$

where $\mathcal{P}_{\mathcal{F}} = \sum_{\mathcal{M}=-\mathcal{F}}^{\mathcal{F}} |\mathcal{F}, \mathcal{M}\rangle\langle\mathcal{F}, \mathcal{M}|$ is the projector onto the subspace with total angular momentum $\mathcal{F}$ and $g_{\mathcal{F}} = 4\pi\hbar^2 a_{\mathcal{F}}/M$ is the interaction strength of the spin-$\mathcal{F}$ channel, characterised by the scattering length $a_{\mathcal{F}}$.

Spinor physics has been particularly studied for spin-1 condensates [287, 288] where the interaction between two atoms is given by $c_0\hat{\mathbb{1}} + c_2\mathbf{J}_1 \cdot \mathbf{J}_2$. It results in collision-driven spin-mixing dynamics, where two atoms initially in the sublevel $|m = 0\rangle$ can coherently and reversely scatter into a pair of atoms in the opposite stretched states $|m = \pm 1\rangle$. The coherent dynamics has a frequency set by the interaction parameter c_2, that depends on the two scattering lengths a_0 and a_2, and has first been observed in spinor condensates of rubidium and sodium atoms [289–292].

Dysprosium atoms can be employed to explore spinor physics with a large spin $J = 8$. The interaction of pairs of atoms via s-wave scattering is fully described by the $J+1 = 9$ scattering lengths associated with the different independent spin channels. A pair of spin-polarised atoms in $|-J\rangle$ interacts through the spin-$2J$ channel only, which depends on a single scattering length a_{16}. This is the only scattering length known to date and equals $a_{16} = 126(10)a_0$, as introduced in Section 1.1.3. The other scattering lengths could be measured using photoassociation spectroscopy [293], from the rate of energy redistribution in a confined atomic cloud via two-body collisions [294] or from the rate of collision-driven coherent spin dynamics for example. Interestingly from the point of view of synthetic dimensions, the spin-exchange interaction terms such as $(m_1, m_2) \to (m_1 - 1, m_2 + 1)$ can be viewed as correlated tunnellings along the synthetic lattice made of the $2J + 1$ Dicke states.

7.2.2 Restriction to the atomic Hall cylinder

We restrict the discussion to the spin states involved in our implementation of an atomic Hall cylinder at low energy and analyse the role of s-wave interactions and magnetic dipole-dipole interactions. The states of the ground band decompose on a set of three coherent states $|\theta = \pi/2, \phi\rangle$ with $\phi = 0$, $2\pi/3$ and $4\pi/3$, which play the role of momentum states along the synthetic cyclic axis r. Because of the symmetry upon spin rotation of angle $2\pi/3$ around z, the collision of a pair of atoms is restricted to a single channel $\phi, \phi' \to \phi, \phi'$ which preserves the number of atoms in each coherent state. As we have already pointed out, atoms in the same coherent states interact only through the spin-$2J$ channel, characterised by the scattering length $a \equiv a_{2J}$. The symmetry upon spin rotation of angle $2\pi/3$ around z also implies that the interaction of atoms in different coherent states is given by a single yet unknown scattering length a', given by a linear combination of the $2J + 1$ scattering lengths $a_{\mathcal{F}}$, whatever the two coherent states among the three possible pairs. The two scattering lengths a and a' can be arbitrarily tuned using a bias magnetic field in the vicinity of a Feshbach resonance.

The magnetic dipole-dipole interactions are described by the potential:

$$V_{\mathrm{dd}}(\mathbf{r}) = \frac{\mu_0 (g_J \mu_B)^2}{4\pi} \frac{\mathbf{J}_1 \cdot \mathbf{J}_2 - 3(\mathbf{J}_1 \cdot \mathbf{e}_r)(\mathbf{J}_2 \cdot \mathbf{e}_r)}{r^3}, \tag{7.8}$$

with $\mathbf{e}_r = \mathbf{r}/r$. In the case of two spin-polarised atoms with a common orientation, it simplifies to the formula in Eq. 1.5, which depends on the distance between the particles and the relative angle between the orientation of the magnetic dipoles and the vector $\mathbf{r}$. Here, we consider the case of two atoms initially in coherent states $|\phi\rangle$ and $|\phi'\rangle$. The vanishing expectation value of the spin operator $\langle\phi_1|\mathbf{J}|\phi_0\rangle \approx 10^{-5}$, for coherent states with $\theta = \pi/2$ and azimuthal angle separated by $2\pi/3$, imposes that the magnetic dipole-dipole interaction conserves the spin states $\phi, \phi' \to \phi, \phi'$. This process also preserves the population in each coherent state. We now restrict the dynamics to a one-dimensional system along the axis x of propagation of the Raman beams. The dynamic along the transverse axes can be frozen by means of strong transverse confinement using optical lattices, for example. In a one-dimensional system, the magnetic dipole-dipole interaction can be incorporated as a contact interaction [295], with a dependence on the orientation of the magnetic dipoles. Its

derivation can be found in Appendix D. We distinguish two contributions depending on whether the two colliding atoms are initially in the same state or not, which correspond to modifications of the a and a' scattering lengths in the contact potential respectively. Overall, the interaction between a pair of atoms, restricted to the ground states of the atomic Hall cylinder, is fully described by only two parameters, that we can control using Feshbach resonances.

To obtain the ground state of the system in the presence of both types of interactions, we consider two approaches: an approximate tight-binding model similar to the extended Bose-Hubbard model, treated in the deep-well limit without global coherence, and an exact simulation of the stationary solution for a pure Bose-Einstein condensate using an imaginary time evolution of the Gross-Pitaevskii equation.

Tight-binding model

We recall the effective Hamiltonian of the atomic Hall cylinder in the momentum state basis:

$$\begin{aligned} H =& \frac{M v_x^2}{2} + V_{\text{eff}}(x), \\ V_{\text{eff}}(x) =& -2t \sum_{\phi=0,\frac{2\pi}{3},\frac{4\pi}{3}} \cos(2kx-\phi)\, |\phi\rangle\langle\phi| \,, \end{aligned} \tag{7.9}$$

where $t \approx t_a + t_b = 18.6(4)$, with t_a and t_b the coupling strengths associated with the processes (a) and (b) involving rank-1 and rank-2 spin couplings respectively. Since the effective potential is diagonal in the momentum state basis $\{|\phi\rangle\}$ and spatially-periodic with period π/k, we can separate the Hamiltonian into three subspaces and apply the Bloch theorem with the formation of a band spectrum with three-fold degeneracy. We define a quasimomentum q_x defined on a Brillouin zone of size $2k$ and the corresponding Bloch states $\psi^{\phi}_{q_x}(x)$. The three-fold degeneracy is the sign of the invariance upon magnetic translation of the exact potential, as defined in Section 6.2, with a corresponding three times larger Brillouin zone and no degeneracy.

The Fourier components of the Bloch states are solutions of the well-known eigenvalue equation of a spinless particle in a lattice of peak-to-peak amplitude $4t$ and period $\pi/k = \lambda/2$. Each state ϕ has a corresponding lattice with a minimum at $\phi/2k$ and the three lattices are shifted with respect to each other by $\lambda/6$, a third of the lattice period. An alternative description uses the so-called Wannier basis whose states are localised around the lattice sites. The Wannier wavefunctions are defined from the Bloch basis by a discrete Fourier transformation. In a one-dimensional system, we can choose them to be real functions that exponentially decay away from the lattice sites. This basis is particularly relevant in the case of a deep lattice potential with $4t \gg E_{\text{rec}}$, which exhibits quasi-flat bands. For example, our realisation of the atomic Hall cylinder lies deep in this regime, with $4t \approx 75 E_{\text{rec}} \gg E_{\text{rec}}$.

We decompose the Hamiltonian on the Wannier basis and restrict the Hilbert space to the ground band only, which is valid for ultracold atoms with zero population in the higher orbitals. We introduce the annihilation operator $\hat{a}_s$ for a particle in the Wannier state centred on the site $R_s = s\pi/3k$ (s integer). More precisely,

we introduce three sets of operators for each ϕ states corresponding to the site $R_j^\phi = j\lambda/2 + \phi/2k$ (j integer), that we rewrite as the $\hat{a}_s$ operators centred on the sites $R_s = R_j^\phi = s\lambda/6$. While the Hamiltonian is diagonal in the Bloch basis, it has off-diagonal terms in the Wannier basis that we interpret as hopping terms from one site to another. The coupling between lattice sites decreases rapidly with the distance between them because the Wannier functions are sharply peaked at the lattice sites. In the so-called tight-binding limit for a very deep lattice potential, we only keep the on-site term and the coupling between neighbouring sites $j \leftrightarrow j+1$, or equivalently $s \leftrightarrow s+3$. We discard the on-site term as it is uniform over all lattice sites and obtain the tight-binding Hamiltonian:

$$H_{\mathrm{TB}} = -J_1 \sum_s (\hat{a}_{s+3}^\dagger \hat{a}_s + \mathrm{hc}). \tag{7.10}$$

The tunneling energy can be computed from the Wannier wavefunctions or, equivalently, from the energy spectrum of the ground band. To a good approximation, it equals a quarter of the residual bandwith of the quasi-flat ground band. Tunneling between more distant sites is strongly reduced, by several orders of magnitude compared to J_1.

We want to treat the two interaction terms for spin states in the same coherent state or in two different coherent states, from Section 7.2.2, in the Wannier basis. Their expression is facilitated by the fact that a Wannier function centered on R_s with $s = 3j + i$ (with the quotient j and the remainder i of the Euclidian division of s by 3) is associated with a single coherent state $|\phi = i2\pi/3\rangle$. Due to the decay of the Wannier functions far from the lattice site, we only keep the two dominant terms:

$$\begin{aligned} V_{\mathrm{int}} =& U_0 \sum_s \frac{\hat{n}_s(\hat{n}_s - 1)}{2} + U_1 \sum_s \hat{n}_s \hat{n}_{s+1}, \\ U_0 =& g \int \mathrm{d}x |w(x)|^4 \quad \text{with} \quad g = \frac{4\pi\hbar^2 a}{M}, \\ U_1 =& g' \int \mathrm{d}x |w(x)|^2 |w(x+\lambda/6)|^2 \quad \text{with} \quad g' = \frac{4\pi\hbar^2 a'}{M}, \end{aligned} \tag{7.11}$$

with $\hat{n}_s = \hat{a}_s^\dagger \hat{a}_s$ the occupation number at site s and $w(x)$ the Wannier function centred on $R = 0$. The Wannier function at site s can be deduced from the Wannier function $w(x)$ centred on $x = 0$ by translation $w_{R_s}(x) = w(x - R_s)$. The first term of the Hamiltonian is an on-site interaction term for a pair of colliding atoms in the same coherent state, governed by the scattering length a. The second one is an interaction term for two atoms in neighbouring sites at distance $\lambda/6$, that correspond to different coherent states, and it is thus characterised by the scattering length a'.

The many-body Hamiltonian reads as follows:

$$H = -J_1 \sum_s (\hat{a}_{s+3}^\dagger \hat{a}_s + \mathrm{hc}) + U_0 \sum_s \frac{\hat{n}_s(\hat{n}_s - 1)}{2} + U_1 \sum_s \hat{n}_s \hat{n}_{s+1}, \tag{7.12}$$

with J_1, U_0 and U_1 positive. The ratio U_1/U_0 can be tuned using Feshbach resonances affecting the scattering lengths a and a'. This Hamiltonian is similar to the extended Bose-Hubbard model and contains the same on-site and nearest-neighbour interaction terms. Their difference stems from the range of the hopping term. However, when the

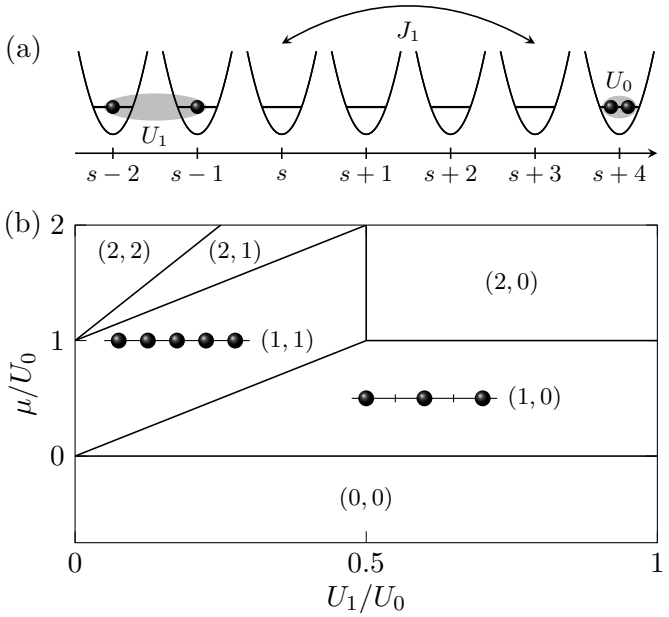

Figure 7.4 – Panel (a): Representation of the terms of the tight-binding Hamiltonian, where the lattices at the position of the minima (every $\lambda/6$) are well-approximated by harmonic oscillators with atoms lying in their ground state only. The J_1 terms couple sites separated by $\lambda/2$, *i.e.* $s \leftrightarrow s+3$ with integer s. The onsite and nearest-neighbour energy costs U_0 and U_1 are represented with grey shaded areas. Panel (b): Phase diagram in the atomic limit ($J_1 \ll U_0, U_1$), with respect to the chemical potential μ/U_0 and the ratio of energy costs U_1/U_0. The phases are characterised by the occupation number of the odd and even sites $(n_{\text{even}}, n_{\text{odd}})$. We represent the occupation of a few lattice sites for the charge-density-wave phase $(1,0)$ (or $(0,1)$) at half filling $\mu/U_0 = 0.5$ and the Mott insulator phase $(1,1)$ at unit filling $\mu/U_0 = 1$.

interaction energies dominate $J_1 \ll U_0, U_1$ which is valid in the regime of deep lattices, the two models become identical and the phase diagram is well established [296, 297]. In the atomic limit $J_1 \ll U_0, U_1$, we expect Mott insulator or charge-density-wave phases with vanishing condensate order parameters. The Mott insulator phase corresponds to a uniform number of particles per site, *i.e.* a Fock state at each site, while a charge-density-wave phase is characterised by a breaking of the translation symmetry with different occupation numbers in odd and even states. We label these phases by the integer occupation numbers $(n_{\text{even}}, n_{\text{odd}})$ in even and odd lattice sites. In particular, the charge-density-wave phase with alternating sites with zero and unit occupations can be viewed as a one-dimensional precursor of the two-dimensional Laughlin state, both of them occurring at half filling. The phase diagram expected in the atomic limit is shown in Fig. 7.4 as a function of the chemical potential μ and the ratio of interaction energies U_1/U_0. The intermediate limit with a non-negligible tunnelling J_1 hosts superfluid phases, which can be treated using a variational minimisation of $\langle\Psi|H - \mu\hat{N}|\Psi\rangle$ with the so-called Gutzwiller ansatz

for the many-body wavefunction $|\Psi\rangle$ [298], which is written as a product state of coherent superpositions of Fock states at each site. In such a treatment, the chemical potential μ is defined as the Lagrange multiplier in the grand canonical ensemble, to force the conservation of the total atom number $\hat{N} = \sum_s \hat{n}_s$ in the minimisation procedure.

Gross-Pitaevskii equation

The dynamic of a pure Bose-Einstein condensate in the mean-field regime of interactions is governed by the so-called Gross-Pitaevskii equation [299], a time-dependent generalisation of the Schrödinger equation with non-linear terms arising from the interactions. We describe the quantum state of our system by a spinor classical field whose components correspond to the different states of the synthetic space. Since we restrict our analysis to the low energy regime with only three populated coherent states $|\phi\rangle$, we consider a spinor with three components $\psi_i(x,t)$, with $0 \leq i < 3$ integer corresponding to $|\phi = i2\pi/3\rangle$. The ground state is given by the stationary solutions of the equation:

$$\left(-\frac{\hbar^2}{2M}\boldsymbol{\nabla}_{\mathbf{r}}^2 + V_{\text{ext}}^{(i)}(\mathbf{r}) + gN|\psi_i(\mathbf{r},t)|^2\right)\psi_i(\mathbf{r},t) + g'N\sum_{j\neq i}|\psi_j(\mathbf{r},t)|^2\psi_j(\mathbf{r},t) = \mathrm{i}\hbar\frac{\partial\psi_i(\mathbf{r},t)}{\partial t}, \tag{7.13}$$

for a wavefunction normalised to unity $\int \mathrm{d}\mathbf{r}\sum_j |\psi_j(\mathbf{r},t)|^2 = 1$. The interaction coupling strengths $g = 4\pi\hbar^2 a/M$ and $g' = 4\pi\hbar^2 a'/M$ correspond to interactions between atoms in the same coherent state and in different states respectively. The external potential $V_{\text{ext}}^{(i)}$ projected on the state $|\phi = i2\pi/3\rangle$ has two contributions:

$$V_{\text{ext}}^{(i)}(\mathbf{r}) = \sum_{s=x,y,z}\frac{1}{2}M\omega_s s^2 - 2t\cos(2kx - \phi). \tag{7.14}$$

where the first one corresponds to a three-dimensional harmonic trap with angular frequencies ω_s ($s = x, y, z$) and the second one is the spin coupling, which is diagonal in the $|\phi\rangle$ states.

We compute the stationary ground state solutions of the multi-component Gross-Pitaevskii equation using evolution in imaginary time [300]. When the on-site interaction term g dominates, we observe a total density modulation of period $\lambda/6$ along x and a modulation of period $\lambda/2$ when considering each ϕ state independently, as shown in the left panels of Fig. 7.5. The energy cost of having several atoms at the same position favours the uniform occupancy of a large number of lattice sites. The trapping potential reduces the population in sites far from the centre of the trap. In the limit of small interaction g and small confinement, the density in the vicinity of each lattice minimum is well approximated by a Wannier function.

The interaction term g' for spin states in different coherent states induces an energy cost for atoms on neighbouring Wannier sites, separated by $\lambda/6$, as the overlap of the corresponding Wannier functions is non-zero. It also adds an energy cost for atoms on more distant sites, the smallest distance being $\lambda/3$, which is smaller by more than two orders of magnitude due to the fast decay of the Wannier function away from their centre. This interaction term favours the alternation of sites with high and low occupancies, with a spontaneous translation symmetry breaking, and creates a total

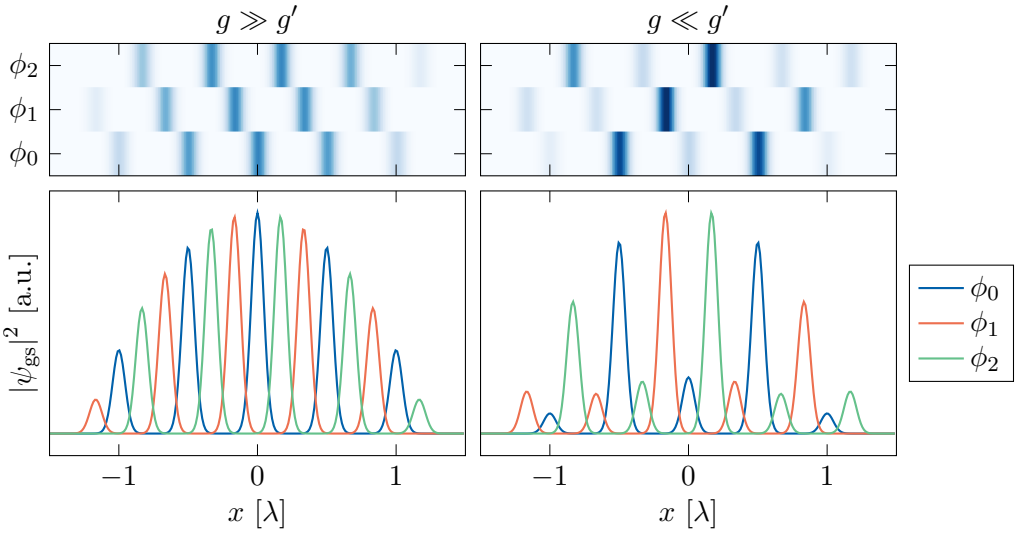

Figure 7.5 – Numerical simulations of the ground state by evolving the Gross-Pitaevskii equation in imaginary time, with the effective model with three internal states ϕ, for the two limits $g \gg g'$ and $g \ll g'$ on the left and right sides respectively. We plot the density of the ground state wavefunctions along x for all three internal states. In the limit of large contact interactions for atoms in different ϕ states, there is a breaking of the discrete translation invariance and the ground state is a charge-density-wave phase.

density modulation of period $\lambda/3$, instead of $\lambda/6$. For an infinite system along x with translation invariance, *i.e.* in the absence of a trapping potential, the ground state of the system is two-fold degenerate with either even or odd Wannier sites having a lower occupancy. The presence of a trapping potential lifts the degeneracy and favours one of the two configurations. When the interaction term g' dominates, the ground state is a charge-density-wave, as can be seen in the right-hand panels of Fig. 7.5. Experimentally, the discrete translation symmetry breaking can be probed in the density profile using high-resolution imaging at the length scale of $\lambda/6 \approx 100\,\mathrm{nm}$ or in the momentum distribution recorded after a time-of-flight expansion, with the observation of additional peaks.

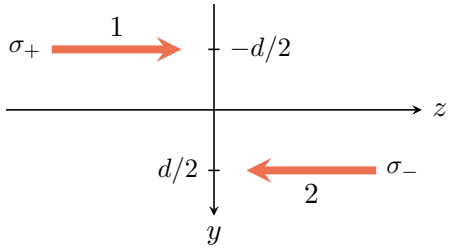

Figure 7.6 – Scheme of two counter-propagating beams 1 and 2, propagating along $\pm\mathbf{z}$ and with opposite circular polarisations inducing $\sigma_\pm$ transitions respectively. They are off-centred along $\mathbf{y}$ by a distance d from each other. The spatial dependence of the total polarisation along $\mathbf{y}$ creates a non-zero artificial gauge field orthogonal to the (y, z) plane.

7.3 Artificial gauge fields with large spin atoms

In this Section, we move away from the concept of synthetic dimensions and consider the implementation of an artificial gauge field for the motion of neutral particles, mediated by light-matter coupling. The realisation of topologically-protected many-body states is still pending and requires the preparation of phases with a small number of particles on the order of the number of magnetic fluxes. In this regime with a filling fraction on the order of unity, strongly-correlated many-body states, such as a Laughlin state at half filling, could be accessed. A first step towards fractional quantum Hall states is the preparation of phases with interacting particles, at large filling fractions where a mean-field approach holds. This corresponds to the regime that we described in this Chapter using the Gross-Pitaevskii equation for example, by treating the interaction on the wavefunction as the effect of a bath of surrounding atoms. The phenomenology of this regime is well established with the appearance of vortices that pierce the sample and allow the magnetic flux to pass through, similarly to type-II superconductivity. Vortices are local minima of the density, characterised by a winding of the wavefunction around their core by a non-trivial integer multiple of 2π [299, 301]. The vortices have a repulsive interaction that favours the formation of a vortex lattice, such as the well-known Abrikosov lattice [38]. We also mention that the presence of vortices has also been investigated theoretically in higher dimensions [302].

This regime of interactions has been initially explored with ultracold atoms using rotating Bose-Einstein condensates [33, 34, 303–305], where the Sagnac phase in the rotating frame plays the role of the Aharonov-Bohm phase. It has been followed by experiments with dressed states using light coupling between internal states, pioneered in the Spielman group [37]. The spatial dependence of the ground state leads to an artificial vector potential for the motion of particles in real space. In their work, they use a magnetic gradient such that there is a spatially-varying Zeeman splitting which modifies the local ground state. Since then, this scheme has been extended to the case of large-spin atoms [306, 307].

Our proposal follows an alternative approach to design the required spatial dependence of the ground state, using off-centred counter-propagating beams [155].

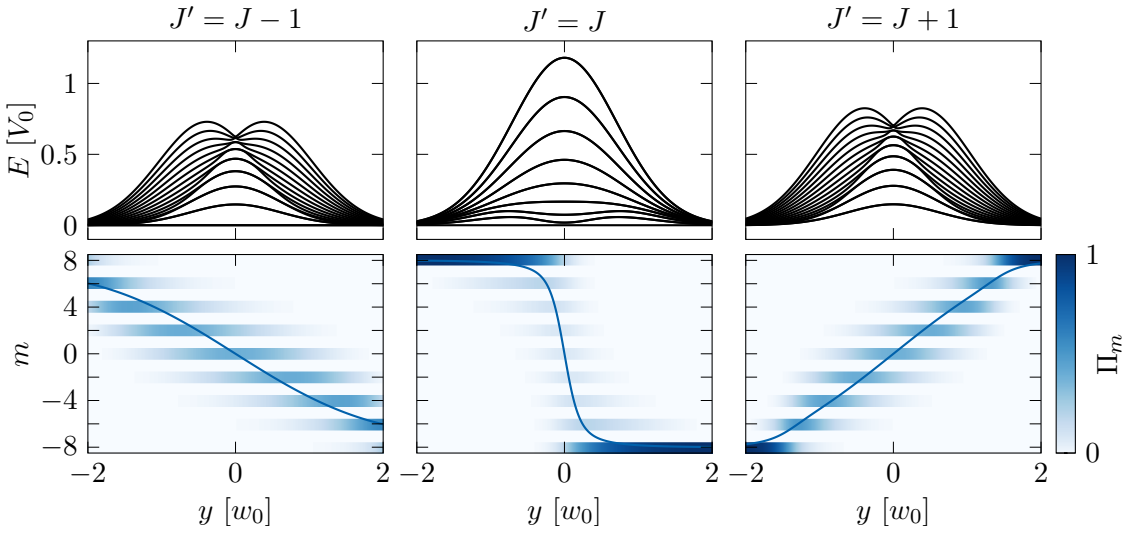

Figure 7.7 – Energy spectrum E (top panels) and spin distribution Π_m of the ground state with the mean projection $\langle \hat{J}_z \rangle$ in solid lines (bottom panels), as a function of the position y in units of the waist of the beams w_0, for the three possible values of the total angular momentum J' of the excited level ($J-1$, J and $J+1$ from left to right). The numerical simulations are performed in the limit of infinite coupling V_0 for which the spin couplings dominate the kinetic energy. If the ground state is two-fold degenerate, we plot the population of the ground state of even parity.

This leads to a smooth variation of the light polarisation over a distance set by the waists and separation of the beams. In this Section, we discuss the feasibility of this proposal and the differences induced by the choice of the optical transition to an excited electronic level with a total angular momentum J'. This study is initiated by the recent installation of a pair of counterpropagating beams at 626.1 nm with $J' = J + 1$ along the gravity axis with opposite circular polarisations, which we use for our implementation of a four-dimensional quantum Hall system.

We consider this problem for any value of J' for generality and work at zero field to suppress the effect of dipolar relaxation. The experimental configuration is represented in Fig. 7.6. The two beams 1 and 2 have the same angular frequency ω_0 and a transverse Gaussian profile $A(y)$ determined by their beam waist w_0. They propagate along $\pm\mathbf{z}$, with opposite circular polarisations $\sigma_\pm$. They are off-centred by $\mp d/2$, with typically $d = w_0/2$, such that the total light field reads as follows:

$$\mathbf{E}(x,y) = \sqrt{A_1(y)^2 + A_2(y)^2}\mathrm{e}^{-\mathrm{i}\omega_0 t}\left(\cos\frac{\theta(y)}{2}\mathrm{e}^{\mathrm{i}kz}\boldsymbol{\epsilon}_+ + \mathrm{e}^{-\varphi}\sin\frac{\theta(y)}{2}\mathrm{e}^{-\mathrm{i}kz}\boldsymbol{\epsilon}_-\right), \quad (7.15)$$

with the relative phase between the two beams φ and the two transverse profiles $A_1(y) = A(y + d/2)$ and $A_2(y) = A(y - d/2)$. We define the mixing angle $\theta(y)$ from the relation $\tan(\theta(y)/2) = A_2(y)/A_1(y)$. Far from the centre along y, the angle $\theta(y)$ approaches 0 for negative y and π for positive y, corresponding to a dominant effect of the beam 1 or 2 respectively, and the ground state is one of the stretched states $|\pm J\rangle$.

At the centre $y = 0$, both beams equally contribute and the ground state depends on the Clebsch-Gordan coefficients and thus on the value of J'. We plot the energy spectrum and the spin distribution of the ground state as a function of the y-position, for the three values of J', in Fig. 7.7. The calculations are performed in the purely spin case, in the absence of coupling between internal and external states, a situation that may seem artificial at first but whose relevance will be revealed later. The beams only couple states of the same parity $m \leftrightarrow m+2$ with two-photon optical transitions involving one σ_+ photon and one σ_- photon, which preserves the parity of the state. This leads to an almost two-fold degeneracy of the ground states for $y \approx 0$, with two states of even and odd parities. For $J' = J-1$, the degeneracy is exact for all angles $\theta(y)$ whereas for $J' = J+1$ it is only approximate and occurs over a wide range, until the ground state gets polarised in either of the stretched states. For $J' = J$ the branch with even parity remains the true ground state for all values of $\theta(y)$, and the first excited state has odd parity and an eigenenergy which approaches that of the ground state in the vicinity of $y = 0$. The ground state at the centre $y = 0$ has distinct properties depending on the spin J' since it is the single state $|0\rangle_x$ for $J' = J$ and the pair of coherent superpositions $(|-8\rangle_x \pm |+8\rangle_x)/\sqrt{2}$ of the stretched states along x, for $J' = J \pm 1$. Moreover, the cases $J' = J$ and $J' = J-1$ have one and two dark states respectively for this choice of light polarisations, meaning that the ground states are not coupled to light and do not suffer from heating due to residual population in the excited state, an interesting feature for practical implementation.

We consider the full Hamiltonian which contains the kinetic energy and a coupling between the spin and the motion along the z axis. After applying a gauge transformation with the unitary operator $U = \exp\left(-\mathrm{i}kz\hat{J}_z\right)$ and without approximation, the total Hamiltonian is given by:

$$\begin{aligned} H &= \hbar^2 \frac{p_x^2 + p_y^2 + (p_z + k\hat{J}_z)^2}{2M} + V_{\mathrm{LS}}(y) \\ V_{\mathrm{LS}}(y) &= U\tilde{V}_{\mathrm{LS}}(x,y)U^\dagger \\ &= V(y)\left[\left(\alpha_0 + \alpha_2\frac{J+1}{2(2J-1)}\right)\hat{\mathbb{1}} + \alpha_1\cos\theta(y)\frac{1}{2J}\hat{J}_z\right. \\ &\qquad \left. + \alpha_2\frac{3}{4J(2J-1)}\left(\sin\theta(y)(\hat{J}_+^2 + \hat{J}_-^2) - 3\hat{J}_z^2\right)\right] \end{aligned} \tag{7.16}$$

with the spatially-varying coupling strength $V(y) = (A_1(y)^2 + A_2(y)^2)3\pi c^2\Gamma/(2\omega_0^3\Delta)$ corresponding to a unit Clebsch-Gordan coefficient. We denote V_0 its maximum value when considering a single beam. The $V_{\mathrm{LS}}(y)$ term is obtained from the coupling $\tilde{V}_{\mathrm{LS}}(x,y)$ induced by the two beams, by the gauge transformation which removes the x-dependence and incorporates it into the kinetic term. We discarded the phase difference φ in the equation above. The momentum $p_z = Mv_z/\hbar - k\hat{J}_z$ is a conserved quantity and the Hamiltonian can be co-diagonalised with it.

The very large coupling regime, where the spin coupling dominates the kinetic energy, is insightful in the understanding of our problem. In this limit, the ground state of the system is simply given by the spin couplings, which we have already computed in Fig. 7.7. It can also be obtained from the energy spectrum calcultated as a function of p_z, as we show in Fig. 7.8(a) for a given y-position. We consider

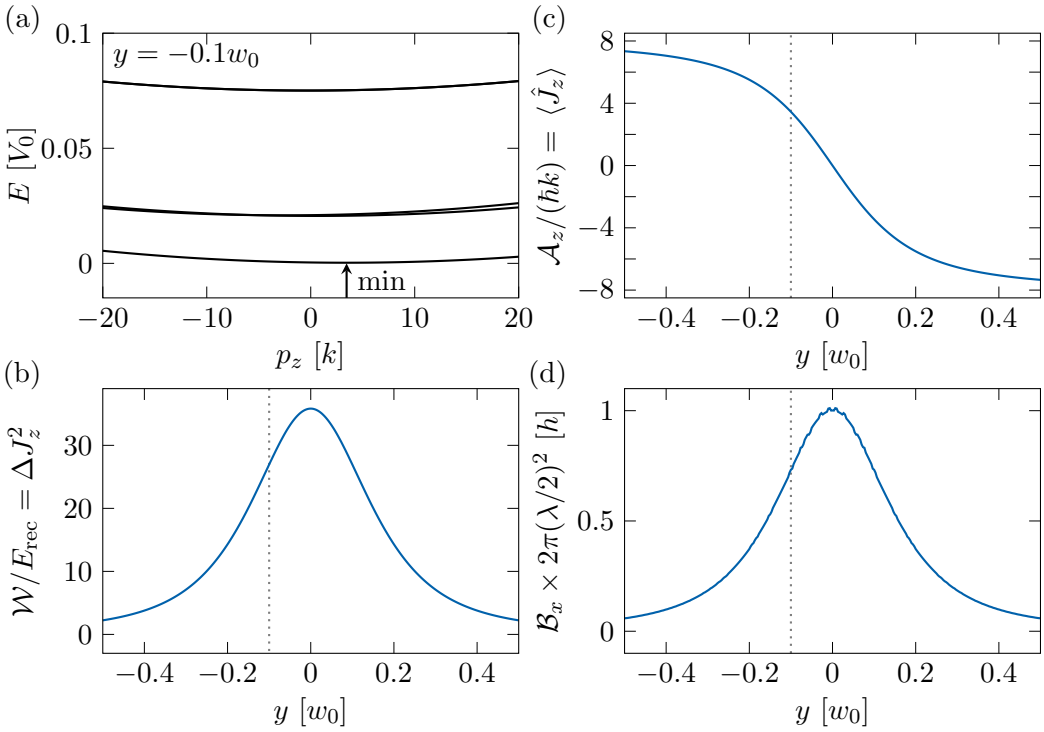

Figure 7.8 – Artificial gauge field for $J' = J$. Panel (a): Energy spectrum computed for a coupling $V_0 = 10^5 E_{\rm rec}$ at the position $y = -0.1w_0$ (marked in the other panels by a vertical dotted grey line), as a function of the conserved momentum p_z. We extract the minimum $p_{\rm min}(y)$, corresponding to the effective vector potential. Panels (b,c,d): Effective scalar potential (b), vector potential (c) and magnetic field (d) obtained from simulations of the energy spectrum, as a function of the position y. The effective magnetic field is expressed by its flux on a disk of radius $\lambda/2$, in units of the flux quantum h for a particle of effective charge $q = 1$.

the transition to $J' = J$, for a very large coupling $V_0 = 10^5 E_{\rm rec}$. This regime is accessible using our Ti-Sapph laser in the vicinity of the transition at 832.8 nm, with two beams of identical waist $w_0 = 50\,\mu$m and a total optical power $P = 4\,$W. The ground band has a dispersive shape and features a single minimum at a momentum denoted $p_{\rm min}(y)$ for each position y. We can expand the energy spectrum around this value as $E_0(y) + (p_z - p_{\rm min}(y))^2/(2M)$. The energy $E_0(y)$ contains the light shift of the ground state and an additional contribution. Interestingly, the former cancels out for the case of a dark state, such as a state of the ground band for $J' = J$ in the large coupling regime, and we are left with the latter only, referred to as an effective scalar potential. The momentum $p_{\rm min}(y)$ corresponds to an effective vector potential $A_z(y)$, constant along z but varying along y. The spatial dependence induces an artificial gauge field with amplitude $B_x = \partial_y A_z(y)$, orthogonal to the (y, z) plane. We plot the effective scalar potential, vector potential and magnetic field in Fig. 7.8(b,c,d). The effective magnetic field is peaked close to the centre $y = 0$ and varies over a distance of typically d of the order of tens micrometres.

This effective magnetic field can be recovered using the formalism of the adiabatic following of a dressed state, as initially described in Section 4.1.2. We recall the effective spinless Hamiltonian for the motion of the atoms:

$$H_{\text{dressed}} = \frac{(\mathbf{p}-\boldsymbol{\mathcal{A}})^2}{2M} + \mathcal{W} + E_0 + V_{\text{ext}},$$
$$\text{with} \quad \begin{cases} \boldsymbol{\mathcal{A}} &= \mathrm{i}\hbar \langle \tilde{\chi}_0 | \boldsymbol{\nabla} \tilde{\chi}_0 \rangle \,, \\ \mathcal{W} &= \hbar^2/(2M) \sum_{n\neq 0} |\, \langle \boldsymbol{\nabla} \tilde{\chi}_n | \tilde{\chi}_0 \rangle \,|^2, \end{cases} \tag{7.17}$$

with the external spin-independent potential V_{ext}, such as a harmonic trap, and the expectation value of the light shift for the ground state E_0, which is zero for a dark state. We define the local eigenstates of the spin coupling term $\tilde{V}_{\text{LS}}(y,z)$ at a given position $|\tilde{\chi}_l\rangle = |\tilde{\chi}_l(y,z)\rangle$, with l an integer index of the eigenstates. The artificial scalar and vector potentials can be rewritten in terms of the spin operators. We apply the gauge transformation defined earlier with unitary operator U and define the wavefunctions $|\chi_l(y)\rangle = U\,|\tilde{\chi}_l(y,z)\rangle$, which are eigenstates of the spin coupling $V_{\text{LS}}(y)$. The gauge transformation suppresses the z-dependence of the eigenstates. We neglect the terms that arise from the spatial variation of $|\chi_l(y)\rangle$. This can be seen as a consequence of the length scale of variation of the ground state along z and y, respectively set by typically $\lambda/2 \approx 400\,\text{nm}$, due to the interference of the two laser beams, and the distance $d = w_0/2 \approx 20\,\mu\text{m}$. As a consequence, the vector and scalar potential are given by:

$$\begin{aligned} \boldsymbol{\mathcal{A}}(y) &= \mathcal{A}_z(y)\mathbf{e}_z = -\hbar k \langle \hat{J}_z \rangle \mathbf{e}_z, \\ \mathcal{W}(y) &= \Delta J_z^2 E_{\text{rec}}, \end{aligned} \tag{7.18}$$

where we used the closure relation $\sum_l |\chi_l\rangle\langle\chi_l| = \hat{\mathbb{1}}$. The spin operators are evaluated for the ground state $|\chi_0(y)\rangle$. The scalar potential creates a repulsive potential centred on $y = 0$, where the artificial gauge field is maximal. Experimentally, it can be compensated by an attractive potential, such as a harmonic or quartic trap with an off-resonant beam or a dipole trap. The artificial gauge field originates from the spatial variation of the vector potential and we obtain $\mathcal{B}_x(y) = -\hbar k \partial_y \langle \hat{J}_z \rangle$ along x, which exactly follows the shape of the scalar potential as a function of y. The linear variation of the vector potential over typically $0.1 w_0 \approx 5\,\mu\text{m}$ leads to a uniform magnetic field in this region. The large total angular momentum $J = 8$ boosts the strength of the effective magnetic field, which scales as J^2. However, it simultaneously enhances the scalar potential by the same factor, in the microkelvin regime for dysprosium atoms. In the limit of very large spin coupling, the ground state is given from the diagonalisation of the purely spin coupling $V_{\text{LS}}(y)$ only, and the energy $E_0(y) = \langle V_{\text{LS}}(y) \rangle$ (zero for a dark state), the effective scalar and vector potentials can be computed directly using Eq. 7.18.

We now focus on the two other possible values of the total angular momentum of the excited state $J' = J \pm 1$. An open question concerns the role of the two-fold degeneracy of the ground state in the effective picture for the dressed atoms. The degeneracy of a set of n states can lead to a non-abelian vector potential, described by a non-diagonal $n \times n$ matrix and not a scalar anymore. In our scheme though,

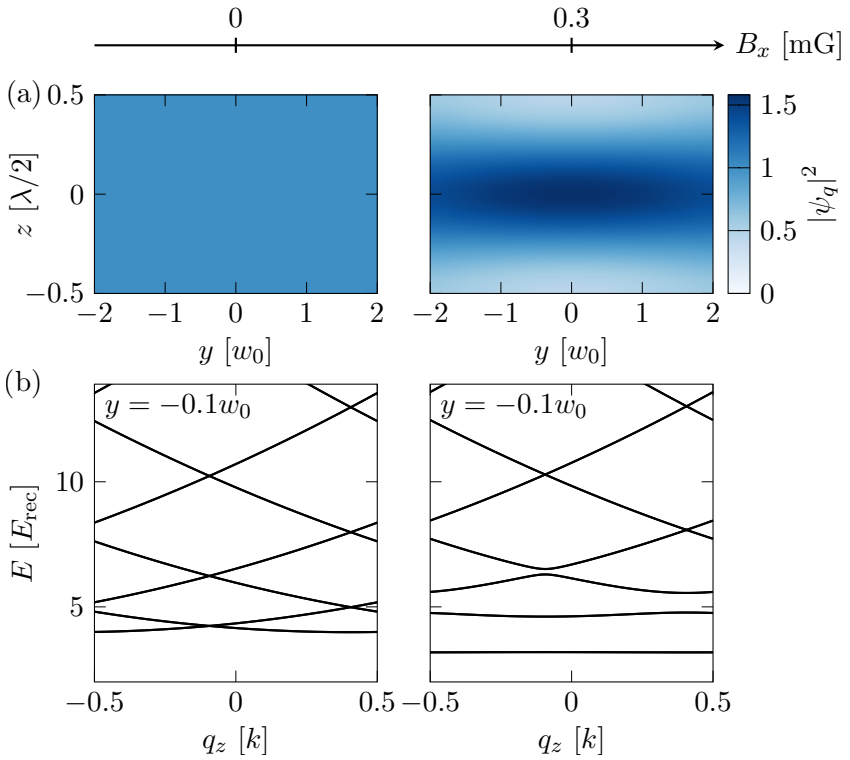

Figure 7.9 – Gauge field for $J' = J - 1$, for two values of the transverse magnetic field B_x of 0 mG and 0.3 mG (about half of the rms value of the magnetic field fluctuations on our experiment) in the left and right panels respectively. Upper panels: Density of the ground Bloch states in the (yz) plane. We restrict the z axis to a region of length $\lambda/2$ due to the periodicity of the total Hamiltonian. Lower panels: Energy spectrum computed for a coupling $V_0 = 10^5 E_{\rm rec}$ at position $y = -0.1w_0$, as a function of the conserved quasimomentum q_z in the first Brillouin zone. Each visible band is quasi-two-fold degenerate.

the vector potential is trivial as it is proportional to the diagonal operator $\hat{J}_z$, and we do not expect new phenomena compared to the case $J' = J$. The degeneracy of the ground states however has a hazardous effect as it facilitates their coupling by small external perturbations. In particular, a perturbation breaking the parity conservation along z, such as a real magnetic field along x, couples the two ground states. This effect is strengthened at $y = 0$ where the ground states are coherent superpositions of opposite stretched states along x. Such superpositions of states that are far in phase space are particularly sensitive to transverse magnetic fields and are strongly modified in their presence. Therefore, a transverse magnetic field has a non-perturbative effect on the system.

We estimate this effect by considering a small magnetic perturbation $\tilde{H}_{\rm pert} = \delta_x \hat{J}_x$. After the gauge transformation, the perturbation becomes $H_{\rm pert} = (\delta_x/2)(\hat{J}_+ \mathrm{e}^{-\mathrm{i}kz} + \mathrm{hc})$ and couples the neighbouring spin states with momentum difference $\pm k$ along z. It breaks the translation invariance along z and the Bloch theorem states that a

quasimomentum q_z defined on a Brillouin zone of size k is conserved. The two dispersive degenerate ground bands are coupled and split into a succession of two-fold degenerate bands with gap openings set by the strength of the perturbation. We compare the situation without perturbation and in the presence of a small magnetic field of $B_x = 0.3\,\mathrm{mG}$, below the rms value of the residual fluctuations of magnetic field on our experimental setup, in Fig. 7.9. For simplicity, we consider the transition to $J' = J - 1$ such that we benefit from the local dark states to enter the regime of very large spin coupling, without suffering from the high heating rate and the strong repulsive potential originating from $E_0(y) = \langle V_{\mathrm{LS}} \rangle$. We numerically compute the band spectrum in the first Brillouin zone and show the densities of the Bloch states at the minimum of the ground band, for all y-positions. We observe a modulation of the state density of period $\lambda/2$ along z and a gap opening of the order of the recoil energy in the presence of a magnetic field of $B_x = 0.3\,\mathrm{mG}$, as shown in Fig. 7.9(b). The gap opening complicates the interpretation of the spatially-varying momentum of the energy minimum as an effective vector potential. Indeed, the ground band becomes quasi-flat, with a bandwidth of the order of $h \times 0.01\,\mathrm{kHz}$, lower than the typical chemical potential $\mu \approx h \times 0.1 - 1\,\mathrm{kHz}$ in experiments with degenerate gases. Moreover, fluctuations of the transverse field induce variations of the density modulation, which would not be reproducible. These arguments question the practical implementation of this scheme in our experiment using a transition to $J' = J \pm 1$, but this remains an open issue. Possible workarounds include the reduction of the field fluctuations using magnetic shielding or more advanced active compensation with additional flux-gate probes for example.

We have discussed the implementation of an artificial gauge field for neutral particles in real space, mediated by an optical coupling between the internal and external degrees of freedom of the atoms. The transition to an excited level with spin $J' = J$ appears to be a convincing candidate as it features local ground states that are non-degenerate dark states. They do not couple to the light field which reduces heating. It allows for a longer lifetime in the trapping potential, a necessary condition for the observation of matter phases where interactions play a significant role, as in vortex lattices.

A

Appendix: Publication

We provide the full text of the article [108], including its appendices, summarised in Chapter 3.

Partitioning dysprosium's electronic spin to reveal entanglement in non-classical states
T. Satoor*, A. Fabre*, J.-B. Bouhiron, A. Evrard, R. Lopes, S. Nascimbene
Physical Review Research 3 (1), 043001 (2021)
* These authors contributed equally

Partitioning dysprosium's electronic spin to reveal entanglement in nonclassical states

Tanish Satoor,* Aurélien Fabre,* Jean-Baptiste Bouhiron, Alexandre Evrard, Raphael Lopes, and Sylvain Nascimbene†
Laboratoire Kastler Brossel, Collège de France, CNRS, ENS-PSL University, Sorbonne Université, 11 Place Marcelin Berthelot, 75005 Paris, France

(Received 30 April 2021; revised 9 July 2021; accepted 20 August 2021; published 1 October 2021)

Quantum spins of mesoscopic size are a well-studied playground for engineering nonclassical states. If the spin represents the collective state of an ensemble of qubits, its nonclassical behavior is linked to entanglement between the qubits. In this paper, we report on an experimental study of entanglement between two subsystems of dysprosium's electronic spin. Its ground state, of angular momentum $J = 8$, can formally be viewed as a set of $2J$ qubits symmetric upon exchange. To access entanglement properties, we partition the spin by optically coupling it to an excited state $J' = J - 1$, which removes a pair of qubits in a state defined by the light polarization. Starting with the well-known W and squeezed states, we extract the concurrence of qubit pairs, which quantifies their nonclassical character. We also directly demonstrate entanglement between the 14- and 2-qubit subsystems via an increase in entropy upon partition. In a complementary set of experiments, we probe decoherence of a state prepared in the excited level $J' = J + 1$ and interpret spontaneous emission as a loss of a qubit pair in a random state. This allows us to contrast the robustness of nonclassical pairwise correlations of the W state with the fragility of the coherence involved in a Schrödinger cat state. Our findings open up the possibility to engineer novel types of entangled atomic ensembles, in which entanglement occurs within each atom's electronic spin as well as between different atoms. Qubit ensembles with large entanglement depth could then be realized with a few atoms only, facilitating the scaling up of quantum-enhanced sensors.

DOI: 10.1103/PhysRevResearch.3.043001

I. INTRODUCTION

Entanglement is a hallmark of nonclassical behavior in compound quantum systems. Minimal entangled systems of qubit pairs, as realized with correlated photon pairs, play a central role in testing the foundations of quantum mechanics [1,2]. Entanglement can also be engineered in many-particle systems [3], such as an ensemble of interacting atoms [4]. In this case, the atoms are not individually addressable, and quantum correlations are indirectly revealed by measuring global properties, such as a squeezed spin projection quadrature [5–8] or via the quantum enhancement of magnetic sensitivity [9–11]. State-of-the-art experiments on photonic systems [12], superconducting qubits [13], trapped ions [14], and Rydberg atom arrays [15] can now produce highly entangled states of tens of individually identifiable qubits, in which entanglement is more readily observable.

Besides quantum state tomography, a wide array of methods have been developed for the detection of entanglement [16,17]. In two-qubit systems, the degree of entanglement is quantified by the concurrence [18,19]. Its direct measurement remains challenging since it requires nonlinear operations on the prepared state [20–23], and it was so far only achieved for photon pairs in pure quantum states [21]. In the case of multipartite systems, the study of entanglement is cumbersome due to the existence of distinct classes of entanglement [24]. It is often revealed using entanglement witnesses, by measuring the fidelity with respect to a given entangled state [25]—the method being limited to simple enough target states.

In this paper, we study quantum entanglement between subsystems of the electronic spin of dysprosium atoms, of angular momentum $J = 8$ in its ground state and prepared in nonclassical spin states. Quantum states with nonclassical correlations have been extensively studied in single large-spin systems, including photon qutrits [26], ground-state atomic spins [27,28], molecules [29], and Rydberg atoms [30]. In the formal analogy between a spin J and a set of $2J$ qubits symmetric upon exchange [31], nonclassicality goes hand in hand with entanglement between the virtual qubits. However, as long as the angular momentum J is conserved, the qubit ensemble cannot be partitioned, and the relevance of entanglement is disputable. Here, we use an optical coupling to an excited electronic state of angular momentum $J' = J - 1$ to partition the 16-qubit ensemble associated with the spin J, giving access to entanglement. The virtual absorption of a photon is interpreted as the annihilation of a qubit pair in a state defined by the light polarization, leaving a set of 14 qubits in the excited electronic level [see Fig. 1(a)]. This process thus realizes a partition of the electronic spin J in two subsystems—the excited electronic spin $J' = J - 1$ and the photon angular momentum $L = 1$. We use this partition to probe entanglement in nonclassical spin states, either by characterizing nonclassical behavior of qubit pairs via the

*These authors contributed equally to this work.
†sylvain.nascimbene@lkb.ens.fr

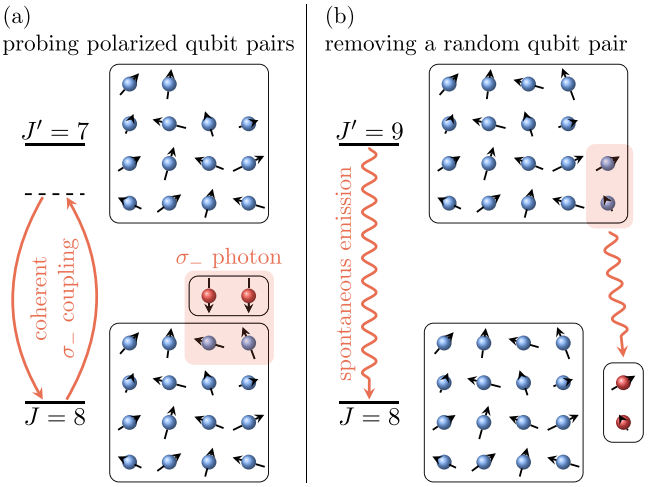

FIG. 1. Scheme of the experiments manipulating qubit pairs in the electronic spin of dysprosium. An electronic spin of angular momentum J can be viewed as a set of $2J$ virtual qubits symmetric upon exchange. (a) The coherent coupling to an excited state $J' = J - 1$ with σ_- polarized light probes the probability to find a qubit pair polarized in $|\uparrow\uparrow\rangle_z$. (b) The spontaneous emission from an excited state $J' = J + 1$ removes a random pair of qubits.

measurement of concurrence or by revealing an increase in entropy upon partition. We extend this protocol to probe decoherence in states prepared in an excited electronic level $J' = J + 1$ [see Fig. 1(b)]. There, the spontaneous emission of a photon drives the system to the electronic ground state J, which corresponds to the removal of a qubit pair randomly drawn from the initial state. We reveal the robustness of nonclassical pairwise correlations with respect to qubit loss, as well as the fragility of coherence in Schrödinger cat states.

This paper is organized as follows. We present in Sec. II the experimental protocol used to measure the properties of qubit pairs extracted from the electronic spin, based on the polarization dependence of the light-spin interaction. In Sec. III, we investigate the nonclassical character of these qubit pairs via the measurement of the concurrence of the reduced two-qubit density matrix and apply it to a W state and a squeezed state. In Sec. IV, we investigate the increase of entropy upon the 14|2 partition as a proof of entanglement for W and Schrödinger cat states, by studying the mixed nature of the reduced two-qubit density matrix. In Sec. V, we study the decoherence upon the loss of a qubit pair triggered by spontaneous emission. We show that nonclassical pairwise correlations are robust with respect to the extraction of qubits. In contrast, the coherence of a Schrödinger cat state is completely destroyed upon qubit loss, due to the complete *which path* information carried by the spontaneously emitted photon's polarization. In another superposition state, we show the existence of a quantum jump leaving the path information hidden, such that maximal-order coherence remains visible. Finally, we present a possible extension of our work to ensembles of dysprosium atoms entangled together using an optical resonator. Such systems would combine entanglement between atoms and within each electronic spin, allowing one to scale up entanglement depth and its application to quantum-enhanced sensing.

II. PAIR HUSIMI FUNCTION MEASUREMENT

A. Probing pairs via light coupling

The electronic ground state $J = 8$ can be interpreted as the sum of $2J = 16$ virtual spin-1/2s, in a state symmetric upon exchange. We discuss here the partition of this qubit ensemble, prepared in a state ρ, through the coupling to an excited electronic level, of angular momentum $J' = 7$. As sketched in Fig. 1(a), the coupling to the excited manifold is induced by light close to the optical transition, via the absorption of a photon. The photon polarization $\boldsymbol{\epsilon}$ defines an $L = 1$ quantum state $|\boldsymbol{\epsilon}\rangle$ that can be considered as a symmetric two-qubit state. We restrict ourselves here to the case of a circular polarization σ_-, which corresponds to qubits polarized in $|\downarrow\downarrow\rangle_z$. Since the excited state contains only $2J' = 14$ qubits, two qubits are removed upon photon absorption. The conservation of angular momentum requires these removed qubits to be polarized in $|\uparrow\uparrow\rangle_z$, the time-reversed state of the absorbed photon's polarization. The excited state ρ' can be then written as a projected state $\rho' = \langle\uparrow\uparrow|_z \rho |\uparrow\uparrow\rangle_z$. The probability for a pair chosen from the 16 qubits to be polarized in $|\uparrow\uparrow\rangle_z$ then reads

$$Q_{\text{pair}}(\mathbf{e}_z) = \text{Tr}\rho',$$

defining the pair Husimi function along the direction $\mathbf{e}_z$. Hence the light absorption properties of the electronic spin J can be linked to the properties of its two-qubit reduced density matrix.

To probe this behavior, we measure the light shift V induced by an off-resonant light beam close to the considered optical transition. The light shift, being induced by virtual photon absorption processes, is proportional to the pair Husimi function, as

$$V/V_0 = Q_{\text{pair}}(\mathbf{e}_z), \quad V_0 = \frac{(dE)^2}{\hbar\Delta},$$

where $d = \langle J-1||\mathbf{d}||J\rangle$ is the reduced dipole matrix element, E is the light electric field amplitude, and Δ is the detuning from resonance.

B. Application to Dicke states

We illustrate our method by measuring the value of the Husimi function $Q_{\text{pair}}(\mathbf{e}_z)$ for an arbitrary Dicke state $|m\rangle$ (with $-J \leqslant m \leqslant J$), which we denote Q_m hereafter.

All our experiments are performed on a cloud of $1.0(1) \times 10^5$ dysprosium atoms (of the bosonic isotope ^{162}Dy), held in an optical dipole trap at a temperature $T = 0.54(3)\ \mu$K. The results described in this paper can be understood by considering a single atom, with the ensemble acting as an averaging mechanism only. The experimental scheme for the Q_m measurement is shown in Fig. 2(a). We prepare the atoms in a coherent state $|m = J\rangle_{\mathbf{n}}$ polarized along a direction $\mathbf{n}$, parametrized by the spherical angles (θ, ϕ). The polar angle θ determines the projection probabilities Π_m along the Dicke states $|m\rangle$, which are significant for values of m close to $J\cos\theta$. We then push the atomic cloud by applying an off-centered laser beam, with circular σ_- polarization and blue detuning with respect to an optical transition at 696 nm. The intensity gradient then leads to a force along x proportional to the light shift [Fig. 2(a)]. After this kick, a magnetic

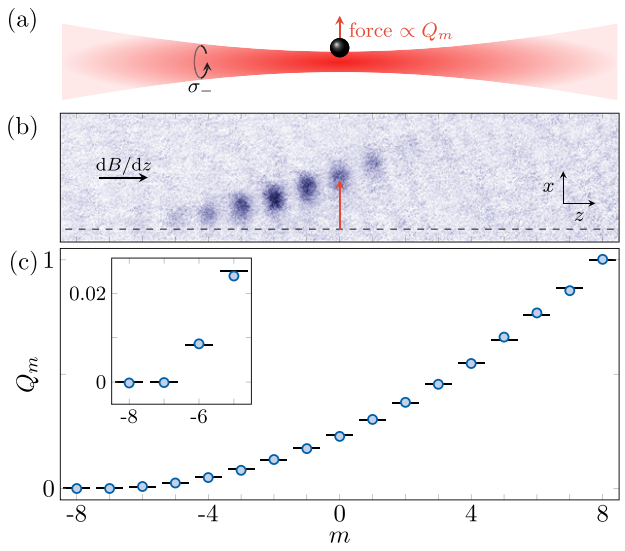

FIG. 2. Husimi function measurement for Dicke states. (a) Scheme of the light shift measurement. We measure the force induced on the atoms by an off-centered laser beam, blue detuned with respect to the optical resonance. (b) Image of an atomic gas prepared in a coherent state of polar angle $\theta \simeq 100°$. The atoms are kicked along x by the laser beam. Subsequently, we apply a magnetic field gradient separating the magnetic sublevels $|m\rangle$ along z during time of flight. The dashed line indicates the mean x position in the absence of the repulsive laser beam. (c) Probability Q_m for a qubit pair taken in the Dicke state $|m\rangle$ to be in $|\uparrow\uparrow\rangle_z$, deduced from the kick amplitudes. In all figures, error bars represent the 1σ statistical uncertainty (here smaller than the blue circles). The black lines are the theoretical values of Eq. (1).

field gradient is applied to spatially separate the different m components along z, which allows us to retrieve the light shift experienced by each Dicke state independently. After a 2.3-ms time of flight, we image the atoms and measure the x displacement for each Dicke state $|m\rangle$ that is significantly populated, and hence their values Q_m. A typical absorption image is shown in Fig. 2(b). Repeating this measurement for various angles θ, we measure the light shifts for all projections m and infer the Q_m values shown in Fig. 2(c) [32].

Our measurements are consistent with an absence of light shift for the states $|m = -J\rangle$ and $|m = -J+1\rangle$; that is, these states are dark with respect to the $J \to J' = J-1$ optical transition for σ_- polarized light. In terms of the underlying qubits, the state $|m = -J\rangle$ only contains $|\downarrow\rangle_z$-polarized qubits, while the state $|m = -J+1\rangle$ has a single qubit in $|\uparrow\rangle_z$. In both cases, a qubit pair cannot be found polarized in $|\uparrow\uparrow\rangle_z$; hence $Q_{-J} = Q_{-J+1} = 0$.

More generally, a Dicke state $|m\rangle$ is composed of $J-m$ qubits in $|\downarrow\rangle_z$ and $J+m$ qubits in $|\uparrow\rangle_z$ [33]. The probability to pick a pair $|\uparrow\uparrow\rangle_z$ simply reads

$$Q_m = \binom{J+m}{2} \Big/ \binom{2J}{2} = \frac{(J+m)(J+m-1)}{2J(2J-1)}, \qquad (1)$$

in good agreement with our measurements.

We use these measurements to probe the Husimi function of states lacking z rotation symmetry. For this, we measure their projection probabilities $\Pi_m(\mathbf{n})$ along $\mathbf{n}$ by combining a spin rotation and a Stern-Gerlach projective measurement along z. We then infer the Husimi function by weighting these probabilities with the Q_m values, as

$$Q_{\text{pair}}(\mathbf{n}) = \sum_m Q_m \Pi_m(\mathbf{n}). \qquad (2)$$

In the following, we use the theoretical values of Eq. (1) rather than the measured ones to avoid propagating systematic errors.

C. Coherent and W states

We first apply the above protocol to the quasiclassical coherent spin state $|m = -J\rangle$ and the W state $|m = -J+1\rangle$. The coherent state can be viewed as a set of $2J$ qubits polarized in $|\downarrow\rangle_z$, forming a nonentangled product state. The W state, which hosts a single qubit in $|\uparrow\rangle_z$, is a paradigmatic state of a fundamental class of entanglement [24], which has been realized and studied in various settings [34–41].

In our experiment, the atoms are initially spin polarized in the coherent state $|m = -J\rangle$. To produce the W state, we confine the system to the two spin states $|m = -J\rangle$ and $|m = -J+1\rangle$ by applying a strong quadratic light shift acting on the other spin states only, leading to a constrained quantum Zeno dynamics [42–44]. An additional resonant radio-frequency π pulse then brings the system to $|m = -J+1\rangle$. The quadratic light shift is produced using the 696-nm laser beam with a σ_- polarization, leading to positive energy shifts for all Dicke states $|m\rangle$, except for $m = -J$ and $-J+1$. We reach a maximum W-state fidelity of 0.91(1), with residual overlaps on other Dicke states below 4% [45].

We report in Figs. 3(a) and 3(b) the measured projection probabilities $\Pi_m(\theta)$ for these two states. For a given projection m, the coherent-state probabilities feature a single peak centered on the expected maximum at $\theta_m = \arccos(m/J)$, shown as red lines. For the W-state probabilities, we observe a double-peaked distribution for all nonstretched states $m \neq \pm J$. This behavior results from the interference between two processes, depending on whether the spin $|\uparrow\rangle_z$ is projected on $|\uparrow\rangle_\theta$ or $|\downarrow\rangle_\theta$. The first (second) process dominates for $\theta \simeq 0$ ($\theta \simeq \pi$), and the two processes destructively interfere at θ_m, as observed in our data.

We combine these measurements to infer the pair Husimi functions using Eq. (2), finding good agreement with theory for both states [see Fig. 3(c)]. In particular, for the coherent state, our data match well the probability $Q_{\text{pair}}(\theta) = \sin^4(\theta/2)$ that two qubits in $|\downarrow\rangle_z$ are projected in $|\uparrow\rangle_\theta$. In the following sections we use these measurements to probe entanglement properties.

III. NONCLASSICALITY OF QUBIT PAIRS

Our first characterization of entanglement of the $2J$-qubit state consists in revealing the nonclassical character of qubits pairs extracted from it.

A. Measure of nonclassicality via the concurrence

The collective state ρ_{pair} of a qubit pair symmetric upon exchange can be written as the state of an angular momentum

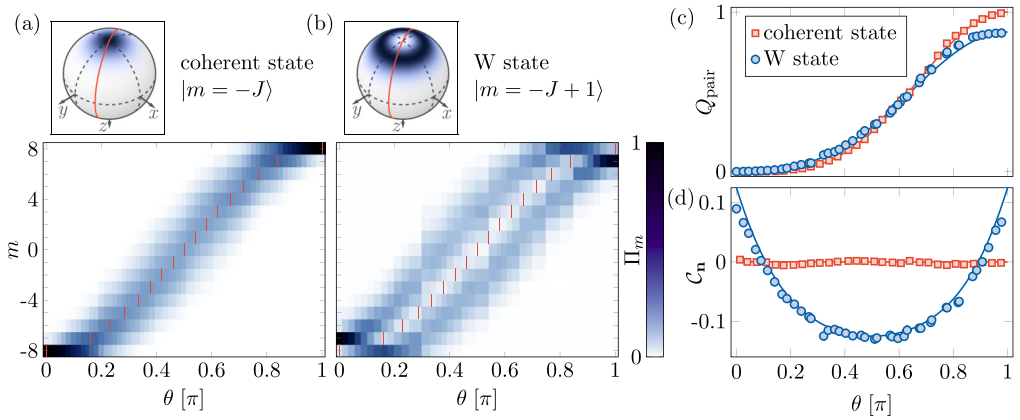

FIG. 3. Qubit pair properties of coherent and W states. (a) and (b) Measured spin projection probabilities Π_m as a function of the polar angle θ, for a coherent spin state (a) and for the W state (b). The red vertical lines indicate the expected maxima for the coherent state, also corresponding to minima for the W state. The top panels represent the considered spin-J states on the Bloch sphere, where the red circles indicate the spanned measurement projection axis. (c) Pair Husimi function Q_{pair} computed from the (a) and (b) data (blue circles and red squares, respectively). The lines correspond to the expected functions $Q_{\text{pair}}(\theta)$ for the coherent and W states (red and blue lines). (d) Distribution $\mathcal{C}_{\mathbf{n}}$ of nonclassical correlations as a function of the polar angle θ. The points $\mathcal{C}_{\mathbf{n}} > 0$ measured for the W state evidence nonclassicality.

$L = 1$. Drawing an analogy with quantum optics [46,47], it will be called classical if it can be expressed as a statistical mixture of quasiclassical coherent states [48], as

$$\rho_{\text{pair}}^{(\text{classical})} = \sum_{\mathbf{n}} w_{\mathbf{n}} ||\mathbf{n}\rangle\langle\mathbf{n}||, \tag{3}$$

where $||\mathbf{n}\rangle$ is a spin-1 coherent state pointing along $\mathbf{n}$, and $w_{\mathbf{n}} \geqslant 0$, $\sum_{\mathbf{n}} w_{\mathbf{n}} = 1$. Coherent states are the only pure states that satisfy the equality

$$Z(\mathbf{n}) \equiv 2\langle L_{\mathbf{n}}^2\rangle - \langle L_{\mathbf{n}}\rangle^2 - 1 = 0 \tag{4}$$

for arbitrary measurement axis $\mathbf{n}$. Then it follows by convexity that $Z(\mathbf{n}) \geqslant 0$ for classical states. As shown in Ref. [48], the existence of a strictly negative value $Z(\mathbf{n})$ constitutes a necessary and sufficient criterion of nonclassicality.

To apply this criterion to our system, we use the connection between the mean values of spin projection and the Husimi function of qubit pairs extracted from the electronic spin J,

$$\langle L_{\mathbf{n}}\rangle = Q_{\text{pair}}(\mathbf{n}) - Q_{\text{pair}}(-\mathbf{n}),$$
$$\langle L_{\mathbf{n}}^2\rangle = Q_{\text{pair}}(\mathbf{n}) + Q_{\text{pair}}(-\mathbf{n}),$$

leading to the expression $Z(\mathbf{n}) = \alpha\,\mathcal{C}_{\mathbf{n}}$, where we introduce the coefficient $\alpha = (\sqrt{Q_{\text{pair}}(-\mathbf{n})} - \sqrt{Q_{\text{pair}}(\mathbf{n})})^2 - 1$ and the distribution

$$\mathcal{C}_{\mathbf{n}} = 1 - (\sqrt{Q_{\text{pair}}(-\mathbf{n})} + \sqrt{Q_{\text{pair}}(\mathbf{n})})^2.$$

The parameter α being negative, nonclassicality is characterized by the existence of a direction $\mathbf{n}$ for which $\mathcal{C}_{\mathbf{n}}$ is strictly positive. This criterion of nonclassicality is equivalent to the bipartite entanglement witness established in Ref. [49].

We show in Fig. 3(d) the distribution $\mathcal{C}_{\mathbf{n}}$ computed from the measured Husimi functions, for the coherent and W states. For these states, symmetric upon rotations around z, we expect $\mathcal{C}_{\mathbf{n}}$ to only depend on the polar angle θ of the measurement axis [50]. For the coherent state, the measured $\mathcal{C}_{\mathbf{n}}$ remains close to zero for all angles θ. Indeed, qubit pairs drawn from this state form themselves a spin-1 coherent state, for which $\mathcal{C}_{\mathbf{n}}$ vanishes according to Eq. (4). For the W state, $\mathcal{C}_{\mathbf{n}}$ takes significantly positive values for θ close to 0 and π, showing a nonclassical character.

We now show that the distribution $\mathcal{C}_{\mathbf{n}}$ can be used to quantify the degree of nonclassicality of a quantum state, defined by its distance from the set of nonclassical states [51]. For a system of two qubits, this geometrical measure can be directly expressed in terms of the concurrence $\mathcal{C}$ [52], the most common measure of pairwise entanglement [18,19]. In our system, qubit pairs should be considered as indivisible quantum objects, such that the concurrence only measures the amount of nonclassical correlations. The concurrence can be explicitly written in terms of the density matrix, but it does not correspond to a directly accessible physical observable. Remarkably, the distribution $\mathcal{C}_{\mathbf{n}}$ can be used to retrieve the concurrence, as

$$\mathcal{C} = \max\left[0, \max_{\mathbf{n}} \mathcal{C}_{\mathbf{n}}\right].$$

This relation was conjectured and numerically checked for randomly generated states in Ref. [53].

For the W state realized in the experiment, the measured $\mathcal{C}_{\mathbf{n}}$ takes its maximum for $\theta = 0$ leading to a concurrence $\mathcal{C} = 0.089(5)$. This value is about 71% of the maximum possible value $\mathcal{C} = 1/J = 0.125$ in a system of $2J$ qubits symmetric upon exchange [54], which would be reached for the W state in the absence of experimental imperfections. In our system, the concurrence is limited by the residual population $\Pi_{-J+2} \simeq 0.03$ in the Dicke state $|m = -J + 2\rangle$ that originates from spin-changing collisions between atoms in $|m = -J + 1\rangle$.

B. Pairwise correlations in a squeezed state

Nonclassical correlations between qubit pairs play a central role in the squeezing of a spin projection quadrature [55]. In this section we extend the measurement of qubit pair properties to a squeezed spin state, which we produce via a nonlinear

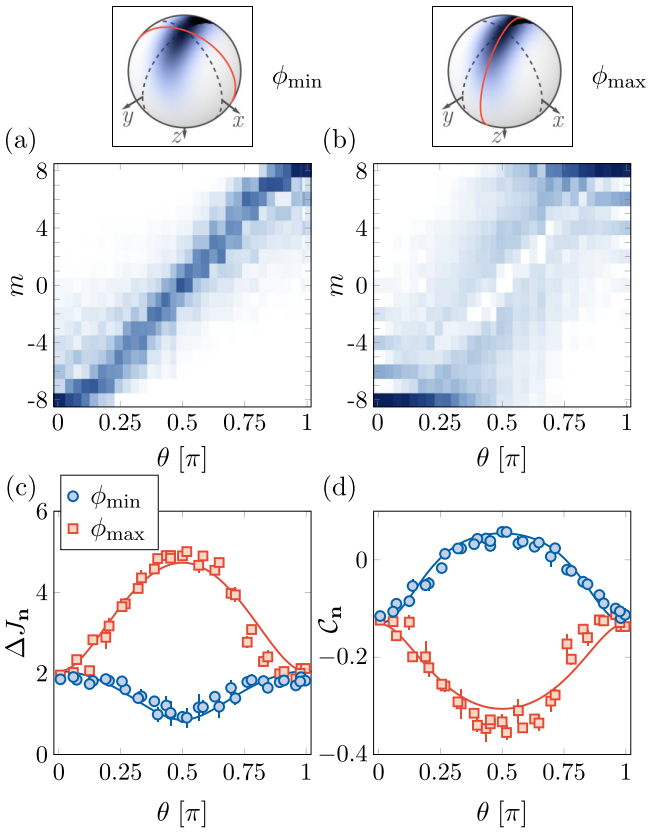

FIG. 4. Qubit pair properties for a squeezed state. (a) and (b) Measured spin projection probabilities Π_m for a squeezed spin state, as a function of the polar angle θ with azimuthal angles $\phi_{\min}$ (a) and $\phi_{\max}$ (b). (c) Spin projection uncertainty $\Delta J_{\mathbf{n}}$ computed from the (a) and (b) data (blue circles and red squares, respectively). The lines correspond to the projection uncertainties expected for the targeted spin state. (d) Distribution $\mathcal{C}_{\mathbf{n}}$ of nonclassical correlations as a function of θ.

spin dynamics. We apply a $\hbar\chi J_x^2$ spin coupling, generated by the spin-dependent light shift of the 696-nm laser beam, using a linear polarization $\mathbf{e}_x$ [56]. This coupling induces a twisting of the spin distribution, leading to the squeezing of a spin projection quadrature [55], as first implemented in atomic Bose-Einstein condensates [8,9]. In our experiment, we apply a nonlinear coupling of strength $\chi = 2\pi \times 32.1(4)$ kHz for a duration $t \simeq 700$ ns, in the presence of a z magnetic field $B = 75(1)$ mG.

In contrast to the Dicke states discussed above, the spin projection probabilities are no longer invariant around z. We show in Figs. 4(a) and 4(b) the probabilities $\Pi_m(\theta, \phi)$ for two azimuthal angles $\phi_{\min} = -0.4(2)$ rad and $\phi_{\max} = \phi_{\min} + \pi/2$, which feature minimal and maximal spin projection uncertainties, respectively. For $\theta = \pi/2$, a minimum spin projection uncertainty $\Delta J_{\min} = 0.92(16)$ is measured at $\phi_{\min}$ [see Fig. 4(c)], in agreement with the value $\Delta J_{\min} = 0.85$ expected for an optimally squeezed state (within the one-axis twisting dynamics). We report in Fig. 4(d) the corresponding distribution $\mathcal{C}_{\mathbf{n}}$. The measured $\mathcal{C}_{\mathbf{n}}$ takes its maximum for $\theta = \pi/2$ and $\phi = \phi_{\min}$, i.e., along the squeezed quadrature direction. This maximum gives a value for the concurrence $\mathcal{C} = 0.058(6)$, in agreement with the expected value of 0.055.

Our measurements can be used to check the direct link between quadrature squeezing and nonclassical pairwise correlations [57]. Indeed, for the states reached via the one-axis twisting dynamics, one expects the concurrence to be expressed in terms of the minimum spin projection uncertainty, as

$$\mathcal{C} = \frac{1 - 2\Delta J_{\min}^2/J}{2J - 1}. \tag{5}$$

From the measured projection quadrature, we calculate a value of 0.053(5) for the right-hand side of Eq. (5), in agreement with the direct measurement of the concurrence.

IV. PROBING ENTANGLEMENT VIA THE SUBSYSTEM ENTROPY

So far, we studied the entanglement of $2J$-qubit states via the nonclassical character of their qubit pairs. In this section, we access entanglement more directly, by probing whether a given state of the spin $J = 8$ is separable with respect to the 14|2 partition performed by the photon absorption. For this, we use the fact that for a separable state, the global state is more disordered than its parts [58]. More precisely, we quantify disorder via the Rényi entropy of infinite order (also called the min-entropy), defined as [59]

$$S_\infty(\rho) = -\ln \lambda_{\max}(\rho),$$

where $\lambda_{\max}$ is the maximum eigenvalue of the density matrix ρ. This eigenvalue corresponds to the maximum possible overlap of ρ with a pure state. To reveal entanglement within a state ρ of the collective spin J, it is thus sufficient to show that the entropy of the reduced pair state ρ_{pair} is strictly higher than that of the original state ρ, i.e., if the conditional entropy satisfies [58]

$$S_\infty(14|2) \equiv S_\infty(\rho) - S_\infty(\rho_{\text{pair}}) < 0.$$

A. Entanglement of the W state

The evaluation of the pair state entropy $S_\infty(\rho_{\text{pair}})$ is based on the tomography of the pair density matrix [60]. Full information on the density matrix is contained in the Husimi function $Q_{\text{pair}}(\mathbf{n})$. We fit the measured Husimi function by a spherical harmonic expansion

$$Q_{\text{pair}}(\mathbf{n}) = \frac{1}{3} + \sqrt{\frac{4\pi}{3}} \sum_{\ell=1}^{2} \sum_{m=-\ell}^{\ell} \lambda_{\ell,m} Y_\ell^m(\mathbf{n}) \tag{6}$$

and infer the density matrix as

$$\rho_{\text{pair}} = \frac{1}{3}\mathbb{1} + \sum_{m=-1}^{1} \lambda_{1,m}\mathcal{L}_m + \sum_{m=-2}^{2} \lambda_{2,m}\mathcal{Q}_m, \tag{7}$$

where the $\mathcal{L}_m$ and $\mathcal{Q}_m$ matrices correspond to the $L = 1$ angular momentum components and quadrupole moments, respectively (see Appendix B).

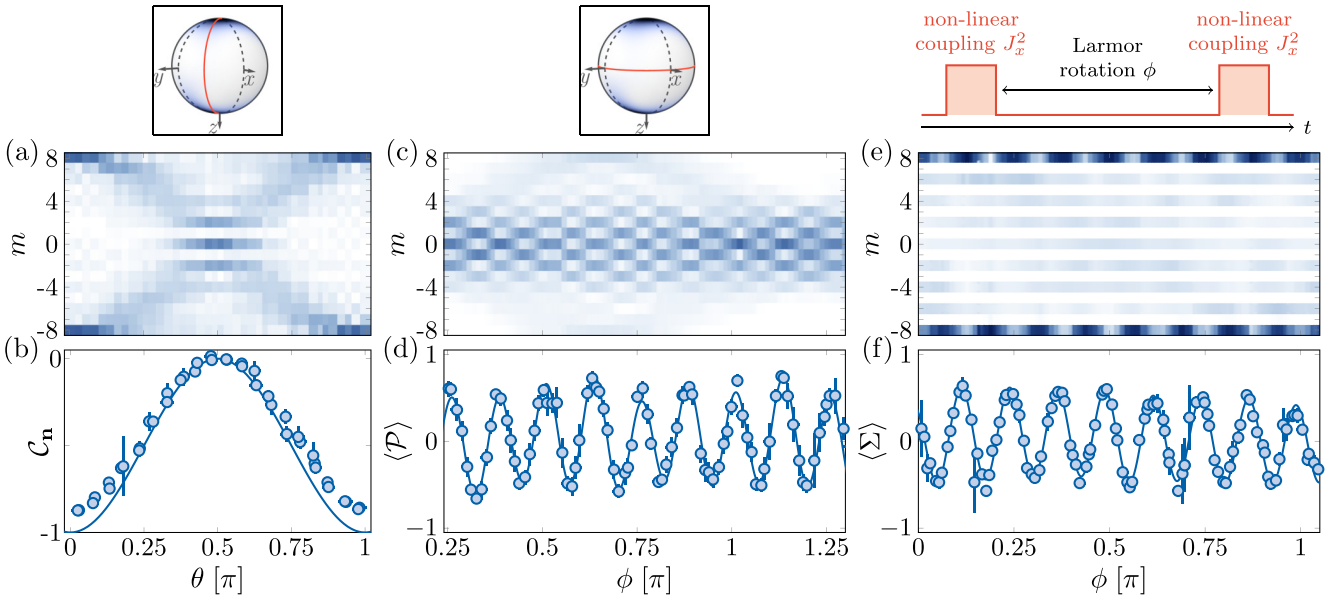

FIG. 5. Characterization of entanglement in a Schrödinger cat state. (a) Measured spin projection probabilities Π_m for a cat state, as a function of the polar angle θ. The azimuthal angle $\phi = 0.86(5)$ rad is chosen such that the two coherent-state Husimi functions destructively interfere for odd m values around $\theta = \pi/2$. (b) Distribution $\mathcal{C}_\mathbf{n}$ inferred from the probabilities shown in (a) (blue circles). The solid line is the expected variation for a perfect cat state. (c) Projection probabilities Π_m measured along equatorial directions ($\theta = \pi/2$) parametrized by the azimuthal angle ϕ. (d) Evolution of the mean parity $\langle\mathcal{P}\rangle$ deduced from (c). (e) Projection probabilities Π_m measured after a Larmor rotation of angle ϕ followed by a second nonlinear evolution. (f) Evolution of the mean sign of even projections $\langle\Sigma\rangle$ deduced from (e). The solid lines in (d) and (f) are fits with a Fourier series.

We apply this protocol to the W state, taking into account the slight variation of the Husimi function $Q_{\text{pair}}(\mathbf{n})$ with respect to the azimuthal angle ϕ in the prepared state [50]. We infer a density matrix

$$\rho_{\text{pair}} \simeq \begin{pmatrix} 0.88 & 0.01+0.05i & -0.01-0.01i \\ 0.01-0.05i & 0.12 & 0.01i \\ -0.01+0.01i & -0.01i & 0 \end{pmatrix},$$

with typically 1% statistical uncertainty. The reconstructed density matrix matches well the expected one

$$\rho_{\text{pair}} = \begin{pmatrix} 7/8 & 0 & 0 \\ 0 & 1/8 & 0 \\ 0 & 0 & 0 \end{pmatrix}.$$

Diagonalization of the reconstructed density matrix gives a maximum eigenvalue $\lambda_{\max}(\rho_{\text{pair}}) = 0.882(5)$.

We now consider the global spin-J state. The projection probability $\Pi_{-J+1} = 0.91(1)$ with the Dicke state $|m = -J+1\rangle$ provides a lower bound on the maximum overlap $\lambda_{\max}(\rho)$ with pure states.

Combining these results together, we obtain

$$S_\infty(14|2) < -0.03(1).$$

Its negative value shows that the prepared state is not separable with respect to a 14|2 partition, and is thus entangled.

B. Entanglement of a Schrödinger cat state

We now consider the case of a Schrödinger cat state, for which the effect of the 14|2 partition is more striking. Schrödinger cat states, which constitute archetypal states with highly nonclassical properties, have been realized in different types of experiments [30,56,61–77].

The cat state considered here is the coherent superposition of two quasiclassical spin states $|m = \pm J\rangle$ [78]. To produce it, we use the one-axis twisting dynamics discussed above, with a stronger nonlinear coupling $\chi = 2\pi \times 1.25$ MHz and a reduced magnetic field $B = 53.7(1)$ mG. After showing quadrature squeezing at short times ($t \sim 10$ ns), the spin quadratures collapse to a featureless spin distribution, before a revival at a time $t_{\text{cat}} = \pi/(2\chi) = 200$ ns, at which the system forms a coherent superposition of stretched states $|m = \pm J\rangle$ [56].

In Fig. 5(a), we show the measured probabilities $\Pi_m(\mathbf{n})$ for various polar angles θ with a fixed azimuthal angle ϕ. For $\theta = 0$, we confirm the dominant population of the two stretched states, with $\Pi_{-J} = 0.38(2)$ and $\Pi_J = 0.42(2)$. When varying θ, the distribution is a superposition of the contributions of each of the two coherent states forming the cat state. Interestingly, we observe an interference between the two distributions when they overlap, i.e., for $\theta \simeq \pi/2$. As shown in Fig. 5(c), the interference pattern depends on the azimuthal angle ϕ, with an alternation between even- and odd-m projections of period $2\pi/(2J)$ [79].

We first test whether a qubit pair extracted from this state features nonclassical behavior. We expect the distribution $\mathcal{C}_\mathbf{n}$ to be rotationally invariant around z and thus study its variation with the polar angle θ in Fig. 5(b) [80]. Our measurements are consistent with $\mathcal{C}_\mathbf{n} < 0$ for all angles θ, showing that the reduced two-qubit state is classical. This measurement highlights the well-known property of this state that any of its subsystems is classical.

We now extend the tomography protocol to the cat state and obtain the reduced two-body density matrix

$$\rho_{\rm pair} \simeq \begin{pmatrix} 0.46 & -0.01i & -0.03+0.05i \\ 0.01i & 0.05 & -0.01i \\ -0.03-0.05i & 0.01i & 0.49 \end{pmatrix},$$

which we compare with the expected matrix

$$\rho_{\rm pair} = \begin{pmatrix} 1/2 & 0 & 0 \\ 0 & 0 & 0 \\ 0 & 0 & 1/2 \end{pmatrix} \tag{8}$$

obtained for a perfect cat state. We compute the maximum eigenvalue $\lambda_{\rm max}(\rho_{\rm pair}) = 0.53(1)$ of the reconstructed matrix.

In order to reveal entanglement in the prepared state, we evaluate its overlap with perfect cat states $|{\rm cat}(\alpha)\rangle = (|m=-J\rangle + e^{i\alpha}|m=J\rangle)/\sqrt{2}$, which constitute a family of pure quantum states. The simple form of these states in the Dicke basis allows us to express the overlap with a state ρ as

$$\mathcal{O}_\alpha = \frac{\rho_{-J,-J} + \rho_{J,J} + 2\,{\rm Re}(\rho_{-J,J}\, e^{i\alpha})}{2},$$

where the diagonal elements $\rho_{m,m}$ correspond to the spin projection probabilities Π_m. The overlap $\mathcal{O}_\alpha$ takes its maximum value $\mathcal{O}$ for $\alpha = -\arg\rho_{-J,J}$, with

$$\mathcal{O} = \frac{\Pi_{-J} + \Pi_J + 2|\rho_{-J,J}|}{2}.$$

We present two protocols giving a lower bound on the extremal coherence $|\rho_{-J,J}|$, both based on the measurement of an observable A defined on the spin J. We consider its mean value in a state obtained after the cat state preparation, followed by a Larmor rotation around z of angle ϕ, as

$$\langle A\rangle(\phi) = \sum_{m,m'} a_{m,m'}\rho_{m',m} e^{i(m'-m)\phi}.$$

The extremal coherence can be singled out by measuring the Fourier coefficient $A_{2J} = |a_{J,-J}\rho_{-J,J}|$ at frequency $2J$ [77,79]. We will use observables that can take values in the interval $[-1, 1]$ only, such that $|a_{J,-J}| \leqslant 1$. The coefficient A_{2J} then provides a lower bound on the extremal coherence $|\rho_{-J,J}|$.

The first observable we consider is the parity $\mathcal{P}$ of the spin projection along an equatorial direction $\mathbf{n} \perp \mathbf{e}_z$—an observable commonly used to characterize cat states [64,65,69,70,75–77]. We fit its oscillation, shown in Fig. 5(d), with a Fourier series, from which we get the Fourier coefficient $\mathcal{P}_{2J} = 0.26(1)$. The second observable uses a nonlinear evolution, obtained by repeating the one-axis twisting evolution used to produce the cat state [56,81–84] [see the scheme in Fig. 5(e)]. In the absence of imperfections, the system is brought to a superposition $\sin(J\phi)|m=-J\rangle + \cos(J\phi)|m=J\rangle$, which allows us to extract the maximal coherence from the projection probabilities in stretched states only. The projection probabilities measured with this protocol are shown in Fig. 5(e). In practice, we observe residual probabilities in other projection values m, with m even only, as expected from parity symmetry. We thus use an observable Σ defined as the sign of the spin projection on even states, with

$$\langle\Sigma\rangle = \sum_{m\ {\rm even}} {\rm sgn}(m)\Pi_m.$$

Its oscillation, shown in Fig. 5(f), gives a Fourier coefficient $\Sigma_{2J} = 0.247(5)$. The advantage of the second method will become clear when we consider a more complex quantum state in the next section.

The two protocols lead to comparable estimates of the extremal coherence. Using the measured probabilities $\Pi_{\pm J}$ quoted above, we infer a lower bound on the overlap $\mathcal{O} \geqslant 0.66(2)$ and thus on the eigenvalue $\lambda_{\rm max}(\rho)$. Together, these measurements provide a conditional entropy

$$S_\infty(14|2) < -0.23(3),$$

which proves entanglement more evidently than for the W state. We note that the requirement $\mathcal{O} > \lambda_{\rm max}(\rho_{\rm pair}) = 0.53(1)$, which we used to demonstrate the nonseparability of the 14|2 partition, is consistent with the entanglement witness $\mathcal{O} > 0.5$ extensively used for cat states [25].

V. DECOHERENCE UPON QUBIT LOSS

We now consider the removal of a pair of qubits randomly drawn from the electronic spin, irrespective of its quantum state. For this purpose, we prepare a quantum state of interest ρ' in an excited level of angular momentum $J' = 9$, corresponding to a symmetric state of $2J' = 18$ qubits [see Fig. 1(b)]. The spontaneous emission of a photon drives the system to the ground state $J = 8$, which has two missing qubits. Since the emitted photon can carry an arbitrary polarization, the process allows for three independent quantum jumps associated with the polarizations $\mathbf{e}_-, \mathbf{e}_z, \mathbf{e}_+$, with $\mathbf{e}_\pm = (\mathbf{e}_x \pm i\mathbf{e}_y)/\sqrt{2}$. The ground-state density matrix then reads

$$\rho = \sum_{\mathbf{e}_u=\mathbf{e}_-,\mathbf{e}_z,\mathbf{e}_+} \langle\mathbf{e}_u|\rho'|\mathbf{e}_u\rangle,$$

which can be simply written as

$$\rho = {\rm Tr}_2\rho',$$

corresponding to the loss of an arbitrary qubit pair.

A. Robustness of pairwise quantum correlations

We first investigate the effect of particle loss on a W state prepared in an excited electronic level of angular momentum $J' = J + 1$, coupled to the ground state with an optical transition of wavelength 626 nm. To produce the state $|m' = -J' + 1\rangle$ in the excited level, we start in the coherent state $|m = -J\rangle$ of the lowest energy manifold and use π polarized resonant light to couple the system to the desired state [see Fig. 6(a)]. As shown in Fig. 6(b), we monitor the Rabi oscillation via the atom recoil upon light absorption. The comparison with a master equation model taking into account spontaneous emission during the Rabi flopping allows us to estimate a fidelity of 0.98 for a pulse duration $t_{\rm pulse} \simeq 62$ ns—the excited state lifetime being $\tau_{\rm exc} \simeq 1.2\ \mu$s [85].

Following the light pulse, we wait for spontaneous emission to occur before measuring the spin state in the ground level. We observe significant populations only in the states $|m = -J\rangle$ and $|m = -J + 1\rangle$, as expected from the selection rule $|m' - m| \leqslant 1$. The state $|m = -J + 1\rangle$ is dominantly populated, showing that, in most cases, the $|\uparrow\rangle$ excitation of the W state is not removed upon the loss of a qubit pair. The

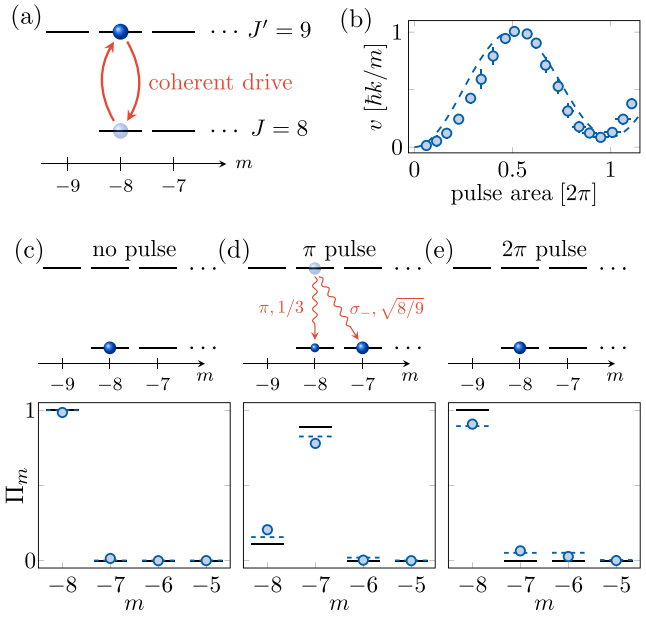

FIG. 6. Loss of a qubit pair in a W state. (a) Scheme for the preparation of the W state in the excited electronic level. (b) Evolution of the mean atom velocity acquired due to the photon absorption recoil, as a function of the light pulse duration. The dashed line is a model taking into account spontaneous emission during the pulse. (c)–(e) Top panels: expected states, with a scheme of spontaneous emission in (d) showing the Clebsch-Gordan coefficients for the two possible quantum jumps. Bottom panels: spin projection probabilities in the absence of the resonant light pulse (c), for a π pulse (d), and for a 2π pulse (e). The solid lines are the probabilities expected for a perfect W state, while the dashed lines use the same model as in (b).

projection probabilities, shown in Fig. 6(d), are close to the expected values $\Pi_{-J+1} = 1/(J+1)$ and $\Pi_{-J} = 1 - \Pi_{-J+1}$, with a residual difference mostly explained by the imperfect state preparation.

The nonclassicality of qubit pairs in the final state is probed via the distribution $\mathcal{C}_{\mathbf{n}}$ introduced in Sec. III A. We remind the reader that $\mathcal{C}_{\mathbf{n}}$ is obtained from the spin projection probabilities along $\mathbf{n}$. Since its maximum value is expected to be reached along z, we only consider projections along this direction, and obtain $\mathcal{C}_z = 0.104(3)$. This value provides a lower bound on the qubit pair concurrence, expected to be $\mathcal{C} = 1/(J+1) \simeq 0.111$ in the initial state. The proximity of the initial state concurrence and the measured one after decay illustrates that losing qubits does not alter nonclassicality of the remaining qubit pairs [24].

B. Fragility of macroscopic coherence

We contrast this behavior with the fragility of entanglement in coherent superpositions of states distant in phase space [86].

We consider two examples, namely, a cat state $|\psi_1\rangle = (|m' = -J'\rangle + |m' = J'\rangle)/\sqrt{2}$ and the superposition $|\psi_2\rangle = (|m' = -J'+1\rangle + |m' = J'-1\rangle)/\sqrt{2}$. Their preparation consists in producing a cat state in the ground manifold $(|m = -J\rangle + |m = J\rangle)/\sqrt{2}$ (see Sec. IV B) and then applying resonant light to couple it to the excited manifold. The state $|\psi_1\rangle$ is produced using an x-linear polarization $\mathbf{e}_x = (\mathbf{e}_+ + \mathbf{e}_-)/\sqrt{2}$, which dominantly couples the stretched states $|m = \pm J\rangle$ to states $|m' = \pm J'\rangle$ [see Fig. 7(a)]. Couplings to states $|m' = \pm(J'-2)\rangle$ also occur, albeit with very small Clebsch-Gordan coefficients, such that these processes can be neglected [87]. The state $|\psi_2\rangle$ is obtained using a z-linear polarization [see Fig. 7(d)]. In both cases, a coherent Rabi oscillation is observed when varying the pulse duration, and the fidelity of the preparation is limited by that of the cat state in the ground level. We show in Appendix C that the coherence of the superposition is maintained during Rabi flopping, by studying the states reached after 2π pulses.

We study the effect of qubit loss, triggered by spontaneous emission, on the superposition states $|\psi_1\rangle$ and $|\psi_2\rangle$. For the cat state $|\psi_1\rangle$, we only expect the population of the stretched states $|m = \pm J\rangle$ [see Fig. 7(b)]. To check the

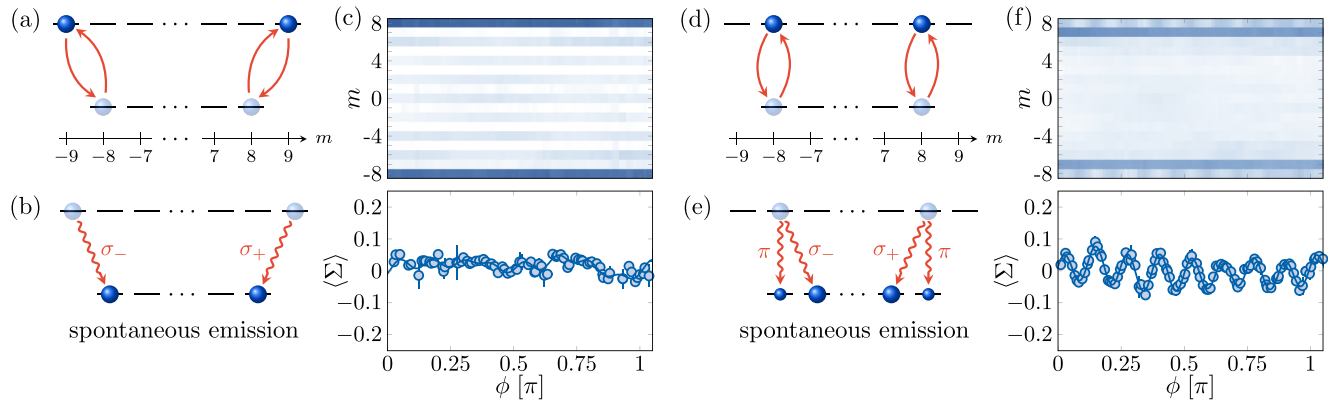

FIG. 7. Loss of a qubit pair from superposition states. (a) Preparation method for the Schrödinger cat state $|\psi_1\rangle$ in the excited electronic level. Given the small values of their Clebsch-Gordan coefficients, we neglect the couplings between $|m = \pm 8\rangle$ and $|m' = \pm 7\rangle$. (b) Scheme of the subsequent spontaneous emission. (c) Top panel: spin projection probabilities measured in the xy plane, as a function of the azimuthal angle ϕ. Bottom panel: The corresponding sign observable $\langle\Sigma\rangle$, together with a fit with a Fourier series. The y-axis range has been reduced compared with Fig. 5(f) to highlight the absence of oscillation. (d)–(f) show the same information for the superposition state $|\psi_2\rangle = (|m' = -8\rangle + |m' = 8\rangle)/\sqrt{2}$.

coherence between them, we measure the sign observable $\langle\Sigma\rangle$ as a function of the azimuthal angle ϕ, as in Sec. IV B. As shown in the bottom panel of Fig. 7(c), its oscillation is completely washed out, with a measured Fourier component $\Sigma_{2J} = 0.006(10)$, indicating an absence of coherence. For the superposition state $|\psi_2\rangle$, we observe dominant projection probabilities in the states $|m = \pm(J-1)\rangle$, corresponding to the spontaneous emission of a $\sigma_\mp$ polarized photon, respectively [see Fig. 7(e)]. We do not measure any significant variation of these probabilities with the azimuthal angle ϕ, excluding coherence between them. We also measure residual projection probabilities in the stretched states $|m = \pm J\rangle$, which occur via the spontaneous emission of a π polarized photon. The advantage of the sign observable Σ becomes clear here: It allows one to test the coherence between the states $|m = \pm J\rangle$, without being perturbed by the atoms populating odd-m states. The measured probabilities in stretched states coherently oscillate as a function of the angle ϕ [see Fig. 7(f)]. More quantitatively, the sign observable, which involves even m only, evolves with a Fourier component $\Sigma_{2J} = 0.024(1)$.

The complete loss of coherence when starting in the cat state $|\psi_1\rangle$ can be interpreted as follows. The spontaneous decay involves two orthogonal polarizations, with a σ_+ polarized photon emitted when starting in the component $|m' = -J'\rangle$, while a σ_- polarized photon is associated with the decay of the state $|m' = J'\rangle$ [see Fig. 7(b)]. The photon polarization thus holds complete *which path* information on the spin state polarization—a term referring to Einstein's version of the double-slit interference experiment [88,89]. In this case, the coherence between the different paths is erased after spontaneous emission.

For the state $|\psi_2\rangle$, the most probable quantum jumps correspond to the emission of σ_+ and σ_- polarized photons, which carry information about the state polarization [see Fig. 7(e)]. In contrast, the quantum jump associated with the emission of a π polarized photon does not give this information, which explains the residual coherence. The measured Fourier coefficient Σ_{2J} corresponds to 9.7(5)% of the value measured in the absence of the excitation. This reduction is consistent with the probability $1/(J+1) \simeq 11.1\%$ of scattering a π polarized photon for the considered state, showing that this channel fully preserves coherence.

VI. SUMMARY AND OUTLOOK

In this paper, we show that the $2J$-qubit ensemble associated with an atomic electronic spin J can be partitioned via the optical coupling to an excited level $J' = J - 1$. Among these qubits, $2J-2$ of them constitute the excited level, and the remaining two are annihilated by the absorbed photon, in a state defined by the light polarization. We investigate this process using atomic dysprosium and use it to probe entanglement in nonclassical states of spin $J = 8$. We fully characterize the nonclassical character of its reduced two-qubit state and study the increase of entropy upon partition as a smoking gun for entanglement.

In a second set of experiments, we consider the partition of an angular momentum $J' = J + 1$ of an excited electronic state. There, a random qubit pair is extracted by spontaneous emission towards the ground state J. We show that nonclassical pairwise correlations are robust to particle loss. In contrast, we observe that coherent superpositions of states distant in phase space are very fragile.

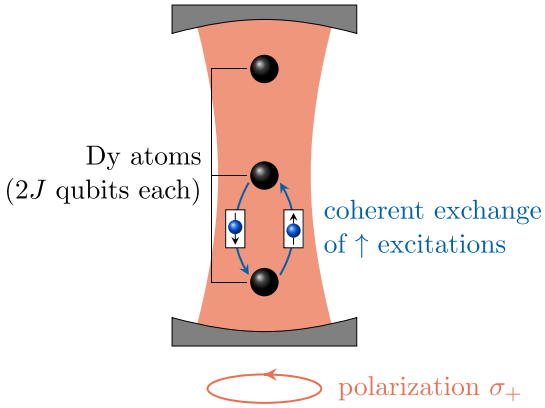

FIG. 8. Proposed scheme for entangling several Dy atoms in an optical resonator. An off-resonant optical cavity in the strong-coupling regime couples an ensemble of N atoms together. For σ_+ polarized cavity light, the total spin projection along z is conserved, and the cavity mediates the coherent exchange of $\uparrow$ qubit excitations between atoms. Such couplings can be used to stabilize a W state, with a single $\uparrow$ excitation symmetrically shared between the $N\times(2J)$ qubits.

In this paper, the study of light-spin interaction is limited to measurements of the electronic spin. A first extension would be to collect the spontaneously emitted photon, whose polarization is entangled with the electronic spin, as for experiments performed with trapped ions, atoms in optical cavities, or solid-state qubits [90–93]. One would thus explicitly access the *which path* information carried by the photon upon spontaneous emission of a Schrödinger cat state. More generally, the photon would allow one to couple qubit pairs from the electronic spin $J = 8$ to "flying qubits," which could then be manipulated to entangle distant atoms [94], and generalize quantum communication schemes to a mesoscopic degree of freedom [95].

Another interesting perspective would be to place the atomic gas in an optical cavity. The electronic spin J of a single atom would be coherently coupled to the cavity light mode, leading to a compound light-spin object [96]. For an atomic ensemble, the cavity light would also couple the electronic spins together, similarly to standard ensembles of spin-1/2 atoms coupled to optical cavities [4,97,98]. For a set of N dysprosium atoms—each hosting $2J$ qubits—the size of the Hilbert space would be $(2J+1)^N$, much smaller than the size 2^{2JN} for the same number of qubits realized with spin-1/2 atoms. This favorable scaling will mitigate decoherence effects associated with, for example, particle loss.

To be more concrete, we show in Fig. 8 an example of an application, with an ensemble of N atoms coupled to σ_+ polarized cavity light. The light mediates the coherent exchange of $|\uparrow\rangle$ excitations among the atoms, which could serve to stabilize a W state with one excitation symmetrically shared among $N \times (2J)$ qubits. Such many-body entangled states could feature a strong quantum enhancement of magnetic

sensitivity [99,100] or serve as a playground for studies of decoherence.

ACKNOWLEDGMENT

This work is supported by the European Union (Grant No. TOPODY 756722 from the European Research Council). We thank Jean Dalibard for stimulating discussions.

APPENDIX A: DEVIATION FROM z ROTATION SYMMETRY IN THE W AND CAT STATES

The W state $|m = -J + 1\rangle$ is invariant upon rotations around z, such that all observables should depend on the polar angle θ only. In practice, the state prepared close to the W state is not perfectly rotationally symmetric, because

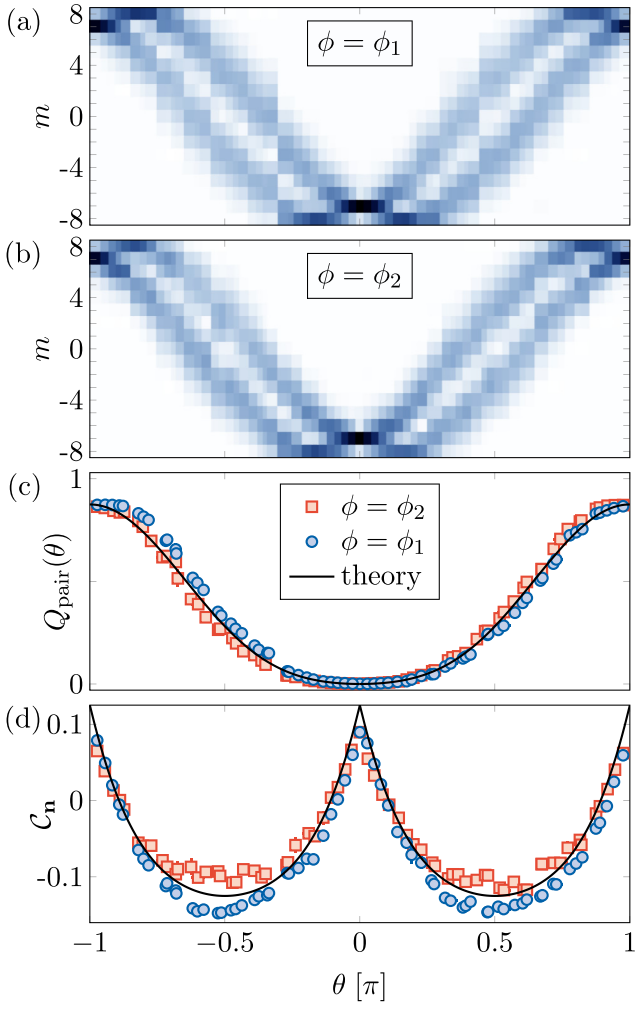

FIG. 9. Deviation from z rotation symmetry in the prepared W state. (a) and (b) Projection probabilities Π_m as a function of the polar angle θ, for $\phi_1 = 0.36(5)$ rad and $\phi_2 = \phi_1 - \pi/2$. (c) Pair Husimi functions Q_{pair} inferred from the (a) and (b) data (blue circles and red squares, respectively). The error bars represent the statistical uncertainty from a bootstrap random sampling analysis. The line corresponds to the expected variation for the W state. (d) Distribution $\mathcal{C}_{\mathbf{n}}$ as a function of θ. The two azimuthal angles ϕ_1 and ϕ_2 are chosen to minimize and maximize the measured $\mathcal{C}_{\mathbf{n}}$, respectively.

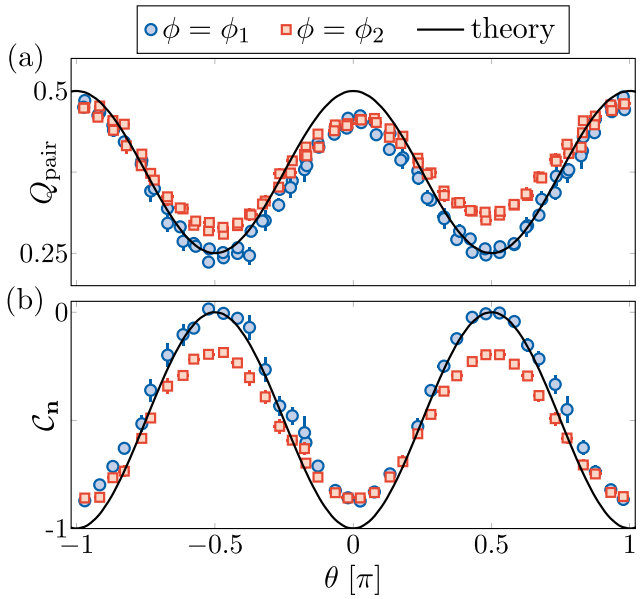

FIG. 10. Deviation from z rotation symmetry in the prepared Schrödinger cat state. (a) Pair Husimi functions Q_{pair} as a function of the polar angle θ, for $\phi_1 = 3.3(1)$ rad and $\phi_2 = \phi_1 - \pi/2$ (blue circles and red squares, respectively). The line corresponds to the expected variation for a perfect cat state. (b) Distribution $\mathcal{C}_{\mathbf{n}}$ as a function of θ deduced from the data in (a).

of a residual coherent admixture with other Dicke states. We measure a small ϕ variation of the measured probability distributions $\Pi_m(\mathbf{n})$, as well as the pair Husimi function Q_{pair} and distribution $\mathcal{C}_{\mathbf{n}}$ deduced from them. We show in Fig. 9 the

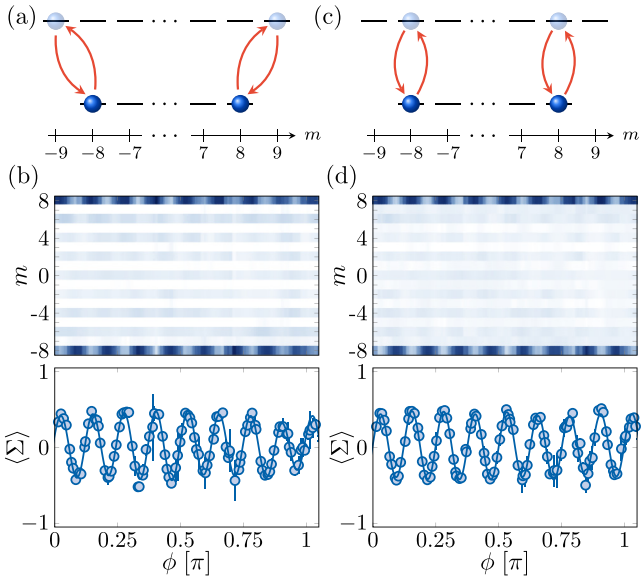

FIG. 11. (a) Scheme of the 2π Rabi oscillation starting in a Schrödinger cat state of the electronic ground level, for an x-polarized laser excitation. (b) Top panel: spin projection probabilities measured in the xy plane, as a function of the azimuthal angle ϕ. Bottom panel: the corresponding sign observable $\langle\Sigma\rangle$, together with a fit with a Fourier series. (c) and (d) show the same information for a z-polarized laser excitation.

measured data for two azimuthal angles $\phi_1 = 0.36(5)$ rad and $\phi_2 = \phi_1 - \pi/2$, for which $\mathcal{C}_\mathbf{n}$ is minimized and maximized, respectively. The data shown in Fig. 3 of the main text correspond to an average over ϕ, the error bars taking into account this dispersion.

The cat state $|m = -J\rangle + |m = J\rangle$ is not rotationally invariant. Yet, its reduced two-body density matrix, given by Eq. (8), is invariant such that the pair Husimi function Q_{pair} and distribution $\mathcal{C}_\mathbf{n}$ should depend on θ only. As for the W state, we measure a slight variation of these quantities with ϕ, as shown in Fig. 10. Since we focus on extracting the concurrence from the maximum of $\mathcal{C}_\mathbf{n}$, we show in the main text the data measured for an azimuthal angle $\phi_1 = 3.3(1)$ rad that maximizes $\mathcal{C}_\mathbf{n}$.

APPENDIX B: SPIN-1 TOMOGRAPHY USING THE PAIR HUSIMI FUNCTION

The Husimi function of a spin-1 quantum state ρ expands on the spherical harmonics Y_ℓ^m with $\ell = 1, 2$ and $|m| \leqslant \ell$, as written in Eq. (6). This linear decomposition allows us to retrieve the density matrix ρ, as given by Eq. (7), where we introduce the operators

$$\mathcal{L}_0 = L_z, \tag{B1}$$

$$\mathcal{L}_{\pm1} = \mp(L_x \pm iL_y)/\sqrt{2}, \tag{B2}$$

$$\mathcal{Q}_0 = \sqrt{\frac{5}{3}}\left(3L_z^2 - 2\right), \tag{B3}$$

$$\mathcal{Q}_{\pm1} = \mp\sqrt{\frac{5}{2}}[(L_x \pm iL_y)L_z + L_z(L_x \pm iL_y)], \tag{B4}$$

$$\mathcal{Q}_{\pm2} = \sqrt{\frac{5}{2}}(L_x \pm iL_y)^2. \tag{B5}$$

APPENDIX C: COHERENCE OF SUPERPOSITION STATES DURING RABI FLOPPING

The preparation of superposition states in the excited electronic state, as studied in Sec. V B, uses coherent Rabi oscillations, starting in a Schrödinger cat state of the ground electronic level $(|m = -J\rangle + |m = J\rangle)/\sqrt{2}$. To check that coherence is maintained during the Rabi oscillation, we study it after a 2π excitation, by measuring the oscillation of the sign observable $\langle\Sigma\rangle$.

As shown in Fig. 11, we find that the coherence $|\rho_{-J,J}|$, estimated by the Fourier component Σ_{2J}, is reduced to 0.202(2) [0.211(6)] for the x-polarized (z-polarized) excitation, i.e., above 80% of the value obtained with no Rabi pulse. These measurements confirm that coherence is preserved during the Rabi oscillation.

[1] S. J. Freedman and J. F. Clauser, Experimental Test of Local Hidden-Variable Theories, Phys. Rev. Lett. **28**, 938 (1972).

[2] A. Aspect, J. Dalibard, and G. Roger, Experimental Test of Bell's Inequalities Using Time-Varying Analyzers, Phys. Rev. Lett. **49**, 1804 (1982).

[3] L. Amico, R. Fazio, A. Osterloh, and V. Vedral, Entanglement in many-body systems, Rev. Mod. Phys. **80**, 517 (2008).

[4] L. Pezzè, A. Smerzi, M. K. Oberthaler, R. Schmied, and P. Treutlein, Quantum metrology with nonclassical states of atomic ensembles, Rev. Mod. Phys. **90**, 035005 (2018).

[5] A. Sørensen, L.-M. Duan, J. I. Cirac, and P. Zoller, Many-particle entanglement with Bose–Einstein condensates, Nature (London) **409**, 63 (2001).

[6] A. S. Sørensen and K. Mølmer, Entanglement and Extreme Spin Squeezing, Phys. Rev. Lett. **86**, 4431 (2001).

[7] J. Esteve, C. Gross, A. Weller, S. Giovanazzi, and M. Oberthaler, Squeezing and entanglement in a Bose–Einstein condensate, Nature (London) **455**, 1216 (2008).

[8] M. F. Riedel, P. Böhi, Y. Li, T. W. Hänsch, A. Sinatra, and P. Treutlein, Atom-chip-based generation of entanglement for quantum metrology, Nature (London) **464**, 1170 (2010).

[9] C. Gross, T. Zibold, E. Nicklas, J. Estève, and M. K. Oberthaler, Nonlinear atom interferometer surpasses classical precision limit, Nature (London) **464**, 1165 (2010).

[10] P. Hyllus, W. Laskowski, R. Krischek, C. Schwemmer, W. Wieczorek, H. Weinfurter, L. Pezzé, and A. Smerzi, Fisher information and multiparticle entanglement, Phys. Rev. A **85**, 022321 (2012).

[11] G. Tóth, Multipartite entanglement and high-precision metrology, Phys. Rev. A **85**, 022322 (2012).

[12] J.-W. Pan, Z.-B. Chen, C.-Y. Lu, H. Weinfurter, A. Zeilinger, and M. Żukowski, Multiphoton entanglement and interferometry, Rev. Mod. Phys. **84**, 777 (2012).

[13] G. Wendin, Quantum information processing with superconducting circuits: A review, Rep. Prog. Phys. **80**, 106001 (2017).

[14] R. Blatt and D. Wineland, Entangled states of trapped atomic ions, Nature (London) **453**, 1008 (2008).

[15] M. Saffman, T. G. Walker, and K. Mølmer, Quantum information with Rydberg atoms, Rev. Mod. Phys. **82**, 2313 (2010).

[16] R. Horodecki, P. Horodecki, M. Horodecki, and K. Horodecki, Quantum entanglement, Rev. Mod. Phys. **81**, 865 (2009).

[17] O. Gühne and G. Tóth, Entanglement detection, Phys. Rep. **474**, 1 (2009).

[18] S. Hill and W. K. Wootters, Entanglement of a Pair of Quantum Bits, Phys. Rev. Lett. **78**, 5022 (1997).

[19] W. K. Wootters, Entanglement of Formation of an Arbitrary State of Two Qubits, Phys. Rev. Lett. **80**, 2245 (1998).

[20] F. A. Bovino, G. Castagnoli, A. Ekert, P. Horodecki, C. M. Alves, and A. V. Sergienko, Direct Measurement of Nonlinear Properties of Bipartite Quantum States, Phys. Rev. Lett. **95**, 240407 (2005).

[21] S. P. Walborn, P. H. Souto Ribeiro, L. Davidovich, F. Mintert, and A. Buchleitner, Experimental determination of entanglement with a single measurement, Nature (London) **440**, 1022 (2006).

[22] C. Schmid, N. Kiesel, W. Wieczorek, H. Weinfurter, F. Mintert, and A. Buchleitner, Experimental Direct Observation of Mixed State Entanglement, Phys. Rev. Lett. **101**, 260505 (2008).

[23] R. Islam, R. Ma, P. M. Preiss, M. Eric Tai, A. Lukin, M. Rispoli, and M. Greiner, Measuring entanglement entropy in a quantum many-body system, Nature (London) **528**, 77 (2015).

[24] W. Dür, G. Vidal, and J. I. Cirac, Three qubits can be entangled in two inequivalent ways, Phys. Rev. A **62**, 062314 (2000).

[25] G. Tóth and O. Gühne, Detecting Genuine Multipartite Entanglement with Two Local Measurements, Phys. Rev. Lett. **94**, 060501 (2005).

[26] R. Lapkiewicz, P. Li, C. Schaeff, N. K. Langford, S. Ramelow, M. Wieśniak, and A. Zeilinger, Experimental non-classicality of an indivisible quantum system, Nature (London) **474**, 490 (2011).

[27] S. Chaudhury, S. Merkel, T. Herr, A. Silberfarb, I. H. Deutsch, and P. S. Jessen, Quantum Control of the Hyperfine Spin of a Cs Atom Ensemble, Phys. Rev. Lett. **99**, 163002 (2007).

[28] T. Fernholz, H. Krauter, K. Jensen, J. F. Sherson, A. S. Sørensen, and E. S. Polzik, Spin Squeezing of Atomic Ensembles via Nuclear-Electronic Spin Entanglement, Phys. Rev. Lett. **101**, 073601 (2008).

[29] D. Gatteschi and R. Sessoli, Quantum tunneling of magnetization and related phenomena in molecular materials, Angew. Chem. Int. Ed. **42**, 268 (2003).

[30] A. Facon, E.-K. Dietsche, D. Grosso, S. Haroche, J.-M. Raimond, M. Brune, and S. Gleyzes, A sensitive electrometer based on a Rydberg atom in a Schrödinger-cat state, Nature (London) **535**, 262 (2016).

[31] E. Majorana, Atomi orientati in campo magnetico variabile, Nuovo Cim. **9**, 43 (1932).

[32] In practice, since the light shift amplitudes strongly vary with m, we vary the pulse duration in the range 10–100 μs and the detuning in the range 50 MHz to 1 GHz, in order to keep similar displacements for all m states (except the dark states). For the smallest detunings, we take into account the corrections to the second-order light shifts. The uncertainties in the laser beam waist $w = 40(5)$ μm and in the excited state lifetime $\tau \simeq 11$ μs [101] lead to a systematic error. We correct an overall 20% error using the constraint $\sum_m Q_m = (2J+1)/3$, which states that in a completely undetermined state, a symmetric qubit pair has 1/3 chance to be in $|\uparrow\uparrow\rangle$.

[33] R. H. Dicke, Coherence in spontaneous radiation processes, Phys. Rev. **93**, 99 (1954).

[34] K. S. Choi, A. Goban, S. B. Papp, S. J. van Enk, and H. J. Kimble, Entanglement of spin waves among four quantum memories, Nature (London) **468**, 412 (2010).

[35] F. Haas, J. Volz, R. Gehr, J. Reichel, and J. Estève, Entangled states of more than 40 atoms in an optical fiber cavity, Science **344**, 180 (2014).

[36] R. McConnell, H. Zhang, J. Hu, S. Ćuk, and V. Vuletić, Entanglement with negative Wigner function of almost 3,000 atoms heralded by one photon, Nature (London) **519**, 439 (2015).

[37] M. Ebert, M. Kwon, T. G. Walker, and M. Saffman, Coherence and Rydberg Blockade of Atomic Ensemble Qubits, Phys. Rev. Lett. **115**, 093601 (2015).

[38] J. Zeiher, P. Schauß, S. Hild, T. Macrì, I. Bloch, and C. Gross, Microscopic Characterization of Scalable Coherent Rydberg Superatoms, Phys. Rev. X **5**, 031015 (2015).

[39] H. Häffner, W. Hänsel, C. F. Roos, J. Benhelm, D. Chek-al-kar, M. Chwalla, T. Körber, U. D. Rapol, M. Riebe, P. O. Schmidt, C. Becher, O. Gühne, W. Dür, and R. Blatt, Scalable multiparticle entanglement of trapped ions, Nature (London) **438**, 643 (2005).

[40] F. Fröwis, P. C. Strassmann, A. Tiranov, C. Gut, J. Lavoie, N. Brunner, F. Bussières, M. Afzelius, and N. Gisin, Experimental certification of millions of genuinely entangled atoms in a solid, Nat. Commun. **8**, 907 (2017).

[41] Y. Pu, Y. Wu, N. Jiang, W. Chang, C. Li, S. Zhang, and L. Duan, Experimental entanglement of 25 individually accessible atomic quantum interfaces, Sci. Adv. **4**, 3931 (2018).

[42] P. Facchi and S. Pascazio, Quantum Zeno Subspaces, Phys. Rev. Lett. **89**, 080401 (2002).

[43] F. Schäfer, I. Herrera, S. Cherukattil, C. Lovecchio, F. S. Cataliotti, F. Caruso, and A. Smerzi, Experimental realization of quantum Zeno dynamics, Nat. Commun. **5**, 3194 (2014).

[44] A. Signoles, A. Facon, D. Grosso, I. Dotsenko, S. Haroche, J.-M. Raimond, M. Brune, and S. Gleyzes, Confined quantum Zeno dynamics of a watched atomic arrow, Nat. Phys. **10**, 715 (2014).

[45] The W-state fidelity is mostly limited by inelastic collisions between atoms, which redistribute the spin among neighboring m states.

[46] E. C. G. Sudarshan, Equivalence of Semiclassical and Quantum Mechanical Descriptions of Statistical Light Beams, Phys. Rev. Lett. **10**, 277 (1963).

[47] R. J. Glauber, Coherent and Incoherent States of the Radiation Field, Phys. Rev. **131**, 2766 (1963).

[48] O. Giraud, P. Braun, and D. Braun, Classicality of spin states, Phys. Rev. A **78**, 042112 (2008).

[49] J. K. Korbicz, J. I. Cirac, and M. Lewenstein, Spin Squeezing Inequalities and Entanglement of N Qubit States, Phys. Rev. Lett. **95**, 120502 (2005).

[50] While the W state is rotationally symmetric around z, we observe in the prepared state a small but significant variation of the projection probabilities with the azimuthal angle ϕ. We show in Figs. 3(b)–3(d) the ϕ-averaged values of our measurements. The variation with ϕ of the measured quantities is taken into account in the error bars and is explicitly shown in Appendix A.

[51] M. Hillery, Nonclassical distance in quantum optics, Phys. Rev. A **35**, 725 (1987).

[52] T.-C. Wei and P. M. Goldbart, Geometric measure of entanglement and applications to bipartite and multipartite quantum states, Phys. Rev. A **68**, 042307 (2003).

[53] J. Vidal, Concurrence in collective models, Phys. Rev. A **73**, 062318 (2006).

[54] M. Koashi, V. Bužek, and N. Imoto, Entangled webs: Tight bound for symmetric sharing of entanglement, Phys. Rev. A **62**, 050302(R) (2000).

[55] M. Kitagawa and M. Ueda, Squeezed spin states, Phys. Rev. A **47**, 5138 (1993).

[56] T. Chalopin, C. Bouazza, A. Evrard, V. Makhalov, D. Dreon, J. Dalibard, L. A. Sidorenkov, and S. Nascimbene, Quantum-enhanced sensing using non-classical spin states of a highly magnetic atom, Nat. Commun. **9**, 4955 (2018).

[57] X. Wang and B. C. Sanders, Spin squeezing and pairwise entanglement for symmetric multiqubit states, Phys. Rev. A **68**, 012101 (2003).

[58] R. Horodecki and M. Horodecki, Information-theoretic aspects of inseparability of mixed states, Phys. Rev. A **54**, 1838 (1996).

[59] R. Konig, R. Renner, and C. Schaffner, The operational meaning of min- and max-entropy, IEEE Trans. Inf. Theory **55**, 4337 (2009).

[60] V. I. Man'ko and O. V. Man'ko, Spin state tomography, J. Exp. Theor. Phys. **85**, 430 (1997).

[61] C. Monroe, D. Meekhof, B. King, and D. J. Wineland, A "Schrödinger cat" superposition state of an atom, Science **272**, 1131 (1996).

[62] M. Brune, E. Hagley, J. Dreyer, X. Maître, A. Maali, C. Wunderlich, J. M. Raimond, and S. Haroche, Observing the Progressive Decoherence of the "Meter" in a Quantum Measurement, Phys. Rev. Lett. **77**, 4887 (1996).

[63] J. R. Friedman, V. Patel, W. Chen, S. Tolpygo, and J. E. Lukens, Quantum superposition of distinct macroscopic states, Nature (London) **406**, 43 (2000).

[64] C. A. Sackett, D. Kielpinski, B. E. King, C. Langer, V. Meyer, C. J. Myatt, M. Rowe, Q. A. Turchette, W. M. Itano, D. J. Wineland, and C. Monroe, Experimental entanglement of four particles, Nature (London) **404**, 256 (2000).

[65] D. Leibfried, E. Knill, S. Seidelin, J. Britton, R. B. Blakestad, J. Chiaverini, D. B. Hume, W. M. Itano, J. D. Jost, C. Langer, R. Ozeri, R. Reichle, and D. J. Wineland, Creation of a six-atom 'Schrödinger cat' state, Nature (London) **438**, 639 (2005).

[66] A. Ourjoumtsev, R. Tualle-Brouri, J. Laurat, and P. Grangier, Generating optical Schrödinger kittens for quantum information processing, Science **312**, 83 (2006).

[67] J. S. Neergaard-Nielsen, B. M. Nielsen, C. Hettich, K. Mølmer, and E. S. Polzik, Generation of a Superposition of Odd Photon Number States for Quantum Information Networks, Phys. Rev. Lett. **97**, 083604 (2006).

[68] S. Deleglise, I. Dotsenko, C. Sayrin, J. Bernu, M. Brune, J.-M. Raimond, and S. Haroche, Reconstruction of non-classical cavity field states with snapshots of their decoherence, Nature (London) **455**, 510 (2008).

[69] T. Monz, P. Schindler, J. T. Barreiro, M. Chwalla, D. Nigg, W. A. Coish, M. Harlander, W. Hänsel, M. Hennrich, and R. Blatt, 14-Qubit Entanglement: Creation and Coherence, Phys. Rev. Lett. **106**, 130506 (2011).

[70] X.-C. Yao, T.-X. Wang, P. Xu, H. Lu, G.-S. Pan, X.-H. Bao, C.-Z. Peng, C.-Y. Lu, Y.-A. Chen, and J.-W. Pan, Observation of eight-photon entanglement, Nat. Photon. **6**, 225 (2012).

[71] G. Kirchmair, B. Vlastakis, Z. Leghtas, S. E. Nigg, H. Paik, E. Ginossar, M. Mirrahimi, L. Frunzio, S. M. Girvin, and R. J. Schoelkopf, Observation of quantum state collapse and revival due to the single-photon Kerr effect, Nature (London) **495**, 205 (2013).

[72] C. L. Degen, F. Reinhard, and P. Cappellaro, Quantum sensing, Rev. Mod. Phys. **89**, 035002 (2017).

[73] X.-L. Wang, Y.-H. Luo, H.-L. Huang, M.-C. Chen, Z.-E. Su, C. Liu, C. Chen, W. Li, Y.-Q. Fang, X. Jiang, J. Zhang, L. Li, N.-L. Liu, C.-Y. Lu, and J.-W. Pan, 18-Qubit Entanglement with Six Photons' Three Degrees of Freedom, Phys. Rev. Lett. **120**, 260502 (2018).

[74] E. K. Dietsche, A. Larrouy, S. Haroche, J. M. Raimond, M. Brune, and S. Gleyzes, High-sensitivity magnetometry with a single atom in a superposition of two circular Rydberg states, Nat. Phys. **15**, 326 (2019).

[75] C. Song, K. Xu, H. Li, Y.-R. Zhang, X. Zhang, W. Liu, Q. Guo, Z. Wang, W. Ren, J. Hao, H. Feng, H. Fan, D. Zheng, D.-W. Wang, H. Wang, and S.-Y. Zhu, Generation of multicomponent atomic Schrödinger cat states of up to 20 qubits, Science **365**, 574 (2019).

[76] A. Omran, H. Levine, A. Keesling, G. Semeghini, T. T. Wang, S. Ebadi, H. Bernien, A. S. Zibrov, H. Pichler, S. Choi, J. Cui, M. Rossignolo, P. Rembold, S. Montangero, T. Calarco, M. Endres, M. Greiner, V. Vuletić, and M. D. Lukin, Generation and manipulation of Schrödinger cat states in Rydberg atom arrays, Science **365**, 570 (2019).

[77] K. X. Wei, I. Lauer, S. Srinivasan, N. Sundaresan, D. T. McClure, D. Toyli, D. C. McKay, J. M. Gambetta, and S. Sheldon, Verifying multipartite entangled Greenberger-Horne-Zeilinger states via multiple quantum coherences, Phys. Rev. A **101**, 032343 (2020).

[78] N. D. Mermin, Extreme Quantum Entanglement in a Superposition of Macroscopically Distinct States, Phys. Rev. Lett. **65**, 1838 (1990).

[79] J. J. Bollinger, W. M. Itano, D. J. Wineland, and D. J. Heinzen, Optimal frequency measurements with maximally correlated states, Phys. Rev. A **54**, R4649(R) (1996).

[80] In practice, we observe a small variation of the measured $\mathcal{C}_{\mathbf{n}}$ with the azimuthal angle ϕ, discussed in Appendix A. We show in Fig. 5(b) the variation of $\mathcal{C}_{\mathbf{n}}$ with the polar angle θ with a fixed angle $\phi = 3.3(1)$ rad, which maximizes the value of $\mathcal{C}_{\mathbf{n}}$.

[81] E. Davis, G. Bentsen, and M. Schleier-Smith, Approaching the Heisenberg Limit without Single-Particle Detection, Phys. Rev. Lett. **116**, 053601 (2016).

[82] D. Linnemann, H. Strobel, W. Muessel, J. Schulz, R. J. Lewis-Swan, K. V. Kheruntsyan, and M. K. Oberthaler, Quantum-Enhanced Sensing Based on Time Reversal of Nonlinear Dynamics, Phys. Rev. Lett. **117**, 013001 (2016).

[83] F. Fröwis, P. Sekatski, and W. Dür, Detecting Large Quantum Fisher Information with Finite Measurement Precision, Phys. Rev. Lett. **116**, 090801 (2016).

[84] T. Macrì, A. Smerzi, and L. Pezzè, Loschmidt echo for quantum metrology, Phys. Rev. A **94**, 010102(R) (2016).

[85] M. Gustavsson, H. Lundberg, L. Nilsson, and S. Svanberg, Lifetime measurements for excited states of rare-earth atoms using pulse modulation of a cw dye-laser beam, J. Opt. Soc. Am. **69**, 984 (1979).

[86] C.-W. Lee and H. Jeong, Quantification of Macroscopic Quantum Superpositions within Phase Space, Phys. Rev. Lett. **106**, 220401 (2011).

[87] The coupling amplitudes between $|m = \pm J\rangle$ and $|m' = \pm(J'-2)\rangle$ are $1/\sqrt{153}$ smaller than the couplings between $|m = \pm J\rangle$ and $|m' = \pm J'\rangle$. When the population of $|m' = \pm J'\rangle$ is maximized, we expect a residual population of the states $|m' = \pm(J'-2)\rangle$ of 3% due to these small couplings.

[88] W. K. Wootters and W. H. Zurek, Complementarity in the double-slit experiment: Quantum nonseparability and a quantitative statement of Bohr's principle, Phys. Rev. D **19**, 473 (1979).

[89] B.-G. Englert, Fringe Visibility and Which-Way Information: An Inequality, Phys. Rev. Lett. **77**, 2154 (1996).

[90] B. B. Blinov, D. L. Moehring, L.-M. Duan, and C. Monroe, Observation of entanglement between a single trapped atom and a single photon, Nature (London) **428**, 153 (2004).

[91] J. Volz, M. Weber, D. Schlenk, W. Rosenfeld, J. Vrana, K. Saucke, C. Kurtsiefer, and H. Weinfurter, Observation of Entanglement of a Single Photon with a Trapped Atom, Phys. Rev. Lett. **96**, 030404 (2006).

[92] T. Wilk, S. C. Webster, A. Kuhn, and G. Rempe, Single-atom single-photon quantum interface, Science **317**, 488 (2007).

[93] E. Togan, Y. Chu, A. S. Trifonov, L. Jiang, J. Maze, L. Childress, M. V. G. Dutt, A. S. Sørensen, P. R. Hemmer, A. S. Zibrov, and M. D. Lukin, Quantum entanglement between an optical photon and a solid-state spin qubit, Nature (London) **466**, 730 (2010).

[94] D. L. Moehring, P. Maunz, S. Olmschenk, K. C. Younge, D. N. Matsukevich, L.-M. Duan, and C. Monroe, Entanglement of single-atom quantum bits at a distance, Nature (London) **449**, 68 (2007).

[95] D. Cozzolino, B. D. Lio, D. Bacco, and L. K. Oxenløwe, High-dimensional quantum communication: Benefits, progress, and future challenges, Adv. Quantum Technol. **2**, 1900038 (2019).

[96] N. Brahms and D. M. Stamper-Kurn, Spin optodynamics analog of cavity optomechanics, Phys. Rev. A **82**, 041804(R) (2010).

[97] F. Brennecke, T. Donner, S. Ritter, T. Bourdel, M. Köhl, and T. Esslinger, Cavity QED with a Bose–Einstein condensate, Nature (London) **450**, 268 (2007).

[98] Y. Colombe, T. Steinmetz, G. Dubois, F. Linke, D. Hunger, and J. Reichel, Strong atom–field coupling for Bose–Einstein condensates in an optical cavity on a chip, Nature (London) **450**, 272 (2007).

[99] L. M. Norris, C. M. Trail, P. S. Jessen, and I. H. Deutsch, Enhanced Squeezing of a Collective Spin via Control of Its Qudit Subsystems, Phys. Rev. Lett. **109**, 173603 (2012).

[100] G. Vitagliano, I. Apellaniz, I. L. Egusquiza, and G. Tóth, Spin squeezing and entanglement for an arbitrary spin, Phys. Rev. A **89**, 032307 (2014).

[101] V. A. Dzuba, V. V. Flambaum, and B. L. Lev, Dynamic polarizabilities and magic wavelengths for dysprosium, Phys. Rev. A **83**, 032502 (2011).

B

Appendix: Transverse cooling

We present the dependence of the efficiency of the transverse cooling with respect to a few experimental parameters: the currents through the three coils that fully control the magnetic field at the position of the atoms and the waveplates that define the polarisation of the forward linearly-polarised beam and the backward beam. We also show a calibration of the frequency of the transverse cooling beams based on the atomic resonance at 421.3 nm.

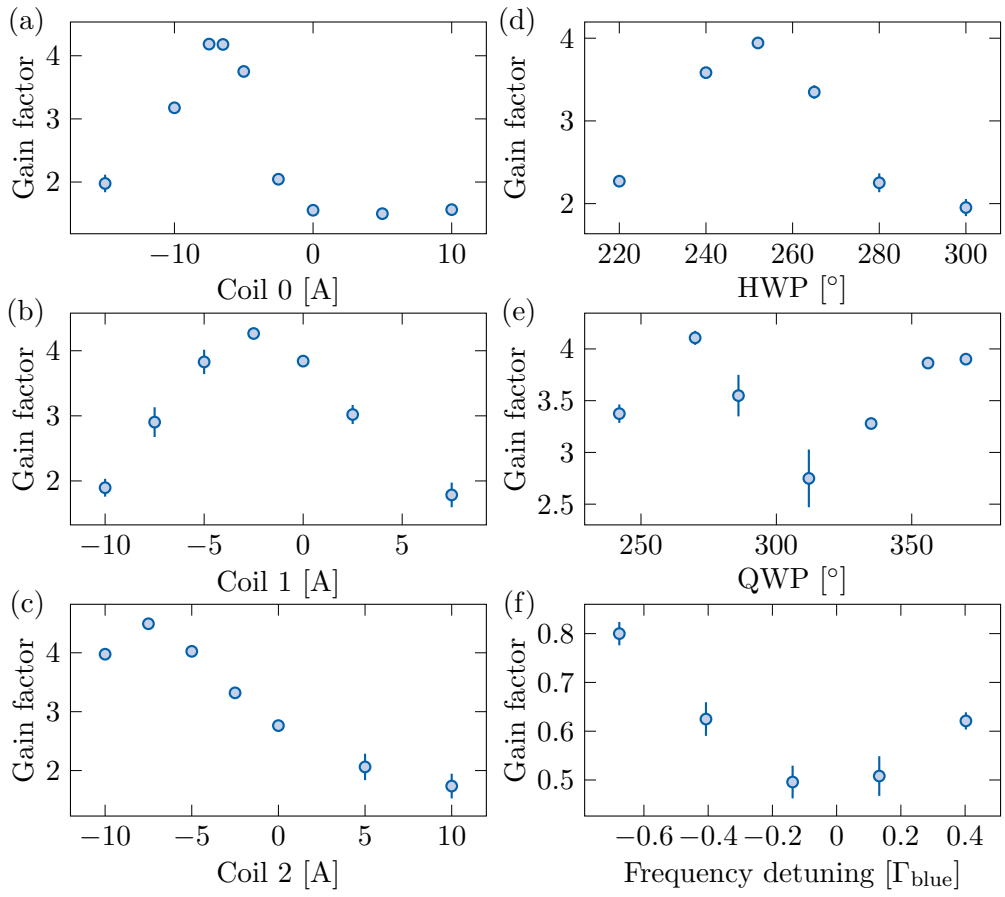

Figure B.1 – Panels (a,b,c,d,e): Gain factor from transverse cooling in the atom number in the MOT with a loading time of 4 s, as a function of the current in the three coils and the half-waveplate angle of the forward beam with linear polarisation and the quarter-waveplate angle of the backward beam. For all parameters, we scan the frequency detuning and extract the gain factor at maximum. Panel (f): Frequency detuning scan with a single forward beam at low power, to calibrate the atomic resonance.

C

Appendix: Imaging improvement

We schematically describe our algorithm for the improvement of the quality of the absorption images and how it depends on a few parameters.

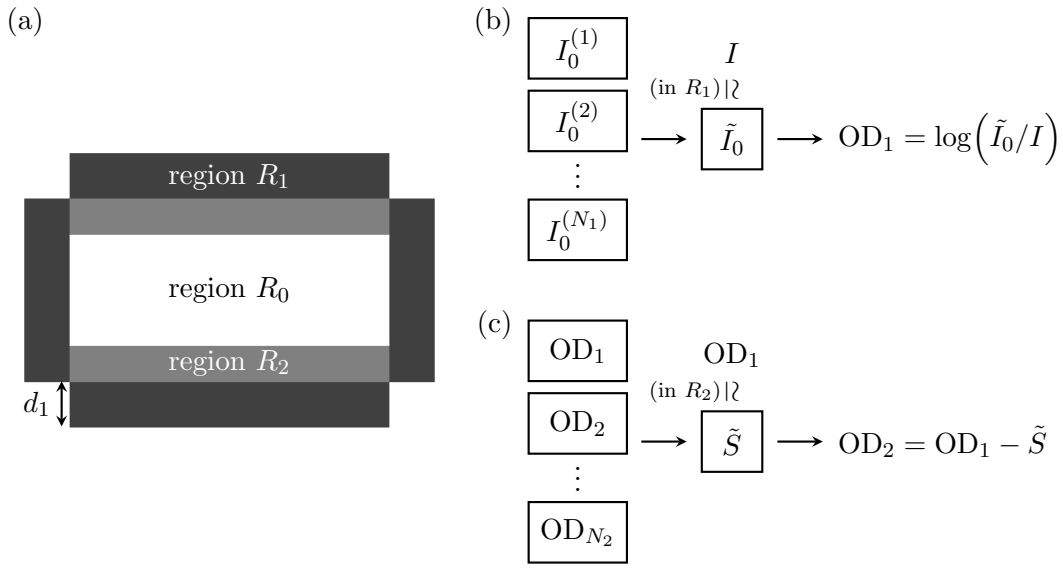

Figure C.1 – Panel (a): Scheme representing an image recorded on the CCD camera. The region R_0 is the region of interest containing atoms. The regions R_1 and R_2 do not contain atoms and are used for the two steps of the image algorithm. Panels (b,c): Schematic representations of the two steps of the algorithm. In (b), an image $\tilde{I}_0$ is constructed from a set of images without atoms based on its proximity in the region R_1 with the image I that contains the atomic signal of interest. We compute the optical density OD_1 using $\tilde{I}_0$. In (c), an optical density $\tilde{S}$ is constructed from a set of ODs without atoms based on its proximity in the region R_2 with the optical density OD_1. We subtract $\tilde{S}$ from OD_1.

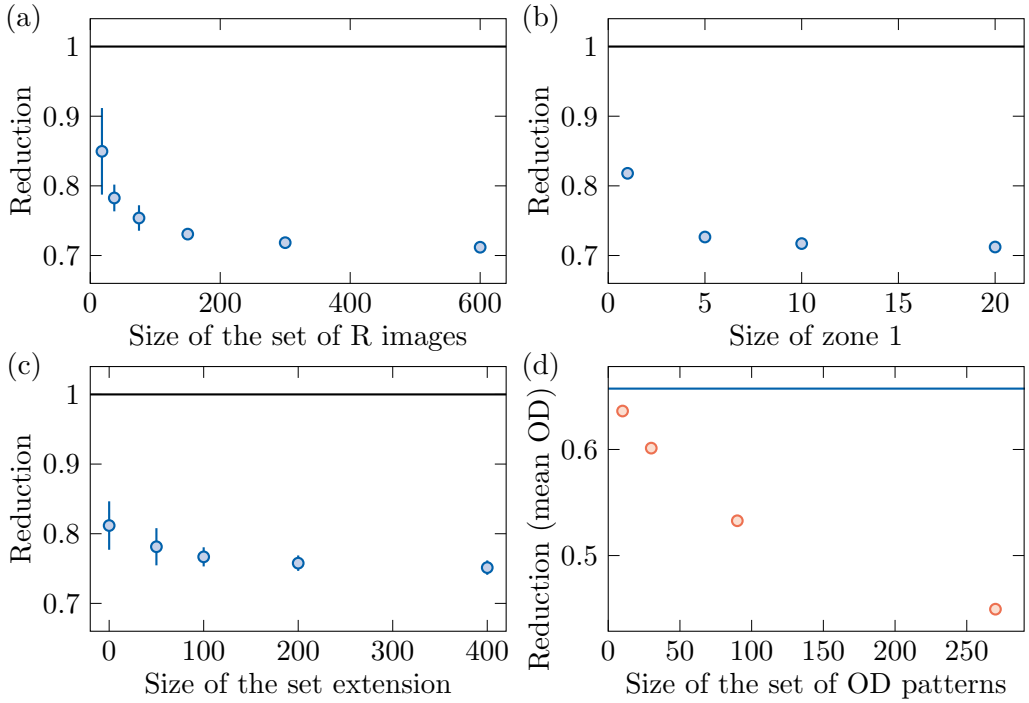

Figure C.2 – Panels (a,b,c): Study of the parameter of the first step of the image algorithm. Reduction of the standard deviation of the pixels in the optical density computed with our algorithm compared to the standard method, as a function of the size N_1 of the set of images $\{I_0^{(n)}\}$, the size of the region R_1 characterised by the distance d_1 and the size of the extension of the set $\{I_0^{(n)}\}$ by shifted such images by a few pixels in any direction, to artificially increase the size of the set. The black lines indicate the standard method. Panel (d): Study of the second step of the image algorithm. Reduction of the standard deviation of the pixels in the averaged optical density $\overline{\text{OD}}$ using the full algorithm for each OD compared to the standard method, as a function of the size N_2 of the set of ODs without atoms. The blue line indicates the case of using the first step of the algorithm only. In all panels, we use experimental sequences without atoms to easily compare the background noise.

D

Appendix: Magnetic dipole-dipole interaction

We derive the expression of the magnetic dipole-dipole interaction at low energy in our implementation of an atomic Hall cylinder. In general, it is described by the potential:

$$V_{\mathrm{dd}}(\mathbf{r}) = \frac{\mu_0 (g_J \mu_B)^2}{4\pi} \frac{\mathbf{J}_1 \cdot \mathbf{J}_2 - 3(\mathbf{J}_1 \cdot \mathbf{e}_r)(\mathbf{J}_2 \cdot \mathbf{e}_r)}{r^3}, \tag{D.1}$$

with $\mathbf{e}_r = \mathbf{r}/r$. We restrict the motion of the particles to a one-dimensional system along the axis x of propagation of the Raman beams. At low energy, the spin states are in the ground band of the system and decompose on the three coherent states $|\phi\rangle$, with an azimuthal angle $\phi = 0$, $2\pi/3$ and $2\pi/4$, and a polar angle $\theta = \pi/2$. The interaction becomes:

$$\langle \phi, \phi' | V_{\mathrm{dd}} | \phi, \phi' \rangle (x) = \frac{\mu_0 (g_J J \mu_B)^2}{4\pi} \frac{\cos(\phi - \phi') - 3\cos(\phi)\cos(\phi')}{x^3}, \tag{D.2}$$

where we used the expectation value of the spin vector operator $\langle \phi | \mathbf{J} | \phi \rangle = J(\cos\phi\, \mathbf{e}_x + \sin\phi\, \mathbf{e}_y)$. The atoms are subjected to a bias magnetic field which sets a Larmor angular frequency δ_z, at which the spin states precess around z. An initial spin state $|\phi\rangle$ evolves as $|\phi + \delta_z t\rangle$ as a function of time t. This leads to a time-dependent interaction term $-3\cos(\phi + \delta_z t)\cos(\phi' + \delta_z t)$. We average out the fast-oscillating term which gives $-(3/2)\cos(\phi - \phi')$ and the total magnetic dipole-dipole interaction writes:

$$\langle \phi, \phi' | V_{\mathrm{dd}} | \phi, \phi' \rangle (x) = -\frac{1}{2} \frac{\mu_0 (g_J J \mu_B)^2}{4\pi} \frac{\cos(\phi - \phi')}{x^3}. \tag{D.3}$$

It can take two different values depending on the $|\phi - \phi'| = 0$ or $2\pi/3$, corresponding to the interaction for atoms in the same coherent state or in different coherent states respectively.

Résumé détaillé

La physique quantique s'est révélée être une théorie efficace pour prédire le comportement des constituants élémentaires de notre univers. Son application aux systèmes macroscopiques a été fructueuse pour l'étude d'effets collectifs, comme le souligne la publication intitulée "More is different" [1]. Les symétries des lois physiques jouent un rôle central dans la description de ces systèmes, tout comme le concept de brisure spontanée de symétrie qui permet d'obtenir des états qui ne respectent pas la symétrie sous-jacente. Le ferromagnétisme dans des matériaux tels que le fer et la cristallisation des atomes pour former des solides appartiennent à cette classe d'états.

La découverte de plateaux de conductivité dans un gaz d'électrons bidimensionnel soumis à un champ magnétique [2], désormais appelé effet Hall quantique entier, a initié de nouvelles recherches théoriques sur les états quantiques électroniques et mis en évidence une nouvelle classification des phases de la matière. Cela a conduit à un échange interdisciplinaire entre la physique et un domaine des mathématiques appelé topologie, mis en évidence pour la première fois par la contribution de Thouless, Kohmoto, Nightingale et Nijs (TKNN) [3] sur la quantification de la conductivité dans les métaux bidimensionnels. La topologie définit des classes de systèmes qui sont géométriquement similaires, ce qui signifie qu'ils peuvent être déformés de façon continue des uns vers les autres. Cette classification est basée sur des invariants topologiques définis pour le système dans son ensemble et ayant des valeurs entières, comme le genre d'une surface tridimensionnelle connectée, c'est-à-dire son nombre d'anses ou de trous.

Ce concept imprègne désormais de nombreux domaines de la physique et est au cœur de ce que l'on appelle les isolants topologiques [4–6]. Ces systèmes sont des isolants normaux en volume mais accueillent des modes conducteurs sur les bords qui sont topologiquement protégés et insensibles au désordre, en raison de l'absence d'états accessibles pour la rétrodiffusion [7]. Ils ont été proposés pour des applications robustes topologiquement protégées, notamment en photonique [8] et en informatique quantique [9]. Les isolants topologiques bidimensionnels appartiennent tous à une classe unique représentée par l'effet Hall quantique de spin [10–13], le pendant de l'effet Hall quantique bidimensionnel avec une symétrie par renversement du temps. Les recherches en cours se concentrent maintenant sur les systèmes à trois dimensions ou plus, par exemple ceux qui possèdent des points de Weyl [14], qui sont classés en fonction de leur dimensionnalité [15] et des invariants entiers, comme un invariant topologique $\mathbb{Z}_2$ pour les systèmes à symétrie par renversement du temps [4, 16]. Cette classification est également valable pour les supraconducteurs topologiques, où les bords possèdent des états liés de Majorana [17].

La contribution séminale de Laughlin à l'effet Hall quantique entier [18] a souligné que les signatures des états topologiques sont accessibles par pompage, un processus de transport de particules dans des potentiels déformés périodiquement. Son travail considère une géométrie cylindrique avec un champ magnétique radial et un flux magnétique longitudinal accordable. Une variation cyclique de l'hamiltonien via le contrôle du flux magnétique induit un mouvement quantifié de particules, à condition que la dynamique soit adiabatique. Le mouvement est protégé par l'invariant topologique non trivial qui caractérise les bandes remplies. Son approche a été étendue à une classe plus large de pompes [19, 20] et étudiée sur diverses plateformes, utilisant des guides d'ondes photoniques [21], des points quantiques [22, 23] ou des atomes froids [24, 25].

Les atomes froids sont au cœur de cette recherche en raison de notre capacité à les contrôler au niveau de l'atome unique, ainsi qu'à l'aide d'un photon unique [26]. Ce domaine de recherche s'est élargi après des percées technologiques avec le développement de sources laser utilisées pour le piégeage et le refroidissement d'échantillons atomiques [27] vers le régime de dégénérescence quantique [28]. Les atomes ultrafroids sont des candidats pertinents pour mettre en pratique l'idée proposée pour la première fois par Feynman [29], de simuler un système quantique en faisant correspondre son hamiltonien à un autre système avec un contrôle plus fin. Des modèles de matière condensée ont été étudiés à l'aide d'atomes froids, bénéficiant de la possibilité de régler facilement certains paramètres expérimentaux, tels que les interactions interatomiques, et de la mesure des observables microscopiques. Par exemple, les réseaux optiques [30], des potentiels périodiques constitués de lumière, et les atomes fermioniques neutres jouent respectivement le rôle d'un potentiel cristallin ionique et des électrons. Dans la limite des potentiels profonds, ces systèmes simulent le modèle de Fermi-Hubbard [31], qui peut accueillir des états fortement corrélés similaires à ceux impliqués dans la supraconductivité à haute température dans les cuprates [32].

L'étude de la physique de Hall quantique avec des atomes froids ne peut être mise en œuvre directement avec un champ magnétique en raison de leur charge neutre. Cette limitation a été surmontée dans des systèmes dans lesquels le mouvement des particules est régi par un analogue du champ magnétique pour une particule chargée, un champ de jauge artificiel. Par exemple, des systèmes de Hall quantique ont été mis en œuvre en utilisant des condensats de Bose-Einstein en rotation [33, 34] et des atomes dans des réseaux secoués [35, 36]. Une autre voie utilise la médiation du spin par un couplage optique aux degrés de liberté externes pour créer un champ de jauge artificiel [37]. Ces plateformes ont atteint le régime où les interactions interatomiques modifient les états quantiques avec l'apparition de vortex organisés en un réseau d'Abrikosov [38], similaire aux vortex dans les supraconducteurs de type II soumis à un champ magnétique. Une extension de ces approches vers des champs de jauge non-abéliens nécessite un couplage spin-orbite entre les états internes quasi-dégénérés et le mouvement atomique, qui a été réalisé dans des systèmes bidimensionnels [39] et récemment dans des systèmes tridimensionnels [40].

Une autre approche pour la simulation de systèmes topologiques repose sur la création d'un système hybride composé de dimensions spatiales et synthétiques, où ces dernières peuvent faire référence aux dimensions encodées dans les degrés

de liberté internes des atomes par exemple [41, 42]. Un couplage externe peut connecter les états électroniques d'un atome, qui sont réinterprétés comme des sites d'un réseau unidimensionnel avec un terme de saut entre voisins. Des champs de jauge artificiels dans de tels systèmes ont été produits en utilisant des transitions optiques à deux photons, qui couplent les états internes avec une phase de saut complexe dépendant de l'espace, similaire à une phase d'Aharonov-Bohm [43, 44]. Les dimensions synthétiques facilitent également l'exploration de systèmes de dimensions supérieures à trois ou de géométrie plus complexe [45], en utilisant une combinaison de couplages de différentes portées par exemple.

Les atomes ayant un grand moment angulaire total dans l'état fondamental sont bien adaptés à de telles applications, car la grande dimension synthétique correspondante permet d'explorer à la fois les modes en volume et de bord en présence d'un champ de jauge artificiel [46]. Les atomes de la famille des lanthanides, tels que le dysprosium avec un moment angulaire total $J = 8$ dans son état fondamental, ont une structure électronique complexe caractérisée par la présence de transitions optiques fines éloignées des transitions larges. Par rapport aux atomes alcalins où de telles transitions isolées ne peuvent être trouvées, le régime de couplage fort avec un chauffage limité est accessible. Les atomes de dysprosium bénéficient également d'une polarisabilité tensorielle non-négligeable au voisinage des transitions étroites qui élargit notre boîte à outils de couplage de spin et de la présence d'interactions dipôle-dipôle magnétiques anisotropes à longue portée qui enrichit les phases de la matière accessibles [47]. Dans cette thèse, nous nous concentrons sur notre implémentation expérimentale d'un cylindre de Hall atomique, avec une dimension cyclique de trois sites encodés dans les degrés de liberté internes des atomes de dysprosium, et sur notre réalisation de la pompe topologique de Laughlin.

Le chapitre 1 décrit les propriétés clés des atomes de dysprosium et leur intérêt pour la mise en œuvre de champs de jauge artificiels. Les atomes de dysprosium ont un grand moment magnétique et un grand moment angulaire total dans le niveau fondamental. Le spectre électronique contient une grande variété de transitions avec des largeurs de raies allant de l'ordre du Hz à quelques dizaines de MHz, qui sont accessibles avec des lasers visibles ou infrarouges. Elles sont bien adaptées à la manipulation des degrés de liberté internes et externes des atomes, comme le refroidissement par laser et la manipulation du spin. Nous présentons les éléments de base de l'interaction lumière-matière, qui est au cœur de toutes les expériences réalisées au cours de cette thèse. Nous présentons brièvement les systèmes laser que nous utilisons pour la manipulation des atomes de dysprosium, et en particulier leur verrouillage en fréquence à l'aide de références atomiques qui a été développé au début de la thèse.

Le chapitre 2 se concentre sur le dispositif expérimental qui produit un échantillon atomique froid. Nous avons une grande dette envers tous les anciens membres de notre groupe de recherche qui ont construit l'expérience et contribué à ses mises à jour successives. Le cycle expérimental complet est présenté, partant d'un jet atomique chaud d'atomes de dysprosium jusqu'à un gaz d'atomes froids piégés proche de la condensation de Bose-Einstein. Nous mentionnons les techniques successives de refroidissement et de piégeage, utilisant le couplage

lumineux résonnant pour le ralentissement Zeeman et pour le piégeage dans un piège magnéto-optique, et le couplage lumineux hors résonance pour le piégeage dans des pièges conservatifs et le refroidissement par évaporation. Certains changements récents sont détaillés. Nous décrivons le refroidissement transverse du jet atomique avec une mélasse optique qui augmente le nombre d'atomes chargés dans le piège magnéto-optique d'un facteur 4, la compensation active des fluctuations du champ magnétique à l'aide d'une sonde magnétique, qui permet d'atteindre un écart type du champ magnétique le long de l'axe vertical de 0.4 mG, et le traitement des images d'absorption pour éliminer les franges et réduire le bruit de fond. Nous donnons un aperçu des techniques expérimentales qui permettent de caractériser les faisceaux laser hors résonance et qui ont été régulièrement utilisées pour l'installation de nouveaux faisceaux. Ces techniques donnent des informations sur l'amplitude du couplage lumineux, la taille du faisceau et sa polarisation.

Le chapitre 3 présente brièvement nos travaux sur l'intrication dans les états quantiques. Nous interprétons le grand spin des atomes de dysprosium comme un ensemble de qubits virtuels de spin 1/2, symétriques par échange de particules, et codant des états non classiques. Nous nous concentrons sur deux états paradigmatiques de deux classes distinctes d'intrication, les états W et chat de Schrödinger. La notion d'intrication dans les états codés est clarifiée en partitionnant optiquement le spin en deux sous-systèmes. Nous montrons que l'état total est plus désordonné que ses parties pour ces deux états, ce qui prouve qu'ils sont intriqués. Nous étudions également la robustesse de l'intrication dans ces états lors de la décohérence par la perte d'une paire de qubits dans un état aléatoire. Ceci est réalisé en préparant des états non-classiques dans un niveau électronique excité avec un moment angulaire total $J' = J + 1$, qui contient virtuellement deux qubits supplémentaires. L'émission spontanée projette l'état sur le niveau électronique fondamental, ce qui correspond à la perte d'une paire de qubits dans un état aléatoire. Notre série d'expériences met en contraste la robustesse de l'intrication par paires dans l'état W avec la fragilité de l'intrication dans l'état chat.

Le chapitre 4 introduit les éléments théoriques de base liés à l'effet Hall quantique. Nous commençons par les notions de courbure de Berry et de phase de Berry, qui jouent un rôle similaire à celles de champ magnétique et de phase d'Aharonov-Bohm. Cette idée est centrale dans la mise en œuvre de champs de jauge artificiels pour les particules neutres à l'aide d'un habillage optique. L'effet Hall, avec sa forme classique et son pendant quantique, est ensuite présenté. Nous nous concentrons sur le cas de la géométrie cylindrique, lié à notre réalisation expérimentale d'un cylindre de Hall quantique. Enfin, en suivant l'argument de Laughlin pour la quantification de la conductivité dans un système de Hall, nous introduisons la notion de pompage topologique et relions ses propriétés à celles d'un système de dimension supérieure. Le cas des fermions en interaction est brièvement discuté, avec l'apparition d'états de Hall quantiques fractionnaires.

Le chapitre 5 détaille notre protocole de codage de deux dimensions synthétiques dans le grand moment angulaire total d'un seul atome de dysprosium, après

une brève revue des dimensions synthétiques avec un accent sur la photonique et les atomes froids. En utilisant des couplages de spin de différentes portées, les degrés de liberté internes sont effectivement décrits comme un cylindre avec une dimension cyclique de trois sites. Des simulations numériques mettent en évidence la dynamique indépendante le long des deux dimensions du cylindre effectif. Nous discutons de la validité de cette image et de sa robustesse face à des variations des paramètres. Ce protocole peut être utilisé pour la création d'un cylindre de Hall, en couplant la dimension synthétique cyclique à une dimension spatiale. Nous présentons un modèle effectif valide à basse énergie avec trois sites couplés cycliquement, qui capture les principales caractéristiques de l'hamiltonien complet.

Le chapitre 6 présente notre réalisation expérimentale d'un cylindre de Hall atomique, fondée sur la proposition décrite dans le chapitre précédent. Nous caractérisons la bande fondamental du système et ses premières excitations, liées au modèle effectif à trois sites. Nous sondons ensuite la réponse transverse à une force le long de la dimension spatiale, typique d'une particule chargée dans un champ magnétique, dans deux séries d'expériences. Cela fournit une première preuve de la quantification de la réponse transverse du système. Nous réalisons l'expérience de pompe topologique de Laughlin, en contrôlant le flux magnétique effectif qui perce le cylindre, et nous mesurons le déplacement du nuage atomique lorsque le flux est augmenté. Nous obtenons une estimation expérimentale de l'invariant topologique non trivial associé à la bande fondamental, le premier nombre de Chern, en faisant la moyenne de nos mesures sur des états couvrant uniformément toute la zone de Brillouin.

Le chapitre 7 traite des extensions de notre réalisation d'un cylindre de Hall atomique. Les premiers résultats expérimentaux sur la création d'un système de Hall à quatre dimensions sont présentés, ce qui prouve notre capacité à manipuler deux dimensions synthétiques indépendantes encodées dans le spin des atomes. Le dispositif expérimental est détaillé ainsi que la caractérisation de la bande fondamentale, qui met en évidence la réponse transverse aux forces le long des axes spatiaux. Nous discutons ensuite des perspectives vers des états à plusieurs corps en présence d'interactions interatomiques. Premièrement, nous considérons l'effet des interactions sur notre cylindre de Hall quantique avec une dimension synthétique et nous caractérisons l'état fondamental attendu dans des expériences réalistes. Ensuite, nous détaillons un protocole pour préparer un champ de jauge artificiel en espace réel, médié par un habillage lumineux, pour des atomes neutres à grand spin et nous analysons l'effet du choix des transitions optiques utilisées pour les transitions Raman à deux photons qui implémentent le champ de jauge.

Bibliography

[1] P. W. Anderson, "More is different", Science **177**, 393–396 (1972) (cited on pages 11, 181).

[2] K. v. Klitzing, G. Dorda, and M. Pepper, "New method for high-accuracy determination of the fine-structure constant based on quantized hall resistance", Physical Review Letters **45**, 494–497 (1980) (cited on pages 11, 61, 181).

[3] D. J. Thouless, M. Kohmoto, M. P. Nightingale, and M. den Nijs, "Quantized hall conductance in a two-dimensional periodic potential", Physical Review Letters **49**, 405–408 (1982) (cited on pages 11, 79, 181).

[4] C. L. Kane and E. J. Mele, "Z_2 Topological order and the quantum spin hall effect", Physical Review Letters **95**, 146802 (2005) (cited on pages 11, 181).

[5] X.-L. Qi and S.-C. Zhang, "The quantum spin hall effect and topological insulators", Physics Today **63**, 33–38 (2010) (cited on pages 11, 181).

[6] M. Z. Hasan and C. L. Kane, "Colloquium: topological insulators", Reviews of Modern Physics **82**, 3045–3067 (2010) (cited on pages 11, 181).

[7] B. I. Halperin, "Quantized hall conductance, current-carrying edge states, and the existence of extended states in a two-dimensional disordered potential", Physical Review B **25**, 2185–2190 (1982) (cited on pages 11, 67, 181).

[8] M. Hafezi, E. A. Demler, M. D. Lukin, and J. M. Taylor, "Robust optical delay lines with topological protection", Nature Physics **7**, 907–912 (2011) (cited on pages 11, 181).

[9] A. Y. Kitaev, "Fault-tolerant quantum computation by anyons", Annals of Physics **303**, 2–30 (2003) (cited on pages 11, 181).

[10] C. L. Kane and E. J. Mele, "Quantum spin hall effect in graphene", Physical Review Letters **95**, 226801 (2005) (cited on pages 11, 181).

[11] B. A. Bernevig and S.-C. Zhang, "Quantum spin hall effect", Physical Review Letters **96**, 106802 (2006) (cited on pages 11, 181).

[12] M. König, S. Wiedmann, C. Brüne, A. Roth, H. Buhmann, L. W. Molenkamp, X.-L. Qi, and S.-C. Zhang, "Quantum spin hall insulator state in hgte quantum wells", Science **318**, 766–770 (2007) (cited on pages 11, 181).

[13] A. Roth, C. Brüne, H. Buhmann, L. W. Molenkamp, J. Maciejko, X.-L. Qi, and S.-C. Zhang, "Nonlocal transport in the quantum spin hall state", Science **325**, 294–297 (2009) (cited on pages 11, 181).

[14]N. P. Armitage, E. J. Mele, and A. Vishwanath, "Weyl and dirac semimetals in three-dimensional solids", Reviews of Modern Physics **90**, 015001 (2018) (cited on pages 11, 181).

[15]A. Kitaev, "Periodic table for topological insulators and superconductors", AIP Conference Proceedings **1134**, 22–30 (2009) (cited on pages 11, 181).

[16]B. Béri and N. R. Cooper, "$\mathcal{Z}_2$ Topological insulators in ultracold atomic gases", Physical Review Letters **107**, 145301 (2011) (cited on pages 11, 103, 181).

[17]X.-L. Qi and S.-C. Zhang, "Topological insulators and superconductors", Reviews of Modern Physics **83**, 1057–1110 (2011) (cited on pages 11, 78, 181).

[18]R. B. Laughlin, "Quantized hall conductivity in two dimensions", Physical Review B **23**, 5632–5633 (1981) (cited on pages 11, 77, 182).

[19]D. J. Thouless, "Quantization of particle transport", Physical Review B **27**, 6083–6087 (1983) (cited on pages 12, 77, 87, 182).

[20]R. Citro and M. Aidelsburger, *Thouless pumping and topology*, Oct. 2022, arXiv:2210.02050 [cond-mat] (cited on pages 12, 182).

[21]Y. E. Kraus, Y. Lahini, Z. Ringel, M. Verbin, and O. Zilberberg, "Topological states and adiabatic pumping in quasicrystals", Physical Review Letters **109**, 106402 (2012) (cited on pages 12, 78, 137, 182).

[22]M. Switkes, C. M. Marcus, K. Campman, and A. C. Gossard, "An adiabatic quantum electron pump", Science **283**, 1905–1908 (1999) (cited on pages 12, 77, 182).

[23]S. K. Watson, R. M. Potok, C. M. Marcus, and V. Umansky, "Experimental realization of a quantum spin pump", Physical Review Letters **91**, 258301 (2003) (cited on pages 12, 77, 182).

[24]M. Lohse, C. Schweizer, O. Zilberberg, M. Aidelsburger, and I. Bloch, "A thouless quantum pump with ultracold bosonic atoms in an optical superlattice", Nature Physics **12**, 350–354 (2016) (cited on pages 12, 78, 182).

[25]S. Nakajima, T. Tomita, S. Taie, T. Ichinose, H. Ozawa, L. Wang, M. Troyer, and Y. Takahashi, "Topological thouless pumping of ultracold fermions", Nature Physics **12**, 296–300 (2016) (cited on pages 12, 78, 182).

[26]S. Gleyzes, S. Kuhr, C. Guerlin, J. Bernu, S. Deléglise, U. Busk Hoff, M. Brune, J.-M. Raimond, and S. Haroche, "Quantum jumps of light recording the birth and death of a photon in a cavity", Nature **446**, 297–300 (2007) (cited on pages 12, 182).

[27]W. D. Phillips, "Nobel lecture: laser cooling and trapping of neutral atoms", Reviews of Modern Physics **70**, 721–741 (1998) (cited on pages 12, 21, 182).

[28]M. H. Anderson, J. R. Ensher, M. R. Matthews, C. E. Wieman, and E. A. Cornell, "Observation of bose-einstein condensation in a dilute atomic vapor", Science **269**, 198–201 (1995) (cited on pages 12, 182).

[29]R. P. Feynman, "Simulating physics with computers", International Journal of Theoretical Physics **21**, 467–488 (1982) (cited on pages 12, 182).

[30]M. Greiner, O. Mandel, T. Esslinger, T. W. Hänsch, and I. Bloch, "Quantum phase transition from a superfluid to a mott insulator in a gas of ultracold atoms", Nature **415**, 39–44 (2002) (cited on pages 12, 182).

[31]J. Hubbard and B. H. Flowers, "Electron correlations in narrow energy bands", Proceedings of the Royal Society of London. Series A. Mathematical and Physical Sciences **276**, 238–257 (1963) (cited on pages 12, 182).

[32]M. R. Norman, "Cuprates—an overview", Journal of Superconductivity and Novel Magnetism **25**, 2131–2134 (2012) (cited on pages 12, 182).

[33]V. Schweikhard, I. Coddington, P. Engels, V. P. Mogendorff, and E. A. Cornell, "Rapidly rotating bose-einstein condensates in and near the lowest landau level", Physical Review Letters **92**, 040404 (2004) (cited on pages 13, 152, 182).

[34]V. Bretin, S. Stock, Y. Seurin, and J. Dalibard, "Fast rotation of a bose-einstein condensate", Physical Review Letters **92**, 050403 (2004) (cited on pages 13, 152, 182).

[35]H. Miyake, G. A. Siviloglou, C. J. Kennedy, W. C. Burton, and W. Ketterle, "Realizing the harper hamiltonian with laser-assisted tunneling in optical lattices", Physical Review Letters **111**, 185302 (2013) (cited on pages 13, 182).

[36]M. Aidelsburger, M. Atala, M. Lohse, J. T. Barreiro, B. Paredes, and I. Bloch, "Realization of the hofstadter hamiltonian with ultracold atoms in optical lattices", Physical Review Letters **111**, 185301 (2013) (cited on pages 13, 182).

[37]Y.-J. Lin, R. L. Compton, K. Jiménez-García, J. V. Porto, and I. B. Spielman, "Synthetic magnetic fields for ultracold neutral atoms", Nature **462**, 628–632 (2009) (cited on pages 13, 66, 85, 152, 182).

[38]A. A. Abrikosov, "The magnetic properties of superconducting alloys", Journal of Physics and Chemistry of Solids **2**, 199–208 (1957) (cited on pages 13, 152, 182).

[39]Z. Wu, L. Zhang, W. Sun, X.-T. Xu, B.-Z. Wang, S.-C. Ji, Y. Deng, S. Chen, X.-J. Liu, and J.-W. Pan, "Realization of two-dimensional spin-orbit coupling for bose-einstein condensates", Science **354**, 83–88 (2016) (cited on pages 13, 182).

[40]Z.-Y. Wang, X.-C. Cheng, B.-Z. Wang, J.-Y. Zhang, Y.-H. Lu, C.-R. Yi, S. Niu, Y. Deng, X.-J. Liu, S. Chen, and J.-W. Pan, "Realization of an ideal weyl semimetal band in a quantum gas with 3d spin-orbit coupling", Science **372**, 271–276 (2021) (cited on pages 13, 182).

[41]O. Boada, A. Celi, J. I. Latorre, and M. Lewenstein, "Quantum simulation of an extra dimension", Physical Review Letters **108**, 133001 (2012) (cited on pages 13, 88, 183).

[42]A. Celi, P. Massignan, J. Ruseckas, N. Goldman, I. B. Spielman, G. Juzeliūnas, and M. Lewenstein, "Synthetic gauge fields in synthetic dimensions", Physical Review Letters **112**, 043001 (2014) (cited on pages 13, 88, 183).

[43]M. Mancini, G. Pagano, G. Cappellini, L. Livi, M. Rider, J. Catani, C. Sias, P. Zoller, M. Inguscio, M. Dalmonte, and L. Fallani, "Observation of chiral edge states with neutral fermions in synthetic hall ribbons", Science **349**, 1510–1513 (2015) (cited on pages 13, 89, 183).

[44]B. K. Stuhl, H.-I. Lu, L. M. Aycock, D. Genkina, and I. B. Spielman, "Visualizing edge states with an atomic bose gas in the quantum hall regime", Science **349**, 1514–1518 (2015) (cited on pages 13, 85, 89, 183).

[45]O. Boada, A. Celi, J. Rodríguez-Laguna, J. I. Latorre, and M. Lewenstein, "Quantum simulation of non-trivial topology", New Journal of Physics **17**, 045007 (2015) (cited on pages 13, 87, 88, 183).

[46]T. Chalopin, T. Satoor, A. Evrard, V. Makhalov, J. Dalibard, R. Lopes, and S. Nascimbene, "Probing chiral edge dynamics and bulk topology of a synthetic hall system", Nature Physics **16**, 1017–1021 (2020) (cited on pages 14, 89, 99, 104, 110, 144, 183).

[47]L. Chomaz, I. Ferrier-Barbut, F. Ferlaino, B. Laburthe-Tolra, B. L. Lev, and T. Pfau, *Dipolar physics: a review of experiments with magnetic quantum gases*, Jan. 2022, arXiv:2201.02672 [cond-mat.quant-gas] (cited on pages 14, 20, 183).

[48]M. Lu, S. H. Youn, and B. L. Lev, "Spectroscopy of a narrow-line laser-cooling transition in atomic dysprosium", Physical Review A **83**, 012510 (2011) (cited on page 19).

[49]W. C. Martin, R. Zalubas, and L. Hagan, *Atomic energy levels - the rare-earth elements* (Jan. 1978) (cited on page 19).

[50]L. Pitaevskii and S. Stringari, *Bose-einstein condensation and superfluidity*, First (Oxford University PressOxford, Jan. 2016) (cited on pages 19, 37).

[51]C. J. Pethick and H. Smith, *Bose–einstein condensation in dilute gases*, Second (Cambridge University Press, Sept. 2008) (cited on page 19).

[52]M. Olshanii and L. Pricoupenko, "Rigorous approach to the problem of ultraviolet divergencies in dilute bose gases", Physical Review Letters **88**, 010402 (2001) (cited on page 19).

[53]S. Inouye, M. R. Andrews, J. Stenger, H.-J. Miesner, D. M. Stamper-Kurn, and W. Ketterle, "Observation of feshbach resonances in a bose–einstein condensate", Nature **392**, 151–154 (1998) (cited on page 20).

[54]C. Chin, R. Grimm, P. Julienne, and E. Tiesinga, "Feshbach resonances in ultracold gases", Reviews of Modern Physics **82**, 1225–1286 (2010) (cited on page 20).

[55]A. Frisch, M. Mark, K. Aikawa, F. Ferlaino, J. L. Bohn, C. Makrides, A. Petrov, and S. Kotochigova, "Quantum chaos in ultracold collisions of gas-phase erbium atoms", Nature **507**, 475–479 (2014) (cited on page 20).

[56]T. Maier, H. Kadau, M. Schmitt, M. Wenzel, I. Ferrier-Barbut, T. Pfau, A. Frisch, S. Baier, K. Aikawa, L. Chomaz, M. J. Mark, F. Ferlaino, C. Makrides, E. Tiesinga, A. Petrov, and S. Kotochigova, "Emergence of chaotic scattering in ultracold er and dy", Physical Review X **5**, 041029 (2015) (cited on page 20).

[57]K. Baumann, N. Q. Burdick, M. Lu, and B. L. Lev, "Observation of low-field fano-feshbach resonances in ultracold gases of dysprosium", Physical Review A **89**, 020701 (2014) (cited on page 20).

[58]T. D. Lee and C. N. Yang, "Many-body problem in quantum mechanics and quantum statistical mechanics", Physical Review **105**, 1119–1120 (1957) (cited on page 20).

[59]T. D. Lee, K. Huang, and C. N. Yang, "Eigenvalues and eigenfunctions of a bose system of hard spheres and its low-temperature properties", Physical Review **106**, 1135–1145 (1957) (cited on page 20).

[60]A. Bulgac, "Dilute quantum droplets", Physical Review Letters **89**, 050402 (2002) (cited on page 20).

[61]D. S. Petrov, "Quantum mechanical stabilization of a collapsing bose-bose mixture", Physical Review Letters **115**, 155302 (2015) (cited on page 20).

[62]F. Böttcher, J.-N. Schmidt, J. Hertkorn, K. S. H. Ng, S. D. Graham, M. Guo, T. Langen, and T. Pfau, "New states of matter with fine-tuned interactions: quantum droplets and dipolar supersolids", Reports on Progress in Physics **84**, 012403 (2020) (cited on page 20).

[63]T. H. Maiman, "Stimulated optical radiation in ruby", Nature **187**, 493–494 (1960) (cited on page 21).

[64]S. Chu, "Nobel lecture: the manipulation of neutral particles", Reviews of Modern Physics **70**, 685–706 (1998) (cited on page 21).

[65]C. N. Cohen-Tannoudji, "Nobel lecture: manipulating atoms with photons", Reviews of Modern Physics **70**, 707–719 (1998) (cited on page 21).

[66]S. Chu, J. E. Bjorkholm, A. Ashkin, and A. Cable, "Experimental observation of optically trapped atoms", Physical Review Letters **57**, 314–317 (1986) (cited on page 21).

[67]C. J. Foot, *Atomic physics*, Oxford Master Series in Physics (Oxford University Press, Oxford, New York, Nov. 2004) (cited on page 22).

[68]G. Lindblad, "On the generators of quantum dynamical semigroups", Communications in Mathematical Physics **48**, 119–130 (1976) (cited on page 23).

[69]V. Gorini, A. Kossakowski, and E. C. G. Sudarshan, "Completely positive dynamical semigroups of n-level systems", Journal of Mathematical Physics **17**, 821–825 (1976) (cited on page 23).

[70]A. Rivas and S. F. Huelga, *Open quantum systems*, SpringerBriefs in Physics (Springer Berlin Heidelberg, Berlin, Heidelberg, 2012) (cited on page 23).

[71]D. A. Lidar, I. L. Chuang, and K. B. Whaley, "Decoherence-free subspaces for quantum computation", Physical Review Letters **81**, 2594–2597 (1998) (cited on page 23).

[72]B. Kraus, H. P. Büchler, S. Diehl, A. Kantian, A. Micheli, and P. Zoller, "Preparation of entangled states by quantum markov processes", Physical Review A **78**, 042307 (2008) (cited on page 23).

[73]J. Dalibard, Y. Castin, and K. Mølmer, "Wave-function approach to dissipative processes in quantum optics", Physical Review Letters **68**, 580–583 (1992) (cited on page 23).

[74]H. Carmichael, *An open systems approach to quantum optics: lectures presented at the université libre de bruxelles october 28 to november 4, 1991*, edited by H. Araki, E. Brézin, J. Ehlers, U. Frisch, K. Hepp, R. L. Jaffe, R. Kippenhahn, H. A. Weidenmüller, J. Wess, J. Zittartz, and W. Beiglböck, Vol. 18, Lecture Notes in Physics Monographs (Springer Berlin Heidelberg, Berlin, Heidelberg, 1993) (cited on page 23).

[75]F. Le Kien, P. Schneeweiss, and A. Rauschenbeutel, "Dynamical polarizability of atoms in arbitrary light fields: general theory and application to cesium", The European Physical Journal D **67**, 92 (2013) (cited on pages 25, 26).

[76]R. Grimm, M. Weidemüller, and Y. B. Ovchinnikov, "Optical dipole traps for neutral atoms", in *Advances in atomic, molecular, and optical physics*, Vol. 42, edited by B. Bederson and H. Walther (Academic Press, Jan. 2000), pp. 95–170 (cited on page 25).

[77]C. Ravensbergen, V. Corre, E. Soave, M. Kreyer, S. Tzanova, E. Kirilov, and R. Grimm, "Accurate determination of the dynamical polarizability of dysprosium", Physical Review Letters **120**, 223001 (2018) (cited on page 25).

[78]I. H. Deutsch and P. S. Jessen, "Quantum-state control in optical lattices", Physical Review A **57**, 1972–1986 (1998) (cited on page 27).

[79]J. Dalibard, F. Gerbier, G. Juzeliūnas, and P. Öhberg, "Colloquium: artificial gauge potentials for neutral atoms", Reviews of Modern Physics **83**, 1523–1543 (2011) (cited on pages 27, 50, 66).

[80]C. E. Wieman and L. Hollberg, "Using diode lasers for atomic physics", Review of Scientific Instruments **62**, 1–20 (1991) (cited on page 28).

[81]I. Manai, A. Molineri, C. Fréjaville, C. Duval, P. Bataille, R. Journet, F. Wiotte, B. Laburthe-Tolra, E. Maréchal, M. Cheneau, and M. Robert-de-Saint-Vincent, "Shelving spectroscopy of the strontium intercombination line", Journal of Physics B: Atomic, Molecular and Optical Physics **53**, 085005 (2020) (cited on page 31).

[82]D. Dreon, "Designing and building an ultracold dysprosium experiment : a new framework for light-spin interaction", PhD thesis (Université Paris sciences et lettres, Université Paris sciences et lettres, 2017) (cited on page 33).

[83]C. Bouazza, "Ultracold dysprosium gas in optical dipole traps : control of interactions between highly magnetic atoms", PhD thesis (Université Paris sciences et lettres, Université Paris sciences et lettres, 2018) (cited on pages 33, 35).

[84]D. Dreon, L. A. Sidorenkov, C. Bouazza, W. Maineult, J. Dalibard, and S. Nascimbene, "Optical cooling and trapping of highly magnetic atoms: the benefits of a spontaneous spin polarization", Journal of Physics B: Atomic, Molecular and Optical Physics **50**, 065005 (2017) (cited on page 35).

[85]S. Schmid, G. Thalhammer, K. Winkler, F. Lang, and J. H. Denschlag, "Long distance transport of ultracold atoms using a 1d optical lattice", New Journal of Physics **8**, 159–159 (2006) (cited on page 36).

[86]T. Klostermann, C. R. Cabrera, H. von Raven, J. F. Wienand, C. Schweizer, I. Bloch, and M. Aidelsburger, "Fast long-distance transport of cold cesium atoms", Physical Review A **105**, 043319 (2022) (cited on page 36).

[87]T. Chalopin, V. Makhalov, C. Bouazza, A. Evrard, A. Barker, M. Lepers, J.-F. Wyart, O. Dulieu, J. Dalibard, R. Lopes, and S. Nascimbene, "Anisotropic light shift and magic polarization of the intercombination line of dysprosium atoms in a far-detuned dipole trap", Physical Review A **98**, 040502 (2018) (cited on pages 36, 37).

[88]C. G. Townsend, N. H. Edwards, C. J. Cooper, K. P. Zetie, C. J. Foot, A. M. Steane, P. Szriftgiser, H. Perrin, and J. Dalibard, "Phase-space density in the magneto-optical trap", Physical Review A **52**, 1423–1440 (1995) (cited on page 37).

[89]F. Dalfovo, S. Giorgini, L. P. Pitaevskii, and S. Stringari, "Theory of bose-einstein condensation in trapped gases", Reviews of Modern Physics **71**, 463–512 (1999) (cited on page 37).

[90]M. Lu, N. Q. Burdick, S. H. Youn, and B. L. Lev, "Strongly dipolar bose-einstein condensate of dysprosium", Physical Review Letters **107**, 190401 (2011) (cited on page 37).

[91]E. Lucioni, L. Tanzi, A. Fregosi, J. Catani, S. Gozzini, M. Inguscio, A. Fioretti, C. Gabbanini, and G. Modugno, "Dysprosium dipolar bose-einstein condensate with broad feshbach resonances", Physical Review A **97**, 060701 (2018) (cited on page 37).

[92]C. Ravensbergen, V. Corre, E. Soave, M. Kreyer, E. Kirilov, and R. Grimm, "Production of a degenerate fermi-fermi mixture of dysprosium and potassium atoms", Physical Review A **98**, 063624 (2018) (cited on page 37).

[93]A. Trautmann, P. Ilzhöfer, G. Durastante, C. Politi, M. Sohmen, M. J. Mark, and F. Ferlaino, "Dipolar quantum mixtures of erbium and dysprosium atoms", Physical Review Letters **121**, 213601 (2018) (cited on page 37).

[94]G. Reinaudi, T. Lahaye, Z. Wang, and D. Guéry-Odelin, "Strong saturation absorption imaging of dense clouds of ultracold atoms", Optics Letters **32**, 3143–3145 (2007) (cited on page 39).

[95]P. D. Lett, W. D. Phillips, S. L. Rolston, C. E. Tanner, R. N. Watts, and C. I. Westbrook, "Optical molasses", JOSA B **6**, 2084–2107 (1989) (cited on page 39).

[96]H. J. Metcalf and P. Straten, *Laser cooling and trapping*, Springer New York, NY (1999) (cited on page 39).

[97]N. Leefer, A. Cingöz, B. Gerber-Siff, A. Sharma, J. R. Torgerson, and D. Budker, "Transverse laser cooling of a thermal atomic beam of dysprosium", Physical Review A **81**, 043427 (2010) (cited on page 40).

[98]T. Maier, H. Kadau, M. Schmitt, A. Griesmaier, and T. Pfau, "Narrow-line magneto-optical trap for dysprosium atoms", Optics Letters **39**, 3138–3141 (2014) (cited on page 40).

[99]F. Mühlbauer, N. Petersen, C. Baumgärtner, L. Maske, and P. Windpassinger, "Systematic optimization of laser cooling of dysprosium", Applied Physics B **124**, 120 (2018) (cited on page 40).

[100]P. Ilzhöfer, G. Durastante, A. Patscheider, A. Trautmann, M. J. Mark, and F. Ferlaino, "Two-species five-beam magneto-optical trap for erbium and dysprosium", Physical Review A **97**, 023633 (2018) (cited on page 40).

[101]B. Song, C. He, Z. Ren, E. Zhao, J. Lee, and G.-B. Jo, "Effective statistical fringe removal algorithm for high-sensitivity imaging of ultracold atoms", Physical Review Applied **14**, 034006 (2020) (cited on page 42).

[102]M. Fleischhauer, A. Imamoglu, and J. P. Marangos, "Electromagnetically induced transparency: optics in coherent media", Reviews of Modern Physics **77**, 633–673 (2005) (cited on page 49).

[103]P. Král, I. Thanopulos, and M. Shapiro, "Colloquium: coherently controlled adiabatic passage", Reviews of Modern Physics **79**, 53–77 (2007) (cited on page 49).

[104]J. Ruseckas, G. Juzeliūnas, P. Öhberg, and M. Fleischhauer, "Non-abelian gauge potentials for ultracold atoms with degenerate dark states", Physical Review Letters **95**, 010404 (2005) (cited on page 50).

[105]M. Kitagawa and M. Ueda, "Squeezed spin states", Physical Review A **47**, 5138–5143 (1993) (cited on page 51).

[106]M. F. Riedel, P. Böhi, Y. Li, T. W. Hänsch, A. Sinatra, and P. Treutlein, "Atom-chip-based generation of entanglement for quantum metrology", Nature **464**, 1170–1173 (2010) (cited on pages 51, 54).

[107]C. Gross, T. Zibold, E. Nicklas, J. Estève, and M. K. Oberthaler, "Nonlinear atom interferometer surpasses classical precision limit", Nature **464**, 1165–1169 (2010) (cited on pages 51, 54).

[108]T. Satoor, A. Fabre, J.-B. Bouhiron, A. Evrard, R. Lopes, and S. Nascimbene, "Partitioning dysprosium's electronic spin to reveal entanglement in nonclassical states", Physical Review Research **3**, 043001 (2021) (cited on pages 53, 159).

[109]E. Schrödinger, "Die gegenwärtige Situation in der Quantenmechanik", Naturwissenschaften **23**, 807–812 (1935) (cited on page 53).

[110]A. Einstein, B. Podolsky, and N. Rosen, "Can quantum-mechanical description of physical reality be considered complete?", Physical Review **47**, 777–780 (1935) (cited on page 53).

[111]J. S. Bell, "On the einstein podolsky rosen paradox", Physics Physique Fizika **1**, 195–200 (1964) (cited on page 53).

[112]A. Aspect, J. Dalibard, and G. Roger, "Experimental test of bell's inequalities using time-varying analyzers", Physical Review Letters **49**, 1804–1807 (1982) (cited on page 53).

[113]R. Horodecki, P. Horodecki, M. Horodecki, and K. Horodecki, "Quantum entanglement", Reviews of Modern Physics **81**, 865–942 (2009) (cited on page 53).

[114]M. A. Nielsen and I. L. Chuang, *Quantum computation and quantum information*, 10th anniversary ed (Cambridge University Press, Cambridge ; New York, 2010) (cited on page 53).

[115]L. Amico, R. Fazio, A. Osterloh, and V. Vedral, "Entanglement in many-body systems", Reviews of Modern Physics **80**, 517–576 (2008) (cited on page 53).

[116]J.-W. Pan, Z.-B. Chen, C.-Y. Lu, H. Weinfurter, A. Zeilinger, and M. Żukowski, "Multiphoton entanglement and interferometry", Reviews of Modern Physics **84**, 777–838 (2012) (cited on page 53).

[117]G. Wendin, "Quantum information processing with superconducting circuits: a review", Reports on Progress in Physics **80**, 106001 (2017) (cited on page 53).

[118]R. Blatt and D. Wineland, "Entangled states of trapped atomic ions", Nature **453**, 1008–1015 (2008) (cited on page 53).

[119]M. Saffman, T. G. Walker, and K. Mølmer, "Quantum information with rydberg atoms", Reviews of Modern Physics **82**, 2313–2363 (2010) (cited on page 53).

[120]L. Pezzè, A. Smerzi, M. K. Oberthaler, R. Schmied, and P. Treutlein, "Quantum metrology with nonclassical states of atomic ensembles", Reviews of Modern Physics **90**, 035005 (2018) (cited on page 53).

[121]A. Sørensen, L.-M. Duan, J. I. Cirac, and P. Zoller, "Many-particle entanglement with bose–einstein condensates", Nature **409**, 63–66 (2001) (cited on page 54).

[122]A. S. Sørensen and K. Mølmer, "Entanglement and extreme spin squeezing", Physical Review Letters **86**, 4431–4434 (2001) (cited on page 54).

[123]J. Estève, C. Gross, A. Weller, S. Giovanazzi, and M. K. Oberthaler, "Squeezing and entanglement in a bose–einstein condensate", Nature **455**, 1216–1219 (2008) (cited on page 54).

[124]P. Hyllus, W. Laskowski, R. Krischek, C. Schwemmer, W. Wieczorek, H. Weinfurter, L. Pezzé, and A. Smerzi, "Fisher information and multiparticle entanglement", Physical Review A **85**, 022321 (2012) (cited on page 54).

[125]G. Tóth, "Multipartite entanglement and high-precision metrology", Physical Review A **85**, 022322 (2012) (cited on page 54).

[126]S. Chaudhury, S. Merkel, T. Herr, A. Silberfarb, I. H. Deutsch, and P. S. Jessen, "Quantum control of the hyperfine spin of a cs atom ensemble", Physical Review Letters **99**, 163002 (2007) (cited on page 54).

[127]T. Fernholz, H. Krauter, K. Jensen, J. F. Sherson, A. S. Sørensen, and E. S. Polzik, "Spin squeezing of atomic ensembles via nuclear-electronic spin entanglement", Physical Review Letters **101**, 073601 (2008) (cited on page 54).

[128]T. Chalopin, C. Bouazza, A. Evrard, V. Makhalov, D. Dreon, J. Dalibard, L. A. Sidorenkov, and S. Nascimbene, "Quantum-enhanced sensing using non-classical spin states of a highly magnetic atom", Nature Communications **9**, 4955 (2018) (cited on page 54).

[129]F. Benatti, R. Floreanini, F. Franchini, and U. Marzolino, "Entanglement in indistinguishable particle systems", Physics Reports, Entanglement in indistinguishable particle systems **878**, 1–27 (2020) (cited on page 54).

[130]O. Gühne and G. Tóth, "Entanglement detection", Physics Reports **474**, 1–75 (2009) (cited on page 54).

[131]S. A. Hill and W. K. Wootters, "Entanglement of a pair of quantum bits", Physical Review Letters **78**, 5022–5025 (1997) (cited on page 54).

[132]G. Tóth and O. Gühne, "Detecting genuine multipartite entanglement with two local measurements", Physical Review Letters **94**, 060501 (2005) (cited on page 54).

[133]R. Horodecki and M. Horodecki, "Information-theoretic aspects of inseparability of mixed states", Physical Review A **54**, 1838–1843 (1996) (cited on page 54).

[134]R. Konig, R. Renner, and C. Schaffner, "The operational meaning of min- and max-entropy", IEEE Transactions on Information Theory **55**, 4337–4347 (2009) (cited on page 54).

[135]W. Dür, G. Vidal, and J. I. Cirac, "Three qubits can be entangled in two inequivalent ways", Physical Review A **62**, 062314 (2000) (cited on page 54).

[136]P. Migdał, J. Rodriguez-Laguna, and M. Lewenstein, "Entanglement classes of permutation-symmetric qudit states: symmetric operations suffice", Physical Review A **88**, 012335 (2013) (cited on page 54).

[137]D. M. Greenberger, M. A. Horne, and A. Zeilinger, *Bell's theorem, quantum theory and conceptions of the universe* (Springer Netherlands, Dordrecht, 1989) (cited on page 54).

[138]D. Bouwmeester, J.-W. Pan, M. Daniell, H. Weinfurter, and A. Zeilinger, "Observation of three-photon greenberger-horne-zeilinger entanglement", Physical Review Letters **82**, 1345–1349 (1999) (cited on page 54).

[139]C. F. Roos, M. Riebe, H. Häffner, W. Hänsel, J. Benhelm, G. P. T. Lancaster, C. Becher, F. Schmidt-Kaler, and R. Blatt, "Control and measurement of three-qubit entangled states", Science **304**, 1478–1480 (2004) (cited on page 54).

[140]J. K. Korbicz, J. I. Cirac, and M. Lewenstein, "Spin squeezing inequalities and entanglement of n qubit states", Physical Review Letters **95**, 120502 (2005) (cited on page 56).

[141]J. Vidal, "Concurrence in collective models", Physical Review A **73**, 062318 (2006) (cited on page 56).

[142]V. I. Man'ko and O. V. Man'ko, "Spin state tomography", Journal of Experimental and Theoretical Physics **85**, 430–434 (1997) (cited on page 56).

[143]J. J. . Bollinger, W. M. Itano, D. J. Wineland, and D. J. Heinzen, "Optimal frequency measurements with maximally correlated states", Physical Review A **54**, R4649–R4652 (1996) (cited on page 58).

[144]C.-W. Lee and H. Jeong, "Quantification of macroscopic quantum superpositions within phase space", Physical Review Letters **106**, 220401 (2011) (cited on page 59).

[145]W. K. Wootters and W. H. Zurek, "Complementarity in the double-slit experiment: quantum nonseparability and a quantitative statement of bohr's principle", Physical Review D **19**, 473–484 (1979) (cited on page 59).

[146]B.-G. Englert, "Fringe visibility and which-way information: an inequality", Physical Review Letters **77**, 2154–2157 (1996) (cited on page 59).

[147]D. L. Moehring, P. Maunz, S. Olmschenk, K. C. Younge, D. N. Matsukevich, L.-M. Duan, and C. Monroe, "Entanglement of single-atom quantum bits at a distance", Nature **449**, 68–71 (2007) (cited on page 60).

[148]D. Cozzolino, B. Da Lio, D. Bacco, and L. K. Oxenløwe, "High-dimensional quantum communication: benefits, progress, and future challenges", Advanced Quantum Technologies **2**, 1900038 (2019) (cited on page 60).

[149]Y. Aharonov and D. Bohm, "Significance of electromagnetic potentials in the quantum theory", Physical Review **115**, 485–491 (1959) (cited on page 61).

[150]M. V. Berry, "Quantal phase factors accompanying adiabatic changes", Proceedings of the Royal Society of London. A. Mathematical and Physical Sciences **392**, 45–57 (1984) (cited on pages 61, 62).

[151]D. Xiao, M.-C. Chang, and Q. Niu, "Berry phase effects on electronic properties", Reviews of Modern Physics **82**, 1959–2007 (2010) (cited on pages 63, 65, 78).

[152]J. Dalibard, "La matière topologique et son exploration avec les gaz quantiques", in (Collège de France, 2017), p. 155 (cited on pages 63, 78).

[153]R. Dum and M. Olshanii, "Gauge structures in atom-laser interaction: bloch oscillations in a dark lattice", Physical Review Letters **76**, 1788–1791 (1996) (cited on pages 65, 66).

[154]G. Juzeliūnas and P. Öhberg, "Slow light in degenerate fermi gases", Physical Review Letters **93**, 033602 (2004) (cited on page 65).

[155]G. Juzeliūnas, J. Ruseckas, P. Öhberg, and M. Fleischhauer, "Light-induced effective magnetic fields for ultracold atoms in planar geometries", Physical Review A **73**, 025602 (2006) (cited on pages 65, 152).

[156]Y.-J. Lin, K. Jiménez-García, and I. B. Spielman, "Spin–orbit-coupled bose–einstein condensates", Nature **471**, 83–86 (2011) (cited on page 66).

[157]N. Goldman, G. Juzeliūnas, P. Öhberg, and I. B. Spielman, "Light-induced gauge fields for ultracold atoms", Reports on Progress in Physics **77**, 126401 (2014) (cited on pages 66, 67).

[158]M. Taherinejad, K. F. Garrity, and D. Vanderbilt, "Wannier center sheets in topological insulators", Physical Review B **89**, 115102 (2014) (cited on pages 67, 130).

[159]C. R. Dean, L. Wang, P. Maher, C. Forsythe, F. Ghahari, Y. Gao, J. Katoch, M. Ishigami, P. Moon, M. Koshino, T. Taniguchi, K. Watanabe, K. L. Shepard, J. Hone, and P. Kim, "Hofstadter's butterfly and the fractal quantum hall effect in moiré superlattices", Nature **497**, 598–602 (2013) (cited on page 67).

[160]L. A. Ponomarenko, R. V. Gorbachev, G. L. Yu, D. C. Elias, R. Jalil, A. A. Patel, A. Mishchenko, A. S. Mayorov, C. R. Woods, J. R. Wallbank, M. Mucha-Kruczynski, B. A. Piot, M. Potemski, I. V. Grigorieva, K. S. Novoselov, F. Guinea, V. I. Fal'ko, and A. K. Geim, "Cloning of dirac fermions in graphene superlattices", Nature **497**, 594–597 (2013) (cited on page 67).

[161]Z. Wang, Y. Chong, J. D. Joannopoulos, and M. Soljačić, "Observation of unidirectional backscattering-immune topological electromagnetic states", Nature **461**, 772–775 (2009) (cited on pages 67, 137).

[162]M. Hafezi, S. Mittal, J. Fan, A. Migdall, and J. M. Taylor, "Imaging topological edge states in silicon photonics", Nature Photonics **7**, 1001–1005 (2013) (cited on page 67).

[163]M. C. Rechtsman, J. M. Zeuner, Y. Plotnik, Y. Lumer, D. Podolsky, F. Dreisow, S. Nolte, M. Segev, and A. Szameit, "Photonic floquet topological insulators", Nature **496**, 196–200 (2013) (cited on page 67).

[164]D. Yoshioka, *The quantum hall effect*, edited by M. Cardona, P. Fulde, K. von Klitzing, H.-J. Queisser, R. Merlin, and H. Störmer, Vol. 133, Springer Series in Solid-State Sciences (Springer Berlin Heidelberg, Berlin, Heidelberg, 2002) (cited on page 67).

[165]B. Douçot, "Introduction to the theory of the integer quantum hall effect", Comptes Rendus Physique, Quantum Hall Effect and Metrology **12**, 323–331 (2011) (cited on page 67).

[166]J. Dalibard, *Le magnétisme artificiel pour les gaz d'atomes froids* (Collège de France, 2013) (cited on page 67).

[167]D. Tong, *Quamtum hall effect* (Cambridge, Centre for Mathematical Sciences, 2016) (cited on page 67).

[168]J. Zak, "Magnetic translation group", Physical Review **134**, A1602–A1606 (1964) (cited on page 69).

[169]E. Brown, "Bloch electrons in a uniform magnetic field", Physical Review **133**, A1038–A1044 (1964) (cited on page 69).

[170]W. Florek, "Local gauge and magnetic translation groups", Acta Physica Polonica A **92**, 399–402 (1997) (cited on page 69).

[171]K. von Klitzing, "The quantized hall effect", Reviews of Modern Physics **58**, 519–531 (1986) (cited on page 72).

[172]Q. Niu and D. J. Thouless, "Quantised adiabatic charge transport in the presence of substrate disorder and many-body interaction", Journal of Physics A: Mathematical and General **17**, 2453–2462 (1984) (cited on page 77).

[173]J. Bellissard, A. van Elst, and H. Schulz- Baldes, "The noncommutative geometry of the quantum hall effect", Journal of Mathematical Physics **35**, 5373–5451 (1994) (cited on page 77).

[174]L. Wang, M. Troyer, and X. Dai, "Topological charge pumping in a one-dimensional optical lattice", Physical Review Letters **111**, 026802 (2013) (cited on pages 78, 81).

[175]R. D. King-Smith and D. Vanderbilt, "Theory of polarization of crystalline solids", Physical Review B **47**, 1651–1654 (1993) (cited on page 78).

[176]R. Resta, "Macroscopic polarization in crystalline dielectrics: the geometric phase approach", Reviews of Modern Physics **66**, 899–915 (1994) (cited on page 78).

[177]R. Resta and D. Vanderbilt, "Theory of polarization: a modern approach", in *Physics of ferroelectrics: a modern perspective*, Topics in Applied Physics (Springer, Berlin, Heidelberg, 2007), pp. 31–68 (cited on page 78).

[178]R. Karplus and J. M. Luttinger, "Hall effect in ferromagnetics", Physical Review **95**, 1154–1160 (1954) (cited on page 79).

[179]E. N. Adams and E. I. Blount, "Energy bands in the presence of an external force field—ii: anomalous velocities", Journal of Physics and Chemistry of Solids **10**, 286–303 (1959) (cited on page 79).

[180]H.-I. Lu, M. Schemmer, L. M. Aycock, D. Genkina, S. Sugawa, and I. B. Spielman, "Geometrical pumping with a bose-einstein condensate", Physical Review Letters **116**, 200402 (2016) (cited on pages 79, 133).

[181]W.-K. Shih and Q. Niu, "Nonadiabatic particle transport in a one-dimensional electron system", Physical Review B **50**, 11902–11910 (1994) (cited on page 80).

[182]L. Privitera, A. Russomanno, R. Citro, and G. E. Santoro, "Nonadiabatic breaking of topological pumping", Physical Review Letters **120**, 106601 (2018) (cited on page 80).

[183]M.-C. Chang and Q. Niu, "Berry phase, hyperorbits, and the hofstadter spectrum", Physical Review Letters **75**, 1348–1351 (1995) (cited on page 81).

[184]M.-C. Chang and Q. Niu, "Berry phase, hyperorbits, and the hofstadter spectrum: semiclassical dynamics in magnetic bloch bands", Physical Review B **53**, 7010–7023 (1996) (cited on pages 81, 144).

[185]D. C. Tsui, H. L. Stormer, and A. C. Gossard, "Two-dimensional magnetotransport in the extreme quantum limit", Physical Review Letters **48**, 1559–1562 (1982) (cited on page 82).

[186]H. L. Stormer, "Nobel lecture: the fractional quantum hall effect", Reviews of Modern Physics **71**, 875–889 (1999) (cited on page 82).

[187]R. E. Prange, S. M. Girvin, J. L. Birman, H. Faissner, and J. W. Lynn, eds., *The quantum hall effect*, Graduate Texts in Contemporary Physics (Springer New York, New York, NY, 1990) (cited on page 82).

[188]T. Neupert, L. Santos, C. Chamon, and C. Mudry, "Fractional quantum hall states at zero magnetic field", Physical Review Letters **106**, 236804 (2011) (cited on page 82).

[189]D. N. Sheng, Z.-C. Gu, K. Sun, and L. Sheng, "Fractional quantum hall effect in the absence of landau levels", Nature Communications **2**, 389 (2011) (cited on page 82).

[190]A. Stern, "Anyons and the quantum hall effect—a pedagogical review", Annals of Physics, January Special Issue 2008 **323**, 204–249 (2008) (cited on page 82).

[191]R. B. Laughlin, "Anomalous quantum hall effect: an incompressible quantum fluid with fractionally charged excitations", Physical Review Letters **50**, 1395–1398 (1983) (cited on page 82).

[192]J. K. Jain, "Composite-fermion approach for the fractional quantum hall effect", Physical Review Letters **63**, 199–202 (1989) (cited on page 82).

[193]G. Moore and N. Read, "Nonabelions in the fractional quantum hall effect", Nuclear Physics B **360**, 362–396 (1991) (cited on page 82).

[194]N. Read and E. Rezayi, "Beyond paired quantum hall states: parafermions and incompressible states in the first excited landau level", Physical Review B **59**, 8084–8092 (1999) (cited on page 82).

[195]N. Cooper, "Rapidly rotating atomic gases", Advances in Physics **57**, 539–616 (2008) (cited on page 82).

[196]E. Cornfeld and E. Sela, "Chiral currents in one-dimensional fractional quantum hall states", Physical Review B **92**, 115446 (2015) (cited on page 83).

[197]A. Petrescu and K. Le Hur, "Chiral mott insulators, meissner effect, and laughlin states in quantum ladders", Physical Review B **91**, 054520 (2015) (cited on page 83).

[198]M. Calvanese Strinati, E. Cornfeld, D. Rossini, S. Barbarino, M. Dalmonte, R. Fazio, E. Sela, and L. Mazza, "Laughlin-like states in bosonic and fermionic atomic synthetic ladders", Physical Review X **7**, 021033 (2017) (cited on page 83).

[199]E. J. Bergholtz and A. Karlhede, "Quantum hall system in tao-thouless limit", Physical Review B **77**, 155308 (2008) (cited on page 83).

[200]R. Tao and D. J. Thouless, "Fractional quantization of hall conductance", Physical Review B **28**, 1142–1144 (1983) (cited on page 83).

[201]B. A. Bernevig and N. Regnault, *Thin-torus limit of fractional topological insulators*, Apr. 2012, arXiv:1204.5682 [cond-mat.str-el] (cited on page 83).

[202]R. B. Laughlin, "Nobel lecture: fractional quantization", Reviews of Modern Physics **71**, 863–874 (1999) (cited on page 84).

[203]P. Marra, R. Citro, and C. Ortix, "Fractional quantization of the topological charge pumping in a one-dimensional superlattice", Physical Review B **91**, 125411 (2015) (cited on page 84).

[204]T.-S. Zeng, W. Zhu, and D. N. Sheng, "Fractional charge pumping of interacting bosons in one-dimensional superlattice", Physical Review B **94**, 235139 (2016) (cited on page 84).

[205]C. Schweizer, M. Lohse, R. Citro, and I. Bloch, "Spin pumping and measurement of spin currents in optical superlattices", Physical Review Letters **117**, 170405 (2016) (cited on page 84).

[206]M. Jürgensen, S. Mukherjee, and M. C. Rechtsman, "Quantized nonlinear thouless pumping", Nature **596**, 63–67 (2021) (cited on page 84).

[207]M. Jürgensen, S. Mukherjee, C. Jörg, and M. C. Rechtsman, *Quantized fractional thouless pumping of solitons*, Jan. 2022, arXiv:2201.08258 [physics.optics] (cited on page 84).

[208]A.-S. Walter, Z. Zhu, M. Gächter, J. Minguzzi, S. Roschinski, K. Sandholzer, K. Viebahn, and T. Esslinger, *Breakdown of quantisation in a hubbard-thouless pump*, Apr. 2022, arXiv:2204.06561 [cond-mat, physics:physics] (cited on page 84).

[209]T.-S. Zeng, C. Wang, and H. Zhai, "Charge pumping of interacting fermion atoms in the synthetic dimension", Physical Review Letters **115**, 095302 (2015) (cited on page 84).

[210]L. Taddia, E. Cornfeld, D. Rossini, L. Mazza, E. Sela, and R. Fazio, "Topological fractional pumping with alkaline-earth-like atoms in synthetic lattices", Physical Review Letters **118**, 230402 (2017) (cited on page 84).

[211]A. Fabre, J.-B. Bouhiron, T. Satoor, R. Lopes, and S. Nascimbene, "Simulating two-dimensional dynamics within a large-size atomic spin", Physical Review A **105**, 013301 (2022) (cited on page 85).

[212]E. Lustig, S. Weimann, Y. Plotnik, Y. Lumer, M. A. Bandres, A. Szameit, and M. Segev, "Photonic topological insulator in synthetic dimensions", Nature **567**, 356–360 (2019) (cited on pages 85, 87).

[213]D. I. Tsomokos, S. Ashhab, and F. Nori, "Using superconducting qubit circuits to engineer exotic lattice systems", Physical Review A **82**, 052311 (2010) (cited on page 86).

[214]D. Jukić and H. Buljan, "Four-dimensional photonic lattices and discrete tesseract solitons", Physical Review A **87**, 013814 (2013) (cited on page 86).

[215]A. Schwartz and B. Fischer, "Laser mode hyper-combs", Optics Express **21**, 6196–6204 (2013) (cited on page 86).

[216]S. Barbarino, M. Dalmonte, R. Fazio, and G. E. Santoro, "Topological phases in frustrated synthetic ladders with an odd number of legs", Physical Review A **97**, 013634 (2018) (cited on page 87).

[217]T. Ozawa, H. M. Price, A. Amo, N. Goldman, M. Hafezi, L. Lu, M. C. Rechtsman, D. Schuster, J. Simon, O. Zilberberg, and I. Carusotto, "Topological photonics", Reviews of Modern Physics **91**, 015006 (2019) (cited on pages 87, 104).

[218]Y. E. Kraus, Z. Ringel, and O. Zilberberg, "Four-dimensional quantum hall effect in a two-dimensional quasicrystal", Physical Review Letters **111**, 226401 (2013) (cited on page 87).

[219]L. Yuan, M. Xiao, Q. Lin, and S. Fan, "Synthetic space with arbitrary dimensions in a few rings undergoing dynamic modulation", Physical Review B **97**, 104105 (2018) (cited on page 87).

[220]T. Ozawa and H. M. Price, "Topological quantum matter in synthetic dimensions", Nature Reviews Physics **1**, 349–357 (2019) (cited on page 87).

[221]L. Yuan, Q. Lin, M. Xiao, and S. Fan, "Synthetic dimension in photonics", Optica **5**, 1396–1405 (2018) (cited on page 88).

[222]E. J. Meier, F. A. An, and B. Gadway, "Atom-optics simulator of lattice transport phenomena", Physical Review A **93**, 051602 (2016) (cited on page 89).

[223]F. A. An, E. J. Meier, and B. Gadway, "Direct observation of chiral currents and magnetic reflection in atomic flux lattices", Science Advances **3**, e1602685 (2017) (cited on page 89).

[224]H. M. Price, T. Ozawa, and N. Goldman, "Synthetic dimensions for cold atoms from shaking a harmonic trap", Physical Review A **95**, 023607 (2017) (cited on pages 89, 104).

[225]G. Salerno, H. M. Price, M. Lebrat, S. Häusler, T. Esslinger, L. Corman, J.-P. Brantut, and N. Goldman, "Quantized hall conductance of a single atomic wire:

a proposal based on synthetic dimensions", Physical Review X **9**, 041001 (2019) (cited on page 89).

[226]C. Oliver, A. Smith, T. Easton, G. Salerno, V. Guarrera, N. Goldman, G. Barontini, and H. M. Price, *Bloch oscillations along a synthetic dimension of atomic trap states*, Dec. 2021, arXiv:2112.10648 [cond-mat, physics:physics, physics:quant-ph] (cited on page 89).

[227]J. H. Kang, J. H. Han, and Y. Shin, "Realization of a cross-linked chiral ladder with neutral fermions in a 1d optical lattice by orbital-momentum coupling", Physical Review Letters **121**, 150403 (2018) (cited on page 89).

[228]L. F. Livi, G. Cappellini, M. Diem, L. Franchi, C. Clivati, M. Frittelli, F. Levi, D. Calonico, J. Catani, M. Inguscio, and L. Fallani, "Synthetic dimensions and spin-orbit coupling with an optical clock transition", Physical Review Letters **117**, 220401 (2016) (cited on page 89).

[229]S. Kolkowitz, S. L. Bromley, T. Bothwell, M. L. Wall, G. E. Marti, A. P. Koller, X. Zhang, A. M. Rey, and J. Ye, "Spin–orbit-coupled fermions in an optical lattice clock", Nature **542**, 66–70 (2017) (cited on page 89).

[230]T. Holstein and H. Primakoff, "Field dependence of the intrinsic domain magnetization of a ferromagnet", Physical Review **58**, 1098–1113 (1940) (cited on page 92).

[231]S. M. Barnett and D. T. Pegg, "Quantum theory of rotation angles", Physical Review A **41**, 3427–3435 (1990) (cited on page 96).

[232]R. Lynch, "The quantum phase problem: a critical review", Physics Reports **256**, 367–436 (1995) (cited on pages 96, 130).

[233]N. Goldman and J. Dalibard, "Periodically driven quantum systems: effective hamiltonians and engineered gauge fields", Physical Review X **4**, 031027 (2014) (cited on page 103).

[234]M. Łącki, H. Pichler, A. Sterdyniak, A. Lyras, V. E. Lembessis, O. Al-Dossary, J. C. Budich, and P. Zoller, "Quantum hall physics with cold atoms in cylindrical optical lattices", Physical Review A **93**, 013604 (2016) (cited on page 104).

[235]L. Barbiero, L. Chomaz, S. Nascimbene, and N. Goldman, "Bose-hubbard physics in synthetic dimensions from interaction trotterization", Physical Review Research **2**, 043340 (2020) (cited on page 104).

[236]M. A. Cazalilla and A. M. Rey, "Ultracold fermi gases with emergent su(N) symmetry", Reports on Progress in Physics **77**, 124401 (2014) (cited on page 105).

[237]B. J. DeSalvo, M. Yan, P. G. Mickelson, Y. N. Martinez de Escobar, and T. C. Killian, "Degenerate fermi gas of ^{87}Sr", Physical Review Letters **105**, 030402 (2010) (cited on page 105).

[238]T. Fukuhara, Y. Takasu, M. Kumakura, and Y. Takahashi, "Degenerate fermi gases of ytterbium", Physical Review Letters **98**, 030401 (2007) (cited on page 105).

[239]C. Honerkamp and W. Hofstetter, "Ultracold fermions and the SU(N) hubbard model", Physical Review Letters **92**, 170403 (2004) (cited on page 105).

[240]M. Hermele, V. Gurarie, and A. M. Rey, "Mott insulators of ultracold fermionic alkaline earth atoms: underconstrained magnetism and chiral spin liquid", Physical Review Letters **103**, 135301 (2009) (cited on page 105).

[241]G. Pagano, M. Mancini, G. Cappellini, P. Lombardi, F. Schäfer, H. Hu, X.-J. Liu, J. Catani, C. Sias, M. Inguscio, and L. Fallani, "A one-dimensional liquid of fermions with tunable spin", Nature Physics **10**, 198–201 (2014) (cited on page 105).

[242]C. Hofrichter, L. Riegger, F. Scazza, M. Höfer, D. R. Fernandes, I. Bloch, and S. Fölling, "Direct probing of the mott crossover in the su(N) fermi-hubbard model", Physical Review X **6**, 021030 (2016) (cited on page 105).

[243]A. Fabre, J.-B. Bouhiron, T. Satoor, R. Lopes, and S. Nascimbene, "Laughlin's topological charge pump in an atomic hall cylinder", Physical Review Letters **128**, 173202 (2022) (cited on page 107).

[244]C.-H. Li, Y. Yan, S.-W. Feng, S. Choudhury, D. B. Blasing, Q. Zhou, and Y. P. Chen, "Bose-einstein condensate on a synthetic topological hall cylinder", PRX Quantum **3**, 010316 (2022) (cited on pages 107, 109, 121).

[245]J. H. Han, J. H. Kang, and Y. Shin, "Band gap closing in a synthetic hall tube of neutral fermions", Physical Review Letters **122**, 065303 (2019) (cited on pages 107, 109, 121).

[246]Q.-Y. Liang, D. Trypogeorgos, A. Valdés-Curiel, J. Tao, M. Zhao, and I. B. Spielman, "Coherence and decoherence in the harper-hofstadter model", Physical Review Research **3**, 023058 (2021) (cited on pages 108, 109, 121, 129).

[247]D. Trypogeorgos, A. Valdés-Curiel, N. Lundblad, and I. B. Spielman, "Synthetic clock transitions via continuous dynamical decoupling", Physical Review A **97**, 013407 (2018) (cited on page 108).

[248]R. P. Anderson, D. Trypogeorgos, A. Valdés-Curiel, Q.-Y. Liang, J. Tao, M. Zhao, T. Andrijauskas, G. Juzeliūnas, and I. B. Spielman, "Realization of a deeply subwavelength adiabatic optical lattice", Physical Review Research **2**, 013149 (2020) (cited on pages 120, 129).

[249]D. R. Hofstadter, "Energy levels and wave functions of bloch electrons in rational and irrational magnetic fields", Physical Review B **14**, 2239–2249 (1976) (cited on page 121).

[250]F. D. M. Haldane, "Model for a quantum hall effect without landau levels: condensed-matter realization of the "parity anomaly"", Physical Review Letters **61**, 2015–2018 (1988) (cited on page 121).

[251]Y. Yan, S.-L. Zhang, S. Choudhury, and Q. Zhou, "Emergent periodic and quasiperiodic lattices on surfaces of synthetic hall tori and synthetic hall cylinders", Physical Review Letters **123**, 260405 (2019) (cited on page 129).

[252]C. Hainaut, I. Manai, J.-F. Clément, J. C. Garreau, P. Szriftgiser, G. Lemarié, N. Cherroret, D. Delande, and R. Chicireanu, "Controlling symmetry and localization with an artificial gauge field in a disordered quantum system", Nature Communications **9**, 1382 (2018) (cited on page 132).

[253]T. Kaluza, "Zum unitätsproblem der physik", Sitzungsber. Preuss. Akad. Wiss. Berlin (Math. Phys.) **1921**, 966–972 (1921) (cited on page 137).

[254]O. Klein, "Quantentheorie und fünfdimensionale Relativitätstheorie", Zeitschrift für Physik **37**, 895–906 (1926) (cited on page 137).

[255]S.-C. Zhang and J. Hu, "A four-dimensional generalization of the quantum hall effect", Science **294**, 823–828 (2001) (cited on pages 137, 138).

[256]H. Elvang and J. Polchinski, "The quantum hall effect on $\mathcal{R}^4$", Comptes Rendus Physique **4**, 405–417 (2003) (cited on page 137).

[257]F. D. M. Haldane and S. Raghu, "Possible realization of directional optical waveguides in photonic crystals with broken time-reversal symmetry", Physical Review Letters **100**, 013904 (2008) (cited on page 137).

[258]L. Lu, H. Gao, and Z. Wang, "Topological one-way fiber of second chern number", Nature Communications **9**, 5384 (2018) (cited on page 137).

[259]C.-K. Chiu, J. C. Y. Teo, A. P. Schnyder, and S. Ryu, "Classification of topological quantum matter with symmetries", Reviews of Modern Physics **88**, 035005 (2016) (cited on page 137).

[260]R.-P. Riwar, M. Houzet, J. S. Meyer, and Y. V. Nazarov, "Multi-terminal josephson junctions as topological matter", Nature Communications **7**, 11167 (2016) (cited on page 137).

[261]H. Weyl, "Elektron und Gravitation. I", Zeitschrift für Physik **56**, 330–352 (1929) (cited on page 138).

[262]X. Wan, A. M. Turner, A. Vishwanath, and S. Y. Savrasov, "Topological semimetal and fermi-arc surface states in the electronic structure of pyrochlore iridates", Physical Review B **83**, 205101 (2011) (cited on page 138).

[263]L. Lu, Z. Wang, D. Ye, L. Ran, L. Fu, J. D. Joannopoulos, and M. Soljačić, "Experimental observation of weyl points", Science **349**, 622–624 (2015) (cited on page 138).

[264]S.-Y. Xu, I. Belopolski, N. Alidoust, M. Neupane, G. Bian, C. Zhang, R. Sankar, G. Chang, Z. Yuan, C.-C. Lee, S.-M. Huang, H. Zheng, J. Ma, D. S. Sanchez, B. Wang, A. Bansil, F. Chou, P. P. Shibayev, H. Lin, S. Jia, and M. Z. Hasan, "Discovery of a weyl fermion semimetal and topological fermi arcs", Science **349**, 613–617 (2015) (cited on page 138).

[265]A. H. Castro Neto, F. Guinea, N. M. R. Peres, K. S. Novoselov, and A. K. Geim, "The electronic properties of graphene", Reviews of Modern Physics **81**, 109–162 (2009) (cited on page 138).

[266]S. Sugawa, F. Salces-Carcoba, A. R. Perry, Y. Yue, and I. B. Spielman, "Second chern number of a quantum-simulated non-abelian yang monopole", Science **360**, 1429–1434 (2018) (cited on page 138).

[267]X. Tan, D.-W. Zhang, W. Zheng, X. Yang, S. Song, Z. Han, Y. Dong, Z. Wang, D. Lan, H. Yan, S.-L. Zhu, and Y. Yu, "Experimental observation of tensor monopoles with a superconducting qudit", Physical Review Letters **126**, 017702 (2021) (cited on page 138).

[268]M. Chen, C. Li, G. Palumbo, Y.-Q. Zhu, N. Goldman, and P. Cappellaro, "A synthetic monopole source of kalb-ramond field in diamond", Science **375**, 1017–1020 (2022) (cited on page 138).

[269]P. A. M. Dirac, "Quantised singularities in the electromagnetic field," Proceedings of the Royal Society of London. Series A, Containing Papers of a Mathematical and Physical Character **133**, 60–72 (1931) (cited on page 138).

[270]C. N. Yang, "Generalization of dirac's monopole to su_2 gauge fields", Journal of Mathematical Physics **19**, 320–328 (1978) (cited on page 138).

[271]V. Celli and N. D. Mermin, "Ground state of an electron gas in a magnetic field", Physical Review **140**, A839–A853 (1965) (cited on page 138).

[272]B. I. Halperin, "Possible states for a three-dimensional electron gas in a strong magnetic field", Japanese Journal of Applied Physics **26**, 1913 (1987) (cited on page 138).

[273]M. Kohmoto, B. I. Halperin, and Y.-S. Wu, "Diophantine equation for the three-dimensional quantum hall effect", Physical Review B **45**, 13488–13493 (1992) (cited on page 138).

[274]F. Tang, Y. Ren, P. Wang, R. Zhong, J. Schneeloch, S. A. Yang, K. Yang, P. A. Lee, G. Gu, Z. Qiao, and L. Zhang, "Three-dimensional quantum hall effect and metal–insulator transition in $zrte_5$", Nature **569**, 537–541 (2019) (cited on page 138).

[275]J. Fröhlich and B. Pedrini, "New applications of the chiral anomaly", in *Mathematical physics 2000* (Imperial College Press, May 2000), pp. 9–47 (cited on page 138).

[276]D. Karabali and V. P. Nair, "Quantum hall effect in higher dimensions", Nuclear Physics B **641**, 533–546 (2002) (cited on page 138).

[277]I. Petrides, H. M. Price, and O. Zilberberg, "Six-dimensional quantum hall effect and three-dimensional topological pumps", Physical Review B **98**, 125431 (2018) (cited on page 138).

[278]C. H. Lee, Y. Wang, Y. Chen, and X. Zhang, "Electromagnetic response of quantum hall systems in dimensions five and six and beyond", Physical Review B **98**, 094434 (2018) (cited on page 138).

[279]M. Lohse, C. Schweizer, H. M. Price, O. Zilberberg, and I. Bloch, "Exploring 4d quantum hall physics with a 2d topological charge pump", Nature **553**, 55–58 (2018) (cited on page 138).

[280]O. Zilberberg, S. Huang, J. Guglielmon, M. Wang, K. P. Chen, Y. E. Kraus, and M. C. Rechtsman, "Photonic topological boundary pumping as a probe of 4d quantum hall physics", Nature **553**, 59–62 (2018) (cited on page 138).

[281]Y. Wang, H. M. Price, B. Zhang, and Y. D. Chong, "Circuit implementation of a four-dimensional topological insulator", Nature Communications **11**, 2356 (2020) (cited on page 138).

[282]H. M. Price and N. R. Cooper, "Mapping the berry curvature from semiclassical dynamics in optical lattices", Physical Review A **85**, 033620 (2012) (cited on page 144).

[283]L. E. Sadler, J. M. Higbie, S. R. Leslie, M. Vengalattore, and D. M. Stamper-Kurn, "Spontaneous symmetry breaking in a quenched ferromagnetic spinor bose–einstein condensate", Nature **443**, 312–315 (2006) (cited on page 145).

[284]J.-y. Choi, W. J. Kwon, and Y.-i. Shin, "Observation of topologically stable 2d skyrmions in an antiferromagnetic spinor bose-einstein condensate", Physical Review Letters **108**, 035301 (2012) (cited on page 145).

[285]D. M. Stamper-Kurn and M. Ueda, "Spinor bose gases: symmetries, magnetism, and quantum dynamics", Reviews of Modern Physics **85**, 1191–1244 (2013) (cited on page 145).

[286]Y. Kawaguchi and M. Ueda, "Spinor bose–einstein condensates", Physics Reports, Spinor Bose–Einstein condensates **520**, 253–381 (2012) (cited on page 145).

[287]T. Ohmi and K. Machida, "Bose-einstein condensation with internal degrees of freedom in alkali atom gases", Journal of the Physical Society of Japan **67**, 1822–1825 (1998) (cited on page 145).

[288]T.-L. Ho, "Spinor bose condensates in optical traps", Physical Review Letters **81**, 742–745 (1998) (cited on page 145).

[289]M.-S. Chang, Q. Qin, W. Zhang, L. You, and M. S. Chapman, "Coherent spinor dynamics in a spin-1 bose condensate", Nature Physics **1**, 111–116 (2005) (cited on page 145).

[290]J. Kronjäger, C. Becker, M. Brinkmann, R. Walser, P. Navez, K. Bongs, and K. Sengstock, "Evolution of a spinor condensate: coherent dynamics, dephasing, and revivals", Physical Review A **72**, 063619 (2005) (cited on page 145).

[291]A. T. Black, E. Gomez, L. D. Turner, S. Jung, and P. D. Lett, "Spinor dynamics in an antiferromagnetic spin-1 condensate", Physical Review Letters **99**, 070403 (2007) (cited on page 145).

[292]Y. Liu, S. Jung, S. E. Maxwell, L. D. Turner, E. Tiesinga, and P. D. Lett, "Quantum phase transitions and continuous observation of spinor dynamics in an antiferromagnetic condensate", Physical Review Letters **102**, 125301 (2009) (cited on page 145).

[293]P. D. Lett, P. S. Julienne, and W. D. Phillips, "Photoassociative spectroscopy of laser-cooled atoms", Annual Review of Physical Chemistry **46**, 423–452 (1995) (cited on page 146).

[294]C. R. Monroe, E. A. Cornell, C. A. Sackett, C. J. Myatt, and C. E. Wieman, "Measurement of cs-cs elastic scattering at t=30 μk", Physical Review Letters **70**, 414–417 (1993) (cited on page 146).

[295]T. Lahaye, C. Menotti, L. Santos, M. Lewenstein, and T. Pfau, "The physics of dipolar bosonic quantum gases", Reports on Progress in Physics **72**, 126401 (2009) (cited on page 146).

[296]D. L. Kovrizhin, G. V. Pai, and S. Sinha, "Density wave and supersolid phases of correlated bosons in an optical lattice", Europhysics Letters **72**, 162 (2005) (cited on page 149).

[297]G. Mazzarella, S. M. Giampaolo, and F. Illuminati, "Extended bose hubbard model of interacting bosonic atoms in optical lattices: from superfluidity to density waves", Physical Review A **73**, 013625 (2006) (cited on page 149).

[298]W. Krauth, M. Caffarel, and J.-P. Bouchaud, "Gutzwiller wave function for a model of strongly interacting bosons", Physical Review B **45**, 3137–3140 (1992) (cited on page 150).

[299]L. P. Pitaevskii and S. Stringari, *Bose-einstein condensation*, International Series of Monographs on Physics (Oxford University Press, Oxford, New York, Apr. 2003) (cited on pages 150, 152).

[300]A. L. Fetter, "Rotating trapped bose-einstein condensates", Reviews of Modern Physics **81**, 647–691 (2009) (cited on page 150).

[301]Y. Castin, Z. Hadzibabic, S. Stock, J. Dalibard, and S. Stringari, "Quantized vortices in the ideal bose gas: a physical realization of random polynomials", Physical Review Letters **96**, 040405 (2006) (cited on page 152).

[302]B. McCanna and H. M. Price, "Superfluid vortices in four spatial dimensions", Physical Review Research **3**, 023105 (2021) (cited on page 152).

[303]F. Chevy, K. W. Madison, and J. Dalibard, "Measurement of the angular momentum of a rotating bose-einstein condensate", Physical Review Letters **85**, 2223–2227 (2000) (cited on page 152).

[304]J. R. Abo-Shaeer, C. Raman, J. M. Vogels, and W. Ketterle, "Observation of vortex lattices in bose-einstein condensates", Science **292**, 476–479 (2001) (cited on page 152).

[305]P. Engels, I. Coddington, P. C. Haljan, V. Schweikhard, and E. A. Cornell, "Observation of long-lived vortex aggregates in rapidly rotating bose-einstein condensates", Physical Review Letters **90**, 170405 (2003) (cited on page 152).

[306]X. Cui, B. Lian, T.-L. Ho, B. L. Lev, and H. Zhai, "Synthetic gauge field with highly magnetic lanthanide atoms", Physical Review A **88**, 011601 (2013) (cited on page 152).

[307]D. Babik, R. Roell, D. Helten, M. Fleischhauer, and M. Weitz, "Synthetic magnetic fields for cold erbium atoms", Physical Review A **101**, 053603 (2020) (cited on page 152).

RÉSUMÉ

Cette thèse présente des études expérimentales réalisées avec des échantillons ultrafroids de dysprosium atomique. Les propriétés électroniques du dysprosium conduisent à un grand moment magnétique, un grand moment angulaire total J=8 dans l'état fondamental électronique et un riche spectre de transitions optiques fines avec des décalages lumineux tensoriels non négligeables. Notre travail repose sur l'utilisation de lasers accordés à proximité de telles transitions pour manipuler les états de spin atomiques. Nous commençons par décrire brièvement un ensemble d'expériences qui étudient l'intrication d'états non classiques préparés dans le niveau fondamental, en partitionnant explicitement le système via un couplage optique.

L'objet principal de ce manuscrit est la réalisation de champs de jauge artificiels pour le mouvement d'atomes neutres. La simulation d'un système de Hall quantique est facilitée par le grand spin dans le niveau électronique fondamental, que nous interprétons comme un réseau synthétique avec 2J+1=17 sites. Ces sites du réseau sont couplés par des transitions Raman à deux photons à l'aide de faisceaux laser contrapropageants, où l'impulsion acquise dans un processus de saut est équivalente à une phase d'Aharonov-Bohm variant dans l'espace. En utilisant une combinaison de couplages de spin de différentes portées, nous préparons de manière effective un cylindre atomique avec un axe cyclique composé de trois sites et un champ radial uniforme, produisant un effet Hall quantique sur sa surface. Nous contrôlons un flux magnétique longitudinal supplémentaire qui perce le cylindre et réalisons l'expérience de pompe topologique de Laughlin, un processus de transport quantifié de particules lié à l'effet Hall quantique entier. Nous mesurons le premier nombre de Chern, un invariant topologique, et confirmons la topologie non triviale de notre système de particules en l'absence d'interaction.

Nous présentons également des résultats expérimentaux préliminaires sur la physique de Hall quantique à quatre dimensions en couplant optiquement deux dimensions synthétiques encodées dans le spin atomique à deux dimensions spatiales. Nous décrivons ensuite théoriquement le rôle des interactions interatomiques sur le cylindre de Hall atomique et mettons en évidence leurs propriétés dans la dimension synthétique. Enfin, nous discutons une proposition pour la réalisation d'un champ de jauge artificiel pour le mouvement des atomes de dysprosium dans l'espace réel, induit par le couplage entre les degrés de liberté internes et externes.

MOTS CLÉS

Gaz quantiques, système topologique, effet Hall quantique

ABSTRACT

This thesis presents experimental studies performed with ultracold samples of atomic dysprosium. The electronic properties of dysprosium lead to a large magnetic moment, a large total angular momentum J=8 in the electronic ground state and a rich spectrum of narrow optical transitions with non-negligible tensor light shifts. Our work relies on using lasers tuned close to such transitions to manipulate atomic spin states and we begin by briefly describing a set of experiments that study the entanglement of non-classical states prepared in the ground level manifold, by explicitly partitioning the system via optical coupling.

The main focus of this manuscript is the realisation of artificial gauge fields for the motion of neutral atoms. The simulation of a quantum Hall system benefits from the large spin in the electronic ground level, which we interpret as a synthetic lattice with 2J+1=17 sites. These lattice sites are coupled by two-photon Raman transitions using counter-propagating laser beams, where the net momentum acquired in a hopping process is equivalent to a spatially varying Aharonov-Bohm phase. Combining spin couplings with different hopping ranges, we effectively engineer an atomic cylinder with a cyclic axis composed of three sites and a uniform radial field, yielding a quantum Hall effect on its surface. We control an additional longitudinal magnetic flux that pierces the cylinder and realise Laughlin's topological charge pump, a quantised particle transport process related to the integer quantum Hall effect. We measure the first Chern number, a topological invariant, and confirm the non-trivial topology of our system of non-interacting particles.

We also present preliminary experimental results on quantum Hall physics in four dimensions by optically coupling two independent synthetic dimensions encoded in the atomic spin to two spatial ones. We then describe theoretically the role of interatomic interactions on the atomic Hall cylinder and highlight their properties along the synthetic dimension. Finally, we discuss a proposal for the realisation of an artificial gauge field for the motion of dysprosium atoms in real space, mediated by the coupling between the internal and external degrees of freedom.

KEYWORDS

Quantum gases, topological system, quantum Hall effect